Leading edge blowing: A targeted approach to reduce aerofoil noise

A Thesis Submitted for the Degree of Doctor of Philosophy

By

Yash Bakrania

Department of Mechanical and Aerospace Engineering, Brunel University London

2026

Abstract

This thesis investigates steady leading-edge blowing as an active flow-control strategy for reducing aerofoil self-noise from a NACA 65(12)-10 aerofoil. The work considers three noise mechanisms: trailing-edge tonal noise, leading-edge broadband turbulence-interaction noise, and separation-stall noise. Far-field acoustic measurements are combined with hot-wire anemometry, surface-pressure measurements, and aerodynamic force measurements so that the acoustic response can be interpreted alongside the underlying flow physics.

The first part of the study examines trailing-edge tonal noise. The results show that leading-edge blowing can strongly suppress the discrete tonal radiation associated with a suction-side laminar separation bubble and the aeroacoustic feedback loop it supports. Under the most effective conditions, tonal levels are reduced by up to 20–25 dB. The main effect is not a large shift in tonal frequency, but a weakening of the organised instability and of the flow-acoustic coupling that sustains the tone.

The second part addresses leading-edge broadband noise under both isotropic and anisotropic turbulent inflow conditions. Here, the effectiveness of the control is found to depend strongly on the incoming turbulence, particularly its length scale, anisotropy, and spatial coherence. When the actuation is suitably matched to the inflow, measurable broadband reductions are achieved. These reductions are linked to a weakening of spanwise coherence and to a shortening of the effective interaction length at the leading edge, showing that the control acts by modifying the structure of the incoming disturbances before they are scattered into sound.

The final part of the thesis considers separation-stall noise at high incidence. In this regime, leading-edge blowing delays the onset of stall-related separation by up to about 3.7° and reduces the associated low-frequency acoustic radiation by up to 5 dB. The measurements show that the blowing modifies the separated-flow topology and weakens the large-scale unsteady structures that dominate the noise generation process.

Overall, the thesis shows that steady leading-edge blowing is more than a case-specific method of reducing noise. It acts as a targeted control strategy that can influence several aerofoil self-noise mechanisms through changes to the near-field flow structure. The central finding is that noise reduction is achieved by weakening the coherence and organisation of the source regions that radiate most efficiently. This provides a basis for the future design of quieter aerofoils and blade sections using tunable leading-edge actuation in applications such as aircraft, turbomachinery, propellers, and wind turbines.

Acknowledgement

I would like to express my sincere gratitude to my supervisor, Prof. Tze Pei Chong, for his unwavering support, guidance and encouragement throughout my PhD. His expertise and patience have been fundamental to the successful completion of this work. I am also very grateful to Dr. James Tyacke for his persistent support in helping me develop my CFD skills, particularly during the early stages of my research.

I would further like to thank Mr. Kevin Robinson for his invaluable technical support in enabling my experimental work and for his guidance on complex experimental setups.

My heartfelt thanks go to my peers, Dr. Max Scholz, Dr. Philip Woodhead and Mrs. Mansi Bhardwaj, for their assistance, insightful discussions and company during my research experiments.

Finally, I am profoundly grateful to my family and friends for their patience, understanding and constant support throughout this PhD.

Contents

List of Figures

Symbols

Table 1: Symbols appearing with subscripts and/or superscripts in the thesis

Symbol	Meaning
A_{PS}	*[Integration domain over the measured wake plane (Pressure Side)]*

Continued on next page

Symbol	Meaning
A_{SS}	*[Integration domain over the measured wake plane (Suction Side)]*
B_k	*[Exclusion frequency window around the k-th shedding tone]*
C_D	*[Drag Coefficient]*
C_L	*[Lift Coefficient]*
C_μ	*[Momentum coefficient of blowing]*
C_p	*[Pressure Coefficient]*
G_{11}	*[Autospectrum of hot-wire signal at reference probe (signal 1)]*
G_{12}	*[Cross-spectrum between signals 1 and 2]*
G_{22}	*[Autospectrum of hot-wire signal at traversing probe (signal 2)]*
L_x	*[Streamwise integral length scale]*
P_1/P_2	*[Acoustic Power]*
Φ_{pp}	*[One-sided far-field pressure power spectral density]*
Φ_{uu}	*[One-sided streamwise velocity power spectral density]*
Q_j	*[Volumetric flow rate per orifice]*
R_{12}	*[Normalised two-point cross-correlation]*
R^2	*[Coefficient of determination]*
S_{pp}	*[One-sided pressure power spectral density]*
T_a	*[Ambient temperature at measurement]*
T_i	*[Turbulence Intensity]*
T_∞	*[Free-stream (ambient) temperature]*
T_w	*[Hot-wire temperature]*
U_c	*[Convection velocity]*
U_∞	*[Freestream Velocity (u-component)]*
U_j	*[Jet exit velocity at the blowing orifices]*
$U_{\max}$	*[Maximum Velocity (u-component)]*
V_x	*[Voltage signal (x-component)]*
V_y	*[Voltage signal (y-component)]*
V_z	*[Voltage signal (z-component)]*
c_0	*[Speed of sound (ambient)]*
δ_ω	*[Vorticity thickness of the wake]*
d_j	*[Jet (orifice) diameter]*
ℓ_x	*[Streamwise correlation length scale]*
ℓ_z	*[Spanwise correlation length scale]*
f_1	*[Lower bound of the broadband integration band]*
f_2	*[Upper bound of the broadband integration band]*
f_k	*[Frequency of the k-th tonal component]*
f_s	*[Sampling frequency]*

Continued on next page

Symbol	Meaning
f_t	*[Dominant tonal (trailing-edge) frequency]*
γ^2	*[Magnitude-squared coherence between two signals]*
ω_x	*[Streamwise vorticity component]*
p_∞	*[Free-stream (ambient) static pressure]*
p'	*[Fluctuating acoustic pressure]*
ρ_0	*[Ambient air density]*
ρ_∞	*[Free-stream air density]*
σ^2	*[Variance of the fluctuating velocity signal]*
τ_c	*[Convection time delay]*
t_c	*[Convective time scale]*
t_t	*[Tonal time scale]*
u_1	*[Reference-point streamwise velocity fluctuation signal]*
u_2	*[Second-point streamwise velocity fluctuation signal]*
u'	*[Fluctuating streamwise velocity component]*
v'	*[Fluctuating wall-normal (cross-stream) velocity component]*

Subscripts

Table 2: Subscripts used in the thesis

Subscript	Meaning
D	*[Drag]*
L	*[Lift]*
M	*[Mean]*
PS	*[Pressure Side]*
SS	*[Suction Side]*
a	*[Ambient (air)]*
c	*[Chordwise]*
h	*[Hot-wire]*
∞	*[Free-stream]*
j	*[Jet (blowing) quantity]*
$\max$	*[Maximum value]*
μ	*[Momentum coefficient]*
ω	*[Vorticity based]*
p	*[Pressure]*
pp	*[Pressure–pressure spectrum]*

Subscript	Meaning
t	*[Tonal]*
u	*[Streamwise velocity component]*
uu	*[Velocity–velocity autospectrum]*
x	*[Streamwise component]*
y	*[Wall normal component]*
z	*[Spanwise component]*

List of Abbreviations

Table 3: List of abbreviations used in this thesis

Abbrev.	Meaning
OAPWL	*[Overall Sound Power Level]*
OASPL	*[Overall Sound Pressure Level]*
PWL	*[Sound Power Level]*
SPL	*[Sound Pressure Level]*
LEB	*[Leading-Edge Blowing]*
LEBN	*[Leading-Edge Broadband Noise]*
LSB	*[Laminar Separation Bubble]*
T-S	*[Tollmien–Schlichting]*
TBL	*[Turbulent Boundary Layer]*
BPM	*[Brooks, Pope, and Marcolini]*
CAA	*[Civil Aviation Authority]*
CAD	*[Computer Aided Design]*
CFD	*[Computational Fluid Dynamics]*
FFT	*[Fast Fourier Transform]*
FWH	*[Ffowcs-Williams and Hawkings]*
LES	*[Large Eddy Simulation]*
PSD	*[Power Spectral Density]*
RANS	*[Reynolds-Averaged Navier-Stokes]*
TI	*[Turbulence Intensity]*
BB	*[Broadband]*
CCP	*[Constant Current Power]*
CTA	*[Constant Temperature Anemometer]*
DES	*[Detached Eddy Simulation]*

Continued on next page

Abbrev.	Meaning
FF	*[Far-Field]*
HW	*[Hot Wire]*
SLS	*[Selective Laser Sintering]*
NACA	*[National Advisory Committee for Aeronautics]*
NASA	*[National Aeronautics and Space Administration]*
ICAO	*[International Civil Aviation Organization]*
JASA	*[The Journal of the Acoustical Society of America]*
JFM	*[Journal of Fluid Mechanics]*
JSV	*[Journal of Sound and Vibration]*
A/D	*[Analog-to-Digital]*
CD	*[Drag Coefficient]*
CL	*[Lift Coefficient]*
LE	*[Leading-Edge]*
LHS	*[Left Hand Side]*
PS	*[Pressure Side]*
RHS	*[Right Hand Side]*
SS	*[Suction Side]*
TE	*[Trailing-Edge]*

Chapter 1

Introduction

1.1 Background & Motivation

Aircraft noise is widely recognised as one of the most persistent environmental challenges associated with modern aviation. Unlike emissions, which disperse globally, noise is a localised pollutant. Its impact is felt most acutely by communities living around airports, where it contributes to annoyance, sleep disturbance, and longer-term health concerns [1]. For airport authorities, noise also acts as a practical constraint. It shapes flight scheduling, restricts night operations, and in many cases limits future airport expansion. In this way, noise is not only an environmental issue but also a direct barrier to the continued growth of air transport [2].

Over the past several decades, international aviation bodies have responded by introducing progressively stricter certification standards [3]. The International Civil Aviation Organization (ICAO), for example, has tightened its Chapter 3, 4, and 14 limits, requiring manufacturers to demonstrate lower acoustic footprints with each new generation of aircraft. These regulatory pressures, combined with rising air traffic demand, have made the reduction of aircraft noise an ongoing technological priority.

Much of the progress achieved so far has come from advances in propulsion systems. The transition from early turbojet engines to modern high-bypass-ratio turbofans produced a step change in noise emissions. As illustrated in Figure 1.1, the overall acoustic footprint of a typical modern wide-body airliner is strongly influenced by propulsion-related sources: engine noise remains dominated by jet and fan contributions, with fan noise becoming particularly prominent during approach. Jet exhaust noise, once the dominant contributor to total aircraft noise, was significantly reduced due to lower exhaust velocities [4, 5]. Today, the acoustic signature of commercial aircraft is no longer dominated by jet noise but by a broader mix of sources. In particular, during approach and landing, when engines operate at reduced thrust, airframe noise has become increasingly important.

Airframe noise originates from the unsteady interaction between turbulent flows and aircraft structures such as flaps, slats, landing gear, and trailing edges. Even in the absence of these

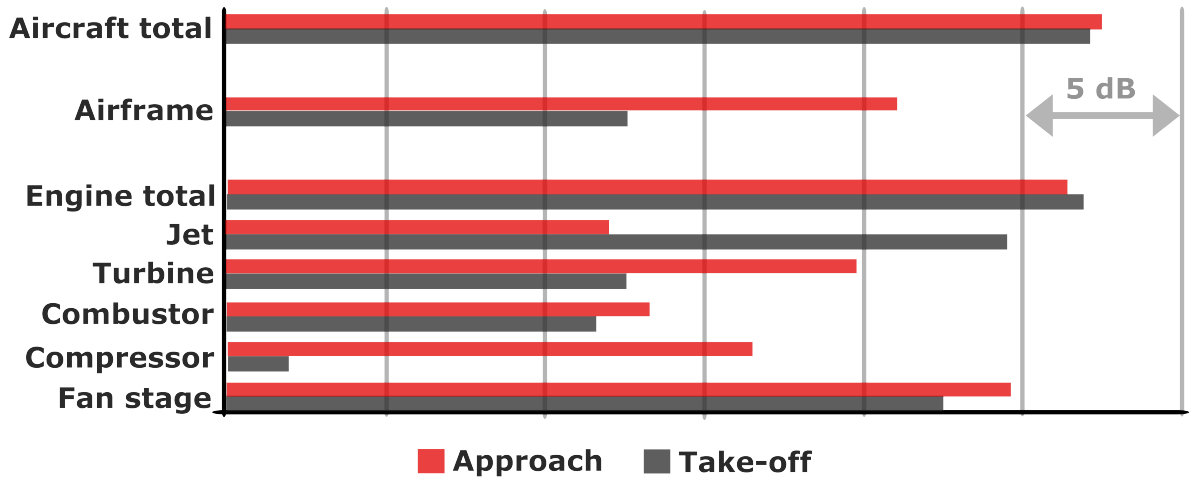

Figure 1.1: Noise contributions from components on a typical modern wide-body airliner. Adapted from Wevolver, “Reducing the noise emission from an aircraft engine at its source”.

devices, a clean wing section is not silent. An isolated airfoil generates what is termed airfoil self-noise. This form of noise persists even without inflow turbulence or installation effects, which makes it one of the most fundamental and widely studied problems in aeroacoustics [6].

The persistence of airfoil self-noise has two important implications. First, it defines a baseline noise level that cannot be avoided simply by retracting high-lift devices or optimising geometry. Second, because the underlying physical mechanisms are generic, self-noise is relevant across a wide range of applications. The same processes that limit the acoustic performance of aircraft wings are also present in turbomachinery blades, propellers, and wind turbines [7]. As such, developing strategies to better understand and control self-noise is of both scientific and industrial significance.

1.2 The Challenge of Airfoil Self-Noise

Airfoil self-noise is a fundamental source of aerodynamic sound and arises from the unsteady interaction between boundary layer turbulence and the sharp edges of a lifting surface. Unlike installation effects or external turbulence, it is intrinsic to the airfoil itself. This means that even an isolated airfoil in uniform flow will radiate sound, making self-noise a canonical benchmark problem in aeroacoustics [6].

Several mechanisms contribute to airfoil self-noise, each governed by different aspects of boundary layer physics. One of the most widely studied is trailing-edge turbulent boundary layer (TBL–TE) noise, generated when turbulent eddies convect past the trailing edge and scatter into acoustic waves [8]. This process is broadband in nature and typically dominates at moderate Reynolds numbers where the boundary layer remains attached.

Another important mechanism is tonal noise, which often manifests as discrete, narrowband peaks in the acoustic spectrum. These tones are associated with laminar boundary layer instabilities and their subsequent interaction with the trailing edge. In many cases, an acoustic feedback loop forms between the airfoil surface and the trailing edge, leading to strong tonal radiation at preferred frequencies [9, 10]. Tonal noise has been observed in a wide range of airfoils, particularly at transitional Reynolds numbers, and is often one of the most distinctive signatures of self-noise.

A third mechanism is leading-edge broadband noise, which is produced when incoming turbulence impinges on the leading edge of an airfoil. The unsteady pressure field of the inflow is scattered into sound at the stagnation region, producing a broadband acoustic signature [11]. Although this mechanism requires external turbulence, it is often grouped with self-noise processes because it depends directly on airfoil geometry and boundary layer development. Leading-edge noise is especially relevant to turbomachinery blades and rotors, where inflow turbulence levels are naturally high.

Finally, separation-induced noise occurs when the boundary layer becomes highly unsteady near stall. As the angle of attack increases, large-scale vortical structures form in the separated shear layer and shed downstream, radiating strong low-frequency sound [12]. This mechanism not only influences the acoustic field but also signals aerodynamic performance losses, which makes it of particular interest for flow control research.

In practice, these mechanisms rarely occur in isolation. Their relative importance depends on Reynolds number, Mach number, angle of attack, and airfoil geometry, and in many operating conditions they overlap to produce a complex and broadband acoustic spectrum [7]. This complexity has made airfoil self-noise both a challenging and an enduring research problem.

Understanding these noise sources is critical for two reasons. From a scientific perspective, they reveal the fundamental coupling between unsteady aerodynamics and sound radiation, offering insight into one of the most classical aeroacoustic problems. From a practical standpoint, they define the baseline or “floor” of airframe noise, the minimum noise that a lifting surface will radiate even when free from additional devices or inflow disturbances. For this reason, airfoil self-noise remains an ideal target for developing and testing new noise control strategies.

1.3 Current Approaches to Noise Reduction

Over the past two decades, a variety of strategies have been developed in an effort to mitigate airfoil self-noise. The majority of these can be grouped under the umbrella of passive flow control, where geometric modifications are introduced to alter the flow without requiring external energy input. Among the most prominent are trailing-edge serrations, which disrupt the coherence of turbulent structures as they convect past the trailing edge and thereby reduce the efficiency of acoustic scattering [13, 14]. Another widely studied device is the wavy leading edge, inspired by the flippers of humpback whales, which can alter vortex dynamics, modify flow attachment, and delay stall [15, 16]. In addition, several surface treatments have been investigated, including riblets

designed to influence boundary layer development and porous trailing edges intended to reduce pressure fluctuations at the surface [17, 18].

These approaches have demonstrated significant acoustic benefits in specific conditions. Trailing edge serrations, for example, are now considered one of the most effective passive treatments for broadband trailing-edge noise. Wavy leading edges have been shown to reduce the strength of turbulence–airfoil interaction noise, particularly when the incident turbulence has scales comparable to the imposed waviness. Porous materials, meanwhile, continue to attract attention for their ability to damp wall-pressure fluctuations and reduce the strength of scattering at the edge.

Despite their promise, passive devices also present several important limitations. Their mechanisms of action are not always fully understood, which makes it difficult to predict their effectiveness across different operating regimes [19]. Even when their benefits are clear, they are inherently inflexible. Once designed and manufactured, their geometry cannot be altered in response to changing operating states. This makes them less suitable for real aircraft, which operate across a wide range of speeds, angles of attack, and atmospheric conditions.

In parallel with experimental work, advances in computational aeroacoustics (CAA) have expanded the ability to predict airfoil noise and to test noise control concepts. High-fidelity methods such as Large Eddy Simulation (LES), Detached Eddy Simulation (DES), and hybrid RANS–LES approaches, when coupled with acoustic analogies such as those of Lighthill or Ffowcs Williams Hawkings, have produced valuable insight into the physics of trailing-edge and leading-edge noise [20, 21, 22]. These methods have been especially useful in clarifying the role of coherent structures in scattering processes. However, despite their strengths, CAA methods remain computationally expensive at the Reynolds numbers of practical interest, and transitional or separated flows are particularly challenging to capture with high accuracy.

Taken together, these limitations highlight the present state of the field: although noise reduction is clearly possible, current methods are either too rigid, in the case of passive control devices, or too resource-intensive, in the case of numerical simulations. This gap underlines the need for alternative approaches that can combine physical effectiveness with adaptability and practical feasibility.

1.4 Active Flow Control

The constraints of passive devices have encouraged growing interest in active flow control, which adds energy or momentum into the boundary layer to achieve aerodynamic and acoustic benefits. Unlike passive treatments, active strategies can be tuned in real time to match the prevailing flow state [23, 24]. This adaptability is especially valuable for aircraft, since operating conditions such as Reynolds number, angle of attack, and turbulence intensity vary continuously throughout a flight. An active system could in principle allow an aircraft to adjust its noise reduction strategy dynamically, rather than being limited by the fixed geometry of a passive device.

Several active techniques have been investigated in the aeroacoustics literature. These include

synthetic jets, which add periodic disturbances to influence shear layer development; plasma actuators, which generate small-scale momentum addition without moving parts; and steady or pulsed blowing and suction [25, 26], which directly alter boundary layer momentum. While each of these has demonstrated potential in specific contexts, the approach most relevant here is leading-edge blowing. Introducing momentum at the front of the airfoil affects boundary layer development at its earliest stage. This has two consequences of particular importance: it can suppress or delay separation at high incidence, which reduces low-frequency separation noise, and it can modify the way turbulent structures interact with the leading and trailing edges, which alters both tonal and broadband acoustic radiation [27].

Experimental studies have already shown that leading-edge blowing can reduce far-field noise levels. Most of these investigations, however, have concentrated on the acoustic results. Much less attention has been given to the flow mechanisms that bring about this reduction. The precise way in which momentum injection alters instability growth, vortex formation, or surface pressure fluctuations remains poorly understood [28].

This lack of mechanistic clarity represents an important gap in the field. Without it, it is difficult to optimise leading-edge blowing for maximum benefit, to predict how it will perform across different operating conditions, or to scale the method to practical aerodynamic surfaces. Addressing this gap forms the central motivation for the present research.

1.5 Research Aims and Questions

The overarching aim of this thesis is to investigate the potential of leading-edge blowing as a method of active aeroacoustic control, with particular emphasis on uncovering the physical mechanisms that underpin the observed reductions in airfoil self-noise. While previous studies have shown that leading-edge blowing can attenuate tonal and broadband noise, the mechanisms responsible for these changes are not yet well understood. This work therefore seeks not only to quantify the acoustic impact of the method, but also to establish the flow physics that govern its effectiveness.

The central research question guiding this investigation is:

> *How does leading-edge blowing influence the flow structures responsible for airfoil self-noise, and to what extent can it mitigate tonal, broadband, and stall-related noise mechanisms?*

To address this overarching question, the thesis defines three specific objectives:

1. **Quantify the acoustic effects of leading-edge blowing:** Systematic wind tunnel experiments are used to measure airfoil self-noise over a representative range of flow conditions, blowing rates, and angles of attack. The study focuses on three canonical self-noise mechanisms: trailing-edge tonal noise, leading-edge turbulent broadband noise, and stall-induced

separation noise. The primary objective is to establish for each mechanism the conditions under which leading-edge blowing yields measurable reductions in radiated sound.

2. **Correlate flow features with noise attenuation:** Detailed flow diagnostics are applied to operating points that exhibit significant acoustic changes. By relating modifications in boundary-layer development, wake organisation, and separation behaviour to the observed variations in sound radiation, the study seeks to move beyond a purely empirical description of noise reduction and towards a mechanistic understanding of how leading-edge blowing alters the underlying source fields.

3. **Assess the robustness and operating envelope of leading-edge blowing as an active control strategy:** By mapping the acoustic and aerodynamic response of the airfoil across the relevant parameter space of free-stream velocity, angle of attack, and blowing configuration, the study evaluates the range over which leading-edge blowing provides robust noise attenuation for each self-noise mechanism, and identifies regimes in which its effectiveness degrades or trade-offs with aerodynamic performance emerge.

Together, these aims provide a coherent framework for assessing the potential of leading-edge blowing as a practical aeroacoustic control method. The thesis is designed to move from measurement and quantification, to explanation and mechanism, and finally to comparison and evaluation, thereby providing both scientific understanding and practical context.

1.6 Thesis Structure

The remainder of this thesis is organised into a sequence of chapters that build from background and methodology towards the presentation of results and their interpretation. Each chapter is designed to contribute a distinct element to the overall narrative, while together they provide a coherent examination of the role of leading-edge blowing in reducing airfoil self-noise.

- **Chapter 2** provides a detailed review of the literature. It surveys the fundamental mechanisms of airfoil self-noise, examines the development of passive noise control strategies, and highlights the emergence of active methods. Particular attention is given to leading-edge blowing, situating the present work within the broader context of aeroacoustic research.

- **Chapter 3** describes the experimental methodology. This includes the wind tunnel facility, the instrumentation used for both acoustic and aerodynamic measurements, and the data acquisition and processing techniques. The chapter establishes the basis for reproducibility and provides the framework through which subsequent results are obtained.

- **Chapter 4** presents detailed acoustic and supporting flow measurements for the trailing-edge tonal noise configuration. A systematic parametric study of free-stream velocity, angle of attack, and leading-edge blowing rate is performed to quantify the sensitivity of the tonal

peak and its harmonics to the imposed actuation. The chapter identifies blowing configurations that yield the largest and most robust reductions in tonal levels, assesses their effectiveness relative to the baseline, and interprets these trends in terms of modifications to boundary-layer stability, separation behaviour, and wake organisation at the trailing edge.

- **Chapter 5** addresses leading-edge broadband interaction noise under controlled inflow turbulence. Two distinct turbulence-generation configurations are considered: an approximately isotropic field produced by passive grids and an anisotropic field generated by a cylinder–airfoil arrangement. For each inflow condition, far-field noise measurements are acquired over a range of angles of attack, leading-edge blowing rates, cylinder–leading-edge spacings, and turbulence parameters in order to quantify the sensitivity of the broadband spectra to the imposed actuation. Emphasis is placed on identifying combinations of blowing and inflow conditions that yield robust reductions in leading-edge noise levels. Complementary flow measurements are then conducted for the anisotropic configuration to relate the observed acoustic trends to modifications in the unsteady interaction between the oncoming vortical structures, the stagnation-region flow, and the developing boundary layer at the leading edge.

- **Chapter 6** examines stall-induced separation noise and its modification by leading-edge blowing. Acoustic measurements are acquired over a range of post-stall angles of attack and blowing rates in order to characterise the evolution of the broadband spectra and overall sound levels as the separated flow is progressively altered by the actuation. In parallel, lift and drag measurements are used to quantify the impact of blowing on aerodynamic performance, with particular emphasis on stall onset, lift retention, and the associated noise–performance trade-offs. Complementary flow-field measurements are then employed to relate the observed acoustic trends to changes in the topology and dynamics of the separated region, including the organisation of the shear layer and the extent of the recirculation zone. Finally, coherence analyses between acoustic and unsteady flow or surface-pressure signals are used to identify the dominant source regions and assess how leading-edge blowing modifies the spatial and temporal structure of the underlying noise-generating mechanisms.

- **Chapter 7** concludes the thesis by summarising the main findings, reflecting on their significance for both fundamental aeroacoustics and applied noise control, and identifying avenues for future research.

This structure is intended to guide the reader from context and motivation through methods and results, and finally towards interpretation and conclusions. By progressing in this way, the thesis develops a comprehensive picture of how leading-edge blowing influences airfoil self-noise and the extent to which it may serve as a viable active control strategy.

Chapter 2

Literature Review

2.1 Purpose & Scope

This chapter reviews the literature most relevant to the present investigation of steady leading-edge blowing as an active method for reducing aerofoil self-noise from a NACA 65(12)-10 aerofoil. The focus is placed on three mechanisms that define the experimental chapters of this thesis: trailing-edge tonal noise, leading-edge broadband turbulence-interaction noise, and stall-induced separation noise. These mechanisms arise in different operating regimes, are governed by different source physics, and therefore present different challenges for prediction, interpretation, and control.

The chapter begins with a concise theoretical foundation in aerofoil aeroacoustics. This is not intended as a full review of acoustic theory, but rather to establish the physical framework needed for the later discussion of source mechanisms and control strategies. In particular, the acoustic analogies of Lighthill, Curle, and Ffowcs Williams–Hawkings are introduced to explain why, at low Mach numbers, the dominant radiators of aerofoil noise are typically dipole sources associated with unsteady surface loading. These ideas lead naturally to the prediction models most frequently used in the literature, including Amiet's leading- and trailing-edge scattering formulations and the semi-empirical Brooks–Pope–Marcolini model. Although such models remain central reference points, their limitations under finite thickness, strong loading, transitional flow, and large-scale separation must also be kept in view.

The main body of the chapter is then organised around the three noise mechanisms targeted in this thesis. Trailing-edge tonal noise is reviewed as an instability- and feedback-driven phenomenon involving laminar separation bubbles, amplified instability waves, and acoustic scattering at the trailing edge. Leading-edge broadband noise is examined as a turbulence-interaction problem in which incoming gusts are scattered by the leading edge, with particular attention to turbulence length scale, anisotropy, and coherence. Stall-induced separation noise is then considered in relation to high-incidence separated flow, large-scale coherent structures, and the comparatively less mature state of predictive modelling in this regime.

The chapter then turns to noise-control strategies from a mechanism-based perspective. Passive concepts, including trailing-edge serrations, porous treatments, and leading-edge shaping, are reviewed alongside active approaches such as blowing, suction, synthetic jets, and plasma actuation. Particular emphasis is placed on leading-edge blowing, since it is one of the few control strategies with the potential to influence all three target mechanisms from a single actuation location. By modifying boundary-layer development close to the nose, leading-edge blowing may weaken the laminar-separation-bubble dynamics associated with tonal noise, alter the coherence and effective interaction length of incoming turbulence responsible for leading-edge broadband noise, and delay or reorganise the onset of separation at high incidence. The chapter is therefore structured not only to summarise the current state of knowledge, but also to identify the gaps that motivate the specific objectives of the present study.

2.2 Fundamentals of Aerofoil Aeroacoustics

Aerofoil self-noise has been studied for decades, and much of the modern understanding rests on the development of aeroacoustic theory. At its core, the problem is to explain how unsteady aerodynamic processes generate pressure fluctuations that radiate to the far field as sound. Because the governing fluid equations couple flow and acoustics in a nonlinear way, direct prediction is rarely practical except in highly simplified or computationally intensive settings. To make the problem tractable, researchers reformulated it in terms of acoustic analogies [29] and scattering-based models that isolate the dominant radiating mechanisms. These frameworks remain central to both prediction and physical interpretation, and they provide the theoretical basis for the later discussion of tonal noise, leading-edge broadband noise, and stall-induced separation noise [30].

2.2.1 Acoustic Analogies & Governing Source Types

The first rigorous theoretical treatment came from Lighthill, who recast the Navier–Stokes equations into an inhomogeneous wave equation in which turbulence appears as an equivalent quadrupole source distribution [29]. This was a major step because it showed how aerodynamic flows could generate acoustic radiation without prescribing a sound source in advance. For aerofoils at low Mach numbers, however, Lighthill's original analogy is not by itself sufficient, since the most efficient radiators are generally not quadrupoles in the free field, but fluctuating forces acting on the body surface.

Curle extended the analogy to include rigid boundaries and showed that unsteady surface pressures may be represented as dipole sources of sound [31]. This result is fundamental to aerofoil acoustics because it explains why the leading and trailing edges are such efficient radiating locations. A further generalisation was introduced by Ffowcs Williams and Hawkings, who derived a formulation applicable to moving and permeable surfaces [32]. Their equation has since become a standard basis for both theoretical and computational aeroacoustics, since it allows a control

surface surrounding the aerofoil to be treated as an equivalent acoustic source.

For low-speed aerofoils, these developments lead to a simple but important conclusion: the radiated sound field is usually dominated by surface dipoles associated with unsteady loading, while quadrupole contributions from the wake are comparatively weak [33]. Monopoles may arise in special cases involving strong mass injection or suction, but they are usually secondary in conventional aerofoil flows. This hierarchy of source types provides the theoretical context for the remainder of the chapter. In particular, it explains why later sections focus so strongly on edge scattering, unsteady loading, and the flow structures that organise pressure fluctuations near the aerofoil surface.

2.2.2 Scaling Laws and Directivity Patterns

Scaling arguments in aeroacoustics serve two main purposes. First, they indicate how radiated levels should vary with flow speed and geometry. Second, they provide the non-dimensional groups needed to compare results across operating conditions. For low-Mach-number aerofoils, surface-pressure fluctuations acting on the body behave primarily as dipole sources, whereas turbulence in the free field behaves as quadrupole radiation [29, 31, 34]. This distinction matters because it governs both the expected velocity dependence of the sound and the broad form of the radiation pattern.

At the simplest level, classical acoustic-analogy arguments [33, 34] suggest that the radiated intensity from compact dipoles scales approximately as

$$I \propto U_\infty^6,$$

while quadrupole sources scale more steeply as

$$I \propto U_\infty^8.$$

In practice, measured aerofoil self-noise does not always follow a single exponent across the entire spectrum. The apparent scaling depends on whether the quantity of interest is narrowband or integrated, on the relevant frequency range, and on the state of the boundary layer. For trailing-edge-dominated broadband noise, many experimental studies report effective velocity exponents between about five and six in overall level [6, 35], with somewhat steeper behaviour observed when the source becomes acoustically compact.

Frequency scaling is equally important. When frequency is non-dimensionalised using the free-stream velocity and a characteristic aerofoil length, the dominant spectral features often collapse more clearly. For edge-scattering problems, a chord-based Strouhal number is commonly adopted:

$$St_c = \frac{fc}{U_\infty}.$$

In trailing-edge scattering, spectral organisation is linked to the wall-pressure field convecting past

the edge [8]. For leading-edge broadband noise, the same non-dimensional framework is useful, but the spectral shape depends much more directly on the incoming turbulence field [11, 22]. As the inflow integral length scale increases, the dominant energy shifts toward lower St_c, while increasing turbulence intensity raises the radiated level approximately with the square of the incoming fluctuation amplitude [36, 22]. Finite thickness and non-uniform flow near the nose can also weaken the higher-frequency response, causing the leading-edge spectrum to roll off earlier than idealised flat-plate theory would predict [37].

Directivity follows naturally from the source type. A compact dipole produces a figure-of-eight radiation pattern oriented by the fluctuating force. On an aerofoil, this leads to strong radiation roughly normal to the surface and weaker radiation in the chordwise directions. For trailing-edge noise, the pattern is modified by convection and by the geometry of the edge, and many studies report a cardioid-like far-field distribution [6]. Loading tends to bias the radiation toward the suction side, while back-scattering corrections can enhance upstream radiation at selected frequencies [7]. Leading-edge interaction noise typically shows a stronger upstream lobe in addition to downstream radiation, consistent with the gust-scattering process at the nose [11, 22].

Tonal noise introduces an additional level of spectral organisation. The discrete peaks move approximately linearly with U_∞ when plotted in dimensional frequency, while in non-dimensional form they tend to cluster within a relatively narrow band of St_c. The exact position of the dominant tone depends on the interaction between the laminar separation bubble, the amplified instability waves, and the trailing-edge scattering process [9, 10, 12]. Near and beyond stall, the dominant energy shifts toward lower non-dimensional frequencies and the effective source region becomes more extended [38]. In that regime, the apparent velocity scaling is often shallower than in attached-flow trailing-edge-dominated cases, reflecting the growing influence of large-scale coherent structures in the separated shear layer [39]. The radiation pattern remains broadly dipolar, but tends to become wider and more strongly biased toward the suction side [40].

Taken together, these scaling and directivity arguments do not by themselves explain the detailed source physics of aerofoil self-noise, but they provide the framework within which the later mechanisms are interpreted. They clarify why tonal, broadband, and stall-related sources can exhibit different spectral organisation even when radiated by the same aerofoil, and they establish the reference behaviour against which the effects of leading-edge blowing are assessed in the experimental chapters that follow.

2.3 Airfoil Self-Noise Mechanisms

Aerofoil self-noise is not the result of a single mechanism but a combination of several source processes that dominate under different flow conditions [6]. For an aerofoil in nominally smooth inflow, Brooks, Pope and Marcolini distinguish five self-noise components (figure 2.1) [6]. Turbulent-boundary-layer trailing-edge (TBL–TE) noise is the broadband sound generated when turbulent pressure fluctuations in an attached boundary layer convect past the sharp trailing edge and are

scattered into the far field. Separation stall noise is associated with massively separated flow at high incidence, where large, unsteady vortical structures in the separated shear layer and near wake produce predominantly low-frequency dipole radiation.

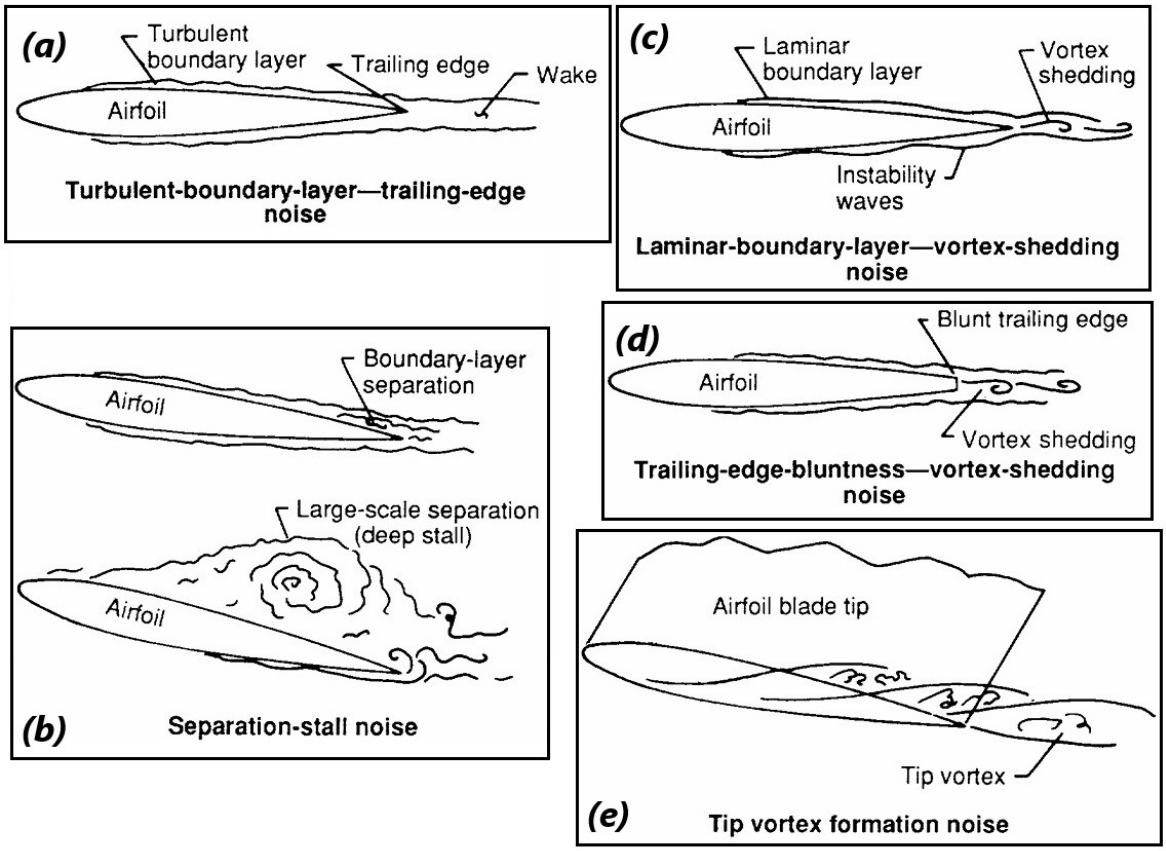

Figure 2.1: Schematic of aerofoil self-noise mechanisms following Brooks, Pope and Marcolini [6]: (a) turbulent-boundary-layer trailing-edge noise, (b) separation stall noise, (c) laminar boundary-layer vortex-shedding noise, (d) bluntness-induced vortex-shedding noise, and (e) tip-vortex formation noise.

Laminar-boundary-layer vortex-shedding noise arises when an extended laminar boundary layer becomes globally unstable and sheds nearly periodic vortices, leading to discrete tonal components that may interact with trailing-edge scattering. Bluntness-induced vortex-shedding noise occurs when a finite trailing-edge thickness behaves as a bluff body, shedding alternating vortices at a Strouhal number based on the edge thickness and radiating narrowband peaks in the spectrum. Finally, tip-vortex formation noise is linked to the unsteady three-dimensional vortex system that develops near the tip of a finite-span lifting surface, which generates broadband sound over a wide range of frequencies.

Of these five components, three mechanisms are of particular importance in the present work. Trailing-edge tonal noise arises when a feedback loop involving a laminar separation bubble, amplified instability waves, and acoustic scattering at the trailing edge establishes discrete tones that

stand out above the broadband background [12, 9, 10, 41]. Leading-edge broadband noise occurs when incoming turbulence interacts with the aerofoil leading edge, producing scattered sound that depends strongly on turbulence intensity and length scales [11, 22]. Finally, stall induced separation noise emerges at higher angles of attack when large coherent structures form in the separated shear layer, radiating predominantly at low frequencies [38, 39, 40]. Each of these sources has distinct spectral characteristics, flow dependencies, and scaling behaviours, and each responds differently to passive and active control strategies. The remainder of this section surveys the state of knowledge for these three mechanisms, setting the foundation for the experimental investigations that follow.

2.3.1 Trailing Edge Tonal Noise

Trailing-edge tonal noise has been one of the most studied and yet persistently challenging aspects of aerofoil aeroacoustics because it cannot be interpreted as a simple extension of the broadband trailing-edge scattering problem. In his seminal work, Amiet formalised broadband trailing-edge noise as the acoustic scattering of turbulent boundary-layer wall-pressure fluctuations by a sharp edge [8]. By contrast, tonal noise appears as discrete, narrowband spectral peaks that emerge only when the boundary layer supports strongly amplified, organised instability content upstream of the trailing edge [8, 6]. For this reason, tonal radiation should not be interpreted as a simple amplification of trailing-edge broadband noise, but as a distinct instability-controlled regime with its own frequency-selection mechanism. Brooks, Pope, and Marcolini documented that these tones are most readily observed at moderate Reynolds numbers and under low free-stream turbulence conditions, where the suction-side boundary layer may remain laminar over a significant fraction of the chord and a laminar separation bubble (LSB) can form [6]. In this regime, the aerofoil–flow system behaves as a coupled hydrodynamic–acoustic oscillator rather than a purely scattering-dominated radiator.

The recognition of this behaviour developed gradually in the literature. Early experimental work by Paterson *et al.* [42] showed that isolated aerofoils in low-turbulence inflow can radiate pronounced discrete tones whose frequencies vary systematically with operating condition, while Fink [43] proposed empirical relations for predicting the dominant tonal frequencies. Although these early studies did not yet provide the modern instability-feedback interpretation, they established two important points that remain central to later work: first, that tonal noise is a distinct regime rather than a minor perturbation of broadband self-noise, and second, that the selected frequencies are constrained by the coupled aerodynamic and acoustic response of the aerofoil system.

A widely accepted mechanism links the discrete tones to the excitation and amplification of boundary-layer instability waves in the presence of an LSB [12, 44]. McAlpine and Nash reported that tonal emission is closely associated with transitional boundary layers in which instability waves grow rapidly, and that the spectral organisation of the hydrodynamic field is a prerequisite for strong acoustic tonality [12, 44]. The physical picture is that a nominally laminar boundary layer

admits Tollmien–Schlichting (T–S) type disturbances, and that adverse pressure gradients promote separation such that a thin separated shear layer forms over the bubble. This shear layer is convectively unstable and can strongly amplify incoming disturbances over a narrow range of frequencies. The amplified disturbances convect downstream as coherent wavepackets, interact with the trailing edge, and scatter efficiently into sound [9, 10]. Importantly, the scattering process does not merely radiate energy; it also produces an acoustic field that can propagate upstream and act back on the near-wall flow, providing the closure required for a feedback loop [9, 10].

Further support for this interpretation has come from studies that directly tracked laminar separation bubble development in tonal-noise cases. Pröbsting and Yarusevych [41] showed that the evolution of the separation bubble and the associated transition process are closely linked to the conditions under which tonal radiation is sustained. Their measurements reinforced the view that the bubble is not merely a passive by-product of the pressure distribution, but an active element of the source mechanism because it defines the instability environment in which narrowband amplification develops. This is particularly relevant to the present work, since any control strategy that modifies the upstream boundary-layer state or the separation-bubble topology may alter tonal radiation through changes in amplification and coherence rather than through trailing-edge scattering alone.

The coupled mechanism is illustrated schematically in Figure 2.2, highlighting the interaction between instability growth, trailing-edge scattering, and upstream acoustic receptivity.

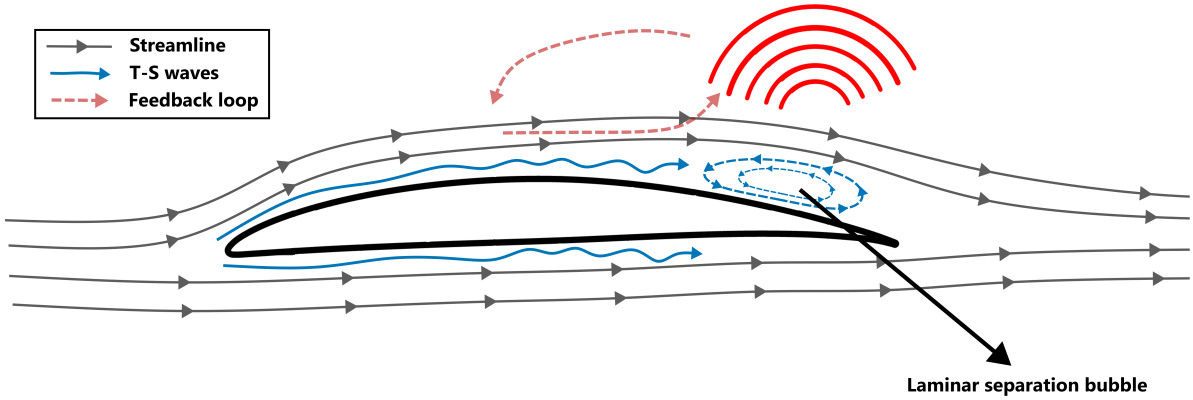

Figure 2.2: Schematic of trailing-edge tonal-noise generation showing T–S wave growth, laminar separation bubble formation, and the aeroacoustic feedback loop.

This interpretation is particularly important for the present thesis, since a control strategy such as leading-edge blowing may reduce tonal radiation either by altering the selected mode or by weakening the gain and coherence of the loop itself.

The feedback-loop interpretation was established in early experimental studies by Arbey and Bataille and later by Lowson and Fiddes, who described tonal noise as the outcome of an aeroacoustic loop linking an upstream instability-amplification region to the trailing-edge scattering site

[9, 10]. Within this framework, the tone frequency is not arbitrary: it is selected by the simultaneous satisfaction of a gain condition (net amplification around the loop) and a phase condition (constructive interference after one loop). The LSB sets a preferred amplification band through its shear-layer dynamics and its effective convective time scales, while the trailing edge sets how efficiently hydrodynamic fluctuations are converted into acoustic radiation. Probsting, Serpieri, and Scarano provided detailed experimental evidence consistent with this coupled-loop picture, showing that the near-wake and boundary-layer disturbance fields contain organised structures whose evolution correlates with the observed tonal output [45]. Their results support the notion that tonal radiation is most intense when the instability content remains narrowband and phase-coherent as it reaches the trailing edge, enabling strong, repeatable scattering and robust upstream feedback.

One of the most recognisable spectral signatures of this mechanism is the so-called “ladder” structure: as flow speed is varied, the dominant tone does not shift continuously but instead exhibits piecewise linear frequency trends punctuated by abrupt jumps, often accompanied by harmonics and multiple coexisting peaks [12, 46]. Chong and Joseph interpreted these features in terms of mode switching between competing loop solutions [46]. In dimensional terms, the dominant tone typically increases approximately linearly with free-stream velocity over each ladder rung, consistent with a convective scaling, whereas in chord-based non-dimensional terms the tones tend to cluster within a relatively narrow band of Strouhal numbers [9, 10, 47, 48].

Tam and Ju emphasised that such clustering is a natural outcome of feedback systems in which both convective amplification (hydrodynamic time scales) and acoustic propagation (upstream travel times and receptivity) constrain the allowable frequencies [47]. Probsting, Scarano, and Morris further reported distinct tonal regimes and transitions, indicating that changes in boundary-layer state and bubble dynamics with Reynolds number and incidence can shift the system between qualitatively different oscillatory behaviours [48].

The sensitivity of tonal noise to surface condition and inflow disturbance follows directly from the mechanism. Because the loop relies on a laminar or weakly transitional boundary layer and a stable instability-amplification region, roughness, trips, or elevated free-stream turbulence can suppress or entirely eliminate tones by triggering earlier transition, weakening the separation bubble, or broadening the instability spectrum such that phase-coherent feedback cannot be maintained [6, 49]. Brooks, Pope, and Marcolini showed that even modest changes to surface condition can dramatically alter tonal strength [6]. Chong similarly highlighted that modifications capable of disrupting bubble dynamics or the downstream coherence of instability waves can collapse the discrete peaks [49]. Angle of attack plays an analogous role through the pressure-gradient distribution: it influences the onset and extent of separation, the bubble length and reattachment location, and therefore the spatial region available for instability growth and the effective feedback path [12, 48]. From a mechanistic standpoint, these dependencies are expected because the bubble acts as both an amplifier and a frequency-selective element, while the trailing edge acts as the principal scattering radiator that converts the organised hydrodynamic field into a tonal acoustic field.

Although the instability-feedback interpretation is now well established, the literature is less clear on the dominant route by which successful control suppresses tonal radiation. In particular, it is not always possible to distinguish whether mitigation arises primarily through a shift in the selected tonal frequency, premature transition that removes the receptive laminar region, a shortening or elimination of the laminar separation bubble, or a reduction in the amplification and coherence of the instability field while the preferred mode remains broadly unchanged. This distinction is especially important for active control strategies, since different control inputs may act on different parts of the loop.

Recent control-oriented studies further highlight this point. Kumar and Bhumkar [50] showed that periodic suction–blowing excitation can substantially modify the tonal content radiated by an aerofoil, confirming that the instability process remains highly receptive to targeted actuation. At the same time, such results do not by themselves resolve whether the dominant effect arises from frequency detuning, from altered transition and separation-bubble development, or from a reduction in the coherence of the amplified instability field. This continuing ambiguity reinforces the need for mechanism-based analysis in tonal-noise control studies, rather than relying on overall acoustic reductions alone.

Although tonal noise is superposed on the broadband trailing-edge noise floor, the underlying physics should be treated as distinct. The broadband component is well described by trailing-edge scattering models, again exemplified by Amiet's formulation in which turbulent wall-pressure spectra and spanwise coherence determine radiated levels [8]. Roger and Moreau reviewed how such broadband mechanisms depend on the turbulent boundary-layer structure and edge scattering, providing a baseline framework against which tonal peaks are often interpreted [7]. In tonal cases, however, the dominant contribution comes from a narrowband, amplified instability field that is not representative of fully developed turbulence and whose amplitude is controlled by feedback rather than by stationary turbulent statistics. Lee *et al.* discussed this practical overlap explicitly: tones often sit on top of a broadband background that remains governed by trailing-edge scattering, but the emergence, strength, and frequency of the tones reflect instability-wave dynamics and loop closure rather than a simple increase in turbulent-wall-pressure level [35]. For this reason, studies of trailing-edge tonal noise typically combine acoustic measurements with diagnostics of boundary-layer state and separation-bubble behaviour, since the tone cannot be understood solely from trailing-edge scattering arguments [6, 45]. Additionally, successful control of tonal noise should be assessed not only in terms of overall level reduction, but also in terms of how the actuation changes peak frequency, spectral organisation, and the coherence of the underlying source field.

Overall, the literature converges on the view that trailing-edge tonal noise is an instability-driven, feedback-controlled aeroacoustic phenomenon in which a laminar or transitional boundary layer, often mediated by a laminar separation bubble, supplies a coherent hydrodynamic disturbance field to the trailing edge [9, 10, 47]. The discrete spectral peaks, ladder structure, and strong sensitivity to inflow and surface condition are therefore direct signatures of a coupled os-

cillator in which instability amplification, trailing-edge scattering, and upstream receptivity jointly determine the tonal outcome [46, 48]. What remains less clearly established is the extent to which active control suppresses tonal noise by detuning the selected mode, by weakening the instability gain, or by collapsing the flow–acoustic coherence that sustains the loop. Resolving this point is one of the central motivations for the present study of leading-edge blowing in Chapter 4.

2.3.2 Leading Edge Broadband Noise

When an aerofoil is immersed in a turbulent inflow, the leading edge becomes a highly efficient scattering site. Incoming velocity fluctuations (gusts) impinge on the stagnation region and generate unsteady loading that radiates sound over a broad frequency range. This mechanism, commonly termed leading-edge broadband interaction noise, is fundamentally distinct from trailing-edge broadband noise because the incident disturbances are external to the boundary layer: the spectral content, coherence, and convection characteristics of the incoming turbulence directly imprint onto the radiated acoustic field [6]. As a result, leading-edge broadband noise is particularly sensitive to inflow characterisation, since the source is governed not only by aerofoil geometry but also by the spatial organisation of the turbulence incident on the nose. In this sense, the aerofoil acts as a linear "gust-to-sound" transducer whose efficiency depends on both the hydrodynamic forcing and the aerodynamic response of the leading-edge region.

The basic gust-scattering process is illustrated schematically in Figure 2.3. The figure highlights how the incoming turbulence length scale, coherence, and leading-edge response together determine the radiated acoustic field.

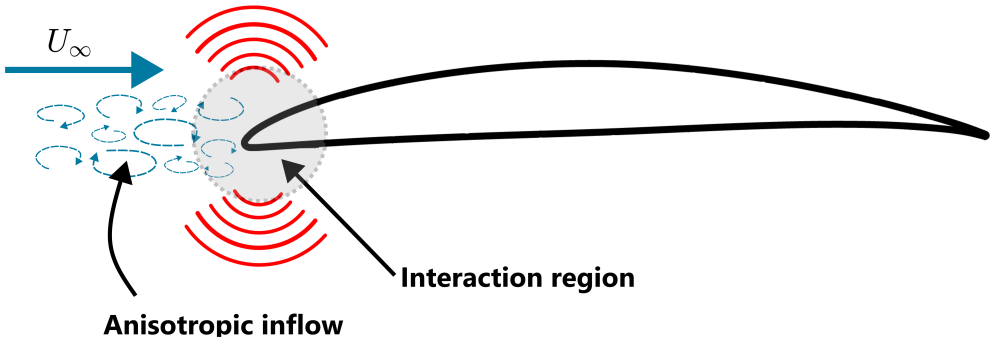

Figure 2.3: Schematic of leading-edge broadband noise generation by turbulent gust scattering at the aerofoil leading edge.

The first comprehensive theoretical treatment was developed by Amiet, who modelled the aerofoil as a thin, flat plate in a uniform mean flow and derived analytical expressions for the far-field acoustic pressure generated by the interaction of convected turbulence with the leading edge [11]. In Amiet's formulation, the turbulence is represented in wavenumber–frequency space and the acoustic field is obtained by combining (i) a linear aerodynamic transfer function relating incident

gust components to unsteady lift, and (ii) an acoustic radiation model for that unsteady lift distribution [11]. A key implication is that the radiated sound is controlled not merely by a single turbulence intensity level, but by the distribution of turbulent energy across streamwise and spanwise wavenumbers and by the degree of spanwise coherence. As emphasised in the review by Ayton and Gill, accurate prediction therefore depends strongly on how the inflow spectrum and correlation are modelled or measured, since different turbulence models with identical intensity can yield markedly different acoustic spectra [22].

The continuing influence of Amiet's framework is evident in later prediction efforts that relax some of its idealisations while retaining the underlying gust-scattering interpretation. Miotto *et al.* [51] extended leading-edge noise prediction to general aerofoil profiles subjected to spanwise-varying inflow conditions, showing that once the incident turbulence is no longer uniform along the span, the resulting unsteady loading and acoustic response cannot be inferred from a single homogeneous inflow description alone. This is important because many practical interaction-noise problems involve non-uniform or wake-like inflow structure even when the basic linear gust-response picture remains valid [22].

A further complication is that many practical inflows are not well approximated as isotropic turbulence. In turbomachinery, rod–aerofoil, and wake–interaction problems, the disturbances incident on the leading edge may be highly anisotropic, may possess strong directional coherence, and may contain embedded narrowband content in addition to the broadband background. Under such conditions, the effective interaction cannot be described fully by turbulence intensity and a single integral length scale alone. The spanwise and streamwise organisation of the incoming structures becomes equally important, both for the radiated spectrum and for the interpretation of how any control strategy modifies the interaction [22, 51].

Once the gust-scattering framework is established, the next question is how the resulting unsteady loading scales and radiates in the far field. Because the dominant acoustic source is fluctuating lift, leading-edge interaction noise is commonly interpreted as a dipole-type radiation mechanism. Under the classical thin-plate assumptions and for sufficiently compact source regions, Amiet's model yields the characteristic dipole-like directivity. The radiated intensity scales strongly with the unsteady loading amplitude, giving the familiar dependence on turbulence intensity: in simplified forms the acoustic power scales approximately with the square of the turbulence intensity, reflecting the linear relationship between incident gust amplitude and unsteady lift [11, 22]. The frequency content is likewise tied to turbulence convection: eddies of characteristic size ℓ convected at approximately the free-stream velocity contribute most strongly near $f \sim U/\ell$, so increasing the integral length scale shifts the spectral peak to lower frequencies, while reducing the length scale moves energy to higher frequencies [11, 6]. Importantly, this mapping is not purely kinematic. The aerofoil response acts as a filter that weights different wavenumber components differently, meaning that changes in spanwise coherence or in the distribution of turbulent wavenumbers can alter spectral shape even when the one-dimensional energy spectrum appears similar [22, 35].

Although Amiet's formulation captures the core physics of the interaction, its practical accuracy depends on assumptions that are not always satisfied for real aerofoils. The flat-plate, thin-aerofoil assumption and the use of an idealised leading edge are most appropriate when the leading-edge radius is small compared with characteristic turbulence length scales and when incidence is modest. In addition, the theory assumes a uniform mean flow and adopts a "frozen turbulence" picture in which gusts are convected past the aerofoil with an approximately constant convection velocity. Departures from these assumptions influence both the aerodynamic transfer function and the arrival statistics of turbulence at the leading edge. For real aerofoils, finite thickness, camber, and angle of attack modify the stagnation region and the effective scattering geometry, thereby changing both the magnitude of unsteady lift and the far-field directivity. A number of authors have therefore developed corrections and extensions that embed leading-edge geometry explicitly into the response. Ayton and Chaitanya examined the role of leading-edge radius and showed that finite-radius effects can significantly alter the predicted interaction, particularly in regimes where the turbulence length scales are comparable to the nose radius [52]. Gill *et al.* and Devenport *et al.* reported that finite thickness and realistic aerofoil shapes can skew the idealised dipole directivity and shift the balance between upstream and downstream lobes relative to the flat-plate prediction [53, 54]. More recently, Zhong *et al.* proposed refined analytical treatments that incorporate aspects of real-aerofoil geometry and incidence, improving agreement across a wider parameter range [37]. Taken together, these works highlight that while Amiet's formulation captures the essential scattering concept, the leading-edge geometry can act as a non-trivial "impedance" that modifies both the aerodynamic receptivity to incoming gusts and the radiation efficiency.

A second major class of deviations arises because the turbulence field that reaches the leading edge is not necessarily identical to the upstream turbulence measured in the free stream. Mean-flow gradients and pressure fields around the nose distort and filter incoming eddies: they can stretch, rotate, and accelerate turbulent structures before they interact with the leading edge, thereby changing the effective wavenumber content and coherence at the interaction site. This issue becomes particularly important for thick noses, cambered profiles, or finite angles of attack, where streamline curvature and strong acceleration occur near the stagnation region. Evers and Peake studied related non-uniform mean-flow effects in cascade-type configurations and demonstrated that mean-flow non-uniformity can significantly modify interaction-noise predictions relative to uniform-flow assumptions [55]. More recent work has addressed how turbulence distortion influences noise for isolated aerofoils. Piccolo *et al.* provided experimental and modelling evidence that leading-edge distortion can lead to measurable changes in both the amplitude and spectral shape of the radiated sound, indicating that the turbulence "seen" by the edge is effectively prefiltered by the mean flow [36]. Complementary analyses by dos Santos *et al.* and Zamponi *et al.* similarly underscore that accounting for distortion can be necessary for quantitative prediction when comparing against experiments with realistic aerofoil geometries and operating conditions [56, 57]. This point is especially important when assessing active control, since the effectiveness of a method such as leading-edge blowing depends on the turbulence field that actually reaches

the interaction region, rather than on the undistorted inflow measured farther upstream.

These theoretical developments are broadly supported by experiments, which also reveal the parameter sensitivities that motivate later refinements. Brooks, Pope, and Marcolini reported clear increases in radiated levels with turbulence intensity and showed that the characteristic spectral peak shifts systematically with the inflow length scale, consistent with the physical picture of convection-driven spectral mapping [6]. At the same time, measurements on thick or cambered aerofoils show departures from flat-plate behaviour, including altered directivity and changes in the relative strength of upstream and downstream radiation lobes [54, 58]. Such deviations are consistent with the idea that real leading-edge geometry changes both the distribution of unsteady lift over the chord and the efficiency with which that lift is converted into far-field sound. From a modelling standpoint, these studies reinforce that agreement with experiments depends not only on the acoustic radiation model but also on accurate representation of the inflow statistics actually incident on the leading edge, including spanwise coherence and any distortion induced by the mean flow [22, 36].

For this reason, controlled interaction-noise experiments play an important role in the literature. By prescribing inflow turbulence with known characteristic scales and coherence properties, such studies make it possible to separate the influence of intensity, length scale, and spatial organisation more systematically than is usually possible in practical operating environments. At the same time, the need for such controlled arrangements also highlights a central limitation of the field: the acoustic response observed under idealised inflow conditions cannot always be transferred directly to wake-dominated or otherwise non-uniform inflows without accounting for directional structure and distortion effects [22, 51].

In practical terms, leading-edge broadband interaction noise is particularly significant in environments where external turbulence is unavoidable, such as turbomachinery blades interacting with wakes, propellers operating in non-uniform inflow, or wind turbines immersed in the atmospheric boundary layer [59, 22]. For the present study, this mechanism is especially valuable because it allows the acoustic response to be related directly to measurable inflow statistics, making it possible to examine systematically how control effectiveness varies with turbulence scale, coherence, and directional structure. It therefore provides a useful bridge between measurable inflow turbulence parameters and radiated acoustics. Because the source is driven primarily by external disturbances rather than by internally generated boundary-layer turbulence, leading-edge interaction noise also offers a useful contrast to trailing-edge broadband noise and to tonal mechanisms associated with laminar separation and feedback, which are often more sensitive to surface condition and boundary-layer state [6, 35]. Consequently, a mechanistic description of leading-edge broadband noise must treat the problem as a coupled interaction between upstream turbulence statistics, mean-flow distortion near the nose, and the leading-edge aerodynamic transfer function that converts gusts into unsteady lift and sound [11, 22, 37].

Overall, the literature establishes leading-edge broadband noise as a gust-scattering mechanism whose strength depends not only on aerofoil geometry but also on the spectral and spatial

organisation of the incoming turbulence. Classical theory, beginning with Amiet, captures the essential interaction physics, while later studies show that finite thickness, angle of attack, and turbulence distortion near the nose can modify both the aerodynamic response and the radiated sound. What remains less clearly established is how active control alters the effective interaction length, coherence, and directional structure of the turbulence incident on the leading edge, particularly under non-ideal and anisotropic inflow conditions. This unresolved point is central to the present thesis and motivates the experimental investigation of leading-edge blowing under both isotropic and anisotropic inflow conditions in Chapter 5.

2.3.3 Stall Induced Separation Noise

Aerofoil noise behaviour changes markedly once the suction-side boundary layer separates at high incidence, because the dominant acoustic sources are no longer confined to a compact region near the trailing edge. For the present thesis, the main interest is static high-incidence separation, where the onset and growth of the separated region alter both the aerodynamic loading and the low-frequency acoustic radiation. Early studies recognised that, near and beyond stall onset, the rapid rise in low-frequency sound cannot be explained by attached-flow trailing-edge scattering mechanisms alone. In the widely used NASA reference work, Brooks, Pope, and Marcolini explicitly introduced a distinct “separation stall” noise component within their semi-empirical aerofoil noise framework [6]. In doing so, they separated this mechanism from turbulent boundary-layer trailing-edge noise and from tonal phenomena associated with laminar separation bubbles, implying that the sound-producing flow physics during stall involves large-scale unsteadiness and pressure fluctuations distributed over a substantial portion of the aerofoil.

Compared with trailing-edge tonal noise and leading-edge broadband interaction noise, the literature on stall-induced separation noise is less mature in both mechanistic modelling and predictive capability. While the low-frequency rise associated with separation is well established, there is less agreement on how best to define the effective source region, how the source evolves from incipient separation to deep stall, and how reliably these processes can be modified by active control.

An important step between this early classification and the more recent mechanistic picture was provided by studies that examined the flow features and self-noise of aerofoils near stall or in stall more directly. Moreau, Roger, and Christophe [60] showed that as separation develops, the radiated sound becomes increasingly governed by the extent and dynamics of the separated region rather than by compact edge-scattering alone. Their work helped establish stall noise as a distributed source problem linked to large-scale separated-flow structures, thereby providing a bridge between the empirical separation-stall category introduced in earlier semi-empirical models and the more detailed source-localisation and flow-diagnostic studies that followed.

A mechanistic picture of stall separation noise has since emerged in which the primary radiators are coherent, unsteady structures within the separated shear layer and the near-wake, which impose large-amplitude, spatially correlated surface-pressure fluctuations on the suction

side. Lacagnina *et al.* combined microphone-array measurements with time-resolved particle image velocimetry and demonstrated that, in the near-stall regime, large coherent vortices in the separated shear layer dominate the acoustic radiation [38]. A key outcome of their study was that the surface-pressure coherence extended far upstream of the trailing edge, confirming that the effective source region in separated flow is significantly more extended than for attached-flow broadband mechanisms. This spatial growth of the coherent source region provides a direct explanation for why stall noise often exhibits strong dipole-like radiation at low to mid frequencies: the dominant pressure field is associated with large-scale lift fluctuations driven by shear-layer dynamics rather than by localised scattering at the trailing edge [6, 38].

The spectral characteristics of stall noise reflect both the onset of separation and the subsequent evolution toward deep stall. Laratro *et al.* reported that as the angle of attack increases beyond stall onset, the spectrum develops a pronounced low-frequency component and the radiation exhibits a broad dipolar directivity that is biased toward the suction side [61]. This behaviour is consistent with a lift-dipole source associated with large-scale, slowly varying separation dynamics and the advection of coherent vortical structures. As separation progresses further, additional spectral organisation may arise. Lacagnina *et al.* observed that when the separated region grows toward deep stall, a relatively narrowband peak can emerge and that its frequency collapses with a projected streamwise length scale based on $c \sin \alpha$, suggesting a transition toward bluff-body-like shedding or global wake modes governed by an effective projected chord [38]. Similar scaling trends were identified for oscillating aerofoils by Raus *et al.*, who showed that the dominant peak frequency collapses with the same projected length scale over a wide range of incidences, reinforcing the interpretation that deep-stall acoustics can be governed by large-scale shedding dynamics rather than by classical attached-flow mechanisms [62].

Recent experimental work has further strengthened the evidence base for the near-stall mechanism and provided higher-fidelity datasets for evaluating models. Jaiswal, Rendón, and Moreau reported detailed aeroacoustic measurements of aerofoils at near-stall conditions, highlighting the strong low-frequency rise associated with separation and relating the acoustic output to the evolving separated-flow state [63]. Complementary work by Branch *et al.* focused on thin-aerofoil stall, with an explicit motivation of improving the applicability of the BPM framework in stalled conditions [64]. While their emphasis includes modelling implications, their measurements reinforce the central point relevant here: once separation sets in, the noise source cannot be treated as a minor modification to attached-flow trailing-edge noise, because the dominant wall-pressure and velocity-field fluctuations become organised over larger spatial scales and shift energy toward lower frequencies [64, 63].

On the modelling side, Bertagnolio *et al.* [65] proposed a semi-empirical stall-noise model based on surface-pressure measurements, showing that the principal low-frequency rise in static stalled conditions can be represented in a reduced-order framework. At the same time, the need for such a dedicated model reinforces the point that stall-induced noise cannot be treated as a minor extension of attached-flow edge-noise prediction. Once the separated region grows and the

source becomes spatially distributed, the underlying assumptions of compactness, fixed source location, and stationary coherence become much harder to sustain.

This is important because it indicates that stall noise should not be treated simply as an intensified form of trailing-edge broadband noise, but as a source regime in which separation topology and large-scale shear-layer organisation become acoustically dominant.

The scaling of stall noise levels with velocity and geometry also differs from canonical attached-flow expectations. Using large-eddy simulations, Turner and Kim demonstrated that in light stall the radiated field remains primarily dipolar but exhibits an effective velocity exponent shallower than the classical U^6 scaling associated with compact dipole sources [39]. This reduction is physically consistent with the non-compact nature of the separated region: as the source region extends over a significant fraction of the chord, the radiated field integrates contributions with partial cancellation and altered coherence, modifying the apparent scaling. Carter and Ganapathisubramani provided experimental support for this picture using data-driven modal analysis applied to wall-pressure fields, showing that suction-side shear-layer dynamics contain the dominant low-frequency energetic content correlated with far-field sound [40]. Geometry influences the separated-flow dynamics and therefore the acoustic outcome: Laratro *et al.* demonstrated that thickness and camber affect both separation behaviour and the resulting spectra and directivity patterns, shifting peak frequencies and changing radiation bias as stall develops [61]. Unlike tonal and leading-edge interaction noise, stall-induced separation noise is closely tied to large changes in aerodynamic state, which means that any successful control strategy must be assessed in terms of both acoustic benefit and aerodynamic consequence. At more extreme conditions, the source composition can change again. Turner and Kim identified quadrupole contributions associated with the near wake in full stall, indicating that at sufficiently deep separation the acoustic field can no longer be modelled as arising purely from surface dipoles, and that volumetric turbulence in the wake can contribute appreciably to the radiated sound [66].

Although dynamic stall studies provide useful insight into large-scale separation-driven acoustics, they should be distinguished from the present context, which concerns static high-incidence separation on a fixed aerofoil.

Dynamic stall introduces additional unsteadiness and hysteresis because the separation state depends not only on instantaneous angle of attack but also on the recent motion history through vortex formation, convection, and shedding. Raus *et al.* showed experimentally that when an aerofoil oscillates through stall, the low-frequency noise “burst” is delayed on the upstroke and persists into the downstroke, producing clear hysteresis in overall level [67, 62]. They further demonstrated that the magnitude and timing of the radiated noise depend on reduced frequency, reflecting competition between the motion time scale and the time scales of shear-layer roll-up and dynamic-stall vortex evolution. However, the mechanisms highlighted above indicate why such models face limitations for dynamic stall: the acoustic output is governed by time-resolved separation state, vortex formation and convection, and evolving source coherence, all of which can deviate substantially from quasi-steady assumptions based solely on instantaneous operating

conditions [62, 40]. These difficulties help explain why stall-noise prediction remains less robust than prediction for attached-flow trailing-edge or leading-edge interaction noise.

Overall, the literature shows that stall-induced separation noise differs fundamentally from attached-flow edge-noise mechanisms because the effective source region becomes spatially extended and is dominated by large coherent structures in the separated shear layer and near wake [38, 39, 40]. This explains the characteristic rise in low-frequency radiation, the altered directivity, and the closer coupling between acoustic output and aerodynamic state near stall [61, 63, 64]. What remains less clearly established is how active control reorganises the separated-flow topology, modifies the dominant unsteady structures, and alters the near-wall flow–acoustic coupling that sustains the radiated sound. These unresolved points motivate the present study of leading-edge blowing at high incidence in Chapter 6, where acoustic, aerodynamic, and flow-field measurements are considered together.

2.4 Noise Control Strategies: Passive & Active Approaches

Efforts to reduce aerofoil self-noise have developed along two broad paths: passive geometric modifications and active flow control [59, 68, 69]. In passive approaches, the aerofoil geometry or surface properties are modified so as to alter the formation and scattering of pressure fluctuations without any external energy input. Typical examples include trailing-edge serrations, porous or compliant treatments, and leading-edge shaping inspired by biological adaptations [13, 14, 17, 70, 19]. Active strategies, by contrast, deliberately inject or remove momentum or energy through blowing, suction, or plasma actuation in order to modify instability amplification, separation, or incoming turbulence interactions in a controlled manner [23, 71, 68]. From a source-mechanism perspective, both classes of techniques aim to weaken the hydrodynamic structures that radiate sound, decorrelate the surface-pressure field, or reduce the efficiency of the aeroacoustic scattering process, but they do so with very different degrees of adaptability and system complexity.

From a mechanism-based perspective, passive and active approaches differ not only in implementation but also in the range of source processes they can influence. Passive concepts are often most effective when tailored to a specific scattering or receptivity mechanism, whereas active approaches offer greater adaptability and, in some cases, the potential to influence multiple mechanisms from a single actuation location. The following subsections review these two classes of control in turn, with particular emphasis on the extent to which they can address trailing-edge tonal noise, leading-edge broadband interaction noise, and stall-induced separation noise.

2.4.1 Passive Control at Leading & Trailing Edges

Passive modifications to aerofoil geometry remain among the most widely explored strategies for self-noise reduction. They require no external energy input and can be integrated into the aerofoil structure itself, making them attractive for applications ranging from wind turbines to aircraft high-

lift systems. The central idea is to weaken the efficiency of aeroacoustic radiation by modifying either (i) the way turbulent boundary-layer fluctuations are scattered at the trailing edge, or (ii) the way incoming disturbances are received and converted into unsteady loading at the leading edge. In both cases, the aim is typically to reduce the spatial coherence and effective strength of the surface-pressure field responsible for sound generation [59].

Representative passive edge treatments are shown schematically in Figure 2.4. Although these concepts differ in geometry and implementation, they share a common objective: to reduce the strength and coherence of the unsteady loading that is ultimately scattered into sound. In the present context, porous and serrated trailing edges primarily target trailing-edge broadband noise, whereas serrated leading edges are intended to weaken turbulence–aerofoil interaction noise by modifying leading-edge receptivity and the spatial organisation of the induced loading.

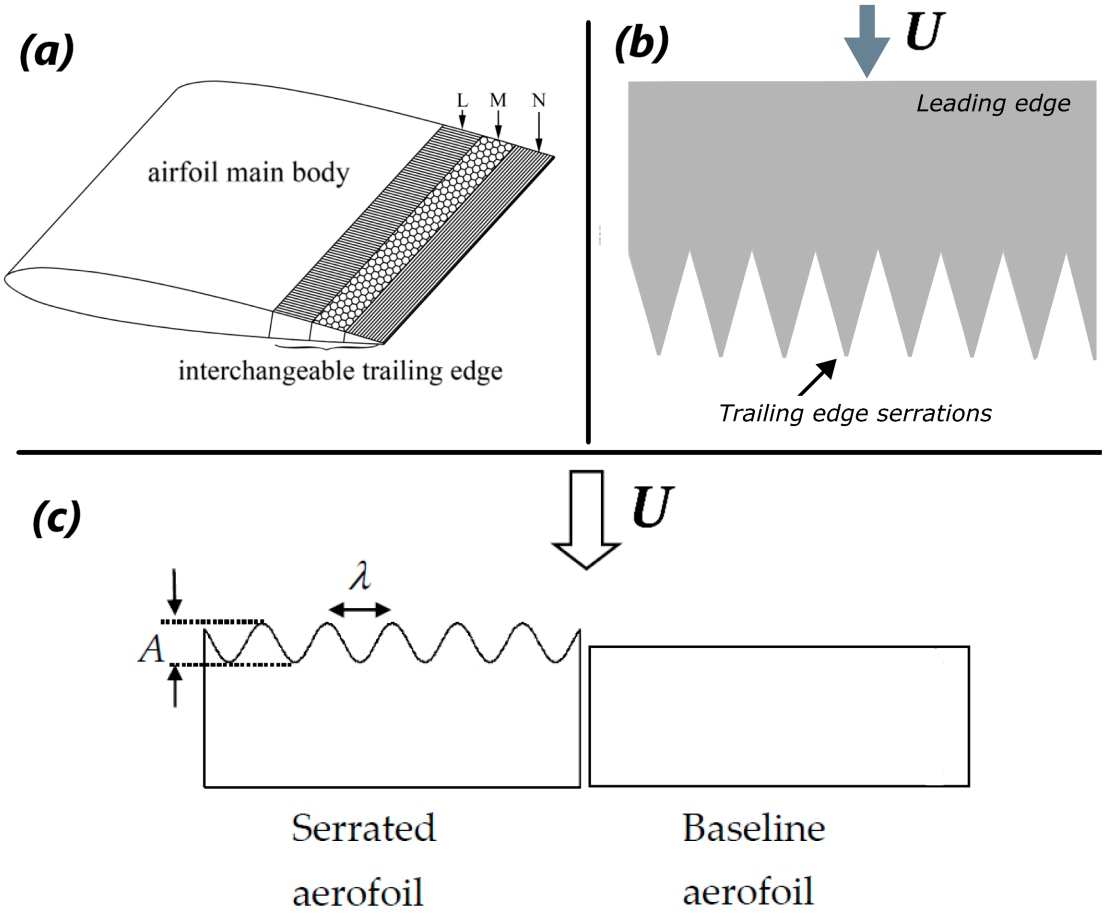

Figure 2.4: Representative passive edge treatments for aerofoil noise reduction: (a) porous trailing edge, (b) schematic serrated trailing edge, and (c) serrated leading edge. Panels (a) and (c) reproduced from Wang et al. [72] and Al-Okbi et al. [73].

One of the most extensively studied passive approaches is the use of serrated trailing edges. Serrations have been shown to reduce broadband trailing-edge noise across a wide range of Reynolds numbers by modifying the phase relationship of the scattered pressure fluctuations along

the spanwise-varying edge. Howe's analytical model [13] established the foundational mechanism, showing that sawtooth geometries can promote partial destructive interference in the far field and thereby reduce radiated levels. Experiments by Gruber, Joseph, and Chong [14] reported reductions of order 2–5 dB in OASPL, depending on geometry and operating condition, and linked this performance to changes in the spanwise organisation of surface-pressure fluctuations and wake structure. Brooks and Humphreys [74] confirmed comparable reductions in controlled wind-tunnel tests, showing that serrations can deliver several decibels of reduction over mid-frequency bands without severe aerodynamic penalties when appropriately designed. More recent results, such as those of Woodhead *et al.* [75], further demonstrated that geometric details beyond the basic planform shape, in particular serration flap angle, can enhance or diminish performance by several decibels. Taken together, these studies show that serrated trailing edges should be treated not as universally optimal add-ons, but as mechanism-sensitive devices whose performance depends strongly on geometric tuning and operating condition.

Porous trailing-edge treatments form another important class of passive control, motivated by the idea that a permeable edge modifies both the near-edge hydrodynamics and the effective acoustic boundary condition seen by edge-scattered pressure fluctuations. Geyer *et al.* [17] reported broadband noise reductions of around a few decibels in OASPL for porous inserts, while also noting that permeability can introduce side effects such as increased radiation at very low frequencies depending on the configuration. Rubio Carpio *et al.* [18] studied the underlying boundary-layer response and demonstrated that the achieved reduction is sensitive to porosity distribution and Reynolds number, consistent with the view that porous edges alter the wall-pressure spectrum and its coherence as well as the scattering efficiency at the edge. Together, these studies show that porosity can be effective as a broadband trailing-edge treatment, but that its performance is coupled to structural design constraints and to the flow state near the edge, which must be accounted for if reductions are to be robust.

Leading-edge modifications provide a complementary route that targets turbulence-aerofoil interaction noise by altering the receptivity and unsteady loading generated as incoming disturbances encounter the stagnation region. Bio-inspired leading-edge shaping has been a major theme in this area. Fish and Battle [15] described how the tubercles on humpback whale flippers can promote beneficial aerodynamic performance, which later motivated aeroacoustic adaptations aimed at disrupting coherent gust-leading-edge interactions. Kim *et al.* [16] showed that sinusoidal leading-edge geometries can reduce leading-edge broadband noise, with effectiveness depending strongly on the relationship between the inflow turbulence length scales and the geometric wavelength of the waviness. Chaitanya *et al.* [76] extended this to three-dimensional configurations and demonstrated that reductions (of order several decibels, depending on operating condition) are closely tied to how the leading-edge geometry redistributes spanwise coherence and modifies the near-leading-edge unsteady loading response.

Beyond sinusoidal shaping, leading-edge serrations have also been used explicitly as passive interaction-noise treatments. Narayanan *et al.* [77] reported leading-edge noise reductions at-

tributable to spanwise de-correlation and modification of the gust-to-loading transfer, reinforcing the interpretation that interaction noise can be mitigated by fragmenting coherent excitation into smaller, less correlated patches along the span. Chong *et al.* [78] further examined the influence of leading-edge serration geometry and operating parameters, highlighting that the achievable reduction is highly design-dependent and that the most effective configurations align the geometric length scales with those of the incoming turbulence. To support design and comparison across configurations, Biedermann *et al.* [79] developed a statistical–empirical modelling framework for aerofoil noise with leading-edge serrations, providing a practical route to relate serration parameters and inflow conditions to expected acoustic outcomes. In parallel to geometric shaping, porous leading-edge concepts have also emerged as a passive method to modify leading-edge receptivity and scattering: Bowen *et al.* [80] demonstrated that leading-edge porosity can reduce turbulence–aerofoil interaction noise, with the extent of reduction depending on the porosity configuration and inflow condition, consistent with the idea that permeability can attenuate unsteady loading and weaken the efficiency of the leading-edge scattering process.

More broadly, a number of studies have explored combining edge concepts or transferring insights between leading- and trailing-edge treatments. Clark *et al.* [19] summarised and demonstrated bio-inspired trailing-edge noise control concepts that emphasise coherence reduction and scattering modification, while Teruna *et al.* [81] investigated porous materials and serrations in a rod–aerofoil interaction configuration, illustrating how passive treatments can be assessed in more realistic, interaction-driven inflow environments where both leading-edge reception and trailing-edge scattering may contribute to the measured sound. These efforts underscore that passive devices are rarely “single-effect” in practice: they often act simultaneously on turbulence structure, surface-pressure coherence, and scattering efficiency.

Taken together, these studies show that passive edge treatments can produce meaningful reductions in aerofoil self-noise by weakening coherent scattering, reducing effective surface-pressure coherence, or modifying the receptivity of the edge to incoming disturbances. Their strongest performance is usually obtained when the treatment is matched to a specific mechanism, such as trailing-edge broadband noise or leading-edge turbulence-interaction noise, rather than across all operating regimes simultaneously. This mechanism-specific effectiveness is one of the main limitations of passive control and provides part of the motivation for active strategies, particularly when broader operating flexibility is required.

2.4.2 Active Flow Control with Blowing & Suction

Active flow control approaches differ fundamentally from passive strategies in that they introduce external energy into the flow in order to manipulate aerodynamic and aeroacoustic behaviour. In aerofoil self-noise applications, active methods are often grouped into (i) mass-flux actuation such as steady or unsteady blowing and suction, (ii) zero-net-mass-flux actuation such as synthetic jets, and (iii) electrohydrodynamic actuation such as dielectric barrier discharge plasma. These approaches can target the dominant sound-producing flow features directly by weakening instabil-

ity amplification, altering boundary-layer state, disrupting coherent structures in separated shear layers, or reducing the spatial coherence of surface-pressure fluctuations that radiate efficiently [71, 28].

Among the available active concepts, leading-edge blowing is of particular interest because a single actuation location has the potential to influence several distinct aeroacoustic mechanisms. By modifying boundary-layer development close to the nose, it can affect the laminar-separation-bubble dynamics associated with tonal noise, the gust-interaction process responsible for leading-edge broadband noise, and the separated-flow topology that governs stall-induced separation noise. This multi-mechanism reach is the main reason it forms the central active-control concept in the present thesis.

This multi-mechanism potential has been demonstrated in several studies of blowing and suction near the leading edge. By stabilising or eliminating laminar separation bubbles, modifying the receptivity of the leading edge to incoming disturbances, and altering the development of separated shear layers, leading-edge actuation provides a versatile route for targeting multiple self-noise mechanisms. A classic demonstration was provided by Choudhari and Khorrami [27], who showed that steady leading-edge blowing through spanwise slots can suppress discrete tonal components associated with laminar separation bubble instabilities. Their results highlighted that relatively small momentum input, with C_μ on the order of 10^{-3}, can be sufficient to disrupt the hydrodynamic and acoustic feedback loop that locks the tonal frequency.

Beyond steady actuation, unsteady excitation has been explored as a means of targeting specific instability bands more selectively. Kumar and Bhumkar [50] investigated periodic suction blowing excitation as a direct method to modify aerofoil tonal noise, showing that the tonal content can be reshaped through controlled forcing that interferes with the growth and phase coherence of instability waves. In parallel, synthetic jets have been widely studied as practical actuators because they provide periodic momentum injection without net mass addition. The foundational formation and dynamics of synthetic jets were established by Smith and Glezer [25], and Amitay and Glezer [24] demonstrated their strong authority for separation control on stalled aerofoils. Although these studies are primarily aerodynamic, the same flow changes that drive reattachment and modify shear-layer dynamics also address the physical origin of stall-related low-frequency noise by weakening coherent separated structures and reducing large-scale lift fluctuations.

Recent investigations have also focused on broadband noise control, including both leading-edge interaction noise and turbulent boundary-layer trailing-edge noise. Al-Okbi, Chong, and Stalnov [73] reported that steady leading-edge blowing can reduce leading-edge broadband levels by several decibels, and they showed that performance can be enhanced when combined with passive trailing-edge serrations. Their findings support a coupled interpretation in which leading-edge actuation can reduce the strength of the primary turbulence interaction while also modifying the downstream wall-pressure field and the efficiency of trailing-edge scattering. For broadband trailing-edge noise more specifically, Yang *et al.* [82] demonstrated active control of aerofoil turbulent boundary-layer noise using trailing-edge blowing, providing direct evidence that targeted

momentum injection near the edge can alter the near-wall pressure spectra and reduce radiated broadband sound. Closely related diagnostic work by Chong and Muhammad [83] showed that boundary-layer control devices can significantly modify turbulent wall-pressure spectra. While wall-pressure reductions do not translate one-to-one into far-field sound reduction, these measurements are mechanistically important because surface-pressure statistics and coherence are the immediate hydrodynamic drivers of scattering-based aerofoil self-noise.

Blowing and suction have also been applied for stall and dynamic stall control, where the relevant noise mechanisms are governed by time-dependent separation state and coherent vortex evolution. Santra and Greenblatt [84] developed a dynamic stall control model for pitching aerofoils using slot blowing, demonstrating that actuation can alter stall onset and the evolution of separated flow during oscillation. This is directly relevant to aeroacoustics because dynamic stall noise is strongly tied to the formation and convection of large coherent structures. It is important, however, to distinguish between dynamic stall noise characterisation studies and studies that actually include actuation. In particular, Raus *et al.* [62] documented hysteresis and low-frequency noise bursts during pitching cycles, but the work does not itself provide evidence of blowing-based noise reduction. The broader implication is that active strategies aimed at dynamic stall must be evaluated using time-resolved measurements that track both separation dynamics and the resulting acoustic response under actuation.

Plasma actuators provide an alternative active route with different integration and bandwidth trade-offs. Corke, Enloe, and Wilkinson [26] reviewed dielectric barrier discharge plasma actuators as flow-control devices capable of near-wall momentum addition without moving parts, while Huang and Zhang [85] discussed their potential specifically in noise-control contexts. In dynamic stall settings, De Troyer *et al.* [86] demonstrated plasma-based control and modelling on a low-aspect-ratio wing, showing that plasma actuation can meaningfully modify separated-flow development in unsteady conditions. Although plasma studies are not always framed in terms of aerofoil self-noise mechanisms, the demonstrated ability to manipulate separation and shear-layer dynamics makes them particularly relevant to stall-related noise and, in some configurations, to tonal or narrowband components associated with unsteady separation.

Active flow control offers a level of adaptability that passive methods cannot provide, but this advantage is accompanied by practical challenges including actuator placement, power requirements, integration complexity, and sensitivity to operating condition. The effectiveness of a given strategy depends strongly on whether the objective is to suppress tonal feedback, weaken turbulence-interaction noise, or reorganise separated flow near stall. For this reason, not all active methods are equally suited to a unified study of multiple aeroacoustic mechanisms. In the present context, leading-edge blowing is especially attractive because it combines relative implementation simplicity with the ability to influence tonal, broadband, and separation-related noise within a single configuration. This makes it a particularly suitable candidate for the mechanism-led investigation developed in the following chapters.

2.4.3 Comparative Evaluation of Control Methods

The effectiveness of aerofoil-noise control strategies depends on both the underlying source mechanism and the practical constraints of implementation. Passive approaches such as serrated or porous trailing edges, wavy leading edges, and other bio-inspired geometries can provide robust broadband reductions without power input, which makes them attractive for engineering systems where simplicity, reliability, and ease of integration are priorities [14, 17, 76]. Their main limitation is that performance is usually tied to a relatively narrow set of operating conditions and to the mechanism for which the treatment was designed.

Active methods offer greater flexibility because the control input can be varied with operating state. This makes them particularly attractive when the target source mechanism changes with angle of attack, inflow condition, or separation state. However, the practical advantages of active control are balanced by increased system complexity, power requirements, actuator integration issues, and sensitivity to control parameters such as momentum coefficient, forcing frequency, and phase [71, 28]. Their success therefore depends not only on the authority of the actuation, but also on how precisely the control input is matched to the relevant flow instability or source process.

Direct comparisons between passive and active strategies remain limited, but the available literature suggests that the most promising direction may lie in combining them. Passive modifications can provide a robust baseline reduction, while active methods can adaptively target off-design conditions or mechanisms that are highly sensitive to flow state. In this respect, leading-edge blowing is of particular interest because, unlike most passive concepts, it offers the possibility of influencing tonal noise, leading-edge broadband interaction noise, and stall-induced separation noise within a single actuation framework. This multi-mechanism potential is a key reason why it is selected as the central control strategy in the present thesis.

2.5 Summary, Knowledge Gaps, and Link to Research Objectives

This chapter has reviewed the aeroacoustic foundations, self-noise mechanisms, and control strategies most relevant to the present study of the NACA 65(12)-10 aerofoil. The literature shows that trailing-edge tonal noise, leading-edge broadband turbulence-interaction noise, and stall-induced separation noise arise from distinct but strongly coupled flow processes, and that both passive and active control methods can reduce noise under selected conditions. It also shows that leading-edge blowing is one of the few active approaches with the potential to influence all three mechanisms from a single actuation location.

Despite this progress, the review also identifies several unresolved issues that motivate the present study.

1. Existing evidence for leading-edge blowing is fragmented across different noise mechanisms and test configurations. Most prior studies treat tonal noise, turbulence-interaction noise, or

separation-related noise separately. There remains limited experimental evidence showing, within a single aerofoil platform and measurement framework, how steady leading-edge blowing influences all three mechanisms in a consistent and comparable way.

2. Much of the existing literature reports the far-field acoustic outcome of blowing, but gives less attention to the flow physics responsible for the reduction. In particular, the relative roles of laminar-separation-bubble modification, wake reorganisation, turbulence decoherence, and changes in near-wall flow-acoustic coupling are not yet sufficiently resolved.

3. For leading-edge broadband noise, the effectiveness of steady leading-edge blowing has not been linked clearly enough to the properties of the incoming turbulence. The influence of turbulence length scale, anisotropy, and spatial coherence on control effectiveness remains insufficiently established, which limits the ability to generalise the method beyond a narrow set of inflow conditions.

4. For trailing-edge tonal noise, it remains unclear whether successful steady leading-edge blowing acts primarily by changing the selected tonal frequency or by weakening the instability growth and feedback coherence while leaving the preferred mode selection broadly intact. A more direct flow-acoustic interpretation is therefore needed.

5. For separation-stall noise, the literature is less mature than for tonal and broadband mechanisms, particularly in relation to active control. There is limited integrated experimental evidence combining acoustic, aerodynamic, and flow-field measurements to determine whether leading-edge blowing can reduce low-frequency stall noise while also delaying separation and retaining useful aerodynamic performance.

These knowledge gaps define the need for the present thesis and link directly to the research objectives introduced in Section 1.5.

1. The first objective, to quantify the acoustic effects of leading-edge blowing, addresses the need for a consistent experimental assessment across tonal, broadband, and stall-related noise mechanisms, and establishes the conditions under which measurable reductions are obtained.

2. The second objective, to correlate flow features with noise attenuation, addresses the lack of mechanistic clarity in the literature by relating acoustic reductions to changes in separation-bubble behaviour, wake organisation, turbulence coherence, and separated-flow structure.

3. The third objective, to assess the robustness and operating envelope of leading-edge blowing, addresses the need to determine how the method depends on angle of attack, blowing rate, and inflow condition, and to identify the regimes in which benefits weaken or aerodynamic trade-offs emerge.

The remainder of the thesis is structured to address these gaps directly. Chapter 4 examines the influence of leading-edge blowing on trailing-edge tonal noise, with emphasis on feedback disruption and flow-acoustic coherence. Chapter 5 considers leading-edge broadband noise under both isotropic and anisotropic inflow conditions, focusing on the role of turbulence scale and coherence. Chapter 6 then addresses separation-stall noise at high incidence, where both acoustic mitigation and aerodynamic consequences must be assessed together. In this way, the thesis moves from acoustic quantification to physical interpretation, and finally to an evaluation of the practical operating range of the control strategy.

Chapter 3

Experimental Setup

This chapter describes the overall experimental methodology adopted in the present study, including the wind tunnel facilities, aerofoil model and leading-edge blowing system, measurement techniques, calibration procedures, and data-processing approach. Figure 3.1 summarises the main stages of the investigation and shows how the experimental programme, supporting theoretical and empirical framework, and validation steps are connected across the three self-noise mechanisms considered.

As shown in Figure 3.1, the study begins with the definition of the aerofoil configuration, operating variables, and measurement facilities, followed by calibration and baseline characterisation. The investigation then proceeds through three mechanism-specific experimental campaigns corresponding to trailing-edge tonal noise, leading-edge broadband interaction noise, and separation-stall noise. The resulting acoustic, aerodynamic, and flow-field measurements are processed and interpreted using established aeroacoustic frameworks, and are cross-checked for consistency before being synthesised into the final conclusions of the thesis.

The following sections describe the common experimental elements used throughout the thesis. The wind tunnel facilities and flow conditions are introduced first, followed by the aerofoil model and blowing system, and finally the instrumentation and data-processing procedures used to characterise the flow and the radiated sound.

3.1 Wind Tunnel Facilities and Flow Conditions

The experimental campaigns in this thesis were carried out in a set of low-speed wind tunnel facilities, each equipped with different nozzle geometries and test section configurations. This section summarises the relevant characteristics of the facilities that were used. The description is limited to those features that are required to interpret the aerodynamic and acoustic measurements presented later, and to distinguish between the different test campaigns.

In addition to the geometric and acoustic properties of the facilities, the procedures used to define the flow conditions and to correct the angle of attack are introduced. These include the de-

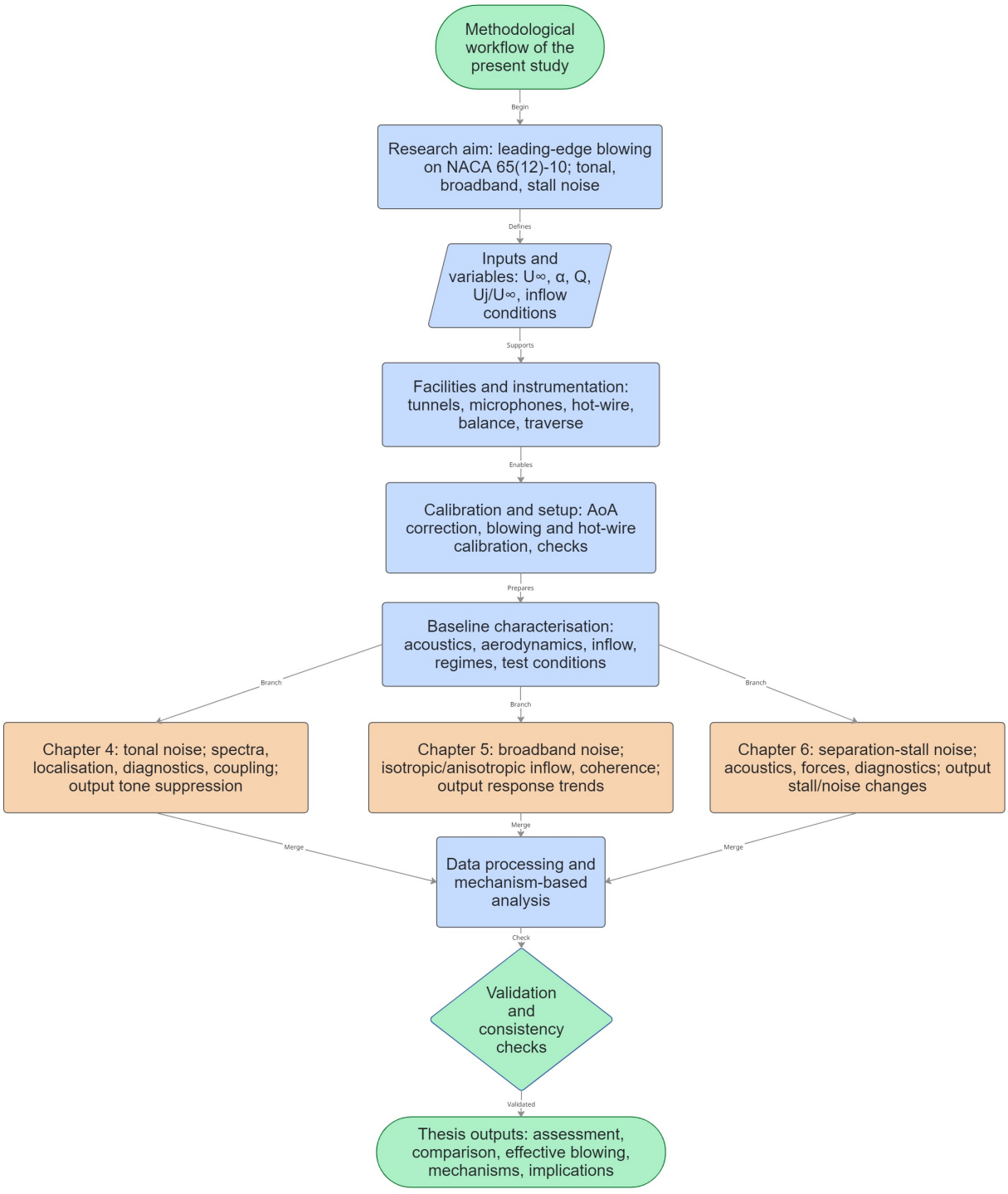

Figure 3.1: Overview of the methodological workflow adopted in the present study, showing the main inputs, experimental stages, supporting theoretical and empirical framework, validation steps, and chapter-wise outputs.

termination of the effective free-stream velocity in each configuration and the correction of nominal angle settings based on reference measurements. The resulting definitions are used throughout the thesis when specifying Reynolds number, Mach number, angle of attack, and related parameters for each experimental case.

3.1.1 Anechoic Chamber

The aeroacoustic measurements in this study were conducted in the aeroacoustics facility at Brunel University of London. The facility consists of a closed anechoic chamber with internal dimensions of $4\ \mathrm{m} \times 5\ \mathrm{m} \times 3.4\ \mathrm{m}$ that encloses an open-jet wind tunnel. The chamber walls, ceiling, and floor are lined with acoustically absorbing foam blocks, as shown in Figure 3.2, which are designed to minimise reflections of acoustic waves within the frequency range of interest. This configuration allows the radiated sound field from the test section to be measured under conditions that approximate a free-field environment.

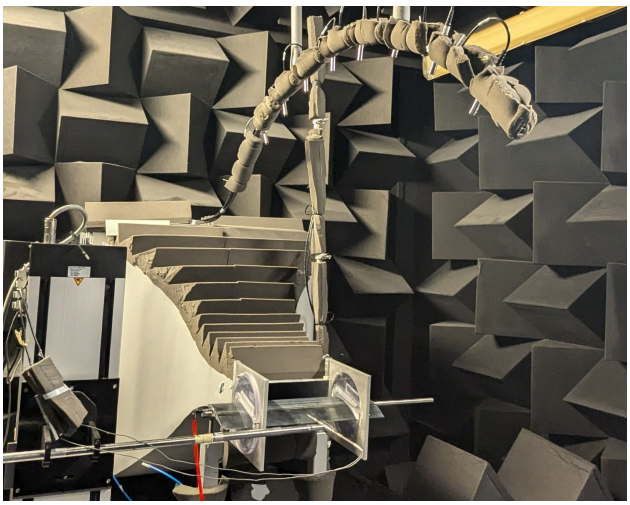

Figure 3.2: Anechoic chamber at Brunel University of London

The open jet issues from a rectangular nozzle into the centre of the chamber and forms a free jet in which the test model is mounted. Depending on the specific experiment, different nozzle geometries were installed at the tunnel exit. In all cases, the acoustic response was recorded using a far-field microphone array located at a distance of $0.97\ \mathrm{m}$ from the model at mid-span, and the flow conditions were adjusted to match the requirements of each campaign. Background noise levels were characterised in the absence of the airfoil, with the side plates in place, in order to quantify the contribution of the facility to the measured spectra and to verify that the self-noise of the airfoil dominated under the operating conditions considered.

3.1.1.1 Nozzle configurations

Two interchangeable rectangular converging nozzles were used at the exit of the open-jet wind tunnel, referred to in the following as Nozzle 1 and Nozzle 2, and illustrated in Figure 3.3. Both nozzles are supplied by the same pressure plenum, with a maximum mass flow rate of $30\ \mathrm{kg\,s^{-1}}$, and discharge into the anechoic chamber described earlier. The chamber dimensions remain fixed at $4\ \mathrm{m} \times 5\ \mathrm{m} \times 3.4\ \mathrm{m}$ for all configurations, and the microphone array and model mounting arrangement are unchanged between tests, which allows direct comparison of measurements obtained with the two nozzle geometries.

Nozzle 1, shown in Figure 3.3(a), is a rectangular converging nozzle with an exit cross-section of $300\ \mathrm{mm} \times 100\ \mathrm{mm}$ (width $\times$ height). The corresponding outlet area is $(100 \times 300)\ \mathrm{mm}^2$, supplied from a square inlet of $(867 \times 867)\ \mathrm{mm}^2$, which gives an area ratio of approximately $25 : 1$. When operated at the maximum mass flow rate, this configuration provides a free-stream velocity at the nozzle exit of up to $U_\infty = 80\ \mathrm{m\,s^{-1}}$. In the potential core of the free jet, the turbulence intensity remains low, with measured values in the range $I = 0.1\%$ to 0.2% at $U_\infty = 20\ \mathrm{m\,s^{-1}}$ and $U_\infty = 30\ \mathrm{m\,s^{-1}}$. These characteristics make Nozzle 1 suitable for detailed broadband trailing-edge and leading-edge noise measurements at moderate angles of attack, where a well-defined, low-turbulence inflow is required.

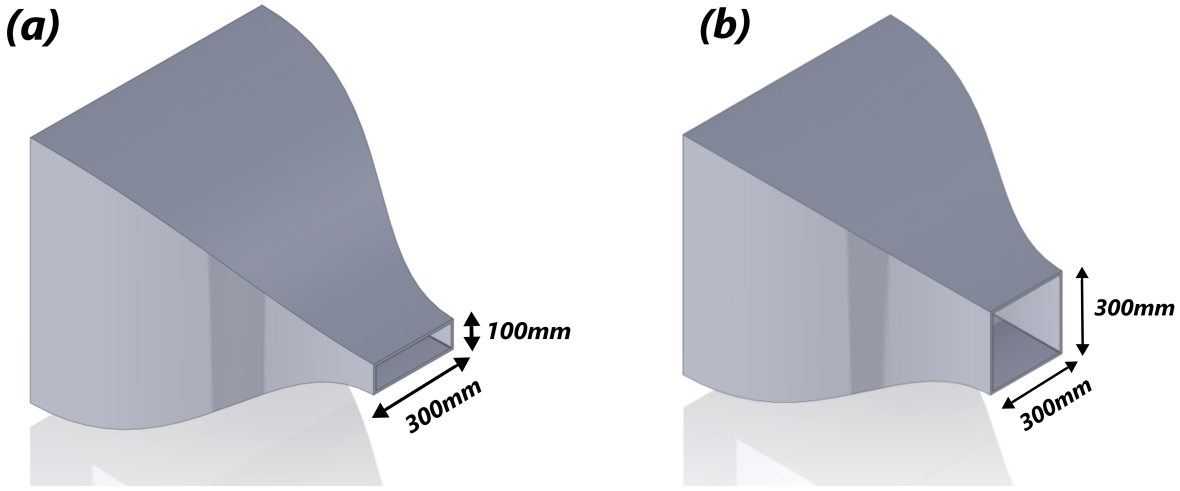

Figure 3.3: Representative CAD views of the two nozzle configurations: (a) Nozzle 1 with the smaller rectangular exit cross-section; (b) Nozzle 2 with the larger exit height used for high angle-of-attack and stall experiments.

For a subset of experiments, in particular those targeting higher angles of attack and stalled flow conditions, a second nozzle with a larger exit area, denoted Nozzle 2 and shown in Figure 3.3(b), was installed at the tunnel exit. The increased jet height of Nozzle 2 provides additional vertical clearance around the airfoil and reduces the likelihood of interaction between the jet shear layer and the separated flow over the model. This is important when investigating near-stall and fully stalled configurations, where the wake thickness and the extent of the separated region are

significantly larger than in attached flow. For a given mass flow rate, the larger exit area of Nozzle 2 leads to a lower nominal jet velocity than in the Nozzle 1 configuration, while still allowing the Reynolds number to be adjusted to match the requirements of each campaign. Apart from the change in exit geometry, all other aspects of the facility, including the anechoic environment and the measurement layout, remain identical, which ensures that differences observed in the results can be attributed to the change in nozzle configuration and associated flow conditions.

3.1.2 Aerodynamic Wind Tunnel

The aerodynamic force measurements were carried out in the Aerodynamic Laboratory at Brunel University. The facility consists of an open-circuit, suction-type low-speed wind tunnel with a closed rectangular test section of $0.50\ \mathrm{m} \times 0.50\ \mathrm{m}$ (height $\times$ width). The flow enters the test section through a converging nozzle with an area ratio of 3:1. Upstream of the nozzle, a series of mesh screens and honeycomb elements are installed to straighten the flow and to attenuate large-scale velocity fluctuations. This arrangement produces a uniform, high-quality free stream in the test section, with a turbulence intensity of approximately 0.2% to 0.3%, which is suitable for precise aerodynamic measurements.

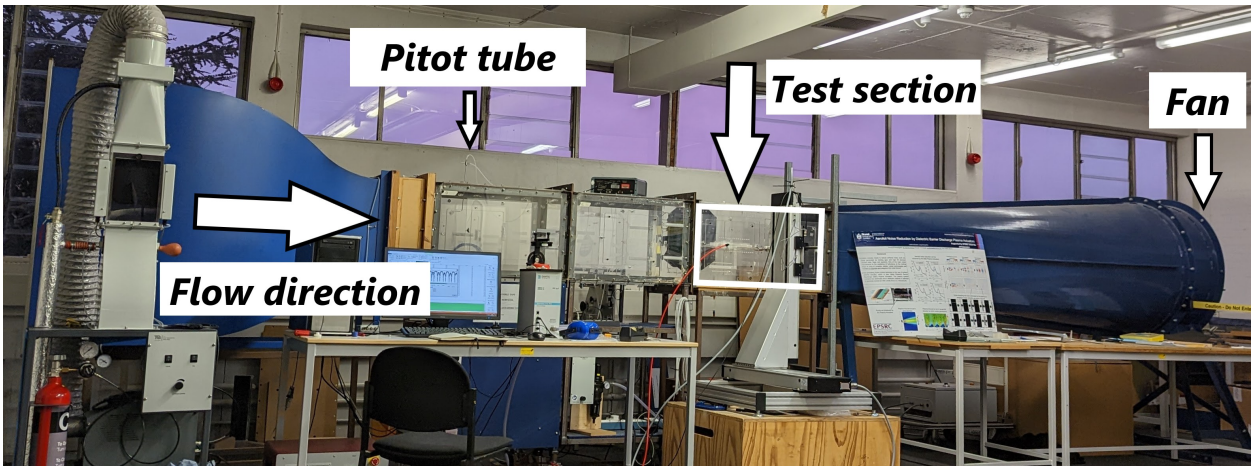

Figure 3.4: Aerodynamic wind tunnel used for force balance measurements

The tunnel is driven by an axial fan located at the exit of the diffuser. The fan has a diameter of $99\ \mathrm{cm}$, is equipped with eight blades set at a pitch angle of $32.5°$, and is powered by a $7.5\ \mathrm{kW}$ motor. Under these conditions, the facility can achieve a maximum free-stream velocity of about $U_\infty = 35\ \mathrm{m\,s^{-1}}$ in the test section. On each side of the closed test section, three interchangeable acrylic glass windows are provided, which permit the installation of different model configurations and allow visual access to the flow and the model during operation.

A three-component force balance (Plint & Partners Ltd.) was used to measure the aerodynamic forces generated by the airfoil model mounted inside the test section. The balance provides simultaneous measurements of lift, drag, and pitching moment, and was the primary instrument

used in this work to quantify the effect of angle of attack and flow control on the global aerodynamic performance of the airfoil (see Figure 3.4).

3.1.3 Flow Conditions and Angle-of-Attack Corrections

3.1.3.1 Definition of flow conditions

In all experiments, the flow conditions are expressed in terms of a reference chord length c and the corresponding chord-based Reynolds number

$$Re_c = \frac{\rho U_\infty c}{\mu},$$

where ρ and μ are the density and dynamic viscosity of air, and U_∞ is the free-stream velocity in the test section. The value of c is defined separately for each facility and nozzle configuration, and corresponds to the geometric chord of the airfoil installed in that configuration. When results from different tunnels or nozzles are compared directly, the associated reference chord is stated explicitly to avoid ambiguity.

In the closed test-section aerodynamic wind tunnel, the airfoil model spans $500\ \mathrm{mm}$ across the $500\ \mathrm{mm} \times 500\ \mathrm{mm}$ test section, so that the effective span closely matches the tunnel width and three-dimensional end effects are minimised. Under these conditions, the projected-area blockage ratio is small, and classical solid-wall interference effects are therefore expected to remain limited within the attached-flow regime.

In the open-jet anechoic facility, a shorter span of $300\ \mathrm{mm}$ is used in order to fit within the free jet issued from the rectangular nozzle while maintaining adequate clearance from the jet boundaries and the side plates. These choices ensure that three-dimensional end effects are controlled and that the spanwise extent of the model is compatible with the measurement aperture of the microphone array.

Unless stated otherwise in the individual test descriptions, the free-stream velocity U_∞ was set in the range $20\ \mathrm{m\,s^{-1}} \leq U_\infty \leq 30\ \mathrm{m\,s^{-1}}$. Within this range, the Mach number remains sufficiently low that compressibility effects can be neglected for both the aerodynamic and acoustic analyses presented in the following chapters. Where tests were conducted outside this range, the corresponding value of U_∞ (and hence Re_c) is stated explicitly in the relevant chapter to avoid ambiguity. All non-dimensional quantities based on U_∞ and c, including Re_c and the various Strouhal numbers introduced later, are defined with respect to these reference flow conditions.

3.1.3.2 Angle-of-attack correction methodology

As discussed above, the experiments were conducted in multiple wind tunnel facilities with different nozzle configurations and mounting arrangements. In each case, the airfoil was set to a prescribed geometric angle of attack α_{geo} based on the mechanical settings of the rig. However, small differences in alignment, jet curvature, and local flow incidence between facilities can lead

to discrepancies between α_{geo} and the effective aerodynamic angle experienced by the airfoil. In order to compare results obtained in the anechoic open-jet facility with those from the closed test-section aerodynamic wind tunnel, a systematic angle-of-attack correction is therefore required.

To help define a unified aerodynamic incidence across all facilities, the geometric angles of attack obtained from Nozzle 1 and Nozzle 2 (defined as α_{N1} and α_{N2}) are mapped onto a reference angle α_{ref} derived from the closed-section wind tunnel (Figure 3.4) lift curve. The reference tunnel is used for this purpose because the model spans the full test-section width and the flow is constrained by solid boundaries, hence reducing sensitivity to free-jet curvature and shear-layer induced flow angularity. In this configuration, a reference lift curve was obtained from surface pressure measurements and the corresponding pressure-derived lift coefficient, providing a robust relationship between lift coefficient and incidence.

Figure 3.5 summarises the data used to construct this correction. In (a), the lift coefficient C_L is plotted as a function of the geometric angle of attack for the three configurations considered. The curves corresponding to Nozzle 1, Nozzle 2, and the reference closed-section tunnel were all obtained from surface pressure measurements at several x/c locations along the airfoil chord. At each location, the pressure coefficient was calculated from the recorded pressure readings as

$$C_p = \frac{p_{\text{channel}} - p_{\text{static}}}{p_{\text{total}} - p_{\text{static}}},$$

where p_{channel} is the pressure measured at the surface tap channel. The resulting C_p distributions on the suction and pressure surfaces were then integrated chordwise using the trapezium rule to obtain C_L.

The lift curves in Figure 3.5(a) show that, over the range of relatively low angles of attack where the flow remains attached, all three configurations exhibit a similar linear trend of C_L with α_{geo}. The slopes of the three curves are comparable, indicating that the basic lift response of the airfoil is consistent between tunnels. The main difference in this regime is a small horizontal shift between the curves, which appears as an offset in the zero-lift angle and in the angle corresponding to a given C_L. This behaviour is consistent with modest differences in the effective incidence experienced by the airfoil, for example due to slight misalignments in the mounting, differences in the local flow direction within the free jet compared to the closed test section, or a combination of both. These systematic offsets motivate the introduction of a correction that maps the geometric angle in each facility to a common reference angle.

At higher geometric angles of attack, the behaviour of Nozzle 2 departs more markedly from that of the reference lift curve. In particular, the $C_L(\alpha_{\text{geo}})$ curve for Nozzle 2 exhibits a double-peak structure once α_{geo} exceeds approximately 12°. This behaviour indicates that, in the Nozzle 2 configuration, the flow over the airfoil undergoes a more complex sequence of separation and partial reattachment as the angle is increased, which modifies the progression of stall and leads to a non-monotonic lift response. Within the operating range used to construct the correction, the lift coefficient varies approximately linearly with geometric angle of attack. Since facility-to-facility discrepancy arises primarily from systematic incidence offsets and small differences in effective flow

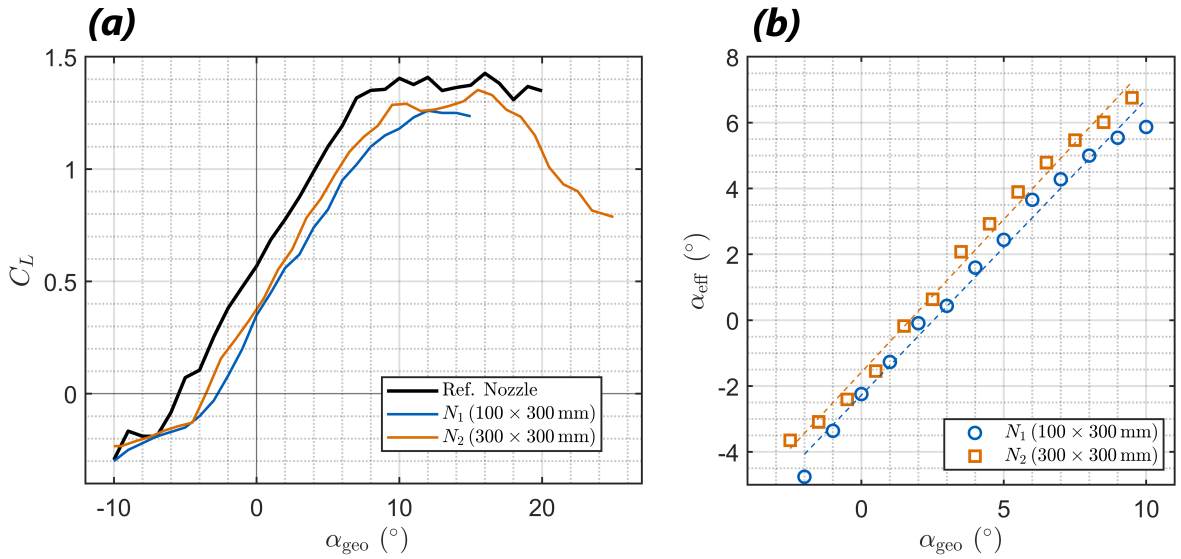

Figure 3.5: (a) Lift coefficient C_L versus geometric angle of attack for the three facilities. (b) Linear relation between reference angle α_{ref} and geometric angles for Nozzle 1 and Nozzle 2 used for angle-of-attack correction.

angularity, the resulting mapping between α_{N} and α_{ref} is expected to be monotonic and approximately linear over the range of angles used for the regression. The regression procedure used to construct the angle-of-attack correction is illustrated in Figure 3.5(b). For each configuration, data points are selected from the approximately linear portion of the lift curves in Figure 3.5(a). For a given value of C_L, the corresponding geometric angle of attack measured in the anechoic facility, α_{N1} or α_{N2}, is paired with the reference angle of attack α_{ref} obtained from the pressure-derived lift curve in the closed-section wind tunnel. This procedure yields two sets of angle pairs, $(\alpha_{\mathrm{N1}}, \alpha_{\mathrm{ref}})$ and $(\alpha_{\mathrm{N2}}, \alpha_{\mathrm{ref}})$, which are then used to determine a linear mapping between the geometric angles in each facility and the chosen reference angle.

In Figure 3.5(b), these pairs are plotted together with the corresponding least-squares linear fits for Nozzle 1 and Nozzle 2. Over the calibration range ($-10° \leq \alpha_{\mathrm{N}} \leq 11°$), the relationship between α_{N} and α_{ref} exhibits negligible curvature and is well represented by a first-order regression. The fitted slopes are close to unity, and the intercepts are small compared to the full range of angles considered, indicating that the main effect of the correction is to account for modest systematic offsets and slight scaling differences between the geometric settings in each tunnel and the effective aerodynamic incidence defined by the reference lift curve.

On this basis, the conversion from geometric angle of attack in the anechoic facility to the reference angle used throughout the thesis is defined by

$$\alpha_{\mathrm{ref}} = 0.8854\,\alpha_{\mathrm{N1}} - 1.1482 \tag{3.1}$$

for data obtained with Nozzle 1, and

$$\alpha_{\mathrm{ref}} = 0.9606\,\alpha_{\mathrm{N2}} - 2.1413 \tag{3.2}$$

for data obtained with Nozzle 2, where all angles are expressed in degrees. Unless stated otherwise, the angle of attack α reported in the following chapters corresponds to α_{ref} computed from Eqs. (3.1) and (3.2) for the appropriate facility. This mapping provides a practical common incidence definition for comparing results obtained in the different facilities.

The correction described above for the large open jet nozzle is based on the approximately linear portion of the lift curves and is therefore most reliable within the attached-flow regime. At higher angles of attack, particularly near and beyond stall, the lift response becomes nonlinear, making the relation between the open-jet and closed-section curves is less direct. The corrected angles in this regime should therefore be regarded as approximate effective incidences.

Nevertheless, while achieving excellent lift-curve slope matching in the pre-stall regime between the reference nozzle and the large open-jet nozzle, the slopes in the stall and post-stall regimes are also closely matched. This suggests that the correlation between effective and geometrical angles of attack remains applicable across the entire investigated range. Ultimately, this approach provides the most consistent method for defining a common incidence reference across the full experimental range.

3.2 Airfoil Model

The experiments in this thesis are based on a single reference airfoil that is implemented, with minor adaptations, in the different wind tunnel facilities. The purpose of this section is to describe the underlying airfoil geometry and the integration of the leading-edge blowing system.

The first part of the section describes the chosen airfoil shape, including the reference profile, chord, and any relevant geometric modifications. The second part focuses on the blowing system, covering the internal plenum layout, the leading-edge orifices, and the definition of the jet exit conditions and actuation parameters used throughout the thesis.

3.2.1 Airfoil Shape

The airfoil used in this work is the NACA 65(12)-10 profile from the NACA 6-series family, shown in Figure 3.6. This profile was selected within the FLOCON [87] consortium as a representative high-lift section for applications such as turbomachinery blades and wind turbine airfoils, and is also employed in FLOCON's linear cascade facility at ECL for combined aerodynamic and acoustic investigations. The NACA 65(12)-10 is characterised by an asymmetric geometry with a relatively high camber, which results in a non-zero lift coefficient at a geometric angle of attack of $\alpha_{\mathrm{geo}} = 0^{\circ}$. This inherent camber and the associated pressure distribution make the profile suitable for

studying trailing-edge and leading-edge self-noise mechanisms under conditions that are relevant to practical lifting configurations.

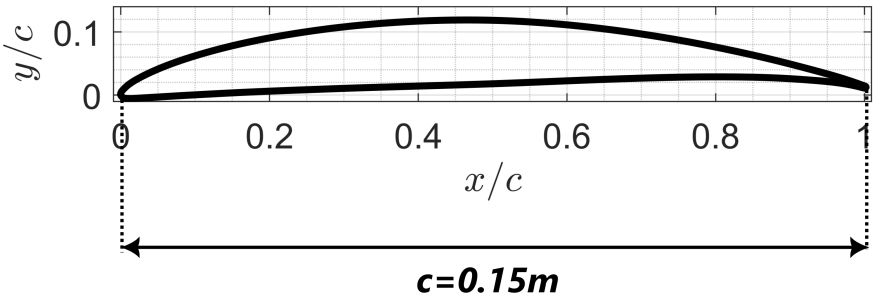

Figure 3.6: Geometry of the NACA 65(12)-10 airfoil used in the experiments.

The airfoil models used in the present experiments were manufactured by selective laser sintering (SLS) from a three-dimensional CAD model of the NACA 65(12)-10 profile generated in Siemens NX 9.0. The SLS process allows accurate reproduction of the designed profile, including local geometric details required for instrumentation and flow control. In particular, the interior of the model incorporates a hollow tubing system that permits air to be supplied through the side of the airfoil and routed internally to spanwise orifices located near the leading edge. This internal architecture provides the structural basis for the mechanical leading-edge blowing system used in the active flow control experiments, which is described in more detail in the following subsection.

3.2.2 Blowing System

Leading-edge blowing is implemented by means of an internal plenum integrated within the airfoil model. Compressed air is supplied externally and routed through a set of internal turning vanes that guide and redistribute the flow along the span before it reaches the leading-edge injection orifices, as illustrated schematically in Figure 3.7(b). This arrangement is designed to promote a uniform supply along the span while fitting within the geometric constraints of the NACA 65(12)-10 profile.

For baseline measurements without blowing, the leading-edge orifices were temporarily sealed using thin adhesive tape applied flush with the surface. This procedure preserves the nominal airfoil geometry and avoids introducing steps or cavities at the leading edge, while allowing a direct comparison between the unforced and actively forced configurations.

3.2.2.1 Quiescent conditions

At the leading edge, air is injected through a row of circular orifices of diameter $d_j = 2\ \mathrm{mm}$, spaced uniformly along the span with a centre-to-centre distance $\lambda = 10\ \mathrm{mm}$. The number of orifices that are active for a given configuration is denoted by n. The compressed-air supply is regulated using

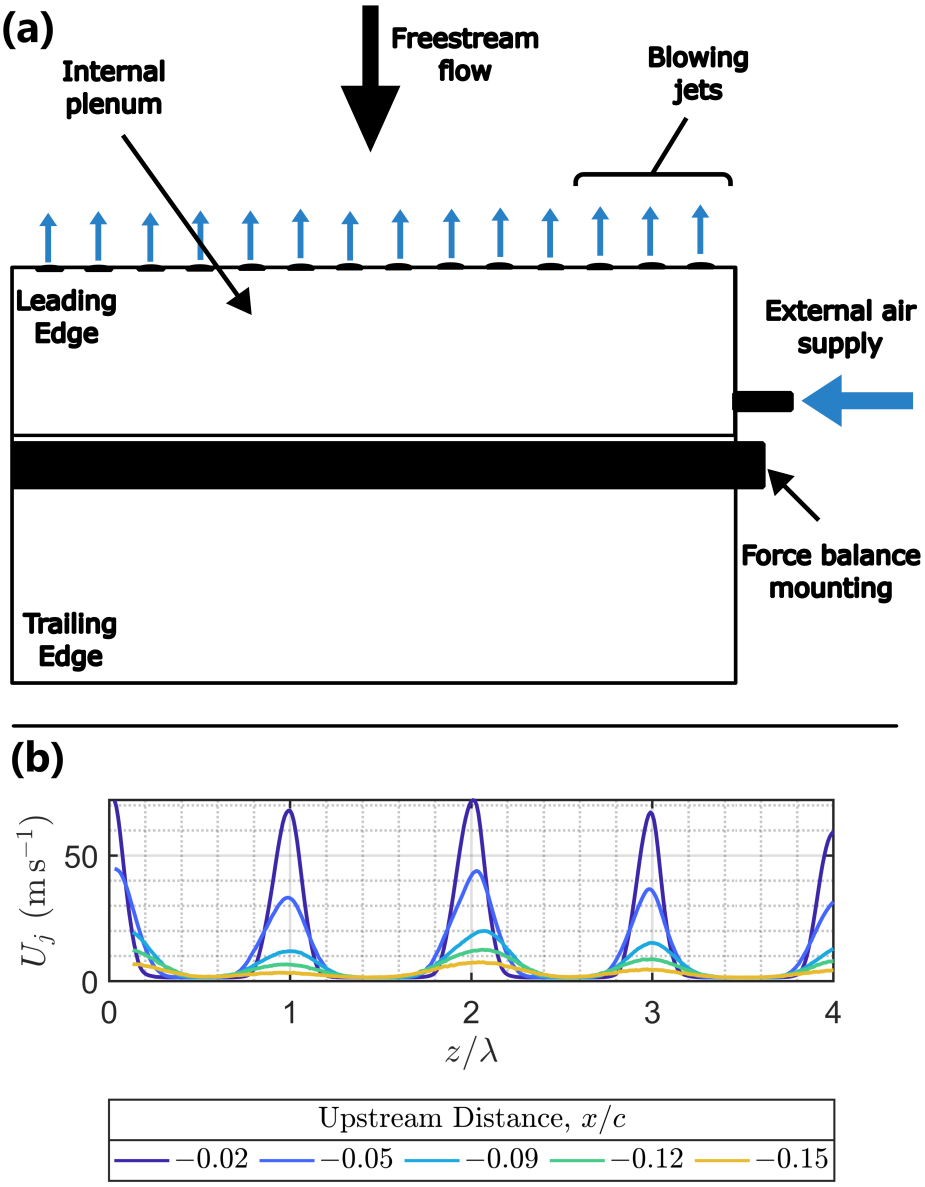

Figure 3.7: (a) Spanwise distribution of time-averaged jet velocity above five adjacent leading-edge orifices at $\alpha = 0°$ and $Q = 400\ \mathrm{L\,min^{-1}}$, measured at several stations in the near field of the jets. (b) Schematic view of the internal blowing system showing the plenum, turning vanes and spanwise distribution of leading-edge orifices with spacing λ.

a digital flow-control valve, which provides a continuous reading of the total volumetric flow rate delivered to the model, Q, in $\mathrm{L\,min^{-1}}$. If the internal plenum distributes the supplied flow evenly, the mean volumetric flow rate passing through each orifice is

$$Q_j = \frac{Q}{n},$$

where Q_j is the flow rate per orifice. This relation is a convenient first estimate and neglects small pressure losses through the internal passages and any minor differences in resistance between individual orifices. As shown later in the jet characterisation results, these effects are small over the operating conditions considered here.

In addition to the overall plenum design, the spanwise uniformity of the leading-edge blowing was assessed using hot-wire measurements acquired at $\alpha = 0^\circ$ with a total flow rate of $Q = 400\ \mathrm{L\,min^{-1}}$. The hot-wire probe (Dantec 55P11) was traversed in the spanwise direction along a line aligned with the row of orifices, with measurements taken above five adjacent blowing holes. The spanwise profile was sampled at several streamwise stations under quiescent conditions to quantify the decay of jet velocity with streamwise distance. For each orifice, the probe was aligned with the jet centreline and traversed in the spanwise direction in increments of $d_j/20$, providing sufficient spatial resolution to quantify the spanwise variation in jet strength close to the exit. The five orifices selected for this assessment were chosen from the central region of the span in order to minimise end effects and ensure that the measurements were representative of the nominal blowing distribution over the main span of the model.

The resulting spanwise velocity distributions are shown in Figure 3.7(a). Over the set of five adjacent orifices, the measured jet velocities exhibit only modest variation, and the profiles at different spanwise positions collapse closely onto one another at each measurement station. This indicates that, for the operating conditions considered, the internal plenum and turning vanes provide a reasonably uniform supply along the span, and that any residual non-uniformity is small compared to the overall jet strength.

Having established that the blowing is reasonably uniform across the central portion of the span and documented how the jet strength decays at streamwise stations close to the exit under quiescent conditions, the analysis is now extended to examine how neighbouring jets develop and interact as they propagate downstream. To do so, the streamwise evolution of the leading-edge jets was examined under quiescent conditions at $\alpha = 0^\circ$ with a total flow rate of $Q = 400\ \mathrm{L\,min^{-1}}$. Two adjacent orifices were selected ($z/\lambda = 1$ and $z/\lambda = 2$ in Figure 3.7), and a series of two-dimensional streamwise–wall-normal planes were measured using a single hot-wire probe traversed through the jet field. For each plane, the mean velocity was obtained from the hot-wire signal and normalised by the maximum jet velocity $U_{\max}$ at that streamwise station. These measurements were then used to construct contour maps of $U/U_{\max}$ at successive streamwise locations. The resulting jet development is shown in Figure 3.8.

At the closest streamwise measurement stations, the contours in Figure 3.8 indicate the presence of two distinct jet cores, each originating from a separate orifice and characterised by a local maximum in $U/U_{\max}$ located close to the airfoil surface. As the flow progresses downstream, the individual jets spread due to shear-layer growth and turbulent mixing, which increases the overlap between neighbouring shear layers. At the highest blowing rate examined, $Q = 400\ \mathrm{L\,min^{-1}}$, the jets remain distinct in the near field but merge into a single, broader region at approximately $x/c \approx -0.75$. Although this analysis is qualitative in nature, it provides a useful indication of the jet

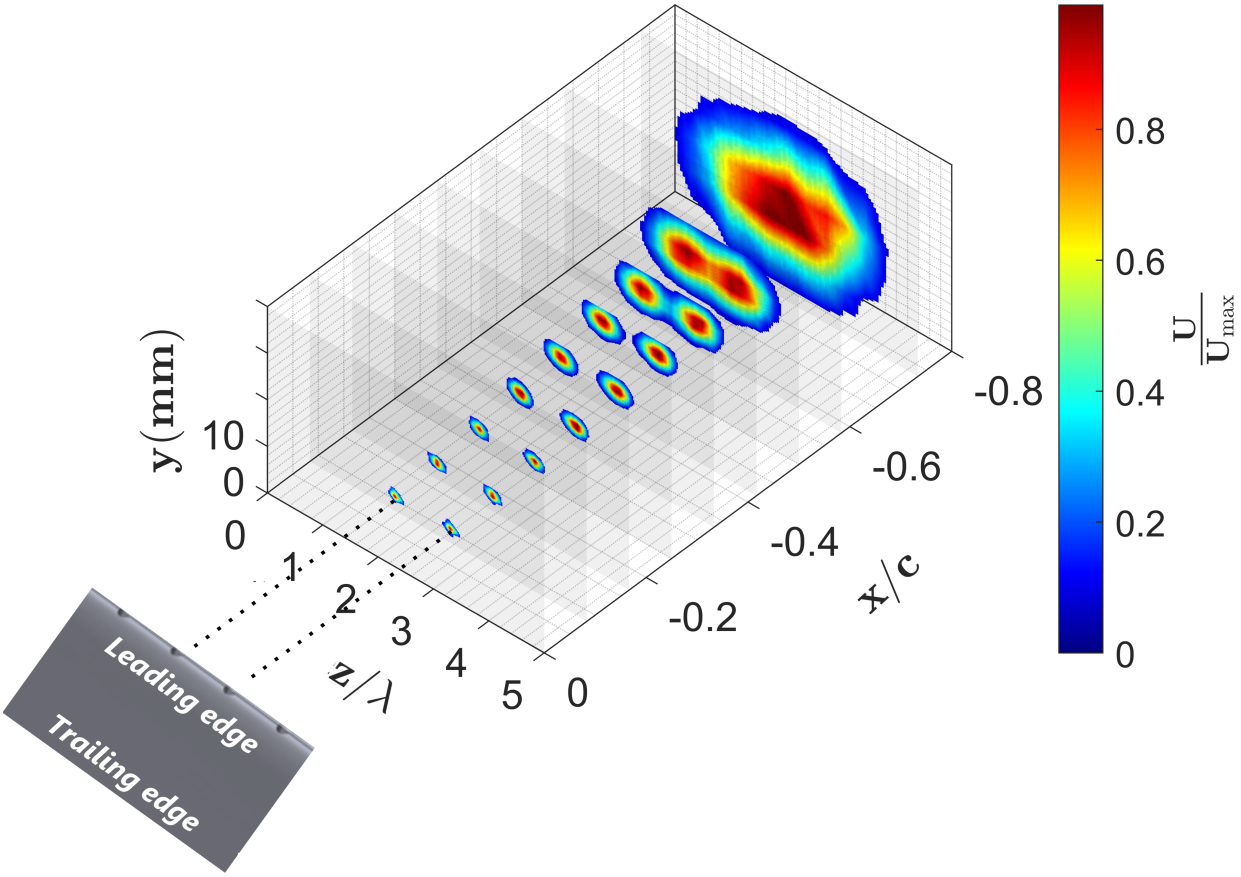

Figure 3.8: Normalised mean velocity contours $U/U_{\max}$ of two adjacent leading-edge jets measured under quiescent conditions using a single hot-wire probe, shown at successive streamwise locations for a total flow rate of $Q = 400\ \mathrm{L\,min^{-1}}$.

spreading and interaction length scale for the operating conditions used in this work.

3.2.2.2 Jet velocity calibration

To quantify the actuation strength in a form that is directly relevant to the local flow control, it is more useful to work with the mean jet velocity U_j rather than the global supply rate Q. In principle, U_j can be estimated using $Q_j = A_j U_j$, where A_j is the cross-sectional area of an orifice. However, this assumes an ideal distribution within the plenum and negligible internal losses. In practice, pressure drops along the internal flow path and local geometric effects can cause the true jet velocity to deviate from this idealised estimate, motivating the direct calibration of U_j described below.

To establish a reliable relationship between the global setting Q and the local jet velocity U_j, a dedicated calibration was carried out using a single hot-wire probe positioned in the centre of the jet emerging from a representative orifice ($z/\lambda = 2$ in Figure 3.7). The total flow rate Q was

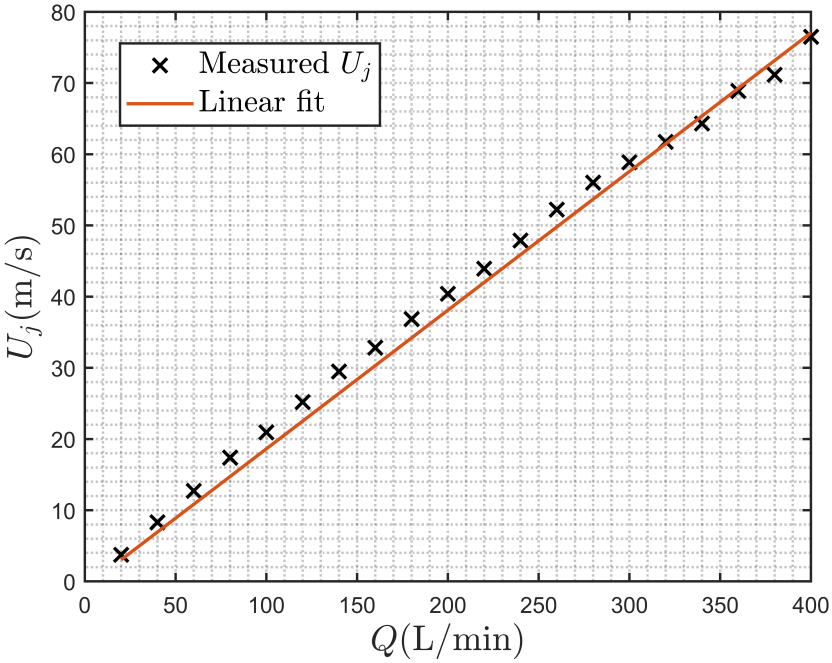

Figure 3.9: Calibration of the leading-edge jet velocity U_j as a function of the total volumetric flow rate Q supplied to the airfoil.

incremented in a series of discrete steps over the range of values used in the experiments, and for each setting the time-averaged jet velocity U_j was measured from the hot-wire signal with the aid of a single wire probe (Dantec 55P11). The calibration was performed over the range $10\ \mathrm{L\,min^{-1}} \leq Q \leq 400\ \mathrm{L\,min^{-1}}$, with the total flow rate incremented in steps of $10\ \mathrm{L\,min^{-1}}$, corresponding to the full set of valve settings used in the experiments. This procedure yielded a set of calibration pairs (Q, U_j), which are plotted in Figure 3.9 as a function of the valve reading in $\mathrm{L\,min^{-1}}$.

The data in Figure 3.9 show that U_j increases approximately linearly with the imposed flow rate Q over the range of operating conditions considered. A least-squares linear fit of the form

$$U_j = a_Q\, Q + b_Q$$

was applied to the calibration points. The resulting best-fit relation between the total volumetric flow rate and the jet velocity is

$$U_j = 0.195\, Q - 0.8636,$$

with U_j in $\mathrm{m\,s^{-1}}$ and Q in $\mathrm{L\,min^{-1}}$. The fit quality is quantified by a coefficient of determination of $R^2 = 0.991$. This regression model is used throughout the thesis to convert the valve setting Q into the corresponding leading-edge jet velocity U_j. This linear relation is applied only within the calibrated range of Q stated above; no extrapolation is used outside this interval. The root-mean-square error of the regression is $\mathrm{RMSE} = 2.0\ \mathrm{m\,s^{-1}}$ over the calibrated range. Relative

to the maximum jet velocity examined ($U_j \approx 77\ \mathrm{m\,s^{-1}}$), this corresponds to an uncertainty of approximately 2–3% at the highest blowing levels, with larger relative uncertainty at very low flow rates.

In order to provide a non-dimensional measure of actuation strength that accounts for variations in freestream velocity, the blowing intensity is reported throughout the thesis in the form of the velocity ratio

$$\frac{U_j}{U_\infty},$$

where U_∞ is the freestream velocity in the relevant facility. This definition ensures that comparisons between cases at different operating conditions are based on a consistent scaling of the jet velocity relative to the incoming flow.

3.2.3 Far-Field Microphone Array

Far-field acoustic measurements were obtained using a circular microphone array with a radius of $0.97\ \mathrm{m}$, centred on the mid-span of the airfoil, as shown in Figure 3.10. The array consists of eight G.R.A.S. 46AE $1/2''$ CCP free-field microphones distributed along an angular sector of $70°$, from $\theta = 50°$ to $\theta = 120°$. Each microphone is located at a distance of $0.97\ \mathrm{m}$ from the leading and trailing edges of the airfoil, and the reference direction $\theta = 90°$ is aligned vertically with the airfoil leading edge. This configuration allows the acquisition of far-field pressure fluctuations for the computation of frequency spectra and directivity patterns over a range of observer angles.

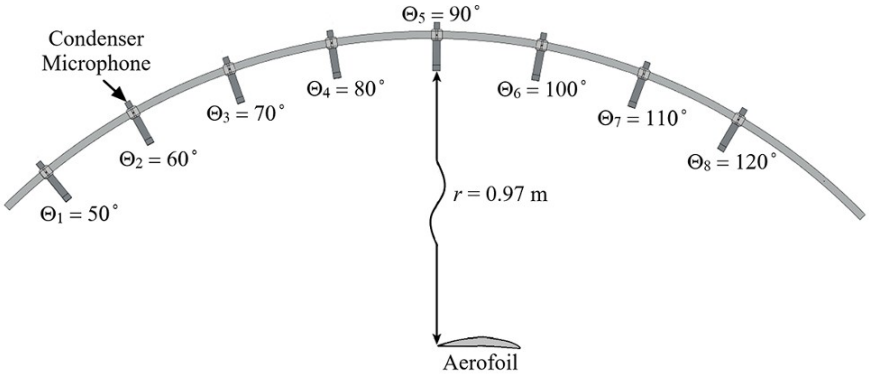

Figure 3.10: Layout of the far-field microphone array around the airfoil, showing the circular arc of radius $0.97\ \mathrm{m}$ and the angular positions of the microphones.

The microphone signals are acquired using a National Instruments PXIe-4464 dynamic signal analyser. Unless stated otherwise, the pressure fluctuations are sampled at $f_s = 40\ \mathrm{kHz}$ for a duration of $20\ \mathrm{s}$ per measurement. Prior to each measurement campaign, all microphones are calibrated with a G.R.A.S. 42AB sound calibrator, which provides a $1\ \mathrm{kHz}$ tone at a known sound pressure level of $114\ \mathrm{dB}$. Acoustic measurements were performed for free-stream velocities in the range $20\ \mathrm{m\,s^{-1}} \leq U_\infty \leq 60\ \mathrm{m\,s^{-1}}$ and for leading-edge blowing rates between $Q = 10$ and

$Q = 400\ \mathrm{L\,min^{-1}}$. Baseline acoustic measurements correspond to the unforced configuration with the leading-edge orifices sealed flush using adhesive tape, i.e. no air supply ($Q = 0$). Unless stated otherwise, these baseline spectra are used as the reference for assessing the effect of blowing.

Power spectral densities (PSDs) of the pressure fluctuations are estimated using Welch's method. The time series from each microphone is divided into overlapping segments of equal length with 50% overlap, so that adjacent segments share half of their data points. A Hamming window is applied to each segment to reduce spectral leakage associated with discontinuities at the segment boundaries. For each windowed segment, the periodogram is obtained from the squared magnitude of the fast Fourier transform (FFT). A transform length of $2^{10} = 1024$ points is used to ensure efficient FFT computation. The final PSD for each microphone signal is computed as the average of the individual segment periodograms, which reduces the variance of the spectral estimate while retaining the relevant frequency content of the acoustic field.

The noise radiation investigated in this thesis is expressed in terms of the sound pressure level (SPL), defined in equation 3.3, and the sound power level spectrum, defined in equation 3.5.

The one-sided sound pressure level spectrum is given by

$$\mathrm{SPL}(f) = 10\log_{10}\left(\frac{S_{pp}(f)}{p_{\mathrm{ref}}^2}\right), \tag{3.3}$$

where $S_{pp}(f)$ is the one-sided pressure power spectral density at frequency f, and p_{ref} is the reference sound pressure, taken as $p_{\mathrm{ref}} = 20\ \mu\mathrm{Pa}$.

Considering the predominantly cylindrical radiation characteristics of airfoil self-noise, the sound field generated by a finite-span airfoil is more appropriately modelled as originating from a line source rather than an isolated point source. In this context, the acoustic radiation is quantified in terms of the sound power level spectrum per unit span, obtained by integrating the far-field pressure spectra over the angular sector covered by the microphone array. The corresponding sound power $W(f)$ and sound power level $\mathrm{PWL}(f)$ are defined as

$$W(f) = \frac{L\,r}{\rho_0 c_0}\sum_{i=1}^{N}\Phi_{pp}(f,\theta_i)\ \Delta\theta, \tag{3.4}$$

$$\mathrm{PWL}(f) = 10\log_{10}\left(\frac{W(f)}{W_0}\right), \tag{3.5}$$

where $\Phi_{pp}(f,\theta_i)$ is the one-sided far-field pressure power spectral density measured at the i-th microphone located at polar angle θ_i, N is the total number of microphones, and $\Delta\theta = 10^\circ$ is the angular spacing between adjacent microphones. The integration is performed over the sector $50^\circ \leq \theta \leq 120^\circ$, which corresponds to the angular aperture of the array. In equation (3.4), L denotes the airfoil span, r is the distance between the trailing edge and the observer, ρ_0 is the ambient air density, and c_0 is the speed of sound. The reference sound power is taken as $W_0 = 10^{-12}\ \mathrm{W\,Hz^{-1}}$, consistent with the standard definition of sound power level.

In addition to the aerodynamic measurements, the intrinsic acoustic contribution of the leading-edge jets was assessed under quiescent conditions. These tests indicated that the actuation introduces a measurable increase in sound pressure levels, predominantly at higher frequencies (typically above $\sim 2\ \mathrm{kHz}$). As the aeroacoustic analysis presented in this thesis focuses on lower-frequency mechanisms associated with airfoil self-noise, the direct jet-noise contribution is not expected to influence the principal conclusions.

3.2.4 Hot-Wire Anemometry

Hot-wire anemometry was employed to obtain time-resolved measurements of the velocity field in the boundary layer and wake of the airfoil. The local velocity vector is denoted by

$$\mathbf{V}(t) = (V_x(t),\, V_y(t),\, V_z(t))\,,$$

where V_x is aligned with the free-stream direction, and V_y and V_z denote the transverse and spanwise components, respectively. The corresponding velocity fluctuations are written as

$$\mathbf{V}'(t) = \big(V_x'(t),\, V_y'(t),\, V_z'(t)\big)\,,$$

with each component obtained by subtracting the local time-averaged velocity from the instantaneous signal.

Two probe types were used in this work: a single-wire probe for one-component measurements, and a cross-wire (X-wire) probe for two-component measurements.

3.2.4.1 Dantec 55P11 Single-Wire Probe

The Dantec 55P11 single-wire probe was used in the present work whenever only the streamwise velocity component was required. In particular, it was employed for survey measurements in the boundary layer and near wake, and for cases where a fine spatial resolution close to the trailing edge was needed. The probe provided measurements of the mean streamwise velocity and its fluctuations, which were used to characterise the local flow field efficiently in regions where the dominant flow direction was already known from the experimental configuration.

3.2.4.2 Dantec 55P61 Cross-Wire Probe

For measurements requiring information on the directional structure of the flow, a Dantec 55P61 cross-wire probe was employed. In the present work, the probe was used to obtain two-component velocity measurements in planes of interest within the wake and in the flow field influenced by leading-edge blowing. Measurements were acquired in two probe orientations, providing (V_x, V_y) and (V_x, V_z) component pairs, which together enabled the reconstruction of the mean-flow and

fluctuation structure needed for the analysis of wake vortices and blowing-related flow development.

3.2.4.3 Calibration and data acquisition

All hot-wire measurements in this thesis were performed using constant-temperature anemometers (CTAs) operated at a prescribed overheat ratio. Based on the expected flow conditions and manufacturer guidelines, an overheat ratio of 1.8 was selected for all probes. The CTA output voltages were digitised using a 16-bit A/D converter at a sampling frequency of $20\ \mathrm{kHz}$. The CTAs allow adjustment of the bridge offset and gain during calibration, ensuring that the dynamic range of the signals is matched to the measurement conditions.

The probes were mounted on a three-axis ISEL traverse system, enabling controlled motion in all spatial directions within the measurement domain. The traverse is driven by stepper motors with a positional resolution of $0.01\ \mathrm{mm}$, which provides precise control over the probe position relative to the airfoil and facilitates the construction of detailed measurement grids in the boundary layer and wake.

3.2.4.4 Velocity calibration

The calibration of the hot-wire probes was performed in the aeroacoustic facility using the open-jet wind tunnel. For each probe, the sensing element was positioned at the centre of the nozzle exit and aligned with the mean flow direction, so that the local velocity was equal to the free-stream value at the nozzle. Prior to acquiring calibration data, the CTA bridge offset and gain were adjusted to ensure a clear separation between the output voltages corresponding to the lowest and highest velocities of interest, while keeping the probe operation within the recommended range of the manufacturer. Once an appropriate voltage range had been established, a series of calibration points was obtained for velocities from $U = 0\ \mathrm{m\,s^{-1}}$ up to approximately $1.4\,U_{\max}$, where $U_{\max}$ is the maximum free-stream velocity used in the measurements. The reference velocity at each calibration setting was recorded using the ThermoPro software linked to the tunnel control system.

A typical calibration curve is shown in Figure 3.11. In the present work, the relationship between the reference velocity U and the CTA output voltage V was represented using a polynomial fit of the form

$$U = A_1 V^n + A_2 V^{n-1} + \cdots + A_n V + A_{n+1}, \tag{3.6}$$

where $A_1, \ldots, A_{n+1}$ are calibration coefficients obtained by least-squares regression. This form was used to provide a smooth representation of the measured calibration data over the operating range considered.

For comparison, the calibration data can also be expressed in the form of King's law,

$$E^2 = B_1 + B_2 U^n, \tag{3.7}$$

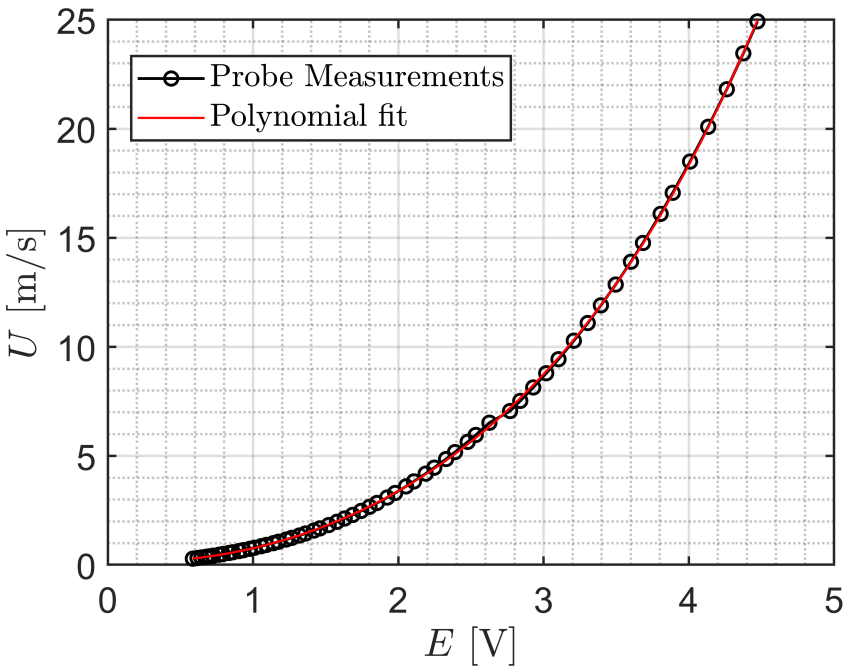

Figure 3.11: Example hot-wire calibration curve showing reference velocity U as a function of CTA output voltage V, together with a polynomial fit of the form given in equation (3.6).

where E is the CTA bridge voltage, U is the reference velocity, and B_1, B_2, and n are fitted constants. An illustrative example of the calibration data represented in this form is shown in Figure 3.12.

An analytical temperature correction was applied in post-processing to compensate for variations in ambient conditions between calibration and measurement. The corrected velocity signal is obtained from

$$V_{\mathrm{corr}}(t) = V(t)\left(\frac{T_w - T_a}{T_w - T_{a,\mathrm{cal}}}\right)^{1/2}, \tag{3.8}$$

where $V(t)$ is the velocity inferred from the calibration at the measurement ambient temperature T_a, $T_{a,\mathrm{cal}}$ is the ambient temperature during the original calibration, and T_w is the effective hot-wire operating temperature. This correction rescales the velocity signal to account for the change in overheating ratio caused by differences in ambient temperature, thereby ensuring consistency with the calibration conditions.

3.2.5 Surface Pressure

3.2.5.1 Steady Surface Pressure

Steady surface pressure measurements were carried out in the open-jet wind tunnel of the aeroacoustic facility in order to determine the chordwise pressure distribution on the NACA 65(12)-10 airfoil. The measurements reported here correspond to a geometric angle of attack $\alpha_{\mathrm{geo}} = 0^\circ$ and

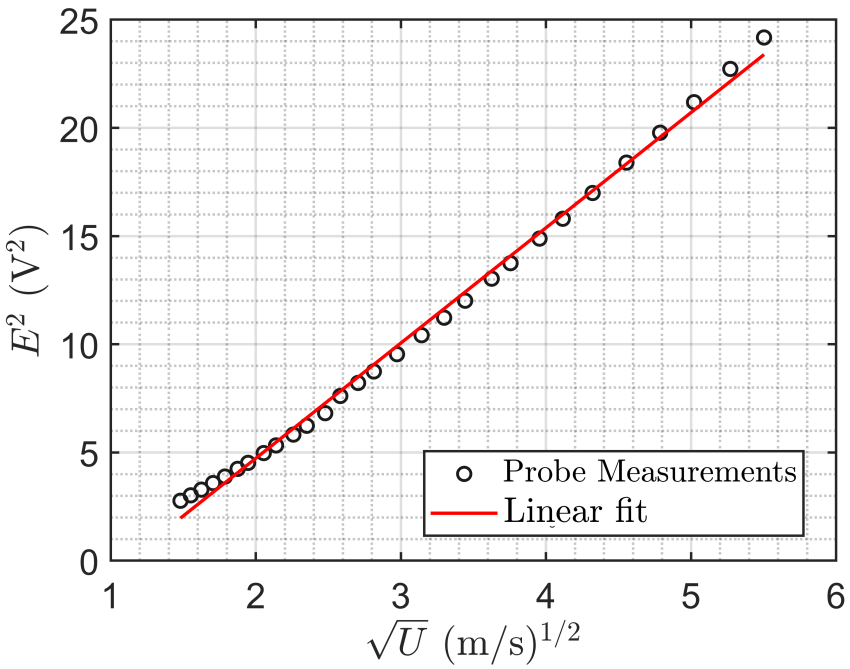

Figure 3.12: Example hot-wire calibration using King's law, showing E^2 as a function of reference velocity U and the fitted curve given by equation (3.7).

a free-stream velocity of $U_\infty = 24\ \mathrm{m\,s^{-1}}$.

A Pitot-static tube located in the free jet was used to determine the reference free-stream static pressure p_∞ and dynamic pressure. Surface static pressures were measured at eight discrete locations on both the pressure and suction sides of the airfoil, using flush-mounted pressure taps connected via tubing to a Furness Control pressure scanner. The scanner was used to switch sequentially between the individual pressure taps and the reference free-stream static pressure.

Differential pressures between each surface tap and the free stream were measured with a Furness FCO510 digital micromanometer. The FCO510 includes an internal data-logging function, which was operated at a sampling rate of $1\ \mathrm{Hz}$ (one reading per second). For each tap location, a total of 20 samples was acquired and subsequently averaged to obtain a steady estimate of the local static pressure.

The steady surface pressure distribution is expressed in terms of the coefficient of static pressure

$$C_p(x) = \frac{p(x) - p_\infty}{\frac{1}{2}\rho_\infty U_\infty^2}, \tag{3.9}$$

where $p(x)$ is the time-averaged static pressure at a given tap location, p_∞ is the free-stream static pressure, ρ_∞ is the free-stream density and U_∞ is the free-stream velocity. The density ρ_∞ is obtained from the ideal-gas relation

$$\rho_\infty = \frac{p_\infty}{R T_\infty}, \tag{3.10}$$

where T_∞ is the free-stream static temperature and R is the specific gas constant for air. The resulting $C_p(x)$ distributions on the pressure and suction sides of the airfoil are used in later chapters to derive aerodynamic coefficients and to assess the influence of leading-edge blowing on the mean loading.

3.2.5.2 Unsteady Surface Pressure

Unsteady surface pressure measurements were obtained using a remote-sensing arrangement in which the internal pressure channels of the airfoil are routed to a miniature microphone located outside the flow. Each surface tap is connected via a short length of tubing to an external adapter, where the pressure fluctuations are sensed by a flush-mounted mini microphone.

In operation, the internal channels of the airfoil transmit the local unsteady pressure from the surface to the remote adapter. The miniature microphone then records the resulting pressure signal, which is digitised and processed in the same manner as the far-field microphones used in the acoustic measurements. Care is taken to keep the tubing lengths and internal volumes as small and as uniform as practicable, to limit additional filtering or delay effects introduced by the remote-sensing arrangement. The resulting unsteady surface pressure signals are used to compute power spectral densities and cross-spectral quantities that link the near-wall pressure field to the far-field acoustic radiation and to the flow structures characterised by hot-wire anemometry.

3.2.6 Beamformer

To identify the dominant aeroacoustic source regions on the airfoil, beamforming maps were produced using OptiNav BeamformX (v6.013) employing conventional frequency-domain delay-and-sum processing. The device consists of a set of microphones distributed over a planar support structure, as illustrated in Figure 3.13. The microphones are arranged in a non-uniform pattern around a central opening that houses the optical camera. This configuration allows simultaneous acquisition of acoustic data and visual images of the airfoil, so that the reconstructed source maps can be directly overlaid on the model geometry.

The beamforming measurements were designed to distinguish between noise generated at the trailing edge and that associated with leading-edge turbulence interaction. Two classes of inflow condition were considered. In the first, the open-jet wind tunnel was operated with a low-turbulence free stream, so that the trailing-edge self-noise of the airfoil dominates the acoustic radiation. In the second, a turbulence-generating grid was installed upstream of the nozzle, increasing the level of incoming turbulence and thereby enhancing the contribution of leading-edge interaction noise. Comparing the resulting source maps under these two conditions provides qualitative and quantitative insight into how the relative importance of leading- and trailing-edge mechanisms changes with inflow turbulence.

For each test condition, the array microphones record time-resolved pressure signals from which cross-spectral matrices are formed in selected frequency bands. A frequency-domain delay-

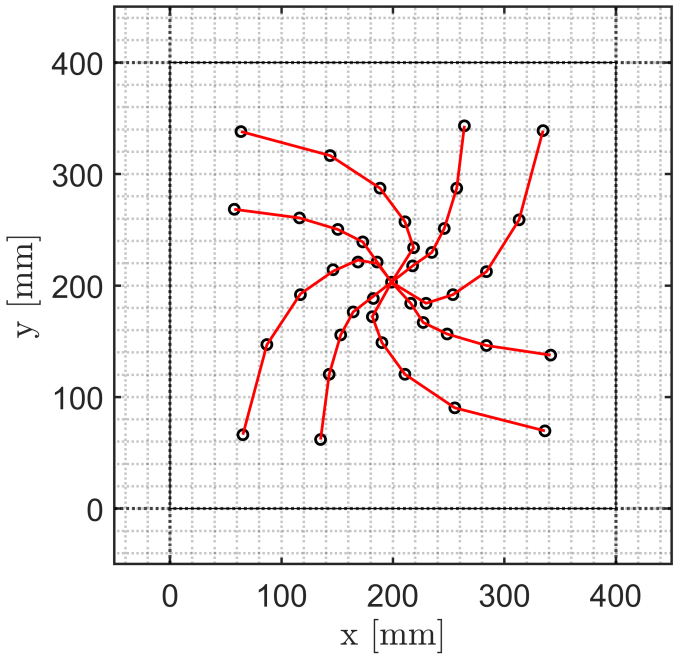

Figure 3.13: Layout of the beamforming array showing the distribution of microphones and the central camera aperture.

and-sum beamforming algorithm is then applied, using the known positions of the microphones and an assumed source plane aligned with the airfoil mid-span. The output is a spatial distribution of acoustic intensity over the source plane, which highlights regions of enhanced sound emission. In the present work, these maps are used primarily to confirm whether the dominant noise originates from the trailing edge, the leading edge, or other features of the setup, and to support the interpretation of the far-field spectra presented in the results chapters.

3.3 Summary

This chapter has defined the common experimental framework used throughout the thesis. The wind tunnel facilities, flow-condition definitions, angle-of-attack correction procedure, aerofoil model, and leading-edge blowing system have been described, together with the calibration methods used to relate the imposed actuation settings to the local jet velocity. The main measurement systems, including the far-field microphone array, hot-wire anemometry, surface-pressure instrumentation, and beamforming arrangement, have also been introduced, along with the principal signal-processing procedures and acoustic metrics used in the later analysis. These elements provide the common methodological basis for the mechanism-specific investigations presented in Chapters 4, 5, and 6.

Chapter 4

Influence of Leading-edge Blowing on Trailing Edge Tonal Noise

4.1 Introduction

Trailing-edge (TE) tonal noise [11] is one of the most distinctive manifestations of airfoil self-noise at low to moderate Reynolds numbers, where laminar–turbulent transition and separation dynamics dominate boundary-layer behaviour. For the NACA 65-series airfoil considered in this work, the tonal noise originates from a self-sustaining aeroacoustic feedback loop that couples laminar boundary-layer instabilities, shear-layer vortex roll-up, and acoustic scattering at the trailing edge. When this feedback condition is satisfied, the system oscillates at discrete frequencies, producing narrowband peaks that can radiate strongly to the far field. Understanding the physical origin of this feedback and identifying robust control strategies remain critical for reducing airfoil self-noise in noise-sensitive applications such as unmanned aerial vehicles, distributed electric propulsion systems, and advanced high-lift configurations.

The onset and strength of tonal noise are intrinsically linked to the formation and evolution of laminar separation bubbles (LSBs) on the airfoil surface. As the angle of attack or Reynolds number changes, the separation and reattachment points of these bubbles shift, modifying both the local instability growth rate and the preferred feedback frequency. The resulting tonal signature therefore provides a sensitive indicator of the underlying laminar–separation dynamics. Suppressing this feedback requires either weakening the instability mechanism itself or interrupting its acoustic reinforcement, both of which can be achieved by modifying the boundary-layer state upstream of the trailing edge.

Among active control techniques, steady leading-edge (LE) blowing has shown particular promise due to its capacity to alter boundary-layer receptivity and delay separation with relatively low energy expenditure. By introducing controlled disturbances near the stagnation region, the technique can reshape the downstream velocity profiles and weaken the vortical structures that sustain the tonal feedback. Nevertheless, the mechanisms through which blowing intensity and

incidence angle interact to determine noise suppression effectiveness remain poorly understood.

This chapter therefore investigates the aeroacoustic response of a NACA 65-series airfoil equipped with a leading-edge blowing system, focusing on how different momentum ratios and angles of attack influence both the tonal noise radiation and the near-field flow topology. Far-field noise measurements obtained using a phased microphone array are analysed in conjunction with surface-pressure and hot-wire anemometry data to identify the flow mechanisms governing tonal noise generation and mitigation. Through this combined experimental approach, the study aims to clarify how steady leading-edge forcing modifies the laminar separation bubble, reorganises wake vorticity, and ultimately alters the coherence of the aeroacoustic feedback loop.

4.2 Experimental Setup

The experimental arrangement used for the tonal noise measurements in this chapter builds upon the general setup described in Chapter 3. Since the primary objective here is to investigate the influence of leading-edge blowing on trailing-edge tonal noise, only the instrumentation and tunnel configuration directly relevant to these results are summarised below.

Far-field acoustic measurements were obtained using the microphone array described in Section 3.2.3, positioned above the test section to capture the radiated sound across a broad frequency range. Unless stated otherwise, the data processing and calibration procedures for the array follow the methodology outlined in Chapter 3.

Flow-field measurements in the wake of the airfoil were performed using two types of hot-wire probes. A **Dantec P11 single-wire probe** was employed to acquire high-resolution measurements of the streamwise velocity component, U, for cases where fine detail in the wake deficit was required. To obtain a complete three-component velocity field and to evaluate vorticity distributions, a **Dantec P61 cross-wire probe** was used. This probe provides simultaneous measurements of two velocity components U and V or U and W, allowing reconstruction of the spanwise vorticity and turbulence statistics essential for understanding the wake dynamics. Both probes were mounted on a two-axis traverse system to capture the velocity field across a two-dimensional measurement plane downstream of the trailing edge.

Since the measurements in this chapter cover a wide range of free-stream velocities, from $U_\infty = 20$ m/s up to 60 m/s, the smaller of the two interchangeable tunnel nozzles (detailed in Section 3.1.1) was selected for Section 4.3 and 4.4. For the synchronous measurements in Section 4.5 and the anisotropic-inflow experiments in Section 5.4, the larger 300 × 300 mm nozzle was used. The pressure-side far-field microphone was a GRAS 46AE 1/2” CCP free-field microphone.

4.3 Far-field noise measurements

4.3.1 Baseline spectral characteristics

The initial step in the investigation was to establish the operating condition at which the trailing-edge tonal noise of the test airfoil is most prominent. To this end, far-field acoustic spectra were obtained for the baseline (no blowing) configuration across a range of free-stream speeds, $U_\infty = 20$–60 m/s. The spectra are presented in terms of the non-dimensional Strouhal number,

$$St = \frac{fc}{U_\infty},$$

where f is frequency and c is the airfoil chord. The sound power level (PWL) is used as the ordinate, referenced to 10^{-12} W.

Figure 4.1 shows that the spectral distribution varies strongly with flow speed. At higher U_∞, the spectra exhibit elevated low-frequency content (broadband hump), while the discrete tonal peaks weaken. The low-frequency hump is comparatively subdued, with the dominant spectral content concentrated in the band $4 \leq St \leq 10$, where the peak level reaches approximately 46 dB. This narrowband feature stands out clearly above the surrounding broadband levels, indicating the presence of a strong feedback-driven instability of the laminar separation bubble and shear layer.

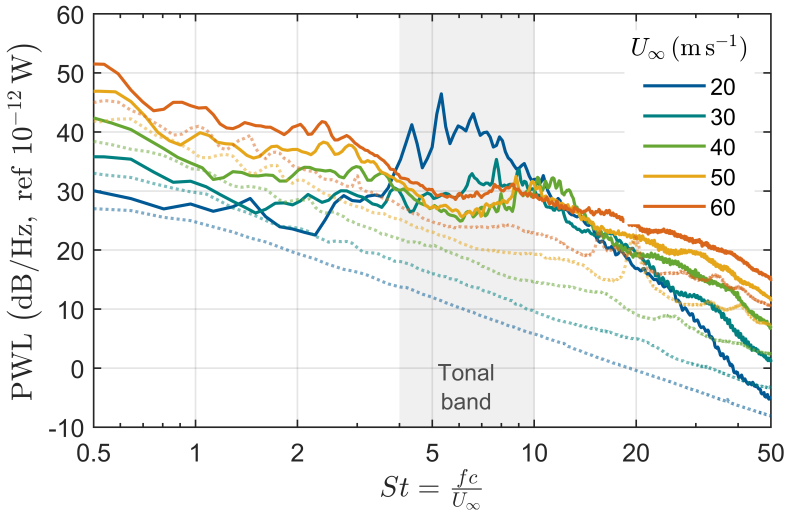

Figure 4.1: Baseline far-field noise spectra (measured **PWL** by solid colored lines, background noise by dashed lines) at multiple speeds, plotted vs. Strouhal number $St = fc/U_\infty$.

The prominence of this peak at 20 m/s motivated the choice of this flow speed as the reference operating condition for all subsequent experiments related to tonal noise control. In the remainder of this chapter, the primary objective is to demonstrate the suppression of this distinct tonal feature

by means of leading-edge blowing.

4.3.2 Tonal Noise Localisation

An important step in clarifying the mechanism of trailing-edge tonal noise is to identify where along the chord the laminar separation bubble forms, as this feature sustains the aeroacoustic feedback loop. The baseline spectra discussed earlier established how tonal noise depends on flow speed and angle of attack, but they did not indicate the chordwise origin of the instability. To investigate this, a set of trip-tape variation tests was performed. In these experiments, one surface of the airfoil was held tripped near the leading edge ($x/c = 0.1$), while the opposite surface was progressively tripped further downstream. By comparing the resulting far-field spectra with the reference case at $x/c = 0.1$, it is possible to determine which surface contributes to bubble formation and to estimate its onset position.

The findings presented show how tonal noise develops as transition is displaced along the suction and pressure sides, revealing the relative influence of each surface and the sensitivity of the underlying instability to angle of attack.

The trip-tape variation experiments were designed to probe the chordwise origin of the instability mechanism by selectively forcing transition on one surface of the airfoil while allowing the other to develop naturally. The general arrangement is illustrated in Figure 4.2. In case (a), a trip tape was fixed permanently at $x/c = 0.1$ on the pressure side of the airfoil, while the position of the suction-side tape was incrementally advanced downstream in steps of $\Delta(x/c) = 0.1$, covering stations from $x/c = 0.1$ to $x/c = 0.9$. In case (b), the procedure was reversed: the suction side was held fixed at $x/c = 0.1$, while the pressure-side tape was moved in the same chordwise increments. In this way, the effective transition point on one surface could be displaced progressively aft, while the opposite surface was kept at an early tripped state to isolate its influence.

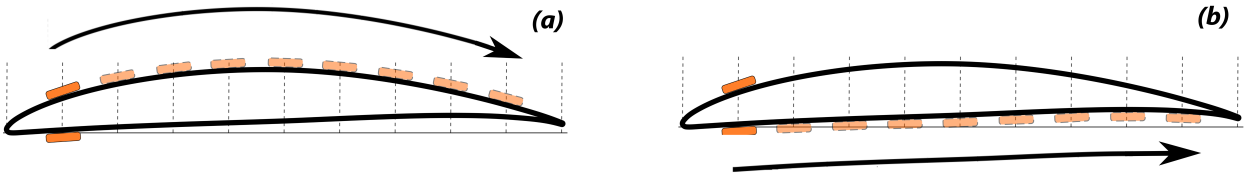

Figure 4.2: Trip-tape variation methodology: (a) suction side incrementally varied while pressure side fixed at $x/c = 0.1$; (b) pressure side varied while suction side fixed. The $x/c = 1.0$ case corresponds to no tape on the varying surface.

For completeness, a hypothetical case corresponding to $x/c = 1.0$ was also defined. In practice, this is treated as equivalent to the absence of a trip tape on the variable surface, such that only the fixed $x/c = 0.1$ tape remained. For example, when the pressure side was fixed at $x/c = 0.1$ and the suction side assigned $x/c = 1.0$, the test condition was physically identical to having a single trip tape applied solely on the pressure side at the leading-edge station. This convention

provides a consistent reference across both suction- and pressure-side variation series.

The trip elements themselves consisted of narrow strips of tape with a uniform thickness of 0.5 mm and a width of 5 mm, applied at the specified chordwise positions. These dimensions were chosen to ensure effective boundary-layer tripping across the range of Reynolds numbers tested, while minimising blockage and acoustic interference. The tape height is sufficiently large relative to the local boundary-layer thickness at the leading edge to trigger transition promptly when located near $x/c = 0.1$, but becomes increasingly less effective at forcing early transition when displaced aft. This systematic arrangement therefore allows the sensitivity of tonal noise generation to the chordwise position of laminar separation bubbles to be inferred with minimal ambiguity.

Figure 4.3 presents the far-field noise spectra obtained from the trip-tape variation experiments. The results are arranged by angle of attack, with separate panels for the suction and pressure sides. Within each panel, the spectra are shown as a function of Strouhal number, $St = fc/U_\infty$, for all chordwise trip locations. This representation provides a direct comparison of how the spectral content evolves as the effective transition point is displaced downstream, thereby offering a fundamental view of the onset and development of tonal components under different aerodynamic conditions. The figure serves as the basis for identifying the chordwise regions most sensitive to tonal noise generation and for distinguishing between suction- and pressure-side contributions.

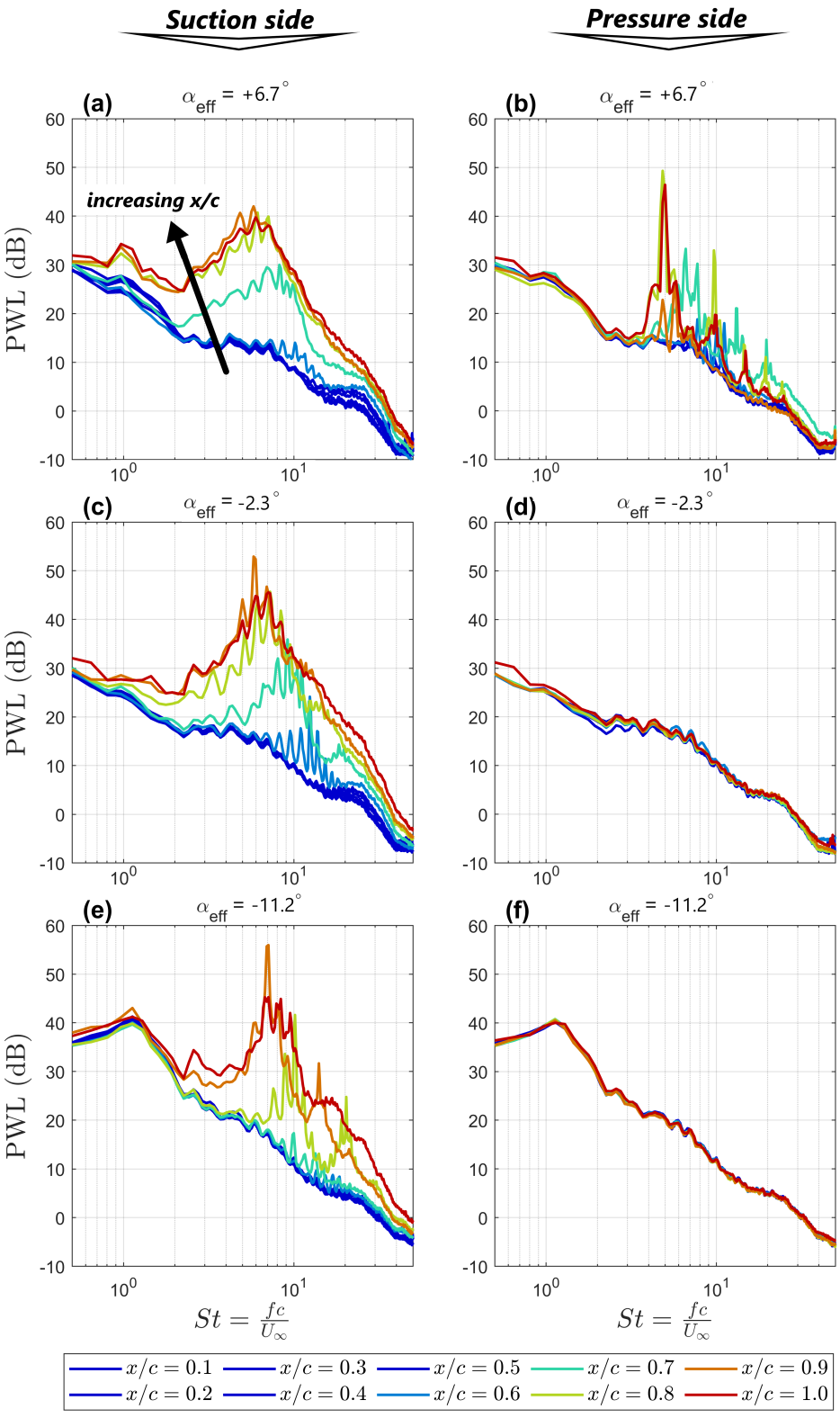

Figure 4.3: Far-field sound power level (PWL) spectra from trip-tape variation at three angles of attack: (a,b) $\alpha = +6.7°$, (c,d) $\alpha = -2.3°$, and (e,f) $\alpha = -11.2°$. Left panels correspond to suction-side variation with the pressure side fixed at $x/c = 0.1$, while right panels show pressure-side variation with the suction side fixed at $x/c = 0.1$.

The far-field spectra obtained from the trip-tape variation tests are shown in Figure 4.3. Across all configurations, the broadband characteristics remain largely unchanged, with only minor differences between suction- and pressure-side variations. A weak low-frequency feature is observed at $\alpha = -11.2^\circ$ (Figure 4.3e,f), where a shallow peak emerges near $St \approx 1$, but otherwise the broadband response is consistent across all cases.

The more prominent changes arise in the tonal components as the trip position is advanced downstream. For the suction-side variation, distinct tonal peaks develop once the tape is placed sufficiently aft of the leading edge. At $\alpha = +6.7^\circ$ (Figure 4.3a), the tonal signatures are relatively broad and full, spanning several harmonics, whereas at lower incidences they become progressively sharper and more discrete (Figure 4.3c,e). This trend suggests that the underlying instability is more energetic and broadband at higher positive angles of attack, where the suction-side separation bubble is both stronger and more receptive to external perturbations, while at lower incidence the feedback loop narrows to a more selective frequency band.

A further common feature of the suction-side cases is the downstream frequency shift associated with the trip location. Once the tonal mode is triggered, increasing x/c systematically displaces the peak to lower Strouhal numbers, consistent with a longer separation bubble and a lower shear-layer instability frequency. This behaviour agrees with previous observations that the preferred feedback frequency scales with bubble length and shear-layer roll-up dynamics [44, 9].

In contrast, the pressure-side variation produces negligible changes at $\alpha = -2.3^\circ$ and $\alpha = -11.2^\circ$ (Figure 4.3d,f), indicating that the separation bubble does not form on that surface at these incidences. Only at $\alpha = +6.7^\circ$ (Figure 4.3b) do tonal features appear, taking the form of sharp, streak-like peaks. The strongest of these occurs at $St \approx 5$, close to the dominant suction-side frequency. However, the pressure-side tones remain narrower and less energetic, lacking the fuller spectral character seen on the suction side. A plausible explanation is that at higher incidence, a secondary instability is triggered on the pressure surface, but it does not sustain the same coherent bubble–shear-layer interaction responsible for the suction-side tones. Similar asymmetries in tonal generation between suction and pressure surfaces have been noted in studies of symmetric and cambered airfoils at positive incidence [43, 42], supporting the interpretation that the suction-side bubble remains the dominant source mechanism.

To complement the frequency-domain view in Figure 4.3, the same dataset is recast in Figure 4.4 as a geometry-referenced ridge plot. At each chordwise station on the suction and pressure sides, the plotted spectrum is the *incremental* level relative to the early-tripped reference, i.e. $\Delta\mathrm{PWL}(St) = \mathrm{PWL}(St;\, x/c) - \mathrm{PWL}(St;\, 0.1)$, and is overlaid at the corresponding x/c location on the airfoil contour. This Δ–representation suppresses common broadband offsets and emphasises the emergence and growth of tonal excess with downstream transition. Panels (a), (b), and (c) show $\alpha = +6.7^\circ$, -2.3°, and -11.2°, respectively. The purpose of this visualisation is to provide an intuitive, spatial map of where tones first appear and how their spectral content evolves along the chord.

The ridge plots in Figure 4.4 make the chordwise development of tonal noise much clearer by

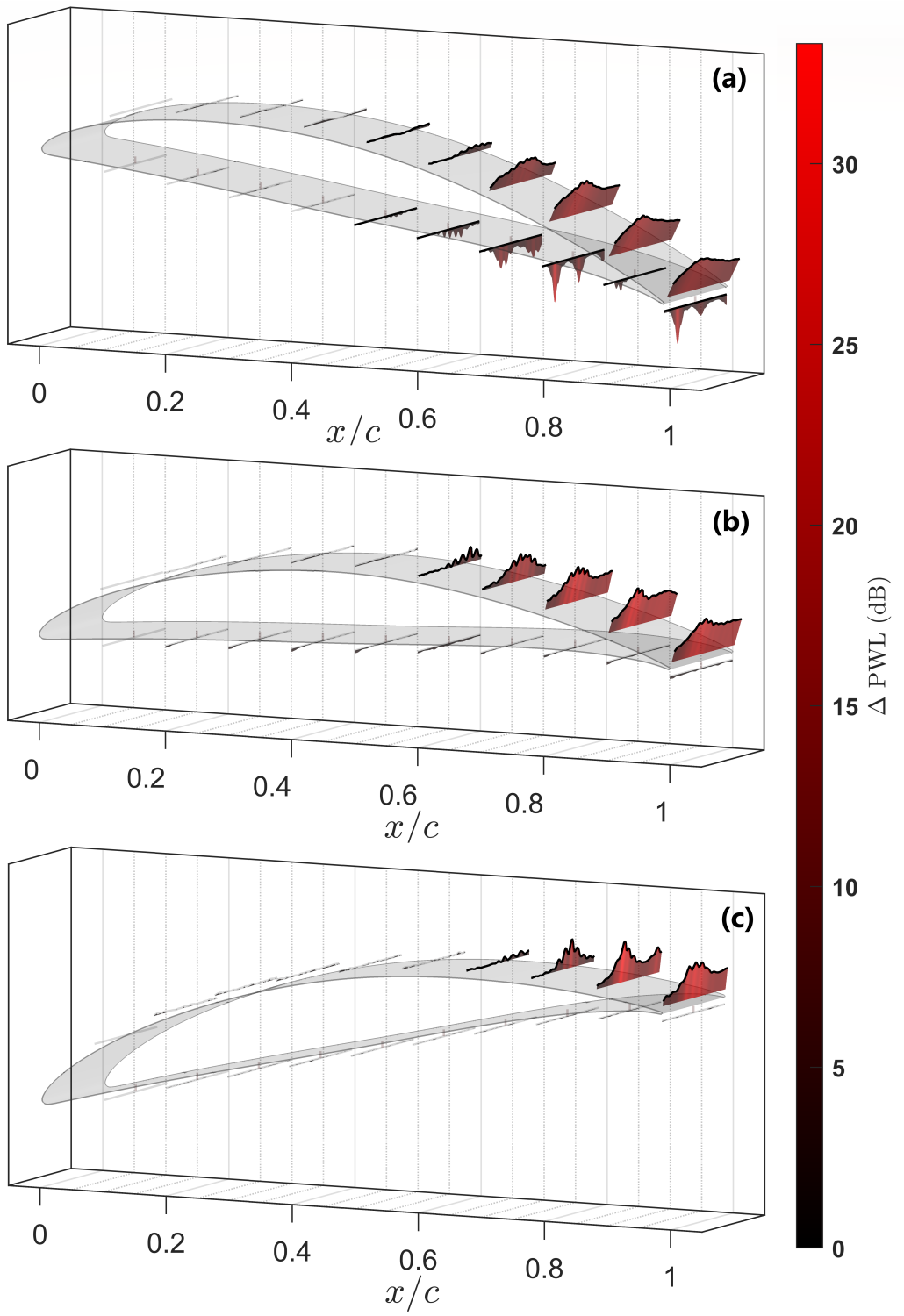

Figure 4.4: Ridge plots of ΔPWL spectra relative to $x/c = 0.1$ over the tonal band $4 \leq St \leq 10$, projected onto the airfoil for (a) $\alpha = +6.7°$, (b) $\alpha = -2.3°$, and (c) $\alpha = -11.2°$. This representation highlights the onset and evolution of tonal noise as transition is displaced downstream along the chord.

embedding the $\Delta\mathrm{PWL}$ spectra directly on the airfoil geometry. For $\alpha = +6.7^\circ$ (panel a), tonal activity emerges earlier along the chord, with both suction and pressure sides showing a rise in $\Delta\mathrm{PWL}$ once the trip is placed beyond mid-chord. The suction side rapidly develops a broad tonal feature centred in the $St = 4$–10 band, while the pressure side produces narrower, streak-like peaks that remain less energetic. At $\alpha = -2.3^\circ$ (panel b), tonal growth is confined to the suction side, with a sharp onset near $x/c = 0.6$ that evolves into a strong, full tonal peak by the trailing edge. The -11.2° case (panel c) shows the latest and weakest onset, with activity delayed until $x/c \approx 0.7$, but eventually producing a distinct tonal feature near the trailing edge.

Beyond the differences in onset location, the ridge plots also reveal a systematic variation in peak amplitude across the three angles of attack. The maximum suction-side $\Delta\mathrm{PWL}$ reaches approximately 30 dB at $\alpha = +6.7^\circ$, rising to around 37 dB at $\alpha = -2.3^\circ$, and attaining nearly 40 dB at $\alpha = -11.2^\circ$. This ordering is somewhat counterintuitive, as the tonal features at higher incidence are broader and visually more dominant, yet the incremental levels relative to the $x/c = 0.1$ baseline are lower. A plausible explanation is that at $\alpha = +6.7^\circ$, the suction-side boundary layer is more unstable even in the early-tripped reference case, so the baseline already contains residual tonal energy that reduces the relative $\Delta\mathrm{PWL}$. At lower incidences, the $x/c = 0.1$ condition is effectively silent, making the growth at downstream trip positions appear as a stronger incremental peak. This interpretation aligns with the idea that higher incidence increases bubble receptivity and broadband amplification, whereas lower incidence maintains a more laminar baseline, allowing the downstream bubble development to stand out more strongly in the incremental measure.

In all cases, the suction-side ridges exhibit a progressive drift of tonal energy towards lower Strouhal numbers with increasing x/c, consistent with a longer separation bubble and reduced shear-layer roll-up frequency. By contrast, the pressure side remains largely inactive except at $\alpha = +6.7^\circ$, where the streaky peaks suggest a secondary, incidence-dependent instability. Taken together, the ridge plots provide an intuitive map of tonal onset, growth, and amplitude variation along the chord, reinforcing the dominant role of the suction-side separation bubble in sustaining the feedback loop while clarifying the more limited role of the pressure surface.

Taken together, the trip-tape variation experiments and their spectral reconstructions establish the suction-side separation bubble as the dominant driver of the tonal feedback loop. For all incidences tested, tones emerge only when transition on the suction surface is displaced sufficiently far downstream, with the onset location advancing forward as the angle of attack increases. The pressure side remains acoustically passive in most cases, contributing only weak, streak-like tones at the highest incidence, which suggests a secondary, less robust feedback path. The systematic frequency reduction with increasing chordwise onset is consistent with the growth of the laminar separation bubble and the associated shift in shear-layer instability scale. While these findings are based on acoustic sensitivity rather than direct boundary-layer surveys, the strong agreement with established models of suction-side driven tonal noise provides compelling evidence of causality. The present results therefore offer a clear localisation of the instability origin, while leaving scope for future work to reinforce this conclusion through detailed flow-field diagnostics or acous-

tic source mapping.

4.3.3 Parametric investigation of leading-edge blowing across angle of attack

Having identified $U_\infty = 20$ m/s as the most suitable flow condition for studying trailing-edge tonal noise, the next step was to investigate systematically the effect of leading-edge blowing across a wide range of blowing rates and angles of attack. The results are presented in Figure 4.5 in the form of waterfall plots showing the change in sound power level, $\Delta\mathrm{PWL}$, relative to the corresponding baseline case. Positive values correspond to a net reduction in radiated noise. Each subplot corresponds to one angle of attack, covering $\alpha = -11.2°$, $-6.8°$, $-2.3°$, $+2.2°$, $+4.5°$, and $+6.7°$, with blowing rates spanning $U_j/U_\infty = 0.15$ up to 3.86. The figure therefore condenses a large dataset into a compact format that enables both angle-of-attack trends and blowing-rate dependencies to be discerned.

Negative incidence ($\alpha = -11.2°$ and $-6.8°$). At $\alpha = -11.2°$, the principal feature is a broadband reduction concentrated at low Strouhal numbers, reaching values of order 10 dB for the largest jet-to-freestream velocity ratios. This reduction occurs at frequencies well below the baseline tonal peak, suggesting that the mechanism is not a direct suppression of the feedback-driven instability, but rather an alteration of large-scale unsteady loading. A plausible interpretation is that, at strongly negative angles, the stagnation point is displaced lower on the airfoil and the suction-side boundary layer is relatively thick, such that momentum injection at the leading edge enhances mixing and disrupts quasi-periodic wake shedding. This explanation is consistent with the observation that the maximum benefit arises at the highest U_j/U_∞, indicating a broadband, momentum-driven effect rather than a resonance-related one.

At $\alpha = -6.8°$, the low-frequency reduction is still visible, but weaker and less consistent across blowing rates. Already, there are signs that energy changes are beginning to emerge in the frequency band corresponding to the baseline tonal peak. In other words, as the angle of attack increases towards zero, the sensitivity of the tonal feedback loop grows and the control begins to interact with this more delicate instability pathway.

Transitioning through $\alpha = -2.3°$ and $+2.2°$. At zero incidence, the low-frequency suppression evident at negative angles almost entirely vanishes, while a modest reduction emerges near the baseline tonal frequency range ($4 \leq St \leq 10$). This represents a clear transition in the action of the control: rather than attenuating broadband unsteadiness at low frequencies, the blowing now begins to influence the instability loop that sustains the tonal mode. At $\alpha = +2.2°$, the trend becomes stronger, with reductions at the tonal frequency becoming the dominant effect. Although the overall level of suppression is modest at this stage, the direction of change indicates that the control mechanism has shifted focus from large-scale wake unsteadiness to targeted disruption of the tonal source.

Positive incidence ($\alpha = +4.5°$ and $+6.7°$). The strongest results are observed at higher positive

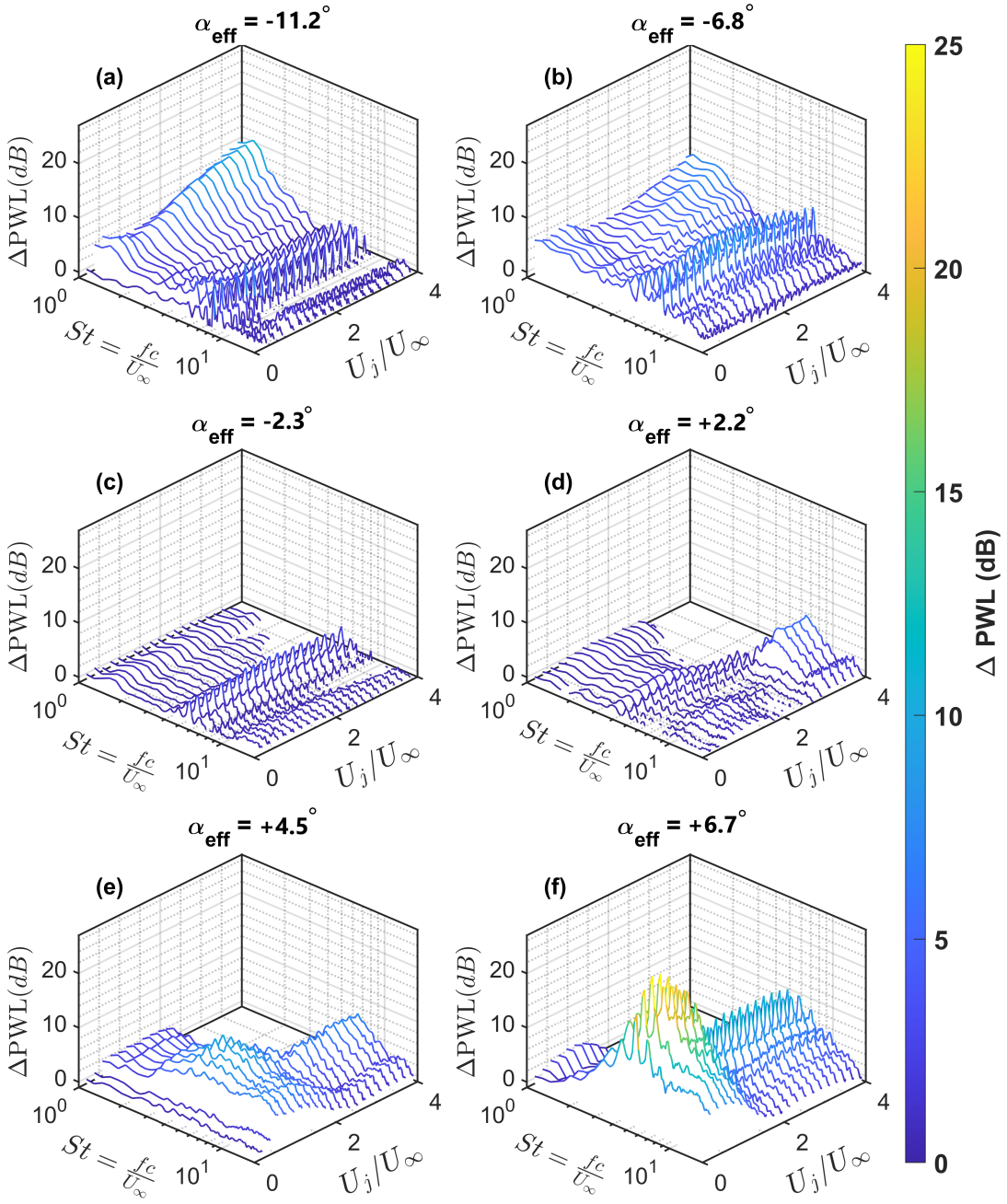

Figure 4.5: Waterfall plots of $\Delta\mathrm{PWL}$ relative to baseline for six angles of attack: (a) $\alpha = -11.2°$, (b) $\alpha = -6.8°$, (c) $\alpha = -2.3°$, (d) $\alpha = +2.2°$, (e) $\alpha = +4.5°$, (f) $\alpha = +6.7°$. Positive values correspond to reductions in radiated sound power.

angles of attack. At $\alpha = +4.5°$, reductions up to 8 dB occur precisely in the Strouhal band of the baseline tonal peak, leaving little ambiguity that the instability feedback loop is being disrupted. At $\alpha = +6.7°$, the reductions are dramatic, reaching up to 25 dB in the tonal band. In these cases, the dependence on blowing rate exhibits a clear non-monotonic character. For low blowing rates, especially $U_j/U_\infty \approx 0.35$, the suppression is highly effective. As the blowing rate increases further, the benefit declines and by $U_j/U_\infty \approx 1.5$ the reductions are already significantly weakened. At the highest blowing rates, performance is poor and in some cases comparable to baseline. This trend suggests that while moderate jet momentum enhances entrainment and destabilises the coherent roll-up responsible for tonal noise, excessive momentum injection thickens the shear layer and sustains unsteady separation, which reintroduces low-frequency fluctuations and undermines tonal suppression.

Overall interpretation. The results demonstrate two key features of leading-edge blowing control. First, its effectiveness is highly dependent on the angle of attack. At negative angles, suppression is achieved primarily at low frequencies and is associated with broadband mixing; at positive angles, tonal suppression dominates, with $\alpha = +6.7°$ providing the most striking reductions. Second, the optimal blowing rate is not necessarily the largest. At higher angles of attack, relatively low momentum ratios are sufficient to disrupt the tonal mechanism effectively, whereas excessive blowing degrades performance. This observation is critical, as it highlights that effective control requires a balance between providing enough energy to disrupt the feedback loop and avoiding over-energisation that produces new unsteady modes.

The waterfall plots in Figure 4.5 therefore establish the fundamental operating envelope of the control technique: the suppression achievable, the dependence on blowing rate, and the range of angles of attack over which benefits occur.

4.3.4 Global performance trends

While the waterfall plots provided detailed insight into the spectral response at each individual angle of attack, it is equally important to condense the information into a form that highlights the global performance envelope of the control strategy. Figure 4.6a presents such a representation in the form of a heatmap, where the abscissa corresponds to angle of attack, the ordinate to jet-to-freestream velocity ratio U_j/U_∞, and the colour indicates the band-limited ΔOAPWL over $4 \leq St \leq 10$. In this way, the figure captures the degree of suppression (or amplification) within the frequency band of greatest interest across the entire tested parameter space.

The map shows that over a wide range of conditions, particularly at negative and near-zero angles of attack, the colour remains close to neutral, indicating little or no change relative to the baseline. This indicates that under these conditions the tonal mechanism is either weak or insensitive to leading-edge forcing. A distinct region of significant reduction, however, is evident at high positive incidence combined with relatively low blowing rates. In this part of the parameter space, $\Delta\mathrm{PWL}$ reaches values as high as 25 dB, consistent with the strong tonal suppression

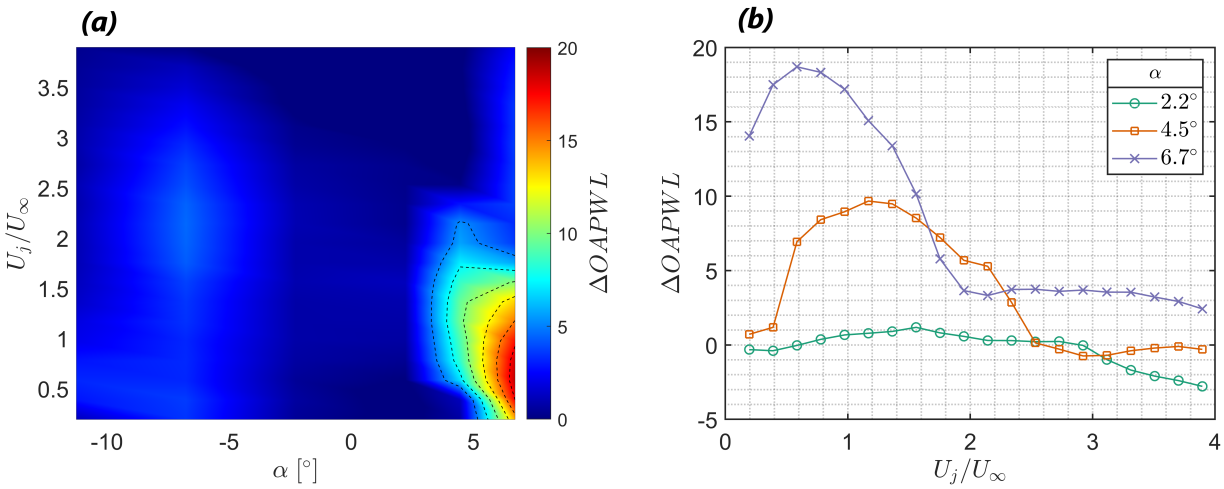

Figure 4.6: (a) Heatmap of the band-limited ΔOAPWL over $4 \leq St \leq 10$ versus α and U_j/U_∞. (b) band-limited ΔOAPWL over $4 \leq St \leq 10$ versus U_j/U_∞ for $\alpha = 2.2°$, $4.5°$, and $6.7°$.

observed in the waterfall spectra at $\alpha = +6.7°$. The area of influence extends modestly to $\alpha \approx +4.5°$, though with reduced magnitude, suggesting that the conditions for optimal suppression are not confined to a single operating point but span a finite region of incidence and jet momentum ratio.

A secondary trend is also visible at higher blowing rates. For large U_j/U_∞, particularly at positive angles of attack, moderate reductions are sustained across a band of conditions. Although the maximum levels of suppression in this regime are substantially lower than those achieved at low rates, the pattern indicates that even strong actuation provides some degree of disruption to the feedback loop. However, the effectiveness is considerably diminished, consistent with the earlier observation that excessive momentum injection thickens the shear layer and sustains residual unsteadiness.

To examine the dependence on blowing rate in greater detail, vertical slices through the heatmap were extracted at $\alpha = +2.2°$, $+4.5°$, and $6.7°$. The resulting curves are shown in Figure 4.6b. Each curve traces the band-limited ΔOAPWL over $4 \leq St \leq 10$ as a function of U_j/U_∞.

At $\alpha = +6.7°$, the response exhibits a well-defined maximum. Starting near zero, the reduction increases rapidly to about 25 dB at $U_j/U_\infty \approx 0.5$. Beyond this optimum, the performance declines steadily, with the reduction levelling off at approximately 11 dB for $U_j/U_\infty > 2$. This non-monotonic trend highlights the importance of tuning the actuation level to the flow instabilities: modest jet momentum is sufficient to destabilise the coherent feedback loop, whereas excessive momentum injection degrades the suppression by altering the shear-layer structure unfavourably.

At $\alpha = +4.5°$, the response retains the same general character but with lower amplitude. The peak reduction is about 10.5 dB, occurring at $U_j/U_\infty \approx 1.2$, with the curve subsequently decreasing towards a residual benefit of around 3 dB at high blowing rates. The shift of the optimum to higher momentum ratios reflects a reduced sensitivity of the flow at this incidence:

greater forcing is required to produce disruption, but the magnitude of suppression remains lower than at $\alpha = +6.7°$.

At $\alpha = +2.2°$, the effect is weak across the entire range of rates. The curve remains nearly flat, with reductions never exceeding 2 dB. The absence of a distinct optimum reflects the weaker tonal mechanism at this angle, leaving little scope for actuation to provide meaningful attenuation.

Taken together, the heatmap and rate-dependence curves provide a clear picture of the control landscape. The most favourable conditions for suppression occur at high incidence and low-to-moderate blowing rates, where the tonal feedback loop is strongest yet still receptive to perturbation. At lower angles of attack, the control is largely ineffective, while at high jet momentum ratios the suppression saturates or diminishes. These findings underscore the necessity of balancing incidence and blowing strength in order to achieve maximum acoustic benefit.

4.3.5 Effect of blowing on tonal frequency and mode selection

The preceding analysis focused primarily on the reduction in sound levels. To complement this, it is equally important to establish whether the actuation alters the frequency of the tonal mode itself, or whether it merely suppresses its amplitude. Figure 4.7 addresses this question by presenting far-field spectra for five representative angles of attack ($\alpha = -11.2°, -6.8°, -2.3°, +2.2°$, and $+6.7°$). For each case, three configurations are compared: the baseline, the most effective low blowing rate ($U_j/U_\infty = 0.35$), and the highest blowing rate ($U_j/U_\infty = 3.86$). The tonal peaks are highlighted with markers to indicate the selected frequency. The sixth panel (f) summarises the variation of peak frequency, expressed as the Strouhal number $St_t = f_t c/U_\infty$, as a function of α for the three cases.

At $\alpha = -11.2°$ (Figure 4.7a), all three spectra exhibit clear tonal peaks of similar magnitude, with no discernible frequency offset. This indicates that at negative incidence, leading-edge blowing has little influence on either the strength or the frequency of the instability responsible for tonal radiation. The same conclusion largely applies to $\alpha = -6.8°$ (Figure 4.7b), although here both blowing cases exhibit a modest reduction in amplitude of approximately 4 dB while the peak frequency remains unchanged. The suppression is minor, and the mechanism sustaining the tonal mode appears insensitive to actuation at these angles.

At $\alpha = -2.3°$ (Figure 4.7c), the behaviour is again similar to that at $\alpha = -11.2°$: the baseline and both blowing cases coincide closely at the tonal peak. A notable difference, however, is that the high-blowing spectrum displays elevated low-frequency energy, suggesting that excessive momentum input at this condition promotes large-scale unsteadiness unrelated to the tonal mechanism. This trend foreshadows the stronger frequency distortions observed at higher incidence.

A marked change is observed at $\alpha = 2.2°$ (Figure 4.7d). Here, the baseline and low blowing cases remain almost identical, both in amplitude and frequency, implying that the low rate has little effect at this intermediate incidence. In contrast, the high blowing case exhibits a significant redistribution of energy: the original tonal peak is suppressed, while a broader peak emerges at much lower frequency. Although this new feature is less sharply defined, it represents a clear shift

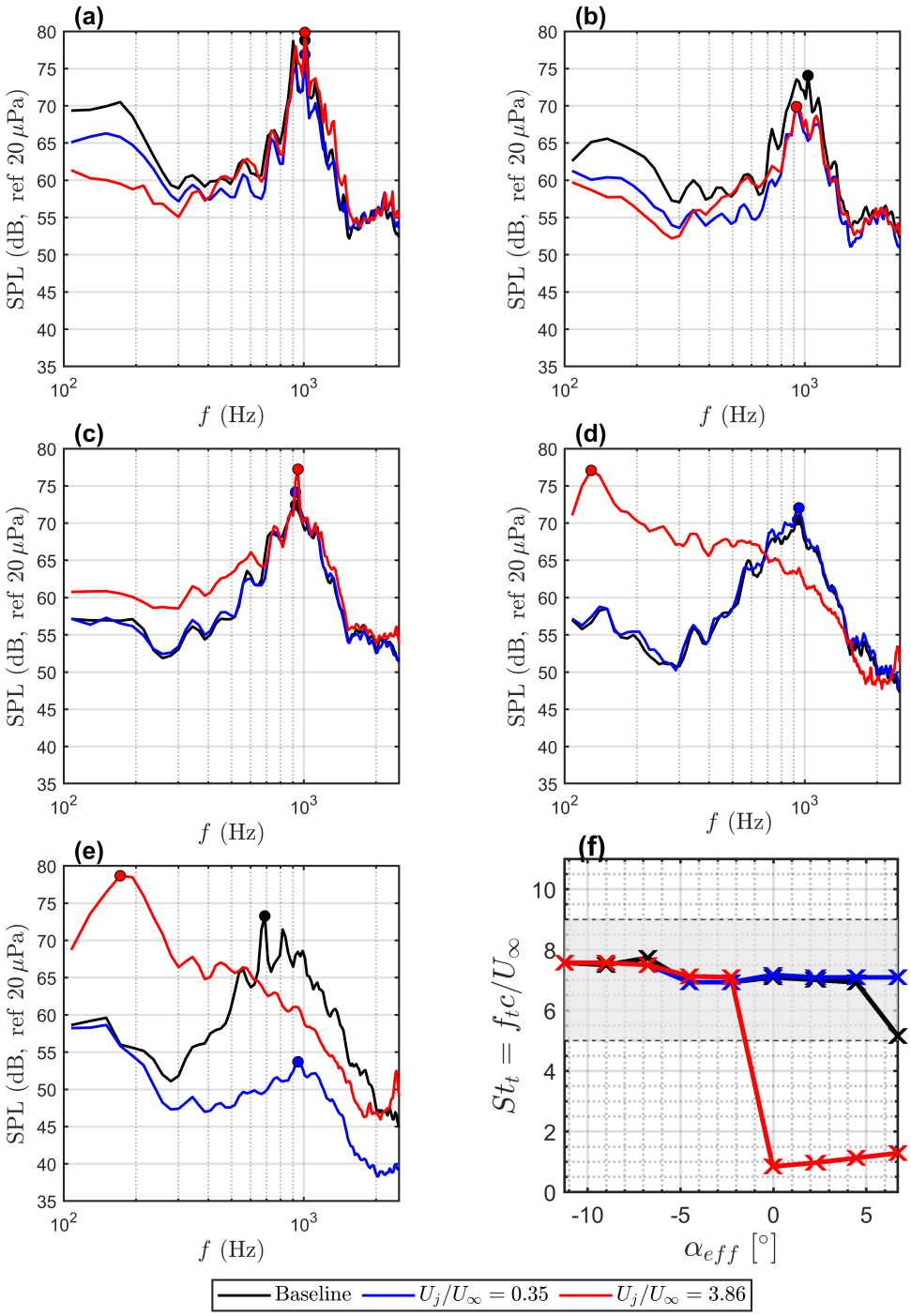

Figure 4.7: (a–e) Far-field SPL spectra at effective angles of attack $\alpha_{\text{eff}} = -11.2°, -6.8°, -2.3°, 2.2°, 6.7°$, comparing baseline, low blowing ($U_j/U_\infty = 0.35$), and high blowing ($U_j/U_\infty = 3.86$); tonal peaks are marked with circles. (f) Peak Strouhal number $St_t = f_t c/U_\infty$ versus α_{eff} for baseline and blowing cases.

in the dominant unsteadiness. The actuation at this level therefore detunes the flow from its natural feedback frequency and replaces the tonal signature with low-frequency content.

At $\alpha = 6.7^\circ$ (Figure 4.7e), the divergence between low and high blowing becomes striking. The baseline peak shifts slightly to lower frequency compared to $\alpha = 2.2^\circ$, consistent with a longer separation bubble and reduced instability frequency at higher incidence. The low blowing case, however, achieves a large reduction in amplitude (up to 25 dB) while maintaining the peak frequency at nearly the same value as the baseline at $\alpha = 2.2^\circ$. This indicates that the fundamental mode has been preserved but its amplification has collapsed. By contrast, the high blowing case continues to displace energy into the low-frequency range, producing a broad feature distinct from the baseline tonal mode.

The trends are summarised in Figure 4.7f, which plots the peak Strouhal number St_t as a function of angle of attack. For negative angles, all three cases cluster tightly near $St_t \approx 7.5$, confirming frequency invariance. At $\alpha \geq -2.3^\circ$, however, the high blowing case undergoes an abrupt drop to $St_t \approx 1$, reflecting the emergence of a fundamentally different mode of unsteadiness. The baseline and low blowing cases, in contrast, remain nearly constant until $\alpha = 6.7^\circ$. At this highest incidence, the baseline St_t decreases to approximately 5.1, whereas the low blowing case retains a higher value of $St_t \approx 7$ while simultaneously reducing the amplitude dramatically.

These results provide several important insights. First, the fundamental frequency of the trailing-edge tonal mode is remarkably robust to moderate leading-edge forcing: the low blowing case leaves the selected St_t almost unchanged across the full range of angles tested. The effect of the control is therefore not to alter the preferred feedback frequency, but to diminish the loop gain and coherence of the instability, particularly at high incidence. Second, excessive actuation fundamentally changes the dynamics: high blowing rates suppress the original tonal mode but replace it with low-frequency, broadband-dominated unsteadiness. This behaviour is consistent with a thickened shear layer and extended separation region, which favour slower, less coherent fluctuations. Third, the fact that low blowing maintains the frequency even at $\alpha = +6.7^\circ$ while suppressing its amplitude highlights a desirable form of control: the instability mechanism is left intact but weakened to the point where it can no longer radiate efficiently.

In summary, the frequency analysis shows a sharp contrast between effective and ineffective control strategies. Low momentum ratios suppress the amplitude of the tonal mode without detuning it, while high momentum ratios eliminate the mode but introduce less favourable low-frequency noise. This reinforces the conclusion that optimum performance arises not from maximum actuation, but from carefully tuned levels that disrupt coherence without fundamentally altering the instability structure.

4.4 Flow Field Results: Hot-Wire Measurements

The far-field acoustic analysis established the key behavioural trends of the leading-edge blowing system, showing that its effectiveness in suppressing tonal noise depends strongly on both angle

of attack and jet momentum ratio. However, while these spectral results reveal how the acoustic output responds to blowing, they do not explain the underlying aerodynamic mechanisms responsible for these changes. To understand the physical origin of the observed tonal suppression, and in particular why low-rate blowing at $\alpha = +6.7^\circ$ achieves complete elimination of the tonal peak whereas similar forcing at $\alpha = -2.3^\circ$ does not, a detailed examination of the wake flow is required.

4.4.1 Wake Flow Measurements

The following section focuses on the time-averaged velocity and vorticity distributions obtained from hot-wire anemometry in a plane located immediately downstream of the trailing edge. As shown in Figure 4.8, the measurement plane was positioned at $x/c = 1.02$, intersecting both the suction and pressure sides of the airfoil. The grid extends over the y–z domain defined in the

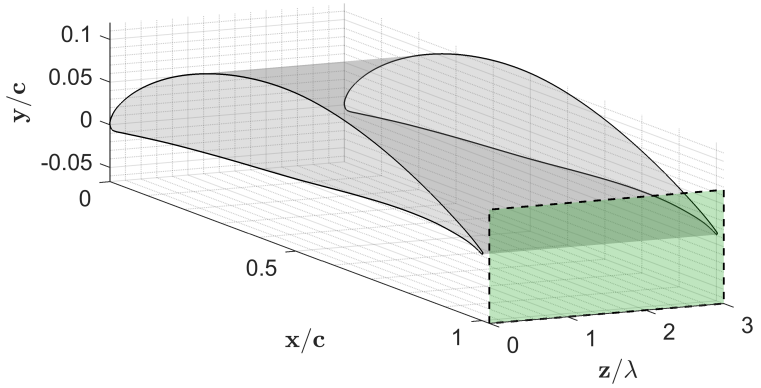

Figure 4.8: Location of the hot-wire measurement plane at $x/c = 1.02$, spanning the wake region across both suction and pressure sides.

subsequent figures, with the spanwise coverage chosen to include the four leading-edge orifices that supply the steady blowing. This arrangement captures the complete near-wake structure and allows direct comparison between baseline and blowing conditions under identical inflow and geometric configurations.

These measurements provide a means of linking the far-field acoustic response to the near-field flow dynamics by revealing how the introduction of steady momentum injection modifies the wake symmetry, shear-layer development, and overall vorticity distribution. In particular, they clarify whether the tonal suppression achieved at high incidence arises from changes in wake coherence or from a redistribution of vorticity that weakens the feedback pathway connecting the trailing edge to the suction-side separation bubble.

The analysis begins with qualitative maps of streamwise vorticity, which illustrate the overall topology of the wake and its evolution across blowing conditions and angles of attack. Streamwise vorticity $\omega_x = \partial w/\partial y - \partial v/\partial z$ is computed from the mean cross-plane velocity field. These are then followed by compact quantitative descriptors, namely the wake symmetry index and the non-dimensional vorticity thickness, which condense the observed structural changes into scalar

metrics of flow balance and shear-layer thickness. Together, these datasets provide a coherent aerodynamic explanation for the distinct acoustic behaviours documented earlier.

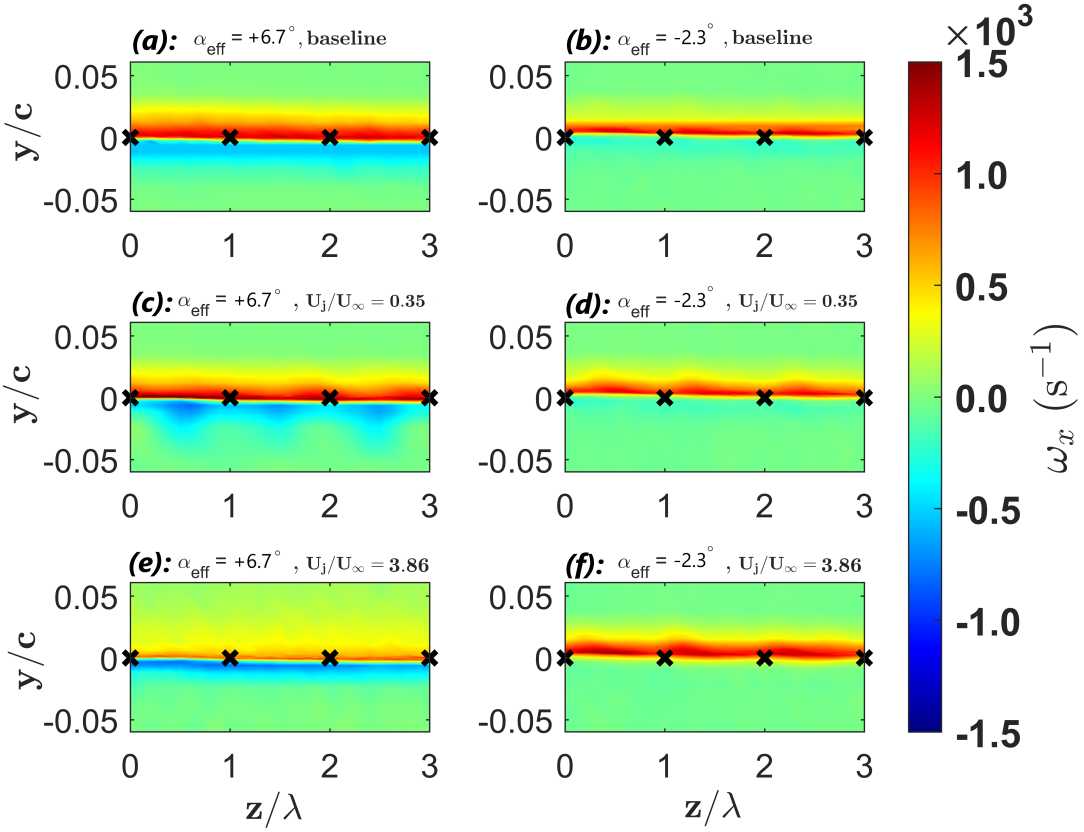

Figure 4.9: Time-averaged streamwise vorticity contours (ω_x, s^{-1}) in the wake plane 1 mm downstream of the trailing edge for baseline and blowing cases at $\alpha_{\text{eff}} = +6.7°$ and $-2.3°$. Panels (a,c,e) correspond to $\alpha_{\text{eff}} = +6.7°$ and (b,d,f) to $\alpha_{\text{eff}} = -2.3°$, showing (a,b): baseline, (c,d): $U_j/U_\infty = 0.35$, and (e,f): $U_j/U_\infty = 3.86$. Crosses mark the spanwise location of leading-edge injection orifices.

The mean streamwise vorticity distributions in Figure 4.9 illustrate how the near-wake topology evolves with leading-edge blowing and angle of attack. In the baseline configuration, both angles of attack exhibit a well-defined pattern of alternating positive and negative vorticity in close proximity to the trailing edge. This alternating structure represents the mutual interaction of the shear layers shed from the suction and pressure sides, a hallmark of the laminar separation bubble dynamics responsible for the discrete tonal emission observed in the acoustic spectra. The regions of positive vorticity correspond to fluid originating from the suction side, while the negative regions are associated with flow from the pressure side. Their close pairing and confinement near the wake centreline indicate a coherent shear-layer roll-up that efficiently supports the feedback loop driving tonal noise generation.

At $\alpha = +6.7°$, the baseline wake displays a slight bias toward the pressure side, consistent with the stronger deflection of the wake under positive incidence. Introducing a low blowing rate

($U_j/U_\infty = 0.35$) significantly modifies this structure: the alternating vorticity regions become more evenly distributed about the centreline, and the overall intensity of the vorticity field is reduced. This behaviour suggests enhanced entrainment and mixing between the two shear layers, leading to partial disruption of the separation bubble on the suction side. The resulting reduction in coherence is consistent with the near-complete suppression of the tonal mode observed acoustically. In contrast, the high blowing condition ($U_j/U_\infty = 3.86$) produces a markedly thicker, less organised vorticity field with diffuse regions of opposite-signed rotation. This indicates over-energisation of the near-wake, where excessive momentum input eliminates small-scale roll-up and replaces it with broadband, incoherent fluctuations, an effect consistent with the emergence of low-frequency noise in the corresponding spectra.

For $\alpha = -2.3°$, the baseline wake is more symmetric but retains a distinct double-layered vorticity structure, suggesting the persistence of laminar separation on the suction side. Low blowing introduces little visible change to the wake, implying that the jets primarily energise the suction-side boundary layer without strongly coupling to the feedback loop. This observation explains why tonal radiation persists at this angle despite suction-side jet entrainment. High blowing at the same incidence produces a broad, diffused vorticity distribution resembling that at $\alpha = +6.7°$, again indicative of shear-layer thickening and a transition toward less coherent, broadband behaviour.

Overall, the vorticity maps demonstrate that moderate blowing effectively restores wake symmetry and reduces vorticity magnitude without fully destroying the underlying structure, whereas excessive blowing leads to a loss of organised shear-layer roll-up. These results reinforce the notion that the most effective tonal suppression occurs when the blowing is sufficiently strong to disturb the separation bubble and weaken the feedback mechanism, yet not so strong as to fully disrupt the aerodynamic coherence of the wake.

4.4.2 Wake Symmetry and Vorticity Thickness

To provide a quantitative description of the wake modifications observed in the vorticity fields, two integral metrics were derived from the interpolated mean velocity data: the wake symmetry index, S, and the non-dimensional vorticity thickness, δ_ω/c. The symmetry index S evaluates the degree of lateral balance of the wake momentum deficit and is defined as

$$S = \frac{\int_{A_{PS}} D \, \mathrm{d}A - \int_{A_{SS}} D \, \mathrm{d}A}{\int_{A_{PS}} D \, \mathrm{d}A + \int_{A_{SS}} D \, \mathrm{d}A}, \tag{4.1}$$

where $D = U_\infty - U$ represents the local velocity deficit, and the subscripts PS and SS denote the pressure and suction sides of the wake, respectively. In practice, the integrals were evaluated over the measured wake plane at $x/c = 1.02$ using the interpolated mean velocity field. The domains A_{PS} and A_{SS} were defined as the regions on either side of the wake centreline ($y = 0$ in the measurement frame), over the same y–z bounds for all cases. The velocity deficit was computed

as $D = U_\infty - U$, with U_∞ taken from the outer (uniform) flow region at the corresponding side of the wake. A perfectly symmetric wake corresponds to $S = 0$, while positive or negative values indicate bias toward the suction or pressure side.

The vorticity thickness, δ_ω/c, characterises the mean shear-layer thickness relative to the airfoil chord and was computed following the classical definition based on the cross-stream velocity gradient,

$$\frac{\delta_\omega}{c} = \frac{1}{c}\frac{U_{\infty,PS} - U_{\infty,SS}}{\max|\partial U/\partial y|}, \tag{4.2}$$

where $U_{\infty,PS}$ and $U_{\infty,SS}$ are the local freestream velocities on the pressure and suction sides, respectively. The quantity $\max|\partial U/\partial y|$ was obtained from the spanwise-averaged wake profile $U(y) = \langle U(y,z)\rangle_z$, with $\partial U/\partial y$ computed from the interpolated field on the measurement grid. A smaller δ_ω/c corresponds to a thinner and more coherent shear layer, whereas larger values indicate wake broadening and reduced flow organisation.

Together, these two parameters provide compact yet physically meaningful descriptors of the wake evolution, linking the observed vorticity structures to measurable aerodynamic asymmetries and shear-layer behaviour. The resulting values for all test cases are summarised in Table 4.1.

Table 4.1: Wake symmetry index S and non-dimensional vorticity thickness δ_ω/c for two angles of attack and three blowing conditions.

$\alpha\,(^\circ)$	U_j/U_∞	S	δ_ω/c
$+6.7$	Baseline	-0.060	0.010
	0.35	0.046	0.009
	3.86	-0.104	0.077
-2.3	Baseline	0.194	0.096
	0.35	0.196	0.096
	3.86	0.040	0.115

The quantitative metrics presented in Table 4.1 corroborate the qualitative observations drawn from the vorticity fields and provide further evidence of the distinct wake response to blowing rate and angle of attack. At $\alpha = +6.7^\circ$, the baseline wake exhibits a slightly negative symmetry index ($S = -0.06$), confirming a weak pressure-side bias consistent with the geometric deflection of the wake under positive incidence. When low-rate blowing is introduced ($U_j/U_\infty = 0.35$), S becomes marginally positive ($S = +0.046$), indicating that the added momentum near the leading edge restores balance between the two sides of the wake. This shift toward symmetry aligns closely with the reduced coherence and diminished tonal content observed in the acoustic spectra, implying that moderate blowing effectively promotes mixing between the shear layers and suppresses the organised roll-up responsible for tonal generation. The vorticity thickness at this condition ($\delta_\omega/c = 0.0091$) remains comparable to the baseline value, suggesting that while the wake becomes more symmetric, it does so without excessive thickening or loss of aerodynamic coherence.

At the same angle of attack, further increasing the blowing rate to $U_j/U_\infty = 3.86$ drives both metrics in the opposite direction. The symmetry index becomes more negative ($S = -0.104$),

and the vorticity thickness rises sharply to $\delta_\omega/c = 0.077$, signifying a pronounced widening and pressure-side displacement of the wake. This outcome is consistent with the vorticity contours, which show a diffused, irregular wake structure, and with the far-field spectra, where the original tonal peak is replaced by low-frequency broadband energy. The large δ_ω/c thus reflects the loss of organised shear-layer roll-up and the emergence of slower, large-scale unsteadiness typical of over-energised flow conditions.

At $\alpha = -2.3°$, the baseline already exhibits a positive symmetry index ($S = +0.194$), implying that the wake is naturally biased toward the suction side at this incidence. Low blowing ($U_j/U_\infty = 0.35$) leaves both S and δ_ω/c essentially unchanged, demonstrating that the jets primarily energise the suction-side boundary layer without inducing significant entrainment or redistribution across the wake centreline. This observation explains why the tonal noise persists under these conditions despite the presence of suction-side entrainment. Only at the highest blowing rate does the wake begin to recentre ($S = +0.040$), but this comes at the cost of a moderate increase in vorticity thickness ($\delta_\omega/c = 0.115$), again indicating shear-layer diffusion and loss of coherence.

Overall, these two metrics provide a concise quantitative framework for interpreting the wake behaviour. Effective tonal suppression occurs when the blowing restores near-symmetric wake development while maintaining a compact shear layer, as seen for $\alpha = +6.7°$ at $U_j/U_\infty = 0.35$. When the actuation either fails to alter the wake asymmetry, as at $\alpha = -2.3°$, or excessively thickens the wake, as under high blowing, the tonal mechanism either persists or transitions into low-frequency broadband noise. These results reinforce the connection between wake symmetry, shear-layer organisation, and the stability of the feedback loop that sustains tonal radiation.

4.4.3 Chord-wise Entrainment

The wake metrics discussed above quantify the end state of the flow, revealing how leading-edge blowing alters the overall symmetry and organisation of the trailing-edge vorticity field. To understand how these changes originate, it is instructive to examine the development of the flow along the chord itself. The tonal feedback process is inherently sensitive to the state of the boundary layer and the evolution of shear-layer disturbances before they reach the trailing edge. Characterising the flow field at intermediate chordwise locations therefore provides essential context for interpreting the observed wake modifications and the associated tonal suppression.

To this end, a series of two-dimensional hot-wire measurement planes were acquired at $\alpha = +6.7°$ for the most effective blowing condition ($U_j/U_\infty = 0.35$). The measurement planes extend from the leading edge to the near-trailing-edge region, covering representative chordwise positions at $x/c = 0.0$, 0.2, 0.4, 0.6, and 0.8. Although these data are limited to a single incidence and blowing rate, they capture the dominant flow features responsible for tonal suppression. The maps reveal how the blowing jets evolve downstream, how the induced shear layers interact with the surface boundary layers, and whether the alternating vortical structures preferentially entrain fluid toward the suction or pressure side. These observations bridge the gap between the local action of the jets and the global wake behaviour quantified earlier, offering a spatially resolved picture of the

control mechanism along the chord.

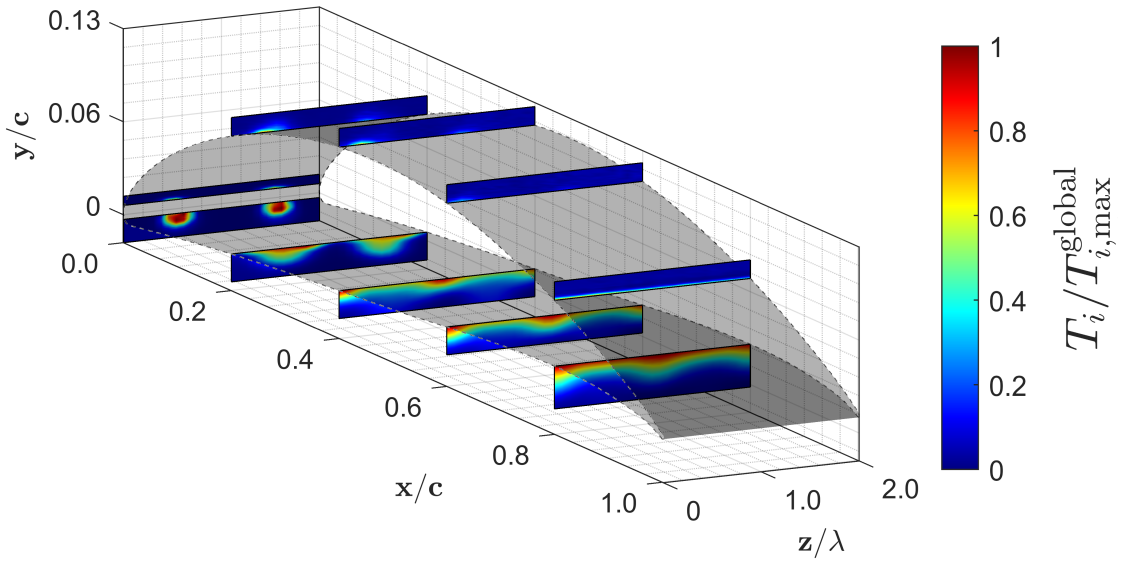

Figure 4.10: Normalised turbulence intensity profiles, $T_i/T_{i,\max}^{\text{global}}$, at several streamwise locations along both the suction and pressure surfaces for the blowing configuration at $U_j/U_\infty = 0.35$ and $\alpha = +6.7°$.

The spatial distribution of the normalised turbulence intensity across multiple chordwise stations is presented in Figure 4.10. Here turbulence intensity is defined as $TI = u_{\text{rms}}/U_\infty$ and is plotted normalised by the global maximum value across all planes, $TI/TI_{\text{global,max}}$. The plots illustrate the development of spanwise coherent structures along both the suction and pressure sides of the airfoil for the blowing configuration at $\boldsymbol{\alpha = 6.7°}$ and $\boldsymbol{U_j/U_\infty = 0.35}$. The most prominent features appear along the pressure surface, where two distinct vortical cores form near the leading edge and progressively merge around $x/c = 0.4$. Downstream of this point, the flow exhibits a gradual spanwise spreading of the high-$T_i/T_{i,\max}^{\text{global}}$ regions, indicating the breakdown and redistribution of the entrained vortical motion. Despite this diffusion, the alternating pattern of elevated and reduced turbulence intensity remains visible at $x/c = 0.8$, suggesting that the entrainment persists as a coherent, spanwise-modulated feature even near the trailing edge.

In contrast, the suction side displays far weaker turbulence levels across all chordwise positions, which is consistent with the vorticity maps in Figure 4.9 that showed the wake being primarily influenced by pressure-side entrainment. The apparent lack of strong suction-side activity in Figure 4.10 can partly be attributed to the global scaling of the colourbar, which suppresses subtle near-surface fluctuations. To address this, supplementary views are provided in Figure 4.11 at two streamwise locations, $x/c = 0.01$ and $x/c = 0.2$. The near–leading-edge plane at $x/c = 0.01$ (Figures 4.11a,b), plotted with an adjusted colour scale for clarity, highlights that the injected jets entrain fluid on *both* surfaces of the airfoil. The turbulence intensity distribution reveals compact vor-

tical structures on the suction side located approximately opposite to the dominant pressure-side core, with both sets of structures aligning closely with the positions of the leading-edge orifices. Although the suction-side features are smaller in scale and weaker in amplitude, their presence indicates that even a moderate blowing ratio of $\boldsymbol{U_j/U_\infty = 0.35}$ generates sufficient cross-surface interaction to influence the suction-side boundary layer.

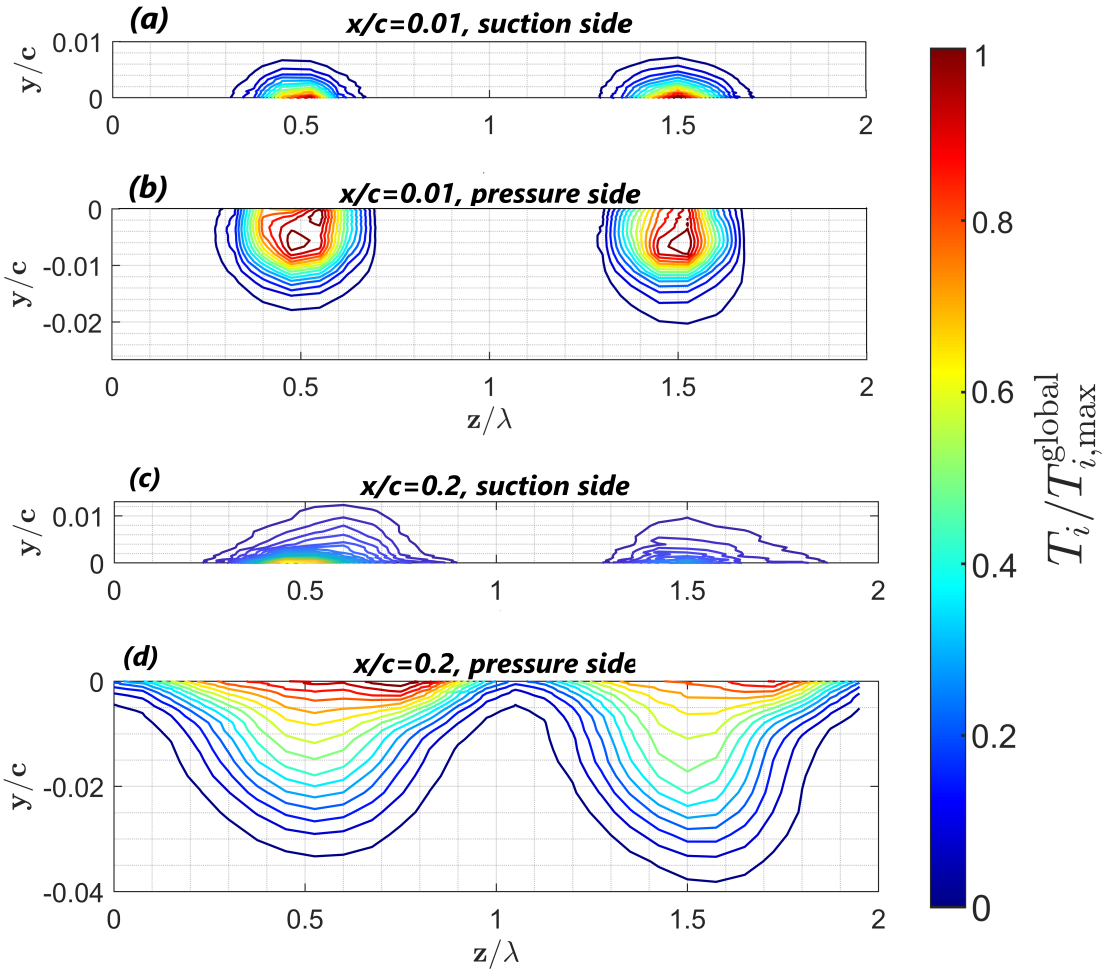

Figure 4.11: Normalised turbulence intensity $T_i/T_{i,\max}^{\text{global}}$ for the $U_j/U_\infty = 0.35$ blowing case: (a,b) plane at $x/c = 0.01$ on the suction and pressure sides, and (c,d) plane at $x/c = 0.2$ on the suction and pressure sides.

Further downstream, the plane at $x/c = 0.2$ (Figures 4.11c,d) shows that these vortical structures persist over both the suction and pressure sides, indicating continued entrainment as the flow progresses toward the trailing edge. On each surface, the intensity levels are reduced compared with $x/c = 0.01$, but the structures have broadened in the spanwise direction, suggesting that the initial jet-induced cores diffuse and spread while retaining a coherent imprint of the actuation pattern. On the pressure side, the turbulence intensity contours also exhibit signs of gradual

lifting away from the wall, consistent with vortical motions that are beginning to detach from the surface as they are convected downstream. This behaviour is plausible at the adverse incidence of $\alpha = 6.7^{\circ}$, where the local pressure gradient encourages the entrained structures to migrate away from the surface as they are swept toward the trailing edge.

Together, these observations indicate that the blowing configuration at $U_j/U_\infty = 0.35$ and $\alpha = 6.7^{\circ}$ produces a three-dimensional entrainment pattern that is not confined to the pressure side alone and persists well beyond the immediate vicinity of the leading edge. The spanwise vortical structures that develop near the leading edge induce cross-surface perturbations capable of influencing the suction-side boundary layer and the upstream conditions feeding the tonal mechanism, while their downstream spreading and partial detachment suggest a modification of the disturbance field as the flow approaches the trailing edge. In combination, these effects act to interrupt the tonal feedback loop responsible for the radiated tonal noise. The coherence and frequency analyses presented in the following section further substantiate this interpretation by quantifying the extent to which these entrained structures modify the flow organisation in the near wake.

While the time-averaged measurements presented thus far establish a clear link between the blowing configuration and the overall wake structure, they do not directly capture the temporal coupling between the unsteady flow field, surface pressure fluctuations, and radiated sound. To address this, the next subsection examines synchronous measurements of velocity, surface pressure, and far-field acoustics. The analysis focuses on coherence-based metrics to quantify how flow disturbances near the airfoil surface correlate with radiated tonal energy, providing a dynamic perspective on the mechanisms responsible for tonal noise suppression.

4.5 Flow–Acoustic Coupling from Synchronous Measurements

The previous analysis established how leading-edge blowing alters the mean flow topology and wake dynamics, providing a clear explanation for the suppression and detuning of trailing-edge tonal noise. However, these time-averaged fields alone do not capture the temporal organisation of the flow or its direct connection to the acoustic field. To investigate the instantaneous coupling between aerodynamic and acoustic fluctuations, a series of synchronous measurements were performed in which the unsteady velocity, surface pressure, and far-field sound were recorded simultaneously.

The primary objective of this analysis is to identify how the fluctuating flow structures near the aerofoil surface interact with the pressure field at the trailing edge and how this interaction changes with blowing rate. In particular, the study examines how the coherence between the unsteady velocity and surface pressure evolves along the chord, and how the surface pressure itself couples with the radiated sound. These relationships provide a dynamic view of the feedback process responsible for tonal noise generation and allow the effects of blowing to be interpreted in terms of changes in hydrodynamic–acoustic connectivity.

Measurements were carried out for the $\alpha = 6.7°$ configuration using two representative blowing conditions: a low momentum ratio ($U_j/U_\infty = 0.35$), corresponding to the most effective noise suppression, and a high momentum ratio ($U_j/U_\infty = 3.86$), associated with the appearance of a lower-frequency mode. The experimental arrangement is illustrated schematically in Figure 4.12, showing the traverse path of the hot-wire probe, the surface pressure taps (red markers), and the far-field microphones aligned with the trailing edge. At each condition, velocity fluctuations were acquired using a traversing hot-wire probe positioned at multiple chordwise stations ($x/c = 0.03$, 0.25, 0.50 and 0.75) on both the suction and pressure sides. The surface pressure was measured at a fixed location near the trailing edge ($x/c = 0.75$), while the far-field pressure was recorded simultaneously by microphones positioned at the same chordwise alignment. Each measurement set therefore provides three time-synchronised signals that describe the local flow, the surface response, and the acoustic radiation associated with a particular chordwise region.

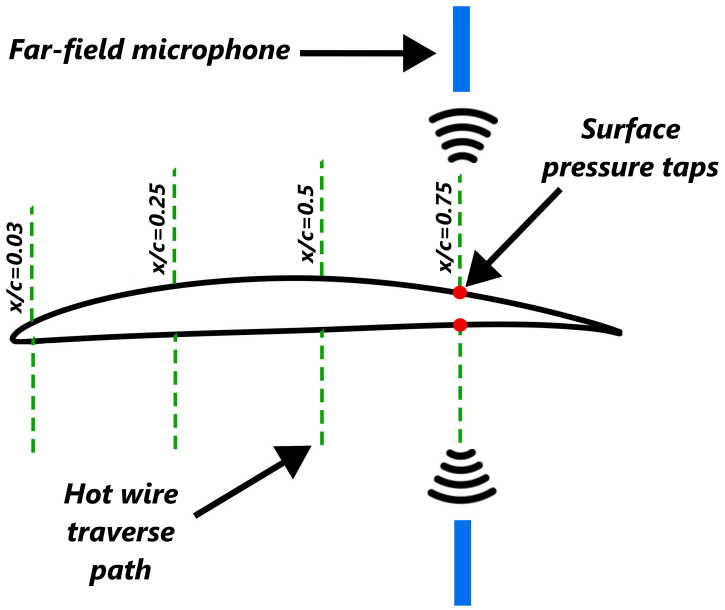

Figure 4.12: Schematic of the synchronous measurement setup showing the traverse path of the hot-wire probe, surface pressure taps (red markers), and far-field microphones aligned with the trailing edge.

By analysing the magnitude-squared coherence between these quantities, the present section quantifies how energy in the fluctuating velocity field couples with surface pressure and subsequently with the radiated sound. The results provide a means to identify where along the chord the hydrodynamic–acoustic link is strongest, how it is affected by blowing intensity, and how the transition from tonal to broadband noise is reflected in the loss of coherence. The following subsections first examine the spectral characteristics of the recorded signals, before presenting a detailed coherence-based analysis that connects the spatial development of the unsteady flow to the radiated acoustic field.

4.5.1 Spectral analysis

The synchronised far-field and surface-pressure spectra, presented in Figure 4.13, provide direct evidence of how the flow–acoustic response evolves under different blowing conditions on both the suction and pressure sides of the aerofoil. The far-field spectra on the suction side [Figure 4.13a] reproduce the characteristic tonal behaviour observed in earlier measurements, with the baseline case exhibiting a distinct and narrow tonal peak in the range 300–2000 Hz. When steady leading-edge blowing is introduced at a moderate jet-to-freestream velocity ratio of $U_j/U_\infty = 0.35$, this tonal feature is entirely suppressed, leaving behind a smooth broadband spectrum with a uniform decay across frequency. Increasing the blowing rate to $U_j/U_\infty = 3.86$ also eliminates the tone but introduces a pronounced low-frequency rise in spectral energy. This behaviour mirrors the trends established in the global acoustic analysis, where excessive momentum input was shown to thicken the shear layer and promote slower, large-scale unsteadiness that replaces the organised tonal radiation with broadband fluctuations.

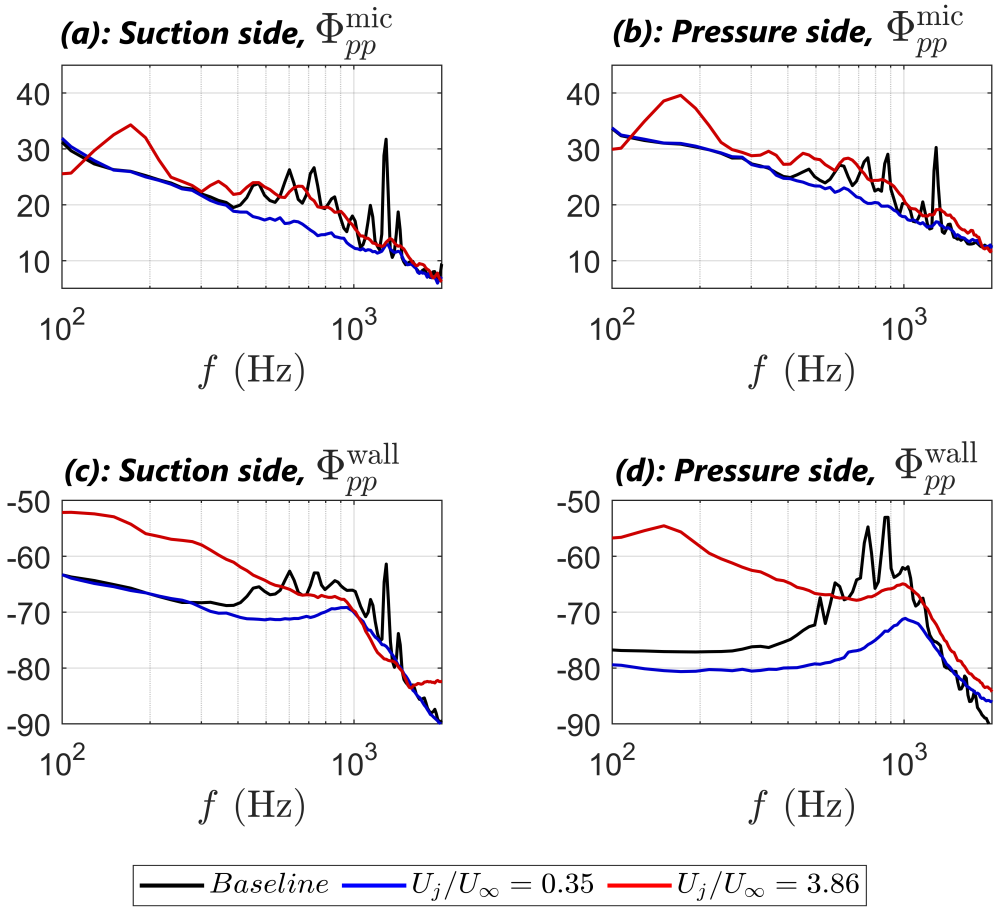

Figure 4.13: Comparison of power spectral densities of pressure fluctuations, Φ_{pp}^{mic} and $\Phi_{pp}^{\mathrm{wall}}$, for the suction and pressure sides at $\alpha = 6.7°$. Panels (a) and (b) show the far-field microphone spectra Φ_{pp}^{mic}, while (c) and (d) present the surface-pressure spectra $\Phi_{pp}^{\mathrm{wall}}$ at $x/c = 0.75$.

The far-field spectra on the pressure side [Figure 4.13b] exhibit similar qualitative behaviour but with subtle distinctions in both amplitude and tone prominence. The baseline tone is weaker than that of the suction side, consistent with earlier observations that the dominant feedback loop originates primarily from the suction-surface separation bubble. Nevertheless, the low-rate blowing ($U_j/U_\infty = 0.35$) again achieves complete tonal suppression, while the high-rate case ($U_j/U_\infty = 3.86$) produces a modest broadband rise concentrated below approximately $500\ \mathrm{Hz}$. The symmetry of this trend across both surfaces reinforces the conclusion that excessive actuation disrupts the wake globally, rather than selectively influencing one side of the aerofoil.

The surface-pressure spectra measured at $x/c = 0.75$ further elucidate the local wall-pressure dynamics responsible for these acoustic changes. On the suction side [Figure 4.13c], the baseline tone occupies the same frequency range as the far-field counterpart, confirming that the wall-pressure fluctuations near the trailing edge are strongly coupled to the radiated sound. The low-blowing case once again suppresses this peak almost entirely, while the high-blowing case exhibits a broadband elevation at lower frequencies. However, this increase is less hump-shaped than in the far-field spectrum, appearing instead as a nearly flat uplift of spectral energy across the low-frequency range. This difference suggests that while the global acoustic field captures the integrated effect of large-scale unsteady motions, the local surface pressure is sensitive mainly to fluctuations near the trailing-edge region, where the influence of the low-frequency modes is weaker or more spatially diffuse.

A similar interpretation applies to the pressure-side wall-pressure spectra [Figure 4.13d]. Here, the baseline tone is more distinct than in the far-field data of Figure 4.13b, again centred within 300–$2000\ \mathrm{Hz}$. The low-blowing case maintains its strong suppressive effect, confirming the robustness of tonal mitigation across both surfaces. In contrast, the high-blowing case exhibits a markedly elevated low-frequency level below $500\ \mathrm{Hz}$, consistent with the redistribution of energy into large-scale motions identified in the wake vorticity maps. The comparatively flatter spectral shape in the surface-pressure data, as opposed to the pronounced hump seen in the far-field spectrum, indicates that the primary source of this low-frequency energy lies away from the pressure tap location, most likely in the outer wake or separated shear layer.

Taken together, the spectral results demonstrate a clear hierarchy in the effect of leading-edge blowing on the coupled flow–acoustic system. The low-rate blowing condition ($U_j/U_\infty = 0.35$) effectively suppresses the coherent feedback loop responsible for tonal noise without altering the underlying frequency content of the flow. In contrast, the high-rate condition ($U_j/U_\infty = 3.86$) over-energises the shear layer, replacing the discrete tonal mechanism with broadband, low-frequency unsteadiness. Taken together, these spectral trends support the interpretation that the most effective suppression is obtained when actuation reduces the narrowband loop coherence (and hence loop gain) without introducing a competing large-scale unsteady mode. In contrast, excessive forcing suppresses the discrete tone but promotes broadband low-frequency unsteadiness.

The coherence spectra between the far-field noise and the unsteady surface pressure at $x/c = 0.75$, shown in Figure 4.14, provide a direct indication of how effectively surface pressure

fluctuations couple to the radiated sound for each blowing configuration. Panel (a) corresponds to the suction side and panel (b) to the pressure side.

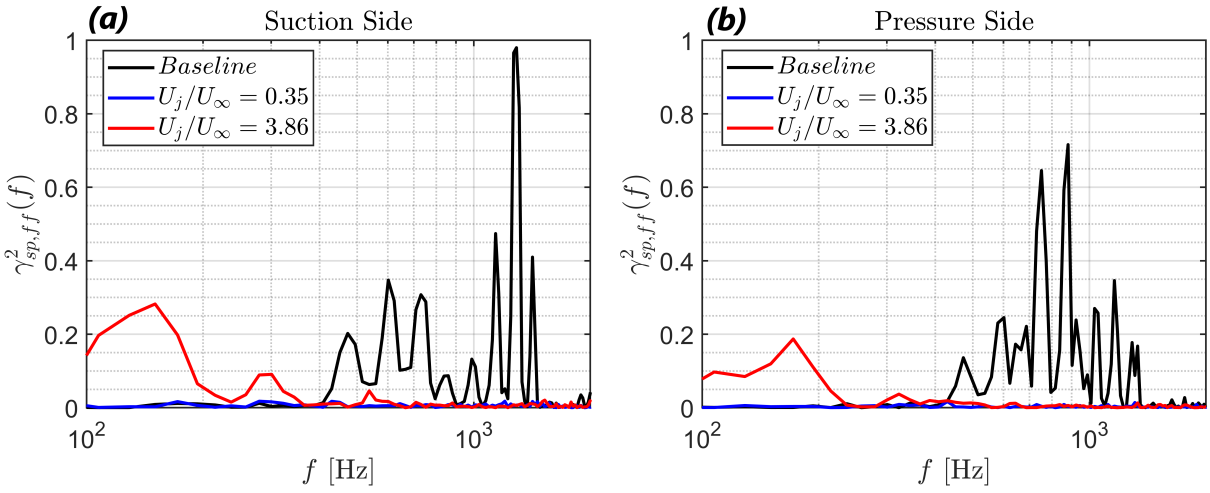

Figure 4.14: Coherence spectra between far-field noise and unsteady surface pressure at $x/c = 0.75$ for $\alpha_{\text{eff}} = 6.7°$. Panel (a) shows the suction-side coherence and panel (b) the pressure-side coherence for the different blowing configurations.

In the baseline condition, a distinct coherence peak appears near $f \approx 1300$ Hz on the suction side, corresponding to a Strouhal number of $St_t \approx 9.75$. This frequency lies within the narrowband region previously identified as the tonal mode in the acoustic spectra, confirming that the tonal radiation originates from a coherent interaction between the surface pressure fluctuations and the far-field sound at this frequency. The magnitude-squared coherence reaches values close to unity locally, indicating a strongly phase-locked feedback process linking the laminar separation bubble and the trailing-edge scattering. On the pressure side, two smaller coherence peaks occur at approximately 750 and 900 Hz, suggesting secondary contributions that are less dominant but likely related to subharmonic or sideband activity associated with the same instability process. Their lower amplitude and broader bandwidth imply a weaker, less organized coupling compared to the suction side, which supports the earlier conclusion that the suction-side bubble governs the tonal generation mechanism.

Introducing leading-edge blowing fundamentally alters this behaviour. For the low momentum-ratio case ($U_j/U_\infty = 0.35$), the coherence collapses across the entire frequency range, remaining below 0.02 for both surfaces. This indicates that, although the local surface-pressure fluctuations persist, they have lost the phase relationship with the far-field sound that characterises the tonal feedback loop. The laminar separation bubble is therefore sufficiently disrupted that its self-sustaining resonance cannot form, which explains the complete disappearance of the tonal peak in the acoustic spectra despite comparable or even higher levels of broadband surface-pressure energy.

At the higher blowing rate ($U_j/U_\infty = 3.86$), the coherence spectra remain largely flat but exhibit

a broad low-frequency hump centred around 150 Hz on both surfaces. On the suction side, the peak magnitude-squared coherence reaches approximately 0.07, while on the pressure side it remains below 0.04. This feature corresponds to the low-frequency broadband elevation observed in the far-field spectra and reflects the emergence of large-scale, slowly varying flow structures in the thickened shear layer. Although these motions contribute modestly to the radiated noise, their relatively low coherence values indicate that the associated pressure field is spatially diffuse and radiates inefficiently.

Taken together, the coherence analysis reinforces the interpretation of the spectral results. The baseline flow exhibits a narrowband, highly coherent coupling between surface pressure and far-field noise at the tonal frequency. The low-blowing condition destroys this coupling, effectively suppressing the tone, while the high-blowing condition replaces it with weak, broadband coherence at low frequencies. These trends confirm that the primary effect of leading-edge blowing is not to remove unsteady pressure fluctuations altogether, but to eliminate the phase-locked feedback mechanism responsible for coherent tonal radiation.

4.5.2 Spatial Distribution of Flow–Acoustic Coherence

To examine how the unsteady flow field couples with the radiated sound, the magnitude-squared coherence between the velocity fluctuations and the far-field pressure was evaluated. This quantity, denoted as $\gamma_{u,p_{\mathrm{mic}}}(f, y/c)$, represents the degree of linear correlation between the local velocity field and the acoustic pressure at a given frequency f and wall-normal position y/c. A value of $\gamma_{u,p_{\mathrm{mic}}} = 1$ corresponds to perfect coherence, while $\gamma_{u,p_{\mathrm{mic}}} = 0$ indicates that the two signals are statistically uncorrelated. Since the far-field microphone captures the radiated component of the aeroacoustic feedback loop, the coherence distribution provides a direct measure of how efficiently velocity fluctuations within the boundary layer and near-wake region contribute to tonal noise generation.

Figure 4.15 presents the coherence maps for the $x/c = 0.75$ plane, where the interaction between the separated shear layer and the trailing-edge wake is most active. The maps show results for both the suction and pressure sides under the baseline condition and for the two blowing rates, $U_j/U_\infty = 0.35$ and 3.86. This figure focuses exclusively on the velocity–far-field coherence, as this quantity most clearly reveals how the local flow field participates in the radiation process. A broader, chordwise comparison of coherence trends will follow in a later subsection.

The baseline configuration displays distinct bands of strong coherence concentrated within the frequency range of approximately 400 to 1300 Hz. These bands coincide precisely with the tonal content previously identified in the far-field and surface-pressure spectra, confirming that the tonal radiation originates from coherent velocity structures within the near-wake. On the suction side, coherence values peak close to the wall and gradually decay with increasing y/c, suggesting that the radiating fluctuations are rooted in the upper portion of the separated shear layer where the laminar-to-turbulent transition process occurs. This slow decay with wall-normal distance implies that the instability maintains spatial organisation as it convects downstream, allowing it to couple

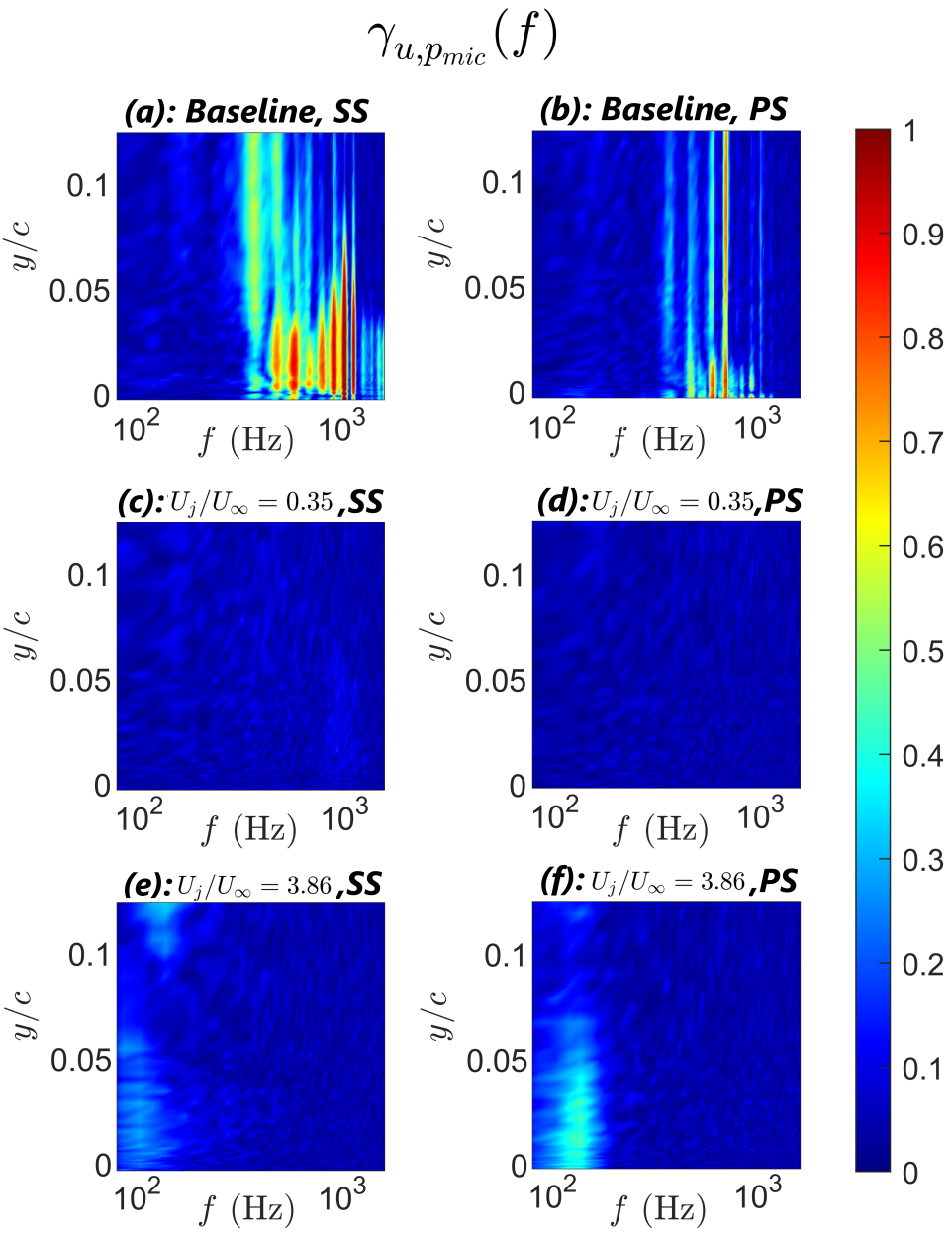

Figure 4.15: Coherence magnitude $\gamma_{u,p_{\mathrm{mic}}}(f, y/c)$ between the streamwise velocity fluctuations and far-field pressure at $x/c = 0.75$ for (a,b) baseline, (c,d) $U_j/U_\infty = 0.35$, and (e,f) $U_j/U_\infty = 3.86$. **Left column:** suction side; **right column:** pressure side.

efficiently with the acoustic field.

The pressure-side coherence pattern exhibits two main tonal features, centred near 750 and 900 Hz. The lower-frequency component (750 Hz) diminishes rapidly above $y/c \approx 0.025$, whereas the 900 Hz tone persists further into the outer flow. This difference suggests that the higher-frequency mode is associated with smaller-scale, more spatially confined structures that retain coherence deeper into the wake, whereas the lower-frequency mode originates from larger mo-

tions confined closer to the wall.

When low-level blowing is introduced ($U_j/U_\infty = 0.35$), these coherent tonal bands vanish almost completely, and $\gamma^2_{u,p_{\mathrm{mic}}}$ falls below 0.1 across the entire frequency range. This indicates that modest actuation suppresses or de-correlates the disturbances that contribute to coherent trailing-edge surface-pressure fluctuations in the baseline case, consistent with a weakened hydrodynamic feedback mechanism. In contrast, high blowing ($U_j/U_\infty = 3.86$) also suppresses the tonal coherence but introduces a new region of enhanced correlation at low frequencies, peaking near 150 Hz with $\gamma^2_{u,p_{\mathrm{mic}}} \approx 0.35$. This low-frequency coherence is substantially stronger on the pressure side than on the suction side, indicating that the increased jet momentum shifts the flow's dominant unsteadiness toward large-scale wake motions that are more strongly aligned with the wall pressure field on the pressure side. The result is a broadband, low-frequency coupling consistent with the raised acoustic levels observed in the far-field spectra for this condition.

Overall, these coherence maps demonstrate that the baseline tonal radiation originates from well-organised vortical fluctuations within the separated shear layer, and that low-level blowing suppresses these structures by disturbing their phase coherence. Excessive actuation, however, replaces the organised tonal mode with broadband wake fluctuations that remain coherent at low frequencies, particularly along the pressure side where the jet entrainment is strongest. These findings provide strong, flow-based support for the interpretation that the observed acoustic response is governed by changes in the strength and organisation of the flow–acoustic coupling, with low-level blowing suppressing the narrowband tonal feedback loop and high blowing promoting a broadband low-frequency coupling.

To enable a consistent comparison of the flow behaviour along the chord, a single representative wall-normal reference location was defined at each streamwise station on the basis of the local turbulence intensity. For every x/c location, wall-normal profiles of the r.m.s. streamwise velocity, $u_{\mathrm{rms}}(y, x/c)$, were constructed from the time-resolved velocity signals by taking the root-mean-square at each y position. These profiles exhibited a well-defined maximum in the wall-normal direction, and the corresponding wall-normal location of this peak, denoted $y_{\mathrm{pk}}(x/c)$, was identified for each chordwise station.

The reference height used in the subsequent analysis was therefore chosen as

$$y_{\mathrm{ref}}(x/c) = y_{\mathrm{pk}}(x/c) = max\left[u_{\mathrm{rms}}(y, x/c)\right],$$

so that all chordwise variations are evaluated with respect to the most energetic part of the boundary layer at each x/c. This procedure effectively collapses the wall-normal dependence into a physically motivated, turbulence-based metric while retaining sensitivity to the local evolution of the boundary-layer structure along the aerofoil surface, and it is this reference height $y_{\mathrm{ref}}(x/c)$ that is adopted for the chordwise coherence distributions presented in the below.

The coherence distributions between the local streamwise velocity fluctuations and the far-field acoustic pressure are presented in Figure 4.16. This position captures the region of strongest hydrodynamic–acoustic interaction within the boundary layer while remaining sufficiently close

to the surface to avoid near-wall artefacts. The figure provides a chordwise overview of how flow–acoustic coupling develops across the suction and pressure surfaces of the aerofoil under the three blowing conditions. Each panel corresponds to a specific chordwise station, progressing from the near leading edge ($x/c = 0.03$) to the trailing edge ($x/c = 0.75$), and illustrates how the coherence spectra evolve as the flow convects downstream. This comparison offers an integrated view of how the hydrodynamic disturbances within the boundary layer communicate with the radiated acoustic field, and how the introduction of steady leading-edge blowing alters this coupling.

At the suction side (panels a, c, e, and g), the baseline configuration exhibits pronounced coherence within the frequency range of approximately 300–900 Hz, most notably at $x/c = 0.03$ (panel a). The relatively high coherence magnitude in this range, despite being upstream of the trailing edge, suggests that some portion of the near-wall unsteadiness is hydrodynamically connected to the outer pressure field rather than to the tonal feedback mechanism associated with the laminar separation bubble near the trailing edge. The similarity of this feature to the coherence observed on the pressure side at the same chordwise position (panel b) supports the interpretation that this peak arises from global flow fluctuations or leading-edge interactions rather than the trailing-edge feedback loop. As the flow convects downstream (panels c and e), the coherence at these intermediate locations diminishes considerably, indicating that the near-wall velocity fluctuations become progressively decorrelated from the far-field pressure as the flow transitions towards a more convective character. At the trailing-edge location ($x/c = 0.75$, panel g), the tonal coherence re-emerges with a sharp and narrowband peak reaching almost unity. This is consistent with the re-establishment of a strong hydrodynamic–acoustic linkage within the characteristic tonal frequency range, consistent with the presence of an organized feedback mechanism in the baseline condition.

Across all chordwise positions, the low blowing rate ($U_j/U_\infty = 0.35$) results in uniformly low coherence levels, remaining below 0.1 throughout the frequency range. This indicates that moderate leading-edge blowing effectively disrupts the upstream–downstream feedback responsible for tonal coupling, consistent with the elimination of tonal peaks seen previously in the far-field and surface-pressure spectra. The high blowing case ($U_j/U_\infty = 3.86$) also suppresses the tonal coherence but introduces a distinct low-frequency coherence increase below approximately 400 Hz. This broadband component reaches its highest amplitude near the leading edge ($x/c = 0.03$, $\gamma_{u,p_{\mathrm{mic}}} \approx 0.28$) and progressively weakens downstream to about 0.22 at $x/c = 0.75$. This behaviour indicates that excessive blowing introduces large-scale, low-frequency flow unsteadiness that remains hydrodynamically coherent with the far-field pressure, but its intensity decays as the disturbances convect towards the trailing edge and dissipate within the boundary layer.

The pressure side coherence distributions (panels b, d, f, and h) show similar general trends but with notable differences in magnitude and spatial evolution. In the baseline condition, the initial station ($x/c = 0.03$) displays a strong coherence peak around 600–800 Hz with a maximum of approximately 0.6, followed by a reduction at mid-chord (panels d and f) and a resurgence at the

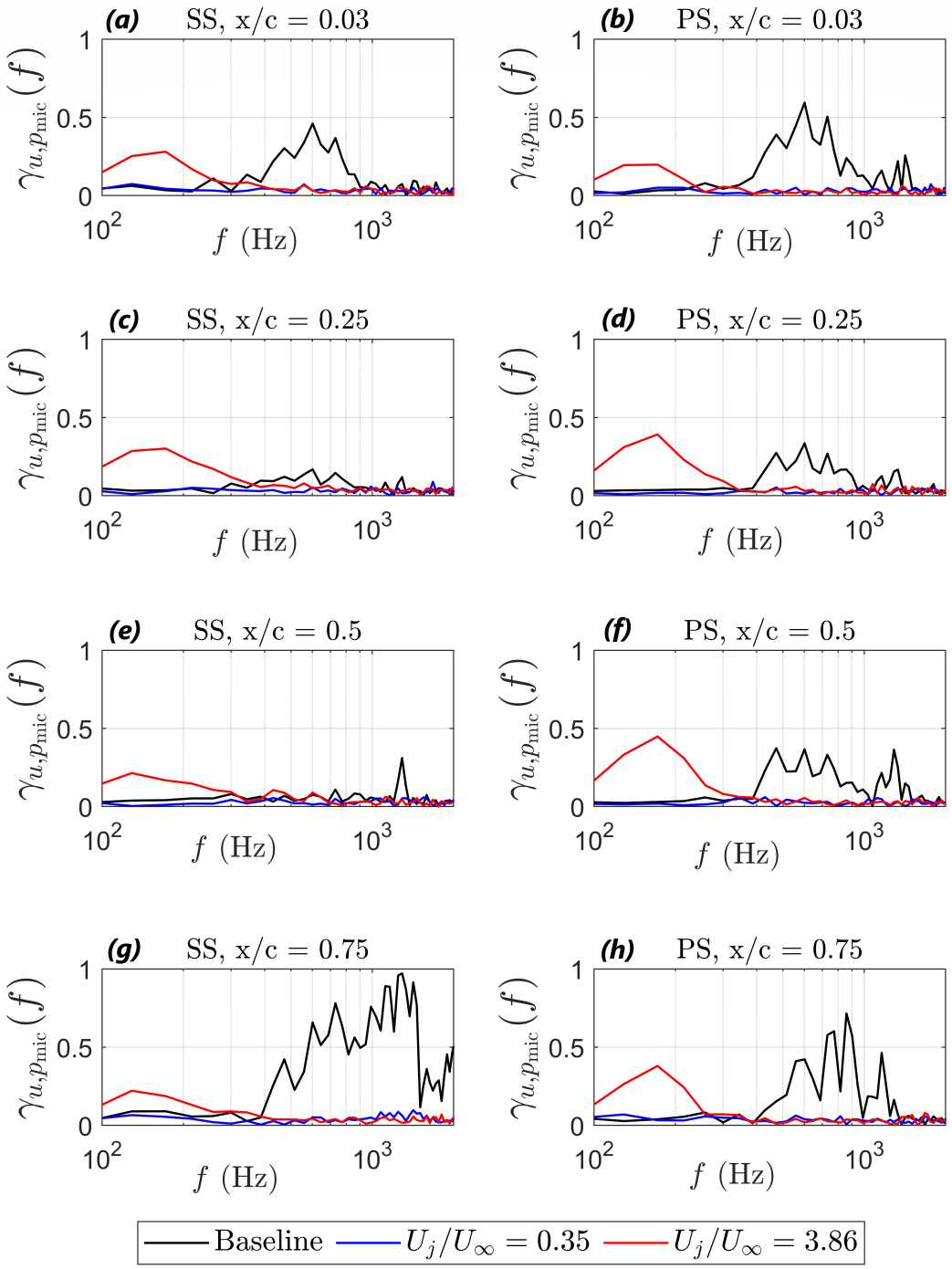

Figure 4.16: Coherence magnitude spectra between streamwise velocity fluctuations and far-field acoustic pressure for different chordwise locations. Panels (a, c, e, g) correspond to the suction side and (b, d, f, h) to the pressure side, at $x/c = 0.03$, 0.25, 0.50, and 0.75 respectively.

trailing edge, where the coherence approaches 0.7. The reappearance of high coherence near the trailing edge again reflects the reactivation of the feedback mechanism that drives tonal noise generation. The low blowing case maintains negligible coherence levels at all chordwise stations, further demonstrating that moderate momentum injection suppresses both tonal and broadband coupling. In contrast, the high blowing condition introduces the same low-frequency coherence as on the suction side, but here it is more pronounced. The pressure-side coherence peak begins at approximately 0.2 near the leading edge and gradually rises to 0.45 by $x/c = 0.75$, suggesting that the low-frequency unsteadiness induced by strong blowing manifests more prominently in the pressure-side boundary layer. This may indicate that the injected momentum interacts with the lower surface flow in a way that enhances large-scale motions capable of coupling with the far-field sound, while the upper surface remains more resistant to these effects due to its more accelerated external flow.

Taken together, these results highlight the distinct influence of the leading-edge blowing rate on the spatial and spectral structure of the flow–acoustic coupling. The baseline configuration shows strong coherence confined to the tonal frequency range near the trailing edge, characteristic of the laminar separation bubble feedback mechanism. Low-rate blowing disrupts this coupling completely, while excessive blowing shifts the coherence towards low-frequency hydrodynamic motions that remain weakly but persistently connected to the acoustic field. These observations reinforce the dual role of leading-edge blowing in simultaneously mitigating tonal feedback and introducing broadband, large-scale unsteadiness when the injected momentum exceeds the optimal range.

The coherence between the local streamwise velocity fluctuations and the unsteady surface pressure is presented in Figure 4.17. As before, the results are evaluated at the reference wall-normal location $y_{\mathrm{ref}}(x/c)$, defined as the height of peak u_{rms} at each chordwise station. Coherence is presented at four chordwise positions ($x/c = 0.03$, 0.25, 0.50, and 0.75) for both the suction and pressure sides of the aerofoil. Unlike the previous figure, where the coherence was evaluated relative to the far-field microphone, the present results quantify the hydrodynamic coupling between the boundary-layer velocity disturbances and the surface pressure fluctuations measured at a fixed location near the trailing edge ($x/c = 0.75$). This configuration allows an assessment of how perturbations generated along the chord contribute to wall-pressure unsteadiness associated with the trailing-edge feedback process.

On the suction side (panels a, c, e, and g), the baseline configuration exhibits weak but distinct coherence in the range of 400–900 Hz at $x/c = 0.03$, with a maximum magnitude of approximately 0.2. The coherence decreases at $x/c = 0.25$, suggesting that the upstream flow disturbances lose correlation with the trailing-edge surface pressure as they convect downstream. At $x/c = 0.75$, the coherence rises sharply, displaying a dominant tone centred near 1200 Hz, reaching a magnitude of approximately 0.95. This strong coupling indicates that the surface pressure fluctuations at the trailing edge are highly coherent with the local velocity perturbations at this location, confirming the presence of a well-organised hydrodynamic feedback loop. Notably, a weak low-frequency

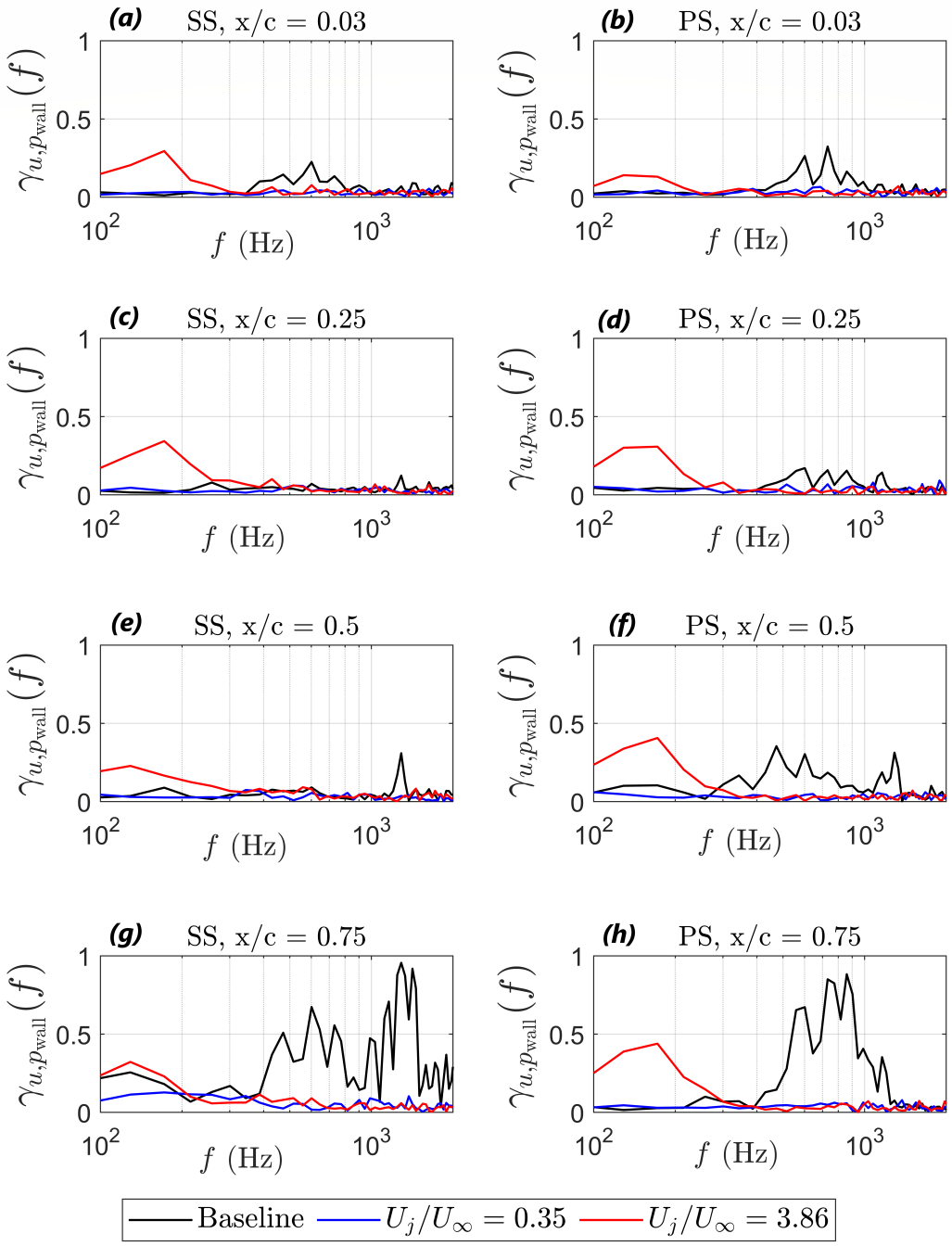

Figure 4.17: Coherence magnitude spectra between streamwise velocity fluctuations and unsteady surface pressure for different chordwise locations. Panels (a, c, e, g) correspond to the suction side and (b, d, f, h) to the pressure side, at $x/c = 0.03$, 0.25, 0.50, and 0.75 respectively.

hump also appears in this baseline case, similar to that observed for the high-blowing condition. This feature likely arises from large-scale unsteady motions in the wake or outer shear layer that

modulate the trailing-edge pressure field even in the absence of actuation.

For the low-blowing condition ($U_j/U_\infty = 0.35$), the coherence remains negligible at all chordwise positions, remaining below 0.1 and showing no trace of the narrowband coupling characteristic of the baseline flow. This behaviour is consistent with a collapse of the phase-locked hydrodynamic–acoustic coupling required to sustain tonal feedback, supporting the interpretation that low-level actuation suppresses tonal radiation by weakening loop coherence and gain. In contrast, the high-blowing condition ($U_j/U_\infty = 3.86$) eliminates the tonal coherence but produces a broadband increase in coupling at low frequencies (below approximately 400 Hz), with coherence magnitudes of about 0.3 near the leading edge and 0.2–0.3 across the mid-chord stations. This behaviour reflects the generation of large-scale, slowly varying flow structures caused by excessive momentum injection. These structures maintain partial coherence with the trailing-edge surface pressure, especially in the lower frequency range associated with the low-frequency hump observed earlier in the far-field spectra.

The pressure-side results (panels b, d, f, and h) exhibit similar global trends but with distinct chordwise evolution. In the baseline configuration, the coherence at $x/c = 0.03$ shows two narrow peaks at approximately 600 and 700 Hz, with magnitudes around 0.3. These features weaken slightly at $x/c = 0.25$ and reappear at $x/c = 0.50$ as multiple tones spanning 300–1300 Hz, reaching values near 0.4. The coherence intensifies further at $x/c = 0.75$, where the tonal coupling becomes dominant with a maximum approaching 0.9. This progression indicates that hydrodynamic disturbances along the pressure surface increasingly contribute to the surface pressure near the trailing edge, reinforcing the feedback responsible for tonal noise generation. For the high-blowing case, a broadband low-frequency coherence develops again, beginning at approximately 0.15 at $x/c = 0.03$ and growing steadily downstream, reaching 0.45 near the trailing edge. This increase suggests that excessive actuation amplifies large-scale fluctuations that remain correlated with the surface pressure, particularly on the lower surface where the local flow is more susceptible to jet-induced instabilities. The low-blowing condition, as before, exhibits almost no coherent activity across the frequency range, confirming that it effectively disrupts both tonal and low-frequency coupling mechanisms.

Overall, these results reinforce the distinct influence of the leading-edge blowing rate on the hydrodynamic–wall pressure interaction. The baseline configuration shows strong narrowband coherence at the trailing edge, consistent with the tonal feedback process. The low-blowing case ($U_j/U_\infty = 0.35$) suppresses this interaction entirely, while the high-blowing case ($U_j/U_\infty = 3.86$) replaces it with a broadband coupling associated with large-scale low-frequency motions. The similarity of the low-frequency behaviour between the suction and pressure sides indicates that these motions likely originate from a global flow instability introduced by excessive actuation, which perturbs the wake and trailing-edge pressure field simultaneously. Together, the $\gamma_{u,p_{\mathrm{wall}}}$ results complement the far-field coherence findings by clarifying how local velocity fluctuations contribute to surface pressure dynamics, thereby bridging the link between near-wall hydrodynamics and acoustic radiation.

4.6 Summary and Conclusions

This chapter has examined the physical mechanisms underlying the suppression of trailing-edge tonal noise through leading-edge blowing. The investigation combined far-field acoustic measurements, surface-pressure spectra, time-resolved velocity data, and coherence analyses to establish how the blowing modifies the laminar separation bubble, alters wake topology, and weakens the aeroacoustic feedback loop responsible for tone generation. The discussion below summarises the principal findings and their physical implications. The identification of an "optimal" actuation level in this chapter does not rely on a single diagnostic. The same trend is observed consistently across (i) the far-field spectra, (ii) the surface-pressure response and its coherence with the far-field, and (iii) the velocity-based coherence maps that localise and then suppress the narrowband coupling responsible for the baseline tone. Together, these independent observables support the interpretation that low-level blowing reduces the effective tonal feedback, whereas excessive blowing suppresses the discrete tone but promotes broadband low-frequency unsteadiness.

- **Acoustic response:** The far-field spectra demonstrated that a low blowing rate ($U_j/U_\infty = 0.35$) consistently removed the discrete tonal peaks characteristic of the baseline flow without detuning the dominant frequency, indicating that the underlying feedback loop was preserved but stabilised. In contrast, a high blowing rate ($U_j/U_\infty = 3.86$) eliminated the tones but introduced broadband amplification at low frequencies, showing that excessive momentum injection replaced coherent feedback with large-scale unsteadiness.

- **Flow-field modification:** Time-averaged vorticity maps revealed that the baseline flow was dominated by alternating streamwise vorticity structures near the trailing edge, consistent with shear-layer roll-up from the suction-side laminar separation bubble. Low blowing disrupted these structures, yielding a more diffuse and symmetric wake, while high blowing thickened the wake and promoted large-scale vortical activity. Quantitative metrics supported these observations: the wake symmetry index became more balanced and the normalised vorticity thickness increased with blowing rate, confirming enhanced mixing and flow distortion.

- **Leading-edge entrainment:** Turbulence-intensity measurements near the leading edge showed that the blowing jets primarily entrain flow along the pressure surface but induce a weaker secondary motion on the suction side. The presence of entrainment on both sides explains the observed tonal suppression at $\alpha = 6.7^\circ$ despite the nominally pressure-side orientation of the jets. The low-rate actuation therefore perturbs both boundary layers sufficiently to disrupt the feedback loop without introducing large-scale instability.

- **Hydrodynamic–acoustic coherence:** The coherence between velocity and far-field pressure ($\gamma_{u,p_{\mathrm{ff}}}$) confirmed that tonal noise arises from highly coherent interactions localised near the trailing edge. Low blowing reduced this coherence to values below 0.1 across all

frequencies, while high blowing replaced it with a broad low-frequency coupling. The coherence between velocity and surface pressure ($\gamma_{u,p_{\mathrm{wall}}}$), with the surface tap fixed at $x/c = 0.75$, provided complementary evidence: the baseline flow showed strong narrowband coherence near $1200\ \mathrm{Hz}$, corresponding to the tonal feedback, whereas low blowing suppressed this link and high blowing produced a broadband low-frequency response associated with wake-scale motions.

- **Overall mechanism:** The collective results support the interpretation that low-rate leading-edge blowing weakens the laminar separation-bubble-driven instability and reduces the phase-locked coherence between the unsteady shear layer and the trailing-edge acoustic field, thereby reducing the effective feedback required to sustain tonal radiation. At higher actuation levels, the tonal pathway is suppressed but replaced by large-scale unsteadiness that enhances low-frequency broadband noise.

In summary, the leading-edge blowing modifies both the aerodynamic and aeroacoustic characteristics of the airfoil in a strongly coupled manner. The optimal condition ($U_j/U_\infty = 0.35$) suppresses tonal radiation by diminishing hydrodynamic–acoustic coherence without destabilising the mean flow, whereas over-blowing ($U_j/U_\infty = 3.86$) destroys the organised feedback only to replace it with large-scale unsteady motion. These results collectively define the aerodynamic and acoustic signatures of effective tonal noise control. The next chapter extends this analysis to the post-stall regime, where large-scale separation and lift recovery become dominant in determining the aerodynamic–acoustic performance.

Chapter 5

Influence of Leading-edge Blowing on Leading Edge Broadband Noise

5.1 Introduction

Leading-edge turbulence interaction noise is a principal broadband component of airfoil self-noise at low to moderate Reynolds numbers. It arises when oncoming turbulent gusts convect toward the stagnation region and are scattered by the leading edge into acoustic waves. Because this mechanism persists across a wide operating envelope and couples strongly to the spanwise organization of the inflow, it is a critical target for noise reduction in fans, rotors, and wind turbines [54, 11, 22, 30].

This chapter examines steady leading-edge blowing as an active control strategy for reducing broadband radiation. The working premise is that blowing can disrupt the spanwise coherence of incoming structures at the leading edge and thereby weaken the efficiency of gust-to-sound conversion. In practical terms, the quantity of interest is the spanwise coherence length at the leading edge, and the question is whether changes in this length correlate with band-limited reductions in far-field sound more strongly than do changes in intensity or convective speed.

5.2 Methodology and Setup

Figure 5.1 shows the anisotropic (rod–airfoil) arrangement used for the flow and acoustic measurements. A cylindrical rod of diameter $D \in \{10, 15, 20\}\,\mathrm{mm}$ is mounted on the nozzle centreline upstream of the airfoil; the airfoil incorporates a leading-edge blowing manifold and orifices. Two rigid side plates span the jet to suppress lateral entrainment and to carry precision rails referenced to the nozzle lip. The key design choice is to *fix the rod* in space and to set the streamwise spacing x/D by *translating the airfoil* along the rails while holding the geometric angle of attack at 0°.

This choice maximises repeatability of the inflow for a given D: keeping the rod fixed on the jet centreline preserves its proximity to the nozzle potential core, the local shear-layer topology and

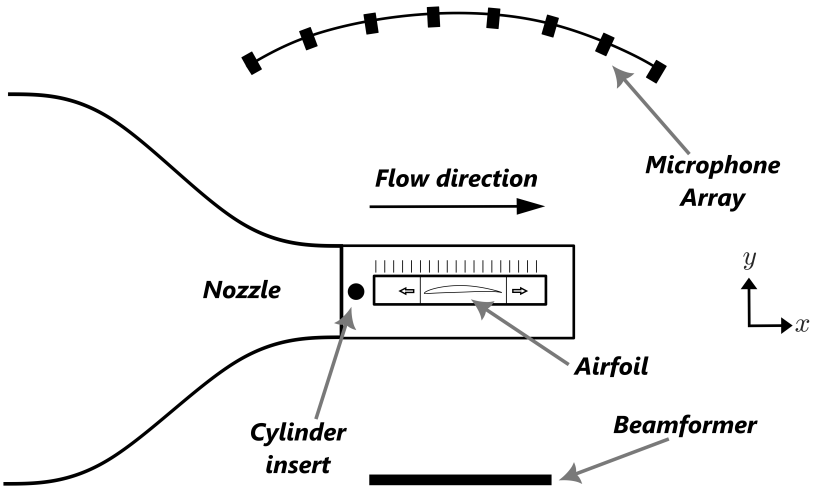

Figure 5.1: Schematic of airfoil and nozzle setup

wall interference, the effective blockage, and the support geometry. In turn, the Strouhal shedding and near-wake statistics at the airfoil station vary primarily with x/D, not with incidental changes to rod alignment or boundary conditions. Practically, the same translation mechanism guarantees that (i) the airfoil's leading-edge apex remains co-planar with the side-plate datum, (ii) the blowing orifices retain a fixed orientation relative to the oncoming wake, and (iii) the measurement coordinate system tied to the side plates is preserved across all x/D.

Together, the nozzle-centred, fixed-rod configuration with streamwise airfoil translation yields a clean parametric variation of x/D with minimal confounding changes in inflow or rig geometry, which is essential for attributing differences in coherence, correlation, and radiated noise to the spacing itself.

Figure 5.2 sketches the cross–correlation mapping used for the anisotropic rod–airfoil case throughout this section. A single hot–wire probe is fixed just upstream of the leading–edge apex, slightly offset in the span to lie adjacent to a blowing orifice; this *reference* sensor provides a continuous time history representative of the inflow encountered at the stagnation region. A second, identical *traversing* probe samples a rectilinear grid in a plane normal to the airfoil chord that spans across two neighbouring orifices in the spanwise direction and extends a short distance upstream in the streamwise direction. The grid spacing is refined in the vicinity of the reference probe to resolve strong gradients in correlation and coherence near the impingement line. At each node, the two probes acquire simultaneous time series, enabling the computation of cross–spectra and magnitude–squared coherence, as well as band-limited and full-band cross-correlations as functions of spatial offset and time lag. This configuration is used for all flow measurements presented in this chapter for the anisotropic inflow, providing a consistent basis to relate jet-induced changes in local turbulence organisation to the observed reductions in leading-edge noise.

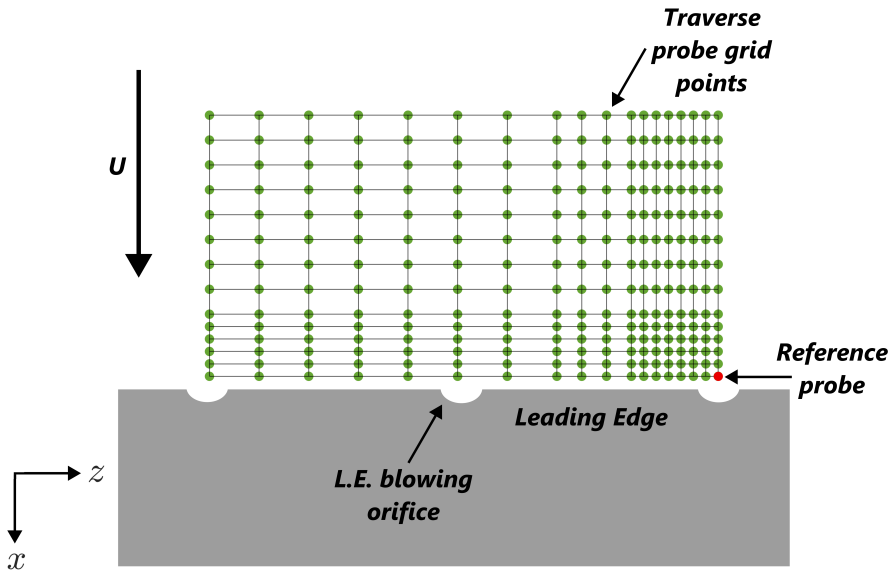

Figure 5.2: Schematic of cross correlation study

5.3 Isotropic Inflow Conditions

The first step in evaluating the efficacy of leading-edge blowing is to establish its behaviour in an inflow that is as homogeneous and directionally unbiased as the facility allows. In this chapter, 'isotropic' is used in the practical experimental sense of a grid-generated, weakly anisotropic inflow without strong coherent wake structures, rather than strict component-wise isotropy. In such conditions, the incident eddies convect toward the leading edge with negligible preferential orientation, and their spanwise correlation is governed mainly by the grid geometry and downstream decay rather than by coherent wake structures. This removes anisotropy and vortex-shedding tones that would otherwise blur the causal link between the actuation and the acoustic response. By starting here, we can determine whether steady injection near the leading edge achieves the intended outcome in its simplest form: a measurable reduction in the spanwise coherence of the incoming fluctuations at the leading edge and a corresponding decrease in band-limited far-field levels. The isotropic cases therefore serve both as a mechanism check and as a baseline against which the more complex rod–airfoil conditions can be interpreted.

Within this section, the analysis is organised to isolate the actuation pathway while keeping the number of moving parts to a minimum. We first document the inflow delivered by each grid at the leading-edge station. We then quantify the acoustic response to blowing across momentum ratios and angles of attack, and relate the observed reductions to changes in near-edge spanwise organisation rather than to intensity alone. Finally, we extract compact indicators that will carry forward into the anisotropic study, including a scale-matching measure between the inflow spanwise length and the orifice layout, and a practical threshold for the onset of control effectiveness.

5.3.1 Inflow Characterisation

To establish a clean reference for the effect of leading-edge blowing, we begin with isotropic-like turbulence generated by square-mesh grids mounted upstream of the nozzle exit. Figure 5.3 defines the two geometric parameters that will be used consistently in what follows. The symbol d denotes the in-plane bar width of the grid members, that is, the projected thickness of each orthogonal strip that determines the local blockage and sets the initial wake thickness downstream. The symbol M denotes the mesh size, taken as the centre-to-centre spacing between adjacent bars in either orthogonal direction. For completeness, the clear opening is $M-d$ and the geometric solidity (blockage fraction) is

$$\sigma \;=\; 1-\left(1-\frac{d}{M}\right)^{2},$$

which is 1 minus the open-area fraction for a square mesh.

A deliberate feature of the present grid set is that *all four grids have the same solidity*, $\sigma = 0.0625$, while (d, M) vary across designs. Holding σ fixed removes blockage as a confounding variable and keeps the mean-flow pressure drop and global contraction effects comparable across grids. By varying M (and therefore d at constant d/M), we change the mesh Reynolds number $Re_M = U_\infty M/\nu$ and the characteristic production and integral scales of the turbulence convecting to the leading-edge station. In this way the data isolate *scale effects* of the inflow on blowing performance at essentially constant blockage.

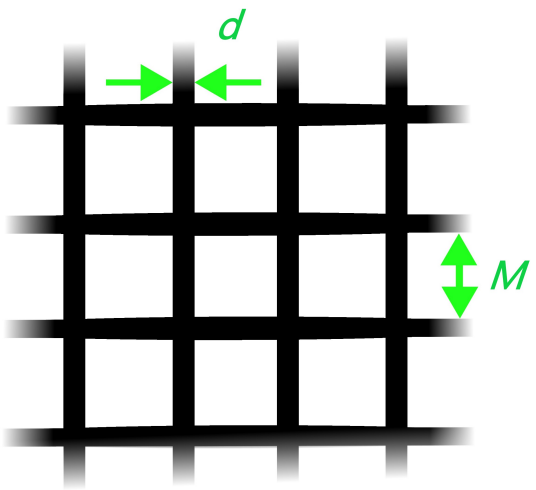

Figure 5.3: Schematic definition of grid geometry. d is the in-plane bar width and M is the centre-to-centre mesh spacing. The solidity is $\sigma = 1-(1-d/M)^2$. All four grids used here have identical solidity $\sigma = 0.0625$, while (d, M) are varied to tune inflow scales at fixed blockage.

The remainder of this subsection documents the inflow delivered by each grid at the airfoil leading-edge location without conflating actuation effects. First, the grids are introduced with

their (d, M) values and derived parameters. Second, we report the streamwise evolution of key inflow statistics at the measurement plane that coincides with the airfoil leading edge. Figure 5.4 presents the results in a two-panel tiled layout: panel (a) shows the centerline turbulence intensity $u_{\mathrm{rms}}/U_\infty$ as a function of the normalized streamwise coordinate x/c, and panel (b) shows the corresponding streamwise integral length L_x along the same axis. Both panels are evaluated on the tunnel centerline in the spanwise and vertical directions, so differences across grids reflect changes in inflow scale and intensity rather than lateral non-uniformity. Vertical reference lines at $x/D_h = 0$ and $x/D_h = 1$ indicate the leading-edge station and one chord length downstream.

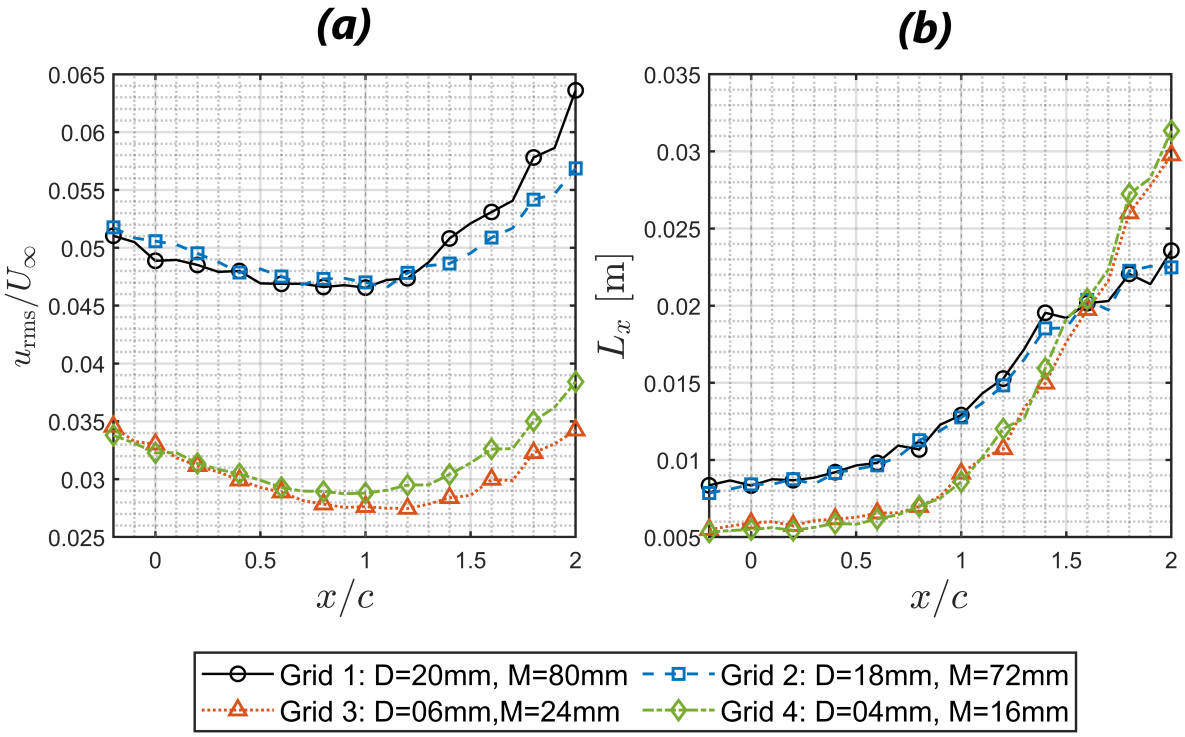

Figure 5.4: Isotropic inflow statistics along the centerline. **(a)** Turbulence intensity $u_{\mathrm{rms}}/U_\infty$ versus x/c. **(b)** Streamwise integral length L_x versus x/c. All four grids share solidity $\sigma = 0.0625$.

Panel (a) shows that the larger-mesh grids (Grid 1: $M = 80$ mm; Grid 2: $M = 72$ mm) generate higher centerline turbulence intensity than the smaller-mesh grids (Grid 3: $M = 24$ mm; Grid 4: $M = 16$ mm) under the same solidity. Near the virtual leading-edge plane ($x/c \approx 0$), Grids 1 and 2 give $u_{\mathrm{rms}}/U_\infty \approx 0.052$, whereas Grids 3 and 4 start near 0.034. All grids follow a similar evolution with x/c: the intensity decreases to a minimum around $x/c \approx 1$ and then increases toward $x/c = 2$. Quantitatively, Grids 1 and 2 drop to ≈ 0.047 by $x/c \approx 1$ and then rise to ≈ 0.064 and ≈ 0.057, respectively, by $x/c = 2$. Grids 3 and 4 decrease from ≈ 0.034 to ≈ 0.028 at $x/c \approx 1$, then rise to ≈ 0.034 and ≈ 0.038 by $x/c = 2$. Since the airfoil is absent in these measurements, the observed dip-and-rise is a property of the grid-generated inflow and facility development along

the centerline, and it is recorded here as part of the baseline that will be used for subsequent comparisons.

Panel (b) reports the streamwise integral length L_x computed from single-point autocorrelation and Taylor's hypothesis. All grids begin with small values near $x/c \approx 0$ and increase with x/c, consistent with a growing streamwise correlation scale along the measurement line. Grids 1 and 2 start at $L_x \approx 8.0 \times 10^{-3}$ m and increase to $\approx 23 \times 10^{-3}$ m. Grids 3 and 4 start lower, near 5.0×10^{-3} m, but grow more rapidly and reach $\approx 31 \times 10^{-3}$ m by $x/c = 2$. Around $x/c \approx 1.4$, Grids 1 and 2 show a reduction in growth rate, while Grids 3 and 4 continue to increase and achieve the largest L_x values (up to $\approx 31 \times 10^{-3}$ m). These differences reflect how varying mesh size at fixed solidity sets distinct initial conditions for integral scales and their subsequent evolution along the centerline in the empty-facility configuration.

For later use, two points are essential. First, the larger-mesh pair (Grids 1–2) supplies a higher-intensity inflow at the virtual leading-edge plane, while the smaller-mesh pair (Grids 3–4) provides lower intensity but achieves larger L_x downstream. Second, despite identical solidity, the different (d, M) choices produce distinct combinations of intensity level and streamwise correlation scale. This spread will be used to test whether blowing performance correlates more strongly with intensity changes or with changes in the organization of incoming structures when the airfoil is installed.

To complement the centreline trends of $u_{\mathrm{rms}}/U_\infty$ and L_x, we now examine the inflow spectra at the leading-edge station for each grid. Figure 5.5 presents the one-sided streamwise velocity power spectral density $\Phi_{uu}(f)$ together with a von Kármán longitudinal reference that is parameterised by the measured fluctuation level σ (with $\sigma^2 = \overline{u'^2}$ for $u'(t) = U(t) - \overline{U}$), the local streamwise integral length L_x, and a convection speed U_c. The comparison uses the standard one-dimensional von Kármán form mapped to frequency under Taylor's hypothesis,

$$S_u(f) \;=\; \frac{4\,\sigma^2\,L_x/U_c}{\left(1 + 70.8\,[f\,L_x/U_c]^2\right)^{5/6}},$$

which is the canonical model for homogeneous, isotropic grid turbulence in frequency space [88, 89]. Agreement in level and spectral shape indicates that the grid-generated inflow is consistent with isotropic-like grid turbulence at the leading-edge plane over the resolved frequency band. Here, 'isotropic-like' refers to the streamwise (longitudinal) statistics inferred from single-component hot-wire spectra; full isotropy and spatial homogeneity across all velocity components are not asserted. This provides a basis for the incident energy distribution and the location of the energy-containing range for each (d, M) case, providing a spectral baseline for interpreting the effects of leading-edge blowing in the sections that follow [4, 35].

Figure 5.5 shows that the measured one-sided velocity spectra conform closely to their von Kármán references for all four grids, indicating an isotropic-like inflow in the longitudinal spectral sense at the leading-edge plane over the resolved band. Panels (a) and (b) sit higher in spectral level than (c) and (d), consistent with their larger fluctuation amplitudes: Grid 1 and Grid 2 have

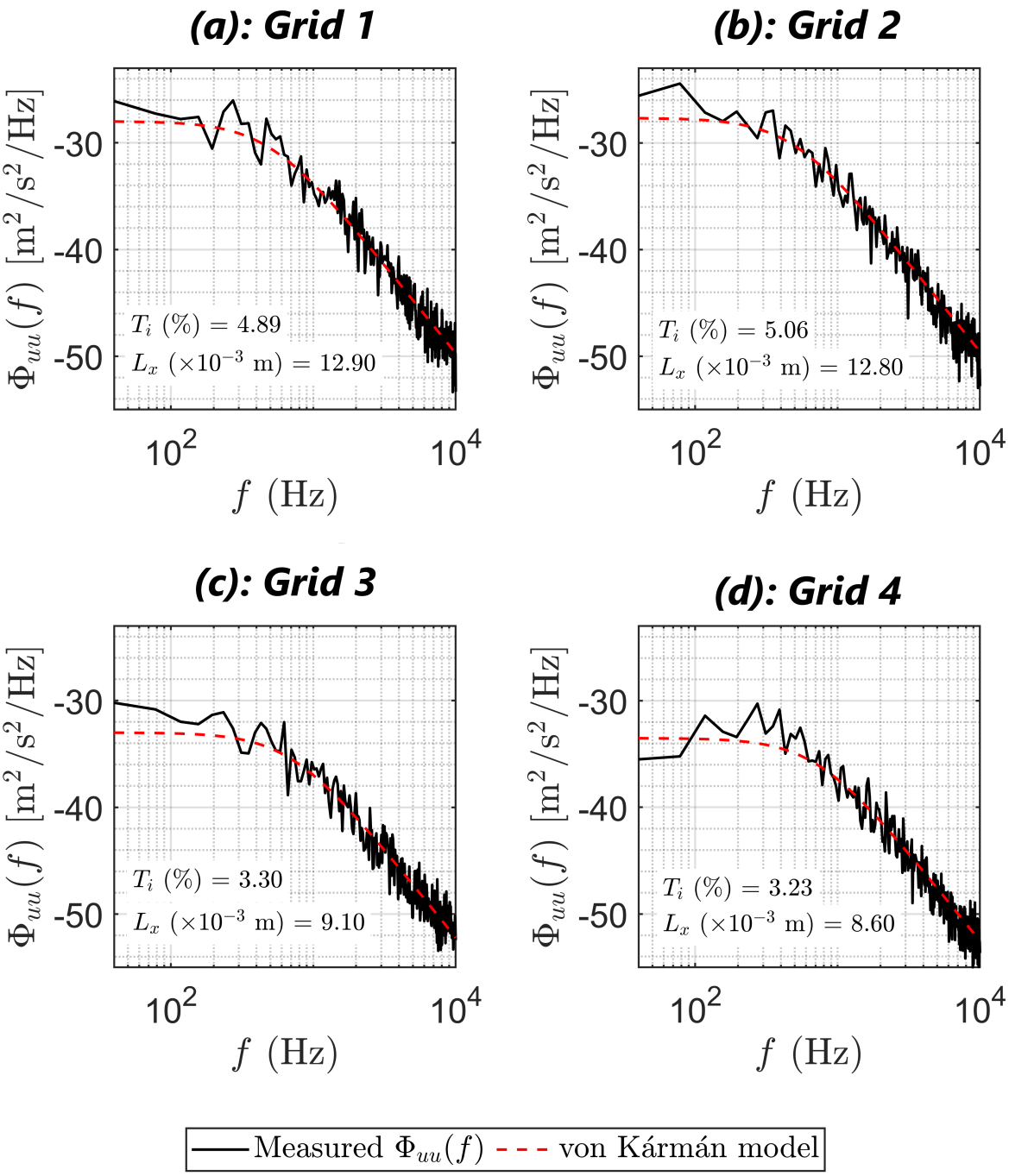

Figure 5.5: Inflow spectra at the leading-edge plane ($x/c = 0$). One-sided streamwise velocity PSD $\Phi_{uu}(f)$ (solid) with von Kármán longitudinal model (dashed) parameterised by measured σ, L_x.

$T_i = 4.89\%$ and 5.06%, whereas Grid 3 and Grid 4 have $T_i = 3.30\%$ and 3.23%. Because the von Kármán model scales in amplitude with σ^2, higher σ yields uniformly elevated spectra in (a)–(b).

The roll-off placement follows the nondimensional group fL_x/U_c: larger streamwise integral scales for Grids 1–2 ($L_x = 12.9,\ 12.8 \times 10^{-3}\,\mathrm{m}$) shift the spectral knee to lower frequency compared with Grids 3–4 ($L_x = 9.1,\ 8.6 \times 10^{-3}\,\mathrm{m}$). In combination, these metrics establish that Grids 1–2 deliver a stronger, slightly larger-scale inflow than Grids 3–4. This spectral baseline complements the centreline trends of $u_{\mathrm{rms}}/U_\infty$ and L_x and fixes the incident energy distribution that will be available for leading-edge scattering in subsequent blowing analyses.

In summary, the inflow measurements establish a clear and internally consistent picture of the turbulence delivered by the four grids at the leading-edge plane. Centreline trends showed that Grids 1–2 carry higher incident energy and slightly larger integral scales than Grids 3–4, and the spectral analysis in Figure 5.5 confirmed that each case is well described by a von Kármán parameterisation using the locally measured σ, L_x, and U_c. The higher levels in grids 1-2 follow from larger σ and T_i, while the lower spectral knees reflect the larger L_x of those grids. Conversely, grids 3-4 exhibit reduced amplitude and a knee shifted to higher frequency, consistent with smaller integral scales. Together with the previously reported streamwise development, these results fix both the intensity and the scale distribution of the turbulence that impinges on the airfoil.

This baseline is the reference against which blowing effects will be judged. In the next subsection, we quantify how steady leading-edge blowing modifies the acoustic response across operating conditions by mapping broadband noise reductions over blowing strength and angle of attack.

5.3.2 Leading-Edge Blowing: Performance Maps

With the inflow statistics fixed at the leading-edge plane, we now quantify how steady leading-edge blowing alters the radiated sound across operating points. This subsection introduces *performance maps* that compare power-weighted level (PWL) spectra with blowing against their corresponding baselines at identical conditions. The metric is reported as *baseline minus blowing*, so positive values denote noise reduction at that frequency. For compact presentation we also form band-limited and overall levels that retain the same sign convention. Blowing input is parameterised by the jet-to-free-stream velocity ratio U_j/U_∞, and the response is mapped over $(U_j/U_\infty, \alpha, U_\infty)$ at fixed geometry.

5.3.2.1 Effect of Angle of Attack

To isolate the effect of incidence, a single reference free-stream speed of $U_\infty = 30\ \mathrm{m\,s^{-1}}$ is used for the angle-of-attack study. All angles reported here are *corrected* according to the procedure described in Chapter 3, Section 3.13, so that comparisons across blowing levels reflect aerodynamic incidence rather than fixture or blockage bias. We begin with the *effect of angle of attack* at $U_\infty = 30\ \mathrm{m\,s^{-1}}$, then extend to speed dependence and cross-grid comparisons.

Before examining the blowing-induced changes, it is useful to establish the baseline acoustic response at the same operating conditions. Figure 5.6 therefore presents the baseline PWL

spectra for the four grids at the three angles of attack used throughout the present angle-of-attack study. These baseline spectra provide the reference state against which the subsequent performance maps are formed.

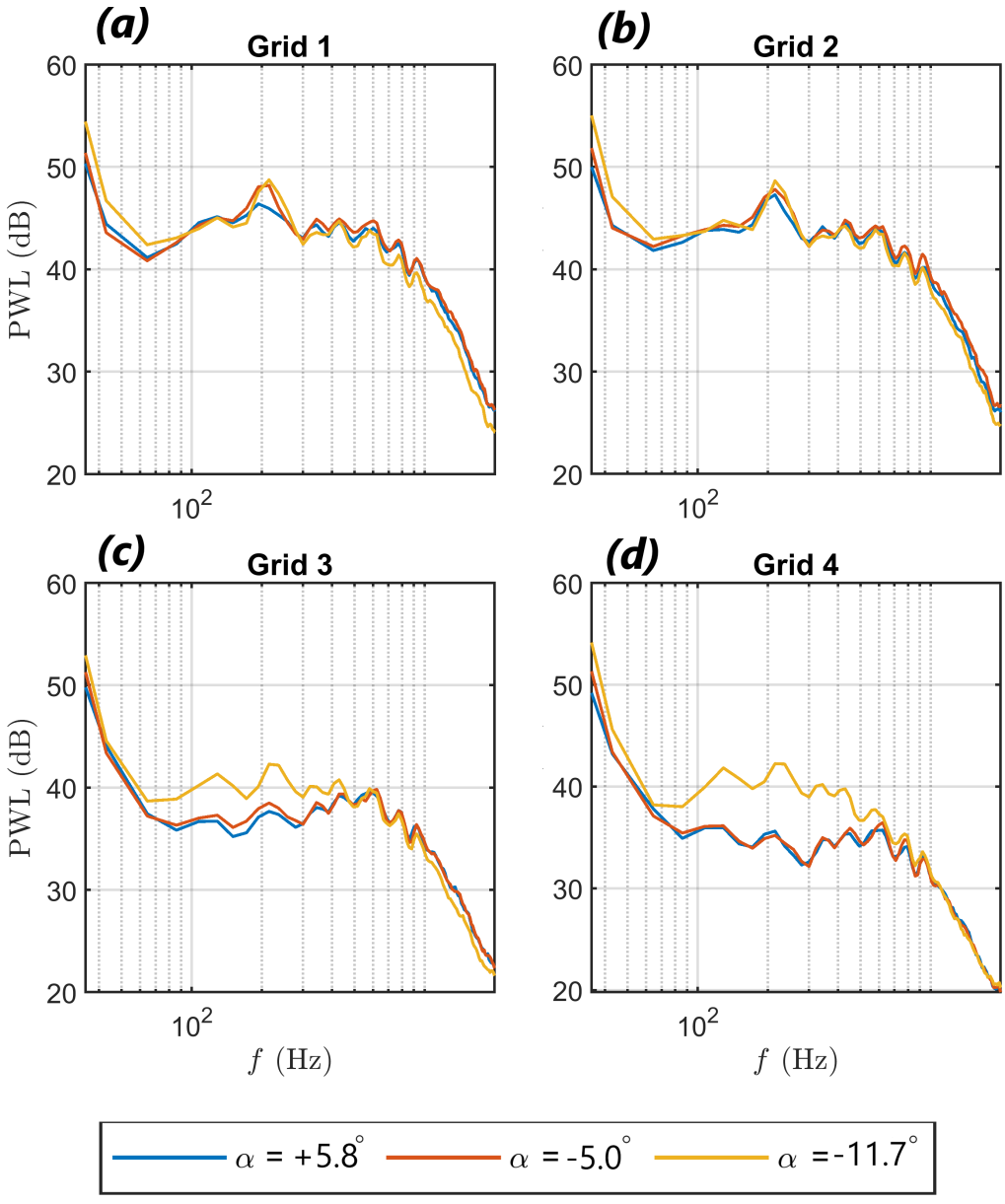

Figure 5.6: Baseline PWL spectra at $U_\infty = 30\ \mathrm{m\,s^{-1}}$ for the angle-of-attack study. Panels (a)–(d) correspond to Grids 1–4, respectively. In each panel, the baseline spectra are shown for the three corrected incidences ($\alpha = +5.8°, -5.0°, -11.7°$) used in the subsequent leading-edge blowing performance maps.

Figure 5.6 shows that the baseline radiated spectrum already depends on both grid and in-

cidence before actuation is introduced. Across the four grids, the spectra at negative incidence generally exhibit stronger low-frequency content than those at positive incidence, indicating that the unforced leading-edge interaction is itself sensitive to the incoming turbulence characteristics and to the aerodynamic orientation of the airfoil. These baseline differences are important because the contour maps discussed next represent reductions relative to these corresponding unforced cases, rather than absolute sound levels.

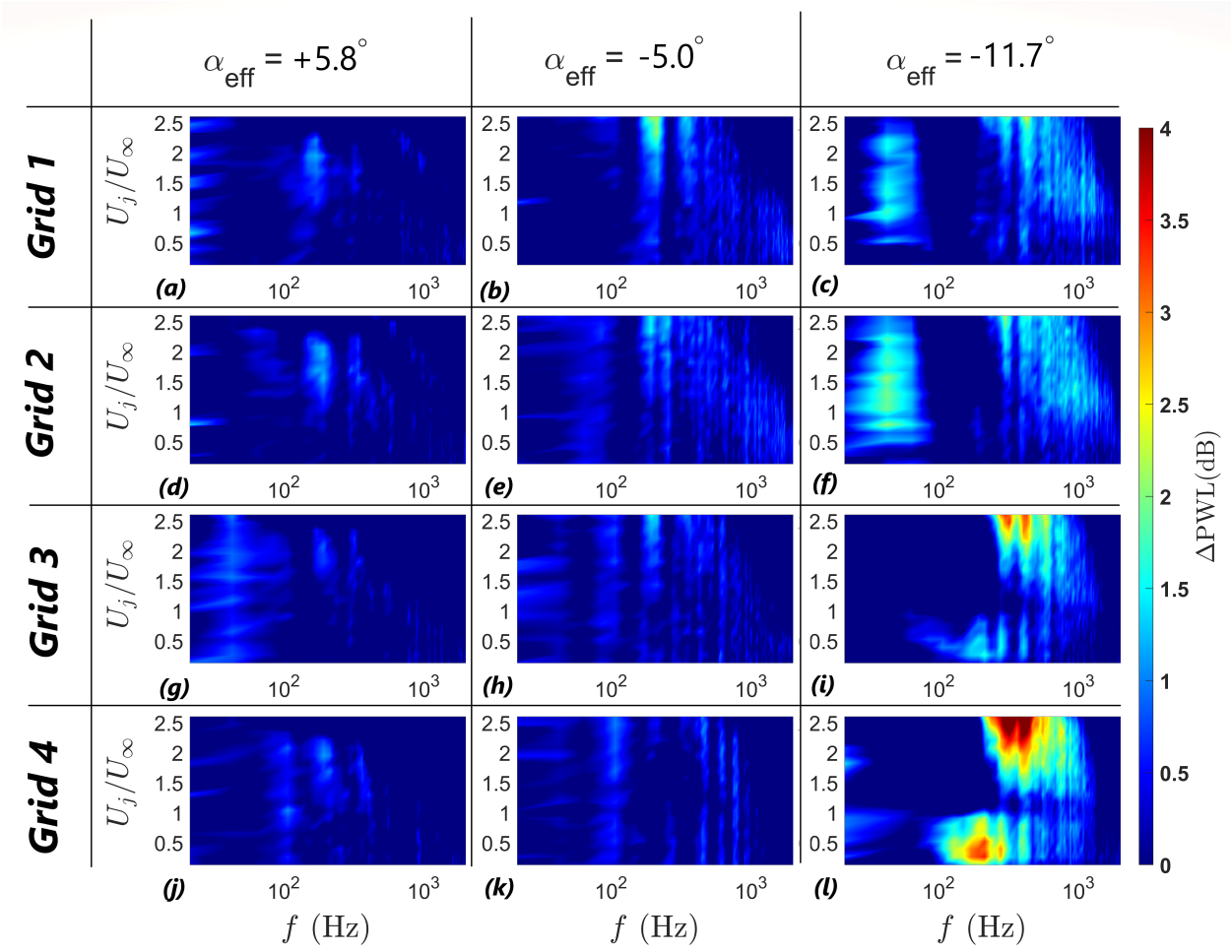

Figure 5.7: Leading-edge blowing performance maps at $U_\infty = 30\ \mathrm{m\,s^{-1}}$. Colour indicates baseline-minus-blowing $\Delta\mathrm{PWL}(f)$ relative to the corresponding baseline spectra in Figure 5.6; positive values denote noise reduction. Columns vary corrected angle of attack: +5.8°, -5.0°, and -11.7°. Rows vary grid (Grid 1–4).

Relative to the corresponding baseline spectra in Figure 5.6, Figure 5.7 summarises the effect of steady leading-edge blowing on the PWL spectrum at the reference speed $U_\infty = 30\ \mathrm{m\,s^{-1}}$ for the three corrected incidences ($+5.8°$, $-5.0°$, $-11.7°$); panel labels identify grid and angle. A clear incidence bias emerges: the largest broadband benefits occur at negative incidence, with modest or negligible changes at positive incidence. At $\alpha = +5.8°$ [Grid 1, panel (a); Grid 2; Grid 3; Grid 4] the maps show minimal reduction, with isolated improvements of up to $\approx 0.7\ \mathrm{dB}$ confined to

100–200 Hz. Reductions strengthen at $\alpha = -5.0°$ [Grid 1, panel (b), and counterparts for the other grids], where the maximum occurs for Grid 1 in the 150–250 Hz band and increases systematically with the jet-to-free-stream ratio U_j/U_∞ up to ≈ 1.5 dB.

The strongest response is obtained at $\alpha = -11.7°$. For Grids 1 and 2 [panels (c) and the corresponding map for Grid 2], broad regions of reduction appear in the low-frequency band 20–100 Hz, with a wide range of U_j/U_∞ remaining effective and peak reductions up to ≈ 2 dB for Grid 2. Additional improvements emerge at higher frequencies (above 200 Hz), where increasing U_j/U_∞ yields progressively larger gains. Grid 3 exhibits a similar high-frequency behaviour without the low-frequency reduction: the dominant improvements lie above ~ 200 Hz and reach ≈ 3.25 dB, again strengthening with U_j/U_∞. Grid 4 shows a distinct two-band pattern at $\alpha = -11.7°$: a lower-frequency window (100–300 Hz) where moderate blowing performs best and higher blowing offers diminishing returns (effective up to $U_j/U_\infty \approx 1.0$, with peaks near 3.5 dB); and a higher-frequency window (~ 250–800 Hz) where greater U_j/U_∞ produces larger benefits down to $U_j/U_\infty \approx 1.3$, with maxima approaching 4 dB.

The incidence bias can be interpreted in terms of the expected leading-edge flow geometry. Although stagnation-point location is not measured directly here, changing α is expected to shift the stagnation region and modify the local streamline curvature near the leading edge. At negative incidence, this is consistent with the jets interacting more directly with the incoming disturbances in the vicinity of the stagnation region, promoting faster distortion of the largest structures and reducing their spanwise organisation before scattering. At positive incidence, the same interaction is expected to be weaker, which would naturally lead to smaller broadband benefits at $\alpha = +5.8°$.

These trends are consistent with the inflow characterisation. Grids 1–2 deliver higher fluctuation levels and larger streamwise scales at the leading-edge plane, so their reductions extend into lower frequencies where the energy-containing eddies are more prominent. Grid 3, with lower σ and smaller L_x, shows little change at the lowest frequencies and responds mainly at higher frequencies where its inflow spectrum carries more energy relative to the knee. Grid 4 combines the lowest σ and L_x with a two-regime response that depends on U_j/U_∞, suggesting different sensitivity of the low- and high-frequency bands to the imposed blowing level. Across all grids, the incidence bias toward $-11.7°$ is therefore consistent with blowing being most effective when the leading-edge geometry and stagnation-line placement favour strong jet–gust interaction and promote spanwise decoherence ahead of the leading-edge scattering.

To reconcile the angle-of-attack dependence with the speed study that follows, we isolate Grid 4 and examine its individual performance maps across a refined set of corrected incidences with emphasis on negative angles. Figure 5.8 assembles $\Delta\mathrm{PWL}$ (baseline minus blowing) for Grid 4 at $-11.7°$ and an additional negative setting $-13.5°$ to test whether further incidence bias enhances the broadband benefit. All angles are corrected using the procedure in Chapter 3 (Section AoA). Focusing on a single grid removes confounding differences in inflow level and streamwise scale, so changes in the maps can be interpreted primarily through the leading-edge flow geometry and jet–gust interaction at fixed inflow.

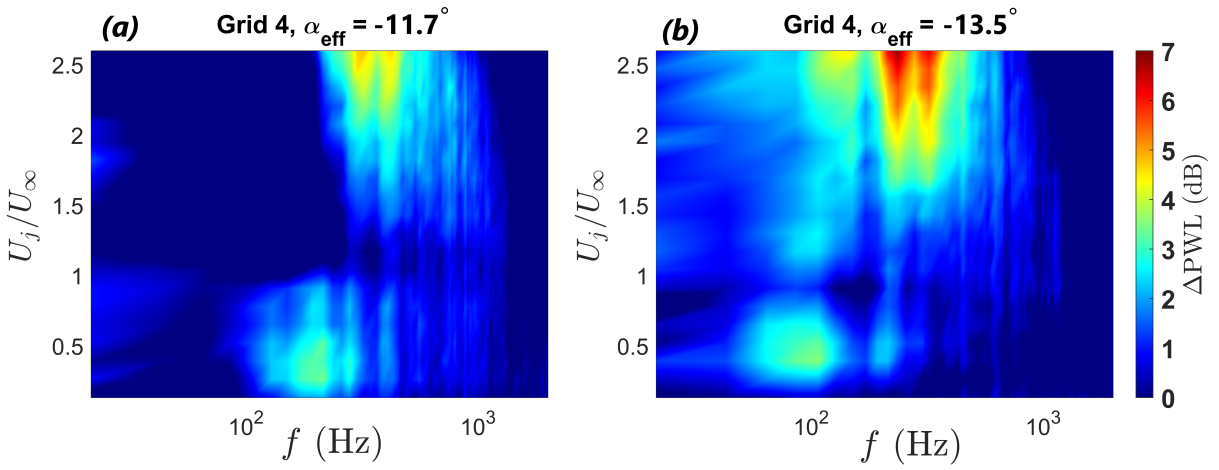

Figure 5.8: Leading-edge blowing performance maps at $U_\infty = 30\ \mathrm{m\,s^{-1}}$ for $\alpha = -11.7°$ and $\alpha = -13.5°$.

Figure 5.8. Panels (a) ($\alpha = -11.7°$) and (b) ($\alpha = -13.5°$) exhibit the characteristic $\Delta\mathrm{PWL}$ reduction ridge that strengthens with increasing jet ratio U_j/U_∞, reaffirming the previously noted secondary trend (larger blowing $\Rightarrow$ larger $\Delta\mathrm{PWL}$). At the more negative incidence, the reduction band expands both spectrally and in blowing range: the lower-frequency onset of the high-$\Delta\mathrm{PWL}$ region shifts down to ~ 100 Hz in (b), whereas in (a) the analogous feature is confined to $\gtrsim 200$ Hz. Furthermore, the $-13.5°$ case attains a peak reduction of ≈ 7 dB over ~ 200–350 Hz and sustains elevated $\Delta\mathrm{PWL}$ across a broader interval of U_j/U_∞, indicating a more robust and persistent control effect over operating conditions.

Collectively, these maps imply that increasing the negative angle of attack enhances blowing efficacy for Grid 4: the maximum $\Delta\mathrm{PWL}$ increases, its spectral onset moves to lower frequencies, and the usable envelope in $(f, U_j/U_\infty)$ widens. On this basis, we select **Grid 4,** $\alpha = -13.5°$ as the reference condition for the next section, where we examine the *flow-speed dependence* of the reduction patterns and assess how the frequency–jet–ratio envelope of $\Delta\mathrm{PWL}$ scales with U_∞.

5.3.2.2 Effect of Flow Speed

Building on the trends established in Figure 5.8, we now *fix* the incidence at the condition that delivered the strongest and most extensive reductions (**Grid 4,** $\alpha = -13.5°$) and examine how the control performance varies with free-stream speed. The goal is to quantify the sensitivity of the reduction envelope to U_∞ when the actuation input is parameterized by the jet ratio U_j/U_∞. Throughout, we retain the previous sign convention, defining $\Delta\mathrm{PWL}(f)$ as baseline minus blowing so that positive values denote a net noise reduction.

To enable cross-speed comparison, the datasets are plotted directly as functions of frequency f (Hz). For completeness, the same maps are shown with blowing specified both as absolute jet speed U_j (Figure 5.9) and as the non-dimensional jet ratio U_j/U_∞ (Figure 5.10), the latter being

used for the following interpretation since it isolates the effect of flow speed on the normalized actuation input. In this representation, we can distinguish three effects: (i) whether the *onset* of meaningful reduction (the lower boundary of the high-$\Delta\mathrm{PWL}$ band) shifts systematically with Reynolds number; (ii) whether the *bandwidth* of beneficial response in $(f,\, U_j/U_\infty)$ space broadens or narrows with speed; and (iii) how the *peak* reduction level scales as U_∞ increases.

The subsequent analysis uses these frequency-domain maps to compare multiple U_∞, quantify the scaling of the reduction envelope, and isolate any residual Reynolds-number trends that are not captured by simple convective considerations. This sets the stage for identifying speed-robust operating windows in $(f,\, U_j/U_\infty)$ that generalize the favorable behavior documented for Grid 4 at $\alpha = -13.5°$.

Figure 5.10. Panels (a)–(f) ($U_\infty = 10$ to $60\ \mathrm{m\,s^{-1}}$) reveal two distinct reduction regimes in $\Delta\mathrm{PWL}$ when viewed in frequency space. First, a *high-frequency* band (in the upper portion of the plotted spectrum) exhibits the strongest benefit at moderate speed: at $20\ \mathrm{m\,s^{-1}}$ the reduction peaks near $9\ \mathrm{dB}$, with a clear monotonic dependence on actuation level (larger $U_j/U_\infty \Rightarrow$ larger $\Delta\mathrm{PWL}$). The same pattern is present at $10\ \mathrm{m\,s^{-1}}$, albeit with a smaller maximum ($\sim 5.5\ \mathrm{dB}$). As speed increases beyond $20\ \mathrm{m\,s^{-1}}$, the peak within this high-frequency band diminishes gradually. Second, a *low-frequency* band (in the lower part of the spectrum) emerges and strengthens with U_∞, culminating at $60\ \mathrm{m\,s^{-1}}$ where reductions up to $\sim 4.5\ \mathrm{dB}$ occur even at relatively modest input ($U_j/U_\infty \approx 0.26$).

The contrasting trends suggest a speed-dependent shift in the dominant noise-producing dynamics and in how blowing interacts with them:

- **High-frequency band (strongest at low–moderate U_∞):** In this range, the reductions grow with U_j/U_∞, consistent with momentum injection modifying the near-leading-edge boundary layer and the local receptivity to incoming disturbances, thereby reducing the efficiency of gust–leading-edge scattering. As U_∞ increases, baseline boundary layers thin and convective time scales shorten; for a fixed non-dimensional input, the jets may penetrate and intermix less effectively relative to the evolving near-nose scales. This would naturally reduce control authority in the high-frequency band and explains the observed decay of peak $\Delta\mathrm{PWL}$ with speed.

- **Low-frequency band (emerges and strengthens with U_∞):** The growth of benefit at low frequency with increasing speed, and its occurrence at comparatively small U_j/U_∞, suggests that larger incoming structures contribute more strongly to the leading-edge interaction process as Re_c increases. A consistent interpretation, without invoking separation or tonal mechanisms, is that rising U_∞ increases the relative acoustic importance of these lower-frequency disturbances in the stagnation-region forcing. Modest blowing can then (i) reduce the spanwise coherence of the incident structures and (ii) shorten their effective interaction length at the leading edge through enhanced dephasing and near-nose mixing. Both effects reduce the efficiency of gust–leading-edge scattering in this lower-frequency band, enabling measurable $\Delta\mathrm{PWL}$ at relatively small actuation levels. Because these structures

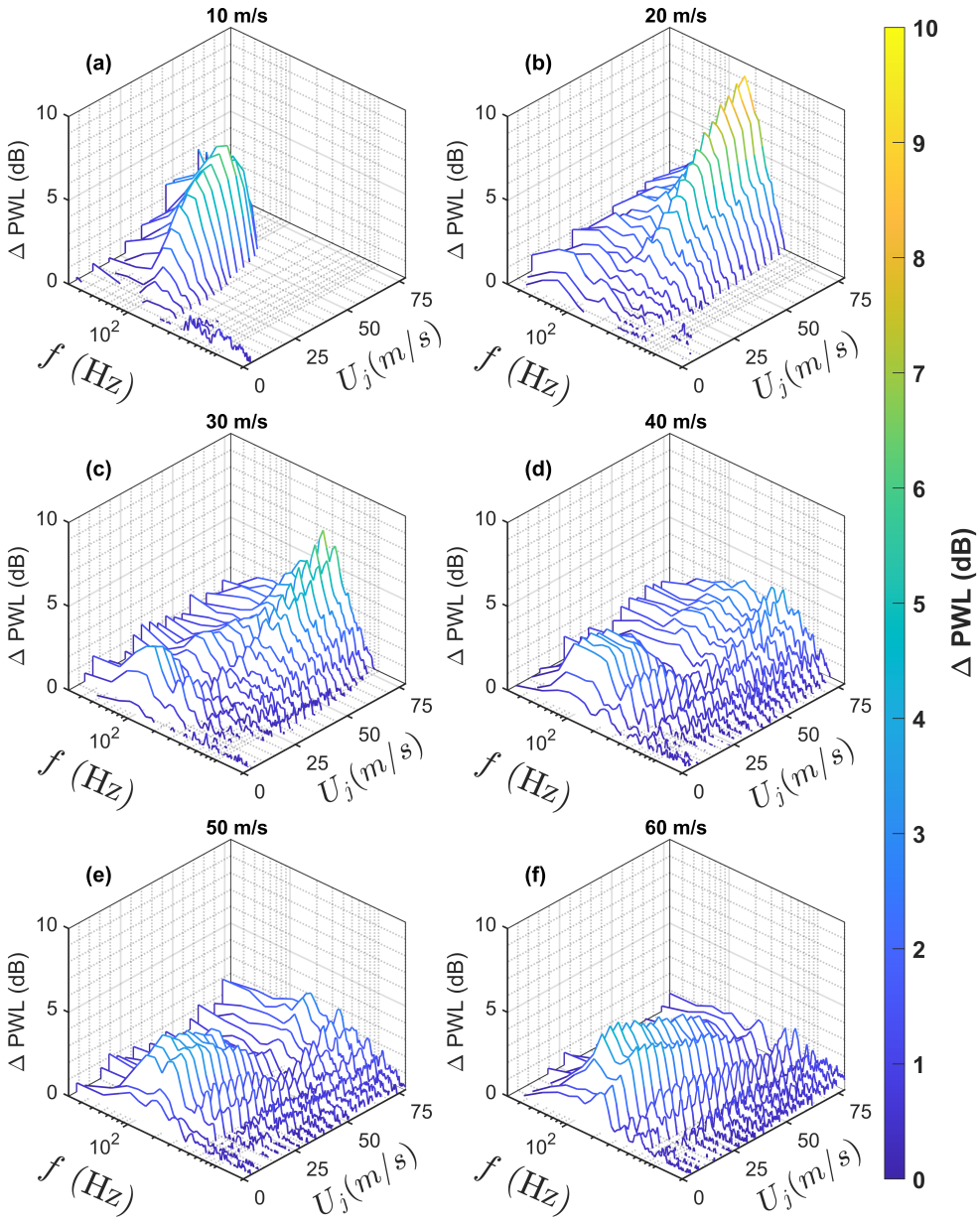

Figure 5.9: Waterfall plots of leading-edge blowing performance for isotropic turbulence–interaction noise. Curves show $\Delta\mathrm{PWL}(f)$ relative to the baseline; positive values indicate noise reduction. Panels (a–f) correspond to $U_\infty = \{10, 20, 30, 40, 50, 60\}\,\mathrm{m\,s^{-1}}$. Blowing rates expressed as jet speed $U_j\,(\mathrm{m\,s^{-1}})$.

are coherence-limited rather than resonance-driven, they can be sensitive to small changes in near-leading-edge organisation, consistent with the reductions observed at low U_j/U_∞.

Together, the maps indicate a crossover from a *high-frequency control-dominant* regime at low–moderate speeds to a *low-frequency control-amenable* regime at higher speeds. In the former, increasing actuation systematically boosts benefit, while in the latter, incremental actuation

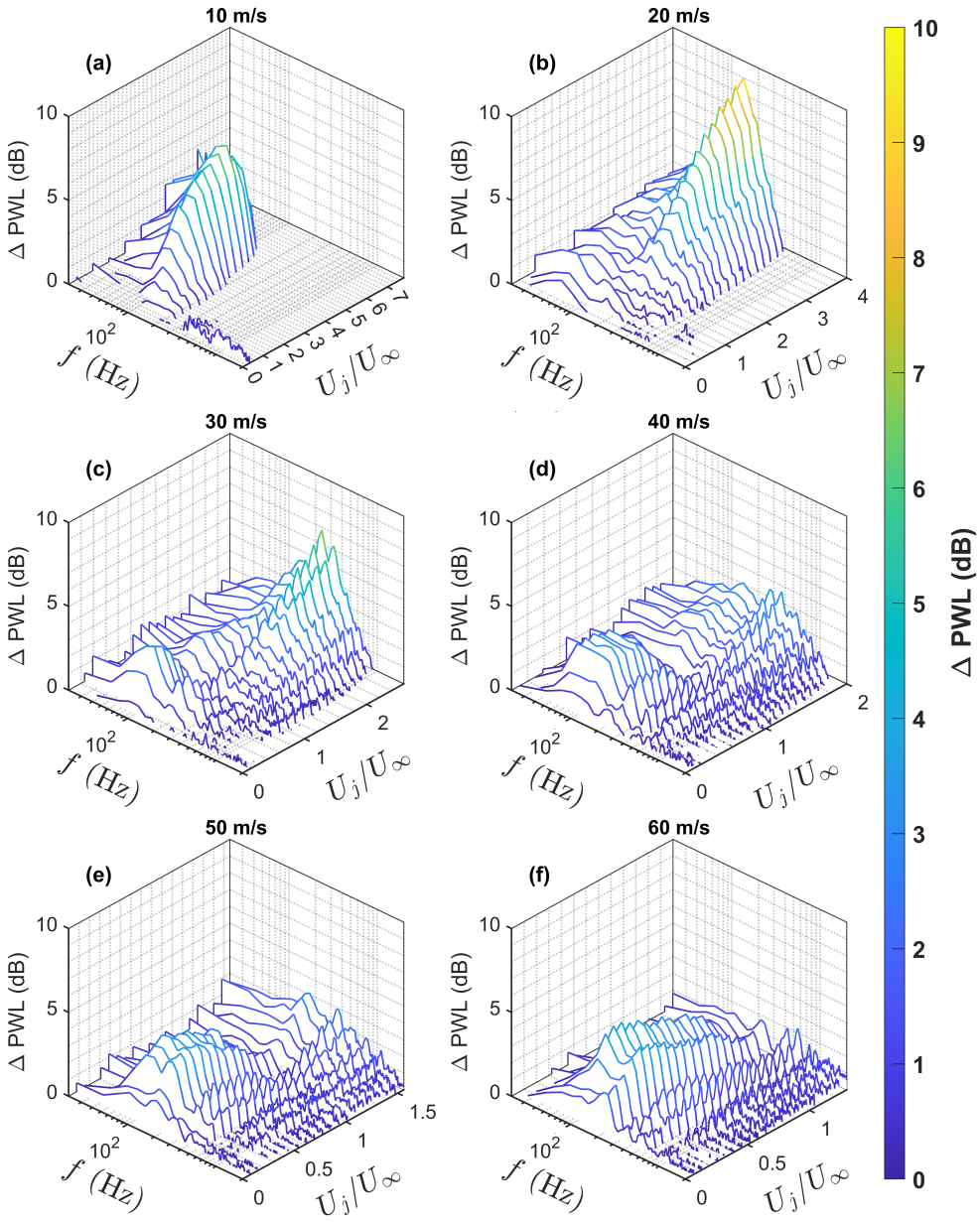

Figure 5.10: Waterfall plots of leading-edge blowing performance for isotropic turbulence–interaction noise. Curves show $\Delta\mathrm{PWL}(f)$ relative to the baseline; positive values indicate noise reduction. Panels (a–f) correspond to $U_\infty = \{10, 20, 30, 40, 50, 60\}\,\mathrm{m\,s^{-1}}$. Blowing rates expressed as jet speed ratio U_j/U_∞.

primarily targets larger structures and yields meaningful reductions without requiring high U_j/U_∞. The net outcome is (i) a tapering of the high-frequency peak with U_∞ and (ii) the emergence of a low-frequency benefit band that intensifies with speed. These explanations are offered as physically consistent interpretations of the observed performance maps; direct near-leading-edge boundary-layer measurements were not available in this campaign.

Practically, the results argue for speed-aware control scheduling: at low–moderate U_∞, prioritise higher U_j/U_∞ to suppress high-frequency content; at higher U_∞, modest input can be redirected to stabilise or de-tune the low-frequency pathway. In summary, *speed-dependent control physics* are evident: the high-frequency reductions are strongest at moderate U_∞ and scale with input, while a low-frequency mode becomes controllable as U_∞ increases, delivering meaningful benefit at modest jet ratios. This dual-regime behaviour provides a clear basis for tailoring the actuation strategy across operating speeds.

5.3.3 Summary

This section established how leading-edge blowing modifies broadband noise generation under isotropic inflow and clarified the operating envelopes that yield reliable reductions. The analysis used $\Delta\mathrm{PWL}$ maps defined as baseline minus blowing so that positive values indicate a net benefit. Across all conditions the reduction increased monotonically with actuation level within the accessible jet-ratio range, which supports the idea that added momentum is an effective lever for modifying near-leading-edge turbulence organisation and reducing gust–leading-edge interaction noise. Angle of attack played a central role: comparing Grid 4 at $\alpha = -11.7°$ and $\alpha = -13.5°$ showed that the more negative incidence produced a larger and more persistent reduction field. These trends point to a stronger modification of the turbulence scales that couple to the leading-edge interaction process when the incidence is more negative, motivating the use of $\alpha = -13.5°$ as the reference for the speed study.

The speed-dependent maps at $\alpha = -13.5°$ revealed two regimes in Strouhal space. A high-St band with $St \approx 0.6$ to 3.2 delivered the largest benefit at moderate speed, with a maximum of about $9\ \mathrm{dB}$ at $U_\infty = 20\ \mathrm{m\,s^{-1}}$, and a clear increase with jet ratio. As U_∞ increased, the peak in this band decayed gradually. In parallel, a low-St band with $St \approx 0.1$ to 0.6 emerged and strengthened with speed, culminating at $U_\infty = 60\ \mathrm{m\,s^{-1}}$ with reductions up to about $4.5\ \mathrm{dB}$ at a modest $U_j/U_\infty \approx 0.26$. A consistent interpretation that does not rely on separation or tonal mechanisms is that actuation shifts the receptivity of the leading edge to the incoming turbulence, and reduces the efficiency of gust–leading-edge scattering in a band-dependent way. At moderate speed, control appears most effective against faster, smaller disturbances associated with the high-St band, whereas at higher speed larger structures become more acoustically important and modest momentum input can reduce their spanwise coherence and effective interaction length at the leading edge, promoting benefit in the low-St band.

In summary, under isotropic inflow the most robust performance is obtained with Grid 4 at $\alpha = -13.5°$, where the reduction envelope is broad in frequency and persistent across jet ratios. The speed study shows a crossover in the dominant controllable scales, with high-St benefit strongest at moderate U_∞ and low-St benefit growing with U_∞. These results provide a clear basis for control scheduling. At lower and moderate speeds, prioritise higher jet ratio to target the high-St content. At higher speeds, retain a modest jet ratio to exploit the sensitivity of larger scales in the low-St range. The next section builds on this operating map to assess how these conclusions extend

beyond isotropic inflow and to what extent the identified regimes remain stable under changes in inflow character and Reynolds number.

5.4 Anisotropic Inflow Conditions

The isotropic grid cases established a baseline in which the incident eddies at the leading edge could be treated as isotropic-like for the purposes of spectral baseline and comparative control trends, so that the effects of steady blowing were read primarily through changes in spanwise organisation and scale. In many applications, however, the inflow is directionally biased and spatially non-uniform: wakes, shear layers, and mean-flow distortions generate Reynolds-stress anisotropy and enhanced spanwise coherence that modify both the amplitude and the directional content of the gust field that drives leading-edge scattering. Within Amiet-type frameworks, the radiated spectrum depends on the spanwise-integrated incident spectrum filtered by the airfoil response [11]; departures from isotropy in the incoming turbulence or non-uniform mean flow therefore alter both the level and the spectral placement of leading-edge broadband radiation [54, 55, 52]. This motivates a controlled study under anisotropic inflow so that any changes in noise with blowing can be related to measurable, direction-dependent features of the incident field.

A compact and well-established laboratory model for anisotropic inflow is the *rod–airfoil* configuration, in which a circular cylinder placed upstream of the airfoil produces a convecting wake with strong shear, organised vortical content, and embedded tonal peaks from vortex shedding that impinges on the leading edge [42]. In this setting, two parameters provide systematic control over the inflow seen by the airfoil: the rod diameter D, which sets the energetic wake scale and the shedding frequency via the cylinder Strouhal relation, and the non-dimensional streamwise spacing x/D, where x is the distance from the rod centre to the airfoil leading-edge apex. Increasing x/D allows the wake to diffuse and reorganise prior to interaction, while changes in D sweep the characteristic gust scales relative to the airfoil chord and the leading-edge radius. At fixed airfoil geometry, $(D, x/D)$ thus tune the anisotropy level, the energy-containing scales, and the spanwise organisation of structures that reach the leading edge, which are features that are known to influence leading-edge receptivity and scattering [11, 54, 51].

In contrast to the grid-turbulence cases, spectra obtained with the rod–airfoil include narrowband shedding tones superposed on a broadband background. Since the present focus is on leading-edge broadband noise, it is necessary to separate tonal and broadband contributions before quantifying the impact of blowing on radiation and coherence-based indicators. The next subsection documents the unforced spectra for each $(D, x/D)$ and introduces the frequency-domain mask used to isolate shedding peaks and their harmonics from the broadband component.

To complement the grid–turbulence baseline, the anisotropic campaign is conducted in the larger nozzle at a reference free–stream of $U_\infty = 24\ \mathrm{m\,s^{-1}}$ (nozzle 2 operating limit). Anisotropy is introduced with a circular rod placed upstream of the airfoil; three diameters are examined, $D = \{10,\ 15,\ 20\}\ \mathrm{mm}$, in order to sweep the energetic wake scale and the associated shedding

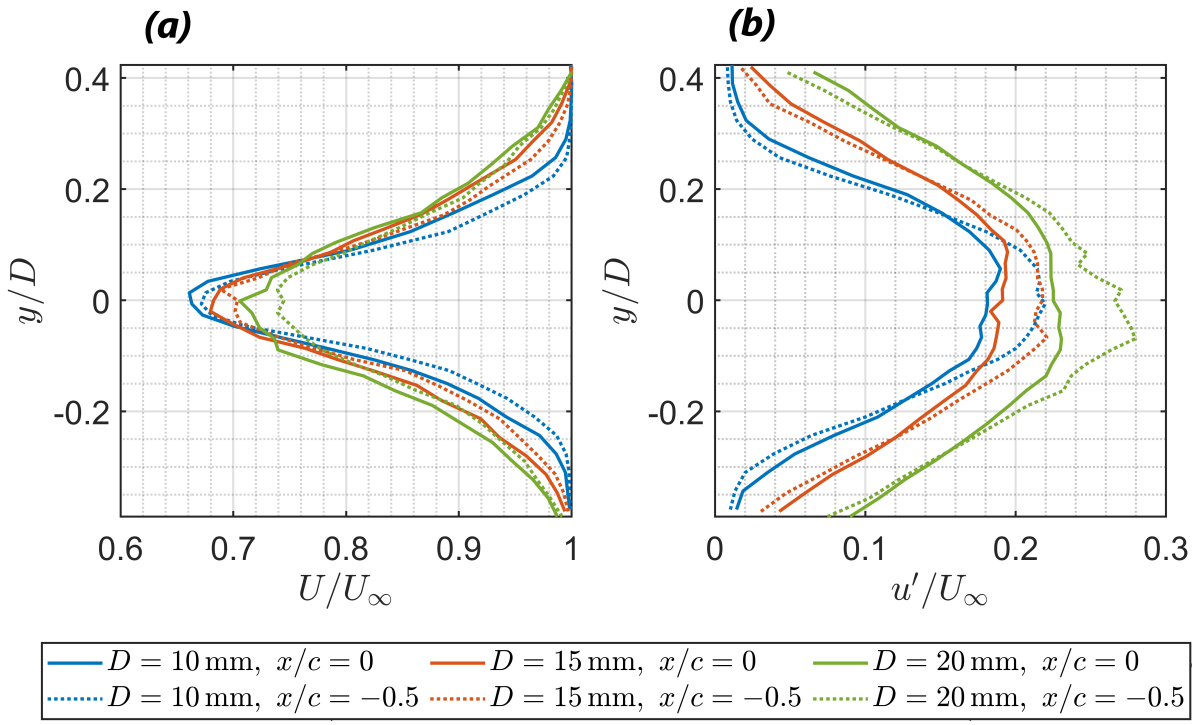

Figure 5.11: Centreline–normal inflow profiles upstream of the airfoil for $D = \{10, 15, 20\}\,\mathrm{mm}$. Panel (a): U/U_∞; panel (b): $T_u = u'/U_\infty$. Each diameter is shown at $x/c = -0.5$ (dotted) and $x/c = 0$ (solid).

frequency while holding the airfoil geometry fixed.

To characterise the inflow that impinges on the leading edge in the rod–airfoil configuration, Figure 5.11 presents centreline–normal profiles of the mean streamwise velocity and turbulence intensity at two streamwise locations immediately upstream of the airfoil: the penultimate measurement plane at $x/c = -0.5$ (dotted) and the leading–edge plane at $x/c = 0$ (solid). Panel (a) shows U/U_∞; panel (b) shows $T_u = u'/U_\infty$. For each rod diameter $D = \{10, 15, 20\}\,\mathrm{mm}$, the transverse coordinate is reported as $(y - y_{\mathrm{ref}})/D$, where y_{ref} aligns the profiles with the leading–edge apex for that diameter, enabling a like–for–like comparison across wakes of different scale. The profiles are extracted from the same two–probe hot–wire dataset used throughout this section (sampling at $20\,\mathrm{kHz}$, $5\,\mathrm{s}$ records), with $u' = \mathrm{rms}\{u(t) - \overline{u}\}$ computed at each y station and normalised by the free stream to form T_u.

The purpose of this figure is twofold. First, U/U_∞ delineates the mean wake deficit and shear on approach to the leading edge, providing the local kinematic context for gust–LE scattering. Second, T_u compactly quantifies the intensity of incoming fluctuations at the same locations and transverse positions, which directly influences the strength of the scattered broadband field when combined with the airfoil's leading–edge receptivity. Showing both $x/c = -0.5$ and $x/c = 0$ isolates the incremental evolution over the final half–chord of approach, while overlaying all three diameters

on common axes highlights how wake scale influences the near-LE inflow that the blowing system must act upon. Across all diameters, the profiles share a common structure: U/U_∞ attains a clear minimum along the projected cylinder centreline in y, and T_u exhibits a corresponding peak in the same region. This coincidence of mean deficit and elevated turbulence intensity indicates that the rods successfully generate a well-localised band of enhanced streamwise fluctuations that convects directly onto the leading-edge apex, providing a controlled and repeatable inflow condition for the subsequent analysis of scattering and control efficacy.

5.4.1 Spectrum characterisation and tonal–broadband masking

Before quantifying blowing effects, the spectra are partitioned into discrete tone regions and a tone–free broadband band using the data in Figure 5.12, where results are shown versus frequency in Hz to highlight how the shedding frequency shifts with rod diameter. The shedding peak and its harmonics are first identified from the *rod–only* spectrum for each diameter. Around each tone frequency f_k a symmetric exclusion window $[f_k(1-\eta),\ f_k(1+\eta)]$ is applied, with η selected so that the masked spectrum, and the resulting ΔL_{bb} trends, are insensitive to small changes in window width over the measured bandwidth. The union of these windows defines the tonal mask. The broadband band is then defined by comparing the *rod+airfoil* spectrum $L_{\mathrm{rf}}(f)$ to the *airfoil–only* baseline $L_{\mathrm{af}}(f)$ at the same operating point. A lower bound f_1 is set just above the lowest masked tone and away from very low frequency artefacts. An upper bound f_2 is chosen as the highest frequency outside the tonal mask where the differential level $\Delta L(f) = L_{\mathrm{rf}}(f) - L_{\mathrm{af}}(f)$ remains above a fixed threshold of $3\ \mathrm{dB}$. This threshold corresponds to a doubling of acoustic power relative to the baseline within that band, since $\Delta L = 10\log_{10}(P_2/P_1)$ gives $P_2/P_1 \approx 2$ at $3\ \mathrm{dB}$. However, high-frequency contamination arising from the leading-edge blowing system necessitates capping the analysis at the onset of blowing-generated noise, approximately $2\,\mathrm{kHz}$. This cap ensures that the reported changes are not driven by blowing self-noise; within the retained band, the results are interpreted as changes in leading-edge interaction noise rather than spectral masking. In the figure, the resulting tone windows appear as translucent green bands and the broadband range as a translucent blue band, overlaid behind all curves to clarify what is excluded and what is retained for broadband metrics.

The *airfoil–only* spectra provide a stable reference across the two spacings used here, $x/D = 10$ and $x/D = 15$, with only minor level differences over the full band. This indicates that translating the airfoil streamwise within this range does not substantially alter its self–noise for the present conditions. In contrast, the *rod+airfoil* spectra show a clear dependence on spacing that strengthens with diameter. For $D = 20\ \mathrm{mm}$ the separation between $x/D = 10$ and $x/D = 15$ is largest, affecting both the vicinity of the masked tones and the broadband floor within the blue band. The disparity is smaller for $D = 15\ \mathrm{mm}$ and smallest for $D = 10\ \mathrm{mm}$. Since the corresponding *airfoil–only* curves do not show a similar shift, the difference arises from the interaction of the anisotropic rod wake with the leading edge rather than installation effects. Physically, increasing D thickens the wake and increases its energy and integral scales at a given x/D; changing x/D

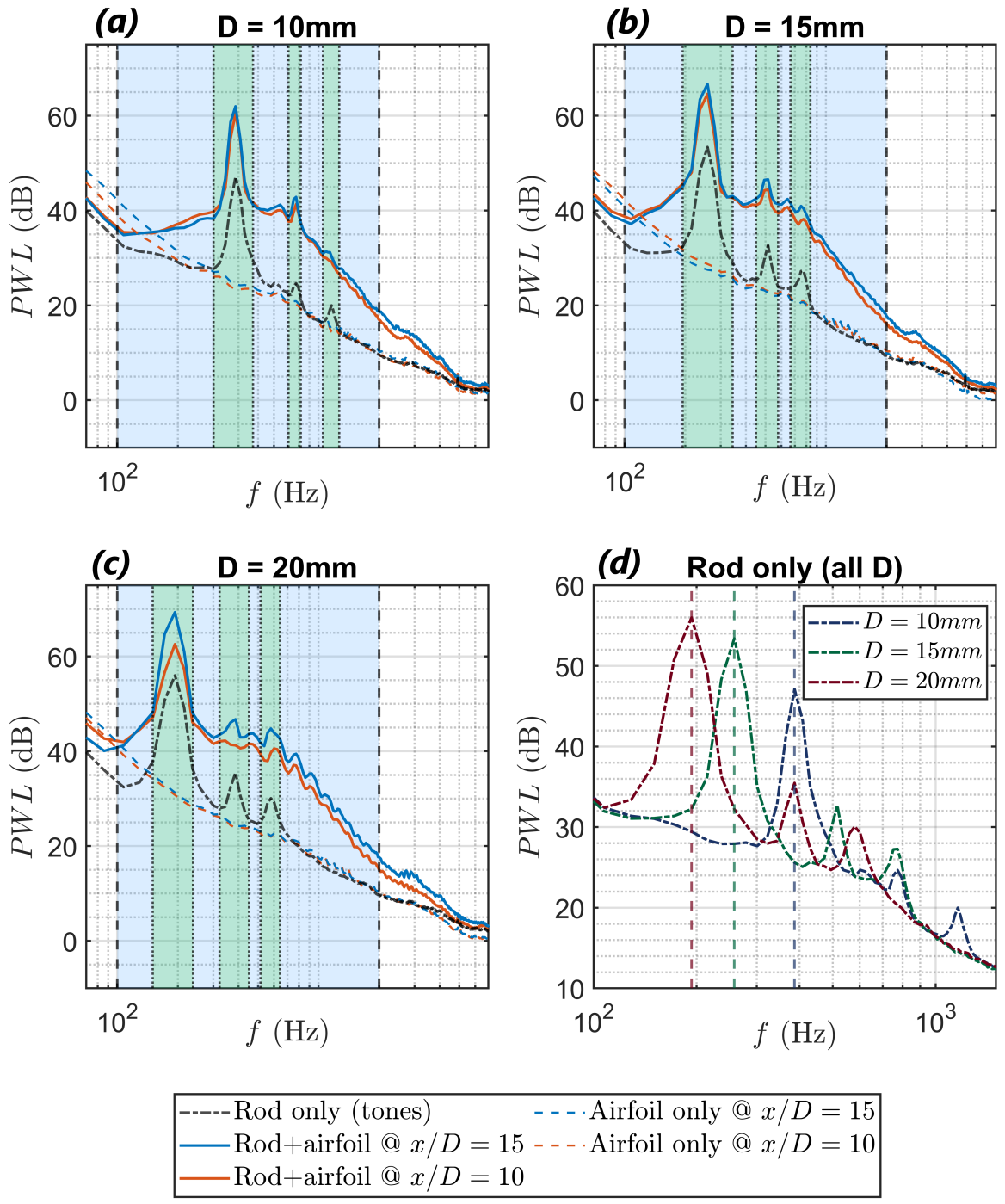

Figure 5.12: Baseline spectra with masks for varying x/D and D. Panels: (a) $D = 10$ mm, (b) $D = 15$ mm, (c) $D = 20$ mm. Each panel shows *rod-only* (tones), *airfoil-only* at $x/D = 10, 15$, and *rod+airfoil* at $x/D = 10, 15$. Semi-transparent green bands indicate tonal exclusion windows; semi-transparent blue bands indicate the broadband band used for LEBN metrics.

then modifies the state of that wake at the airfoil plane through streamwise diffusion and spectral rebalancing. The net result is a stronger leading–edge scattering response for larger D and a

more pronounced sensitivity to x/D, seen as a higher broadband floor in the blue band when the rod and airfoil are combined.

With the masks in place, the diameter dependence is made explicit in *panel (d)* of Figure 5.12, which overlays the *rod-only* tones for all three diameters to emphasise the shift of the dominant shedding peak with D. The measured fundamentals are $f_s \approx 386.72$ Hz for $D = 10$ mm, $f_s \approx 257.81$ Hz for $D = 15$ mm, and $f_s \approx 193.36$ Hz, consistent with the canonical cylinder relation $St = f_s D/U_\infty \approx$ const at fixed U_∞. The green tonal masks in panels (a)–(c) sit squarely over these peaks (and nearby harmonics), ensuring that subsequent broadband metrics exclude shedding-dominated bins.

A final observation is that neither the *rod–only* nor the *airfoil–only* spectra exhibit a marked broadband elevation by themselves over the blue band, whereas the combined *rod+airfoil* spectra do. This points to a mechanism in which the cylinder wake supplies coherent, anisotropic disturbances and the airfoil leading edge scatters those disturbances into broadband radiation. The explicit overlay of the green tone masks and the blue broadband band in Figure 5.12 makes this decomposition transparent and provides a basis for the noise–reduction metrics and performance maps that follow.

5.4.2 Performance of Leading-Edge Blowing: Spectral Overview

Having established tone–broadband partitions for each rod–diameter condition, we now use full spectra to assess how steady leading-edge blowing reshapes the acoustic field across the parameter space. Figure 5.13 presents a compact 3×2 overview: rows sweep rod diameter ($D = 10, 15, 20$ mm) while columns compare two streamwise spacings ($x/D = 10, 15$). In each panel, the baseline spectrum serves as the reference envelope of rod–airfoil interaction; the superposed curves show the response under progressively higher blowing rates (blue to red).

The figure reveals where energy is removed or redistributed relative to the baseline, whether changes remain confined to the neighbourhood of the shedding tones or extend across the broadband band defined earlier, and how these trends depend on the incident wake scale set by $(D, x/D)$.

Figure 5.13 shows a clear, monotonic sensitivity of the far-field spectra to the blowing level across all $(D, x/D)$ cases: as the jet strength is increased, both the masked tonal peaks and the broadband regions are progressively depressed relative to baseline. This trend is consistent with a picture in which steady LE blowing disrupts the phase organisation of the incoming wake and weakens the receptivity of the leading edge, so that (i) discrete shedding content couples less efficiently to acoustic radiation and (ii) the spanwise coherence of energy-containing eddies is reduced across the broadband range. None of the cases, however, fully removes the tones; the masked peaks persist—albeit at lower amplitude—because the jets act at the airfoil and do not extend upstream far enough to suppress the cylinder shedding mechanism itself.

At the lowest frequencies (≈ 100–175 Hz), high blowing occasionally introduces a slight elevation above baseline. A plausible explanation is that strong steady jets add a quasi-steady or very

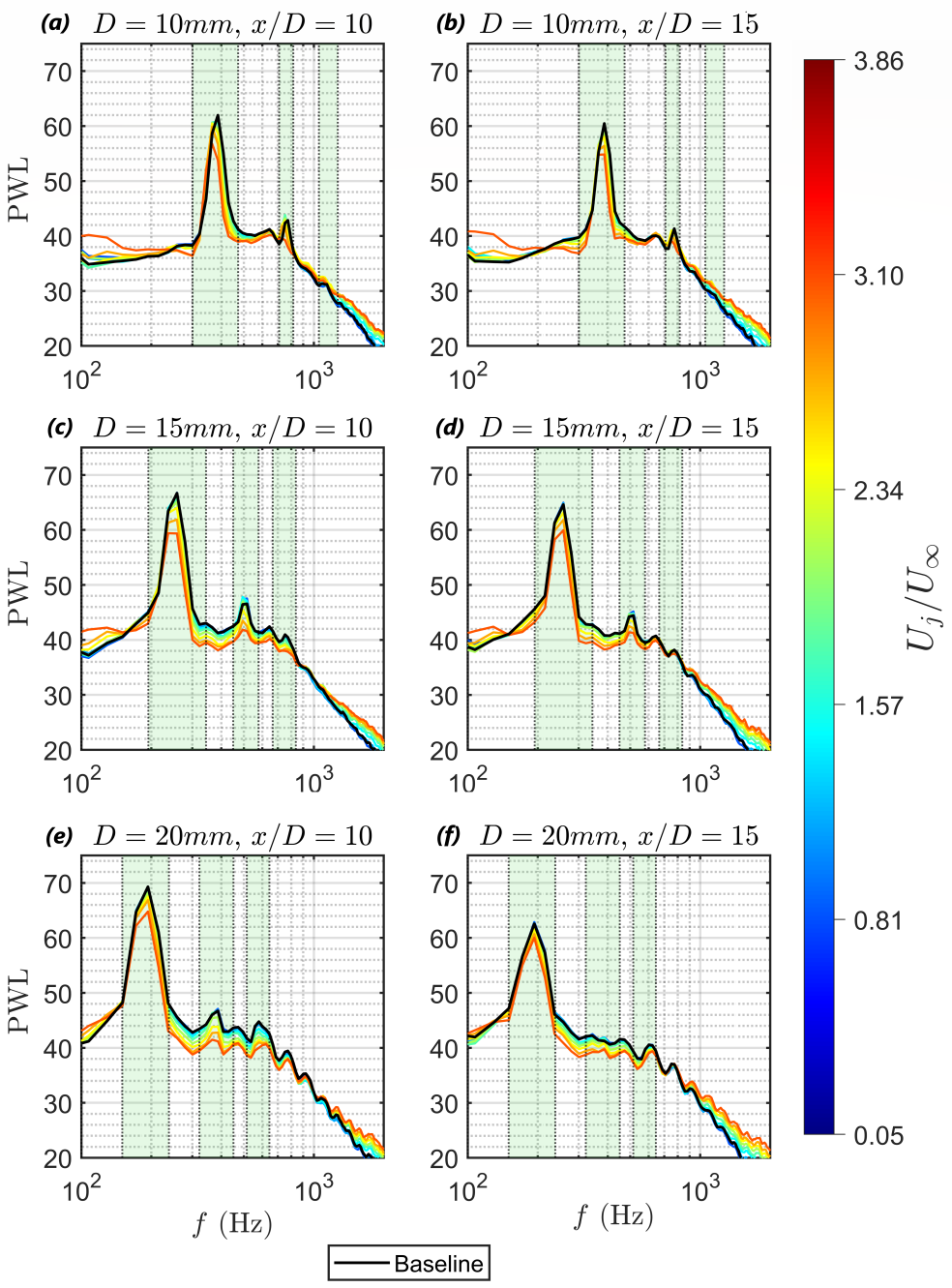

Figure 5.13: PWL spectra for leading-edge blowing configurations at varying D and x/D. Rows correspond to rod diameters $D = 10$, 15, and 20 mm, while columns correspond to streamwise spacings $x/D = 10$ and 15. The baseline and blowing cases are shown to illustrate the spectral response of the leading-edge blowing system. Semi-transparent green bands indicate the frequency ranges where tonal components occur.

low-frequency modulation to the local mean flow near the stagnation region. Such modulation projects predominantly at the lowest Fourier bins and can raise the spectral floor there without undermining the broadband reductions at higher frequencies. The same behaviour has been ob-

served elsewhere in this study under high blowing rates, indicating that it is a robust feature of the actuation rather than an artefact of this rod–airfoil configuration.

A complementary trend across the panels is the spacing dependence: for a given diameter, cases at the larger separation $x/D = 15$ generally exhibit greater broadband attenuation under blowing than their $x/D = 10$ counterparts. A plausible interpretation is that additional convective distance allows the rod wake to diffuse and partially decorrelate before reaching the leading edge, lowering the instantaneous gust coherence and steepening the local mean-shear gradients that the jets can act upon. In this regime the steady jets more effectively disrupt residual spanwise organisation and diminish the efficiency of gust–LE scattering, so incremental increases in U_j/U_∞ translate into larger spectral reductions over the broadband mask. By contrast, at $x/D = 10$ the impinging wake is more compact and coherent, making it harder for the same jet levels to induce sufficient spanwise dephasing to achieve comparable gains.

Across diameters, the broadband regions exhibit the smallest reductions for $D = 10\ \mathrm{mm}$, with noticeably larger benefits for $D = 15$ and $20\ \mathrm{mm}$. This ordering is consistent with the inflow characterisation: larger D delivers wakes with greater fluctuation levels and larger integral scales at the leading-edge plane, so there is more broadband energy (and spanwise organisation) for the jets to dephase and redistribute. In all panels, increasing the blowing level amplifies these effects, underscoring that the primary control lever here is the degree to which the jets disrupt spanwise coherence and attenuate the efficiency of gust–LE scattering, while the residual tonal content remains limited by the upstream shedding physics.

To condense the spectra into quantitative metrics, band-averaged levels for the broadband and tonal parts of each case were computed and then compared to the baseline. Starting from the one-sided PWL spectrum $L(f)$ (dB re $20\,\mu\mathrm{Pa}$), the corresponding linear power is $S(f) = 10^{L(f)/10}$. The broadband band is defined as a contiguous frequency range $[f_1, f_2]$ with the tone windows removed,

$$B_{\mathrm{bb}} = [f_1, f_2] \setminus (B_1 \cup B_2 \cup \cdots),$$

where B_k denotes the exclusion window around the k-th shedding tone (fundamental and harmonics). The broadband level is then taken as the average power over the remaining band,

$$L_{\mathrm{bb}} = 10 \log_{10}\left(\frac{1}{|B_{\mathrm{bb}}|} \int_{f \in B_{\mathrm{bb}}} S(f)\, \mathrm{d}f \right),$$

while the tonal level aggregates the average power across all tone windows,

$$L_{\mathrm{tone}} = 10 \log_{10}\left(\frac{1}{\sum_k |B_k|} \sum_k \int_{f \in B_k} S(f)\, \mathrm{d}f \right).$$

A 0.55 dB uncertainty margin for L_{bb} was estimated by computing L_{bb} for each Welch segment of the time record and taking the scatter across segments. Changes below 0.55 dB are treated as marginal. The same segment-scatter approach is applied to L_{tone}, and the same $0.55\,\mathrm{dB}$ margin

is used as a practical threshold for both band-averaged metrics in this chapter.

For the broadband and tonal metrics, reductions are defined relative to the baseline (no–blowing) case as

$$\Delta L_{\mathrm{bb}} = L_{\mathrm{bb}}^{\mathrm{base}} - L_{\mathrm{bb}}^{\mathrm{blow}}, \qquad \Delta L_{\mathrm{tone}} = L_{\mathrm{tone}}^{\mathrm{base}} - L_{\mathrm{tone}}^{\mathrm{blow}},$$

where $L_{\mathrm{bb}}^{\mathrm{blow}}$ and $L_{\mathrm{tone}}^{\mathrm{blow}}$ denote the corresponding levels at a given blowing condition. Positive values therefore indicate a reduction relative to the baseline.

Before focusing on the maximum-blowing case, it is useful to examine how the broadband reduction evolves across the full range of actuation levels. Figure 5.14 therefore presents ΔL_{bb} as a function of U_j/U_∞ for all six rod–airfoil configurations. This representation complements the full spectra in Figure 5.13 by collapsing the broadband response into a single metric, making it easier to identify whether the benefit from blowing emerges gradually, saturates, or remains negligible for a given wake geometry.

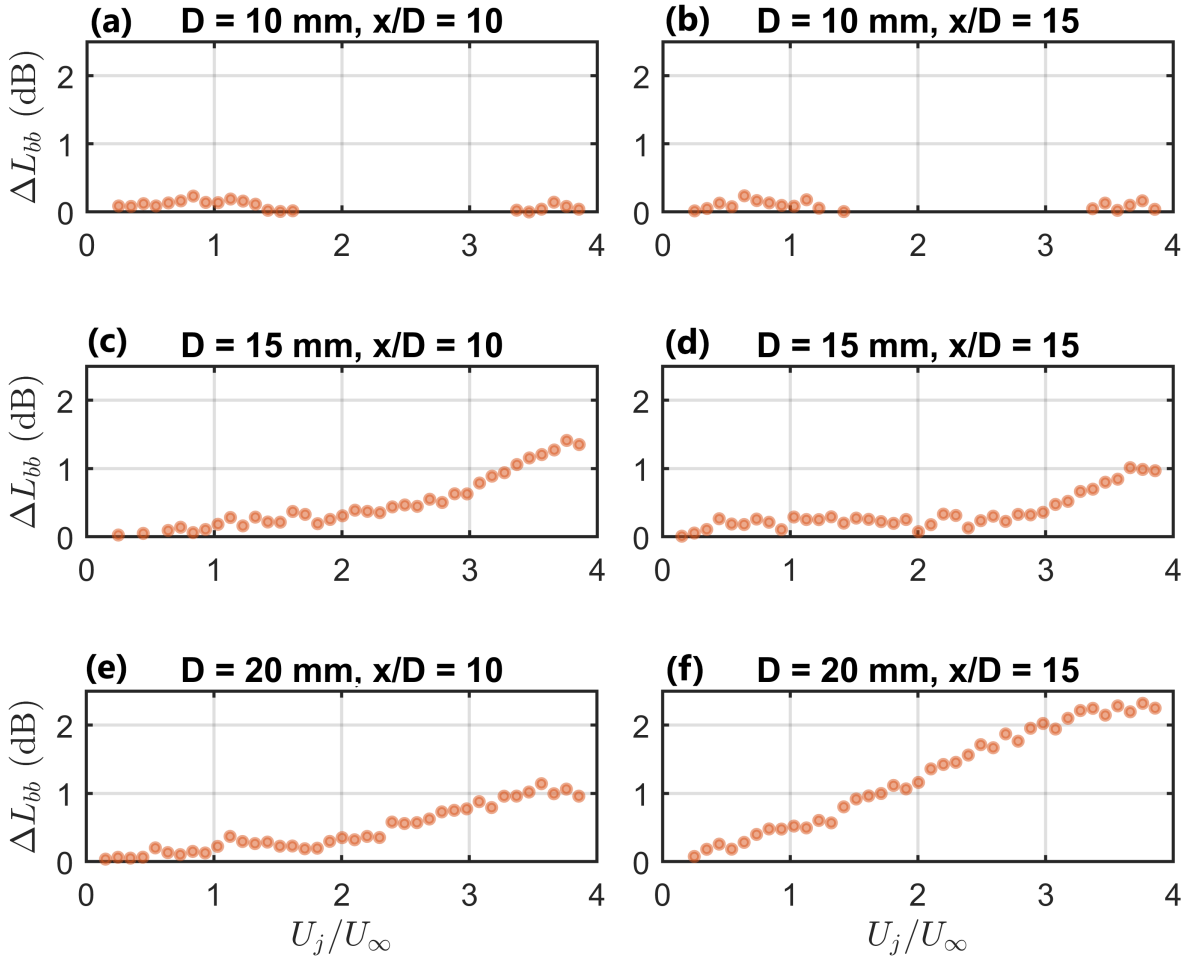

Figure 5.14: Variation of broadband reduction ΔL_{bb} with blowing ratio U_j/U_∞ for all rod–airfoil configurations. Panels (a,b) correspond to $D = 10$ mm with $x/D = 10$ and 15, respectively; panels (c,d) correspond to $D = 15$ mm; and panels (e,f) correspond to $D = 20$ mm.

Figure 5.14 shows that the influence of steady leading-edge blowing on the broadband reduction depends strongly on the wake scale. For the smallest rod diameter, $D = 10\ \mathrm{mm}$, the effect of blowing is minimal at both spacings, with no clear monotonic trend in ΔL_{bb} as U_j/U_∞ increases. In this case the maximum broadband reduction remains only $\Delta L_{\mathrm{bb}} = 0.04\ \mathrm{dB}$, which is far below the adopted uncertainty threshold and indicates that the incoming wake is too weak or too fine-scaled for the present actuation to produce a meaningful change in the broadband interaction noise.

For $D = 15\ \mathrm{mm}$, a clearer response begins to emerge. The data show that larger blowing ratios generally produce larger values of ΔL_{bb}, particularly at the larger spacing $x/D = 15$, indicating that the jets are starting to modify the effective interaction more consistently. The maximum reduction reaches $\Delta L_{\mathrm{bb}} = 1.35\ \mathrm{dB}$, which suggests that once the incoming wake contains sufficient fluctuation energy and spatial organisation, steady blowing can begin to weaken the gust–leading-edge coupling in a measurable way.

The strongest trend appears for $D = 20\ \mathrm{mm}$, where the increase in ΔL_{bb} with U_j/U_∞ becomes more systematic. In these cases the benefit of blowing is most apparent, with the largest broadband reduction reaching $\Delta L_{\mathrm{bb}} = 2.25\ \mathrm{dB}$. This behaviour is consistent with the interpretation developed from the spectral plots: larger-diameter rods generate stronger and more spatially coherent wakes at the leading-edge plane, providing a broader and more energetic interaction field that can be more effectively disrupted by the steady jets.

Taken together, Figure 5.14 shows that broadband reduction does not simply depend on the presence of actuation, but on the extent to which the incoming wake possesses sufficient scale and coherence for the jets to modify the scattering process. It also shows that the largest reductions are obtained only at the higher blowing ratios for the larger rod diameters, which motivates the endpoint comparison based on the maximum actuation level considered.

To compare the endpoint performance across the full test matrix, Figure 5.15 reports the reductions obtained at the highest blowing case ($U_j/U_\infty = 3.86$), i.e. $\Delta L_{\mathrm{bb}} = L_{\mathrm{bb}}^{\mathrm{base}} - L_{\mathrm{bb}}^{\mathrm{max}}$ and $\Delta L_{\mathrm{tone}} = L_{\mathrm{tone}}^{\mathrm{base}} - L_{\mathrm{tone}}^{\mathrm{max}}$. The figure presents these results as two 3×2 tables: panel (a) for ΔL_{tone} and panel (b) for ΔL_{bb}, with rows ordered by diameter (D = 10, 15, 20 mm) and columns by spacing ($x/D = 10, 15$). Within each panel, deeper red shading indicates a larger reduction.

The quantified reductions corroborate the trends identified in Figures 5.13 and 5.14, and clarify the ranking of the cases at the maximum blowing level. For the broadband metric, the largest reductions occur at $x/D = 15$ for the larger diameters, with the maximum decrease obtained for $x/D = 15,\ D = 20\ \mathrm{mm}$ ($\Delta L_{\mathrm{bb}} = 2.25\ \mathrm{dB}$). The case $x/D = 15,\ D = 15\ \mathrm{mm}$ also performs well ($\Delta L_{\mathrm{bb}} = 1.35\ \mathrm{dB}$), whereas the $D = 10\ \mathrm{mm}$ cases remain effectively unchanged. With the adopted $0.55\ \mathrm{dB}$ uncertainty margin, differences between close cases should be treated cautiously; however, $D = 20\ \mathrm{mm}$ at $x/D = 15$ is retained as the reference configuration because it provides the largest observed broadband reduction within the tested matrix.

The ΔL_{tone} values display a different optimum: the largest tonal reduction appears at $x/D = 10,\ D = 15\ \mathrm{mm}$ ($5.86\ \mathrm{dB}$), with $D = 10\ \mathrm{mm}$ and $D = 20\ \mathrm{mm}$ at the same spacing giving $4.39\ \mathrm{dB}$ and $4.03\ \mathrm{dB}$, respectively; moving to $x/D = 15$ lowers the tonal reductions across all diameters

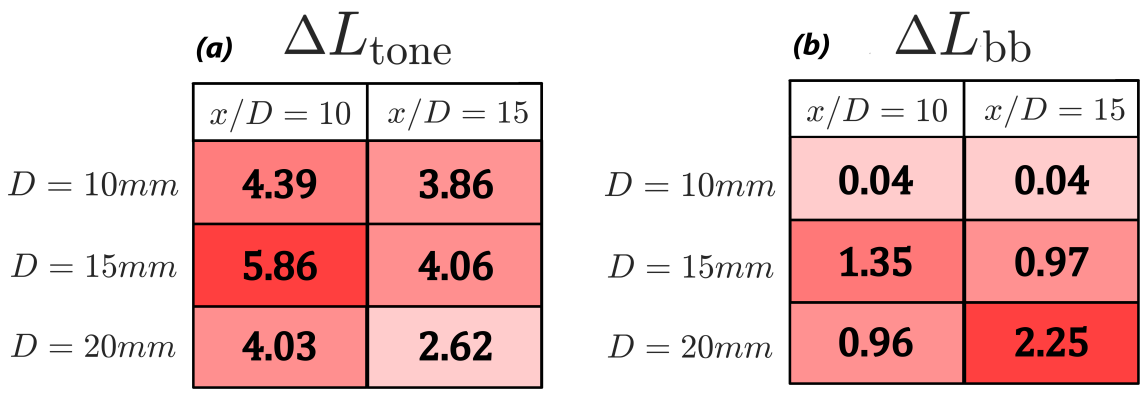

Figure 5.15: Summary of compressed performance metrics based on band-weighted average reductions in tonal and broadband noise. The colour contrast within each cell reflects the magnitude of noise reduction for the corresponding noise type (tonal or broadband).

(down to 2.62 dB for $D = 20$ mm). A plausible interpretation is that tonal content, locked to the cylinder Strouhal shedding and its near harmonics, is most effectively attenuated when the impinging wake retains sufficient coherence and amplitude for the jets to disrupt the phase locking between incoming vortical structures and the leading edge scattering, but not so close that the shedding remains too robust to be influenced by the near-LE actuation. The $D = 15$ mm wake at $x/D = 10$ appears to strike that balance: it is energetic enough to exhibit strong tones yet sufficiently deformable by the jet-induced shear and crossflow to reduce the tonal peaks. Decreasing to $D = 10$ mm weakens the leverage on the tones, while increasing to $D = 20$ mm at the same short spacing likely leaves the shedding too coherent and forceful for the jets to further degrade the phase locking, which limits the attainable tonal drop. At the larger spacing $x/D = 15$, the shedding imprint at the leading edge is more diffused and less tightly coupled to the scattering process, so the same jet forcing yields smaller tone suppression across all D.

In summary, the broadband metric favours the combination that maximises jet-induced spanwise decoherence of the incoming turbulence, and the tonal metric peaks at an intermediate wake strength and shorter spacing that most effectively undermines the phase coherent shedding imprint without it being either too weak to matter or too strong to disrupt. Since the target mechanism in this chapter is broadband leading edge turbulence interaction noise, we carry forward the case that delivers the largest broadband reduction, namely $D = 20$ mm at $x/D = 15$, as the reference configuration for the subsequent analysis.

The beamforming maps in Figure 5.16 provide spatial confirmation of these spectral trends and identify where, physically, the dominant sources reside. Panel (a) shows the baseline configuration (no blowing) for the reference case $D = 20$ mm, $x/D = 15$, evaluated over a frequency band within the tonal range. The reconstructed source distribution exhibits a concentrated region of elevated acoustic level immediately downstream of the rod position, with a median beamformed level of 50.5 dB. This localisation is consistent with vortex shedding from the cylinder wake imprinting

a coherent signature that survives convection to the array, and it supports the interpretation that, within this band, the rod itself is the primary contributor to the measured narrowband content rather than the airfoil leading edge.

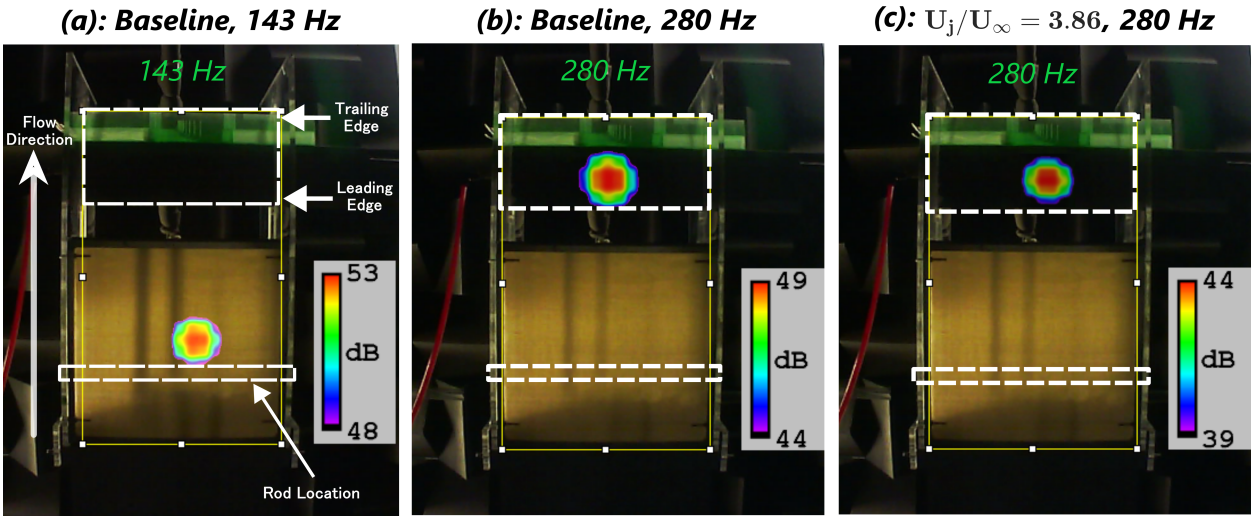

Figure 5.16: Beamformer visualisations at representative frequency bands: one centred on the dominant tonal noise, one within the broadband noise band, and an additional broadband case with the most effective blowing rate applied.

Panel (b) considers the same baseline flow but over a broadband frequency range representative of the leading-edge turbulence–interaction noise. In this band, the dominant beamformed maximum shifts from the rod region to the airfoil nose, with the peak energy tightly clustered around the geometric leading edge and a lower median level of 46.5 dB. This redistribution of acoustic energy from the rod to the leading edge aligns with the far-field spectral measurements, which identify the airfoil as the main radiator in the broadband range once the tonal contribution of the wake shedding is excluded. In other words, when the frequency window isolates the broadband mechanism of interest, the beamforming clearly attributes the noise to the gust–LE scattering process rather than to the upstream cylinder.

Finally, panel (c) presents the same broadband frequency range as panel (b), but with the most effective blowing rate applied, $U_j/U_\infty = 3.86$. The resulting source map retains the leading edge as the primary radiation site, but the overall level in this region is markedly reduced, with the median beamformed level dropping to 41.5 dB. The preservation of source location, combined with the clear reduction in intensity, indicates that the blowing strategy acts by weakening the efficiency of the leading-edge interaction rather than by displacing the source to another part of the airfoil. Taken together, panels (a)–(c) show a coherent picture: the rods introduce tonal shedding that is spatially distinct from the broadband LE source; the broadband mechanism is firmly anchored at the leading edge; and the selected blowing configuration demonstrably attenuates that leading-edge source while leaving its spatial footprint essentially unchanged.

5.4.3 Flow analysis: space–time signatures and coherence

Having identified the operating point that yields the largest broadband noise benefit, the analysis now turns to the underlying flow physics for the anisotropic configuration with $D = 20\ \mathrm{mm}$ and $x/D = 15$. The measurement methodology and probe layout follow the description in the *Experimental setup*: two single hot wires were operated simultaneously at $U_\infty = 20\ \mathrm{m\,s^{-1}}$, with a fixed reference probe positioned just upstream of a leading–edge orifice near the apex and a second probe traversed over a rectilinear grid that spans multiple orifices in z and extends upstream in x. For each grid location, concurrent time series were acquired for $5\ \mathrm{s}$ at $20\ \mathrm{kHz}$, allowing the same inflow realisation to be interrogated in both the time and frequency domains. Three blowing settings are considered: baseline ($U_j/U_\infty = 0$), a least–effective level $U_j/U_\infty = 0.35$, and a most–effective level $U_j/U_\infty = 3.86$.

The objective is to connect the observed acoustic attenuation to measurable changes in the organisation, advection and coherence of the anisotropic structures impinging on the leading edge. To this end, we first extract space–time correlation signatures relative to the reference probe and examine their evolution with lag, which reveals how energetic eddies appear, persist and convect across the mapping plane. We then condense these maps into compact streamwise trends referenced to the leading–edge station to highlight how peak cross–correlation levels vary with blowing. Finally, we quantify frequency–domain coherence and the associated decay lengths in the streamwise and spanwise directions, providing scale–aware measures of how steady blowing alters correlation structure in the vicinity of the leading edge. Together, these views isolate the flow pathway by which the highest blowing level reduces both shedding–locked content and broadband turbulence–interaction noise at the source.

5.4.3.1 Cross–correlation maps (space–time view)

To probe how the impinging structures appear, persist, and convect across the leading–edge plane, we compute the normalized two–point cross–correlation between the fixed reference signal $u_1(t)$ and the traversing signal $u_2(t)$,

$$R_{12}(\tau) = \frac{\langle u_1(t)\, u_2(t+\tau)\rangle}{\sigma_1\, \sigma_2}.$$

Negative lags probe correlations with the traversing point sampling a structure before it reaches the reference line, zero lag represents simultaneous sampling, and positive lags capture the passage of the same structure beyond the reference line. The three lags used here, $-0.5\ \mathrm{ms}$, $0\ \mathrm{ms}$, and $+0.5\ \mathrm{ms}$, are chosen to bracket the expected convection time across the smallest probe separations, $\tau_c \sim \Delta x/U_c$, with U_c of order U_∞, so that the maps capture the build–up, peak, and decay of correlation associated with advection of the energy–containing eddies.

This analysis complements the frequency–domain coherence by adding a time–resolved view of structural ordering and temporal memory in the near field. It is directly relevant to the atten-

uation mechanism because leading–edge scattering is sensitive to both the amplitude and the spanwise organization of the incoming disturbances. Space–time snapshots of R_{12} reveal how steady blowing alters the strength and footprint of correlated motion in the vicinity of the apex, thereby indicating whether reductions in far–field levels arise from weakened structural persistence, reduced spanwise alignment, or both. The figure presents maps at the three lags for the baseline, $U_j/U_\infty = 0.35$, and $U_j/U_\infty = 3.86$ configurations.

At the negative lag $\tau = -0.5$ ms, all configurations exhibit relatively modest cross–correlation

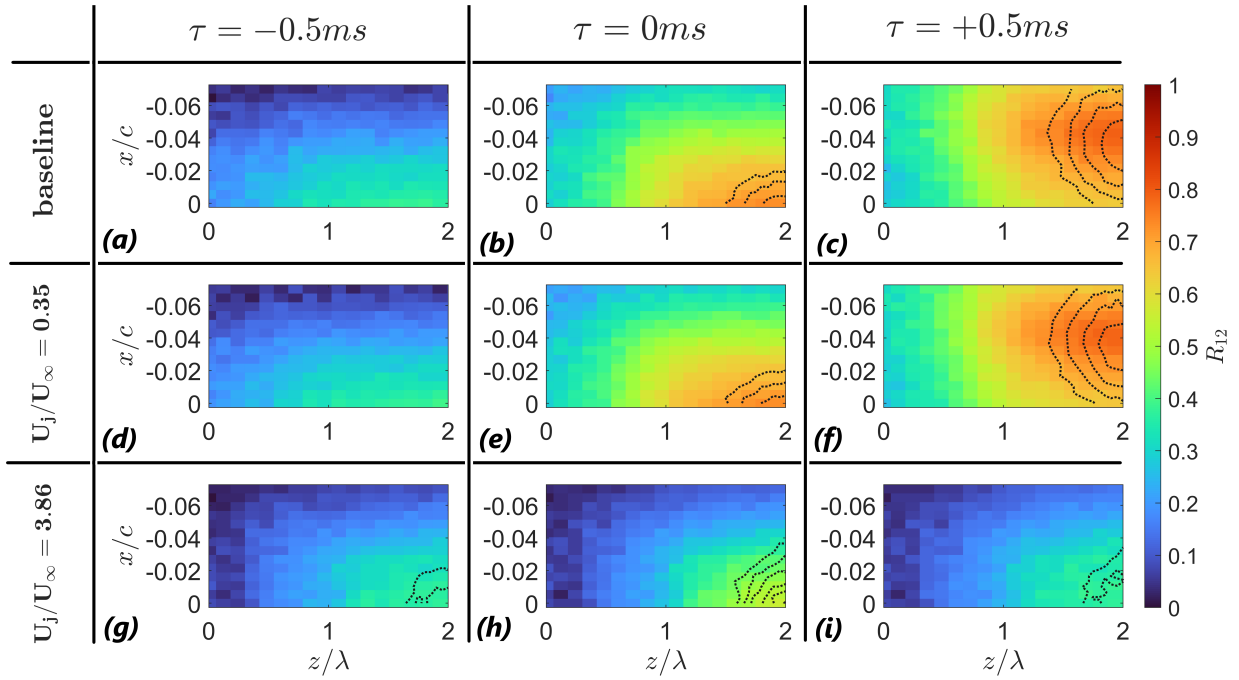

Figure 5.17: Cross-correlation maps $R_{12}(\tau)$ in 2D plane upstream of the leading edge. For each case (baseline, $U_j/U_\infty = 0.35$, and $U_j/U_\infty = 3.86$), maps are shown at time lags $\tau = -0.5$ ms, 0, and $+0.5$ ms. Here $\lambda = 10\,\mathrm{mm}$ is the jet spacing, so z/λ is spanwise separation in jet-spacing units.

magnitudes across the mapped plane, with the highest values concentrated near the leading–edge line $(x/c = 0)$ and at the spanwise location closest to the reference probe $(z/\lambda \approx 2)$, where z is the spanwise coordinate (see Figure 5.2) and $\lambda = 10\,\mathrm{mm}$ is the spacing between adjacent leading-edge blowing jets, so z/λ is the spanwise separation in units of the jet spacing. Peak values approach ≈ 0.3, decaying with increasing distance from the reference location. In the baseline and $U_j/U_\infty = 0.35$ cases this elevated region is broader in the spanwise direction, indicating that nearby points along the leading edge sample a similar portion of the incoming structures. In the $U_j/U_\infty = 3.86$ case the enhanced patch is noticeably more localized around the reference position, consistent with a footprint that is less spanwise extensive at the same pre–passage lag. This difference is naturally interpreted as reduced spanwise organization in the vicinity of the apex when strong blowing is present, so that points offset in z share less of the same eddy content prior

to passage.

At zero lag $\tau = 0$, the baseline and $U_j/U_\infty = 0.35$ maps show a pronounced build–up of correlation that reaches values up to ≈ 0.8 at $(x/c = 0,\, z/\lambda \approx 2)$, with a contiguous high–R_{12} lobe that remains spread along the leading edge. In contrast, the $U_j/U_\infty = 3.86$ case strengthens relative to its -0.5 ms state but remains much lower in magnitude, with a maximum near ≈ 0.42 at the same nominal location. The persistence of a compact peak together with a lower maximum suggests that the structures arriving at the apex are less phase–aligned across span and less repeatable in time. A plausible explanation is that the jets introduce shear and crossflow that distort and dephase the incident wake locally. The result is a smaller fraction of the traversing–reference pair interrogating the same energy–containing motion at any instant, even when their sampling is synchronized.

At the positive lag $\tau = +0.5$ ms, the baseline and $U_j/U_\infty = 0.35$ maps show the expected upstream shift of the peak–correlation lobe, with the core maximum displaced by roughly $\Delta x/c \approx -0.04$ relative to its position at $\tau = 0$. This is consistent with advection of correlated eddies past the reference line over the chosen lag window. By contrast, for $U_j/U_\infty = 3.86$ the map does not exhibit a comparable upstream translation of a strong peak. Instead the correlation returns toward the lower values observed at -0.5 ms and remains concentrated near $(x/c = 0,\, z/\lambda \approx 2)$. Taken together with the weak zero–lag maximum, this pattern indicates a shorter temporal memory and reduced spatial footprint of correlated motion in the high–blowing case. In other words, strong blowing appears to curtail the lifetime and spanwise reach of the structures that couple the traversing and reference signals, while preserving the basic geometric trend that correlation is highest for points nearest to the apex and decays with separation.

The full picture aligns with the acoustic observations. Baseline and low blowing present larger, more spanwise–extensive and more persistent regions of high R_{12} near the apex, which is consistent with stronger spanwise ordering at the leading edge and with the higher far–field levels previously reported. With $U_j/U_\infty = 3.86$, the cross–correlation amplitudes are reduced at all three lags, the lobe is more localized, and the apparent advection imprint is less pronounced. These features indicate diminished structural persistence and spanwise alignment at the scattering plane. Because leading–edge radiation is sensitive to the amplitude and spanwise coherence of the impinging disturbances, the observed reduction and localization of R_{12} under strong blowing provide a space–time counterpart to the upcoming coherence maps and help explain the broadband and tonal noise decreases documented.

The streamwise extracts of the maximum cross–correlation, $R_{12,\max}(x/c)$, taken along the line passing through the reference probe $(z/\lambda = 2)$ consolidate the picture from the maps. For the baseline and the $U_j/U_\infty = 0.35$ case, $R_{12,\max}$ is highest at the station nearest the reference location $(x/c \to 0)$ and decays gradually as the traversing probe moves upstream. This trend follows directly from the overlap argument: points closest to the apex sample nearly the same energy–containing eddies at nearly the same time, whereas increasing streamwise separation reduces both the fraction of eddy volume shared by the two probes and the phase alignment

introduced by advection, leading to a smooth loss of correlation with distance. In contrast, the $U_j/U_\infty = 3.86$ curve lies well below the other two at every x/c, retains the same ordering with a peak at $x/c \approx 0$, but exhibits a more nearly linear, slightly rough decay. The lower level indicates weaker structural persistence at the apex, while the less smooth decline is consistent with increased phase jitter and intermittency of the impinging motions once strong blowing distorts and dephases the incoming wake. Viewing this one–dimensional slice alongside the space–time maps clarifies that the primary effect of high blowing is to suppress the local peak correlation at the leading edge and to shorten the effective streamwise memory of the flow, in line with the reduced spanwise organization and the noise reductions reported earlier. The figure $R12Extract$ therefore provides a concise, streamwise–resolved summary of how the three configurations differ in the strength and spatial footprint of correlated motion at the scattering plane.

Figure 5.18 distils the space–time maps into a one–dimensional diagnostic by plotting the streamwise evolution of the peak cross–correlation, $R_{12,\max}(x/c)$, along the line passing through the reference probe $(z/\lambda = 2)$.

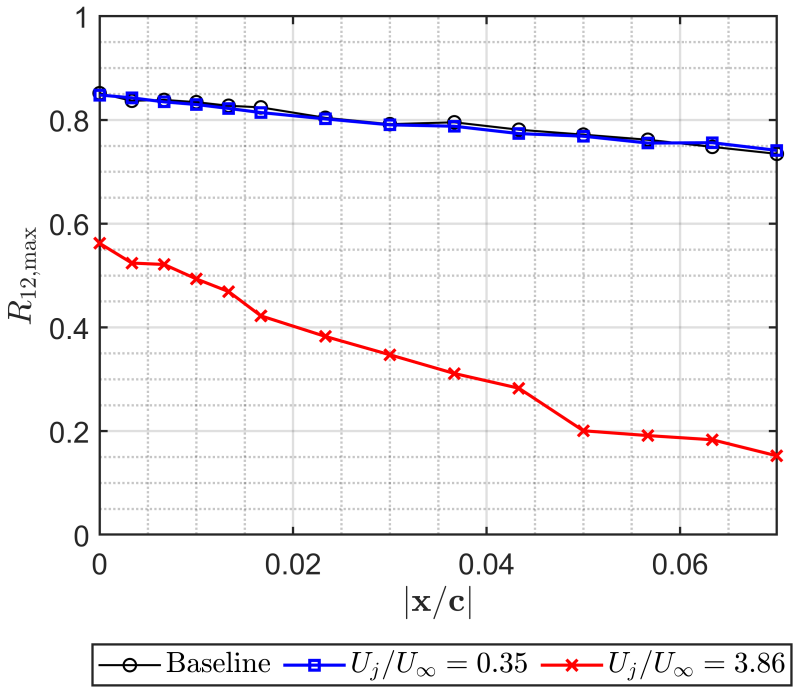

Figure 5.18: Maximum cross-correlation coefficient $R_{12,\max}$ as a function of streamwise distance upstream from the reference probe, for the baseline case and blowing conditions $U_j/U_\infty = 0.35$ and $U_j/U_\infty = 3.86$. This comparison highlights the impact of leading-edge blowing on the upstream coherence of turbulent structures.

For the baseline and the $U_j/U_\infty = 0.35$ case, $R_{12,\max}$ attains its highest value at the station closest to the reference location $(x/c \to 0)$ and then decays smoothly with upstream distance. This behaviour follows directly from eddy–overlap and phase–alignment arguments: at small separa-

tions both sensors interrogate nearly the same energy–containing structures with similar phase, whereas increasing $|x/c|$ reduces the spatial overlap and accumulates phase slippage under advection, yielding a gradual loss of correlation. The $U_j/U_\infty = 3.86$ curve lies markedly below the other two at every x/c, retains a maximum at $x/c \approx 0$, and decays more nearly linearly with a visibly rougher trend. The depressed level reflects the reduced persistence of coherent structures at the apex when strong blowing imposes spanwise dephasing and local shear–induced distortion; the less smooth decline is consistent with enhanced phase jitter and intermittency in the impinging motions. Viewed alongside the lagged maps, Figure 5.18 shows that high blowing suppresses the local peak correlation at the leading edge and shortens the effective streamwise memory of the flow, which is consistent with the spanwise decoherence pathway identified in the acoustic reductions.

5.4.3.2 Coherence Analysis

To quantify how leading-edge blowing reorganises the incoming wake in space and frequency, we construct *coherence maps* from the two–point hot-wire measurements. For each grid location of the traversing probe, the complex cross-spectrum $G_{12}(f)$ and the autospectra $G_{11}(f)$, $G_{22}(f)$ are estimated from the simultaneously sampled time series (20 kHz, 5 s) using Welch averaging. The magnitude-squared coherence

$$\gamma^2(f;\Delta x,\Delta z) \;=\; \frac{|G_{12}(f)|^2}{G_{11}(f)\,G_{22}(f)}$$

is then evaluated between the traversing probe and the fixed reference probe, where $(\Delta x,\Delta z)$ denote the streamwise/spanwise separations relative to the leading-edge station.

Because the physics of interest separates into shedding-dominated tones and turbulence–interaction broadband content, we form band-averaged coherence fields by averaging γ^2 over the frequency masks defined earlier. For a frequency set $\mathcal{B}$ (either the tonal mask or the broadband band),

$$\langle\gamma^2\rangle_{\mathcal{B}}(\Delta x,\Delta z) = \frac{1}{|\mathcal{B}|}\int_{f\in\mathcal{B}} \gamma^2(f;\Delta x,\Delta z)\,\mathrm{d}f,$$

where $|\mathcal{B}| = \int_{f\in\mathcal{B}}\mathrm{d}f$ is the bandwidth. In practice, this is the arithmetic mean of γ^2 across the frequency bins within $\mathcal{B}$, giving a simple and consistent summary over the analysed band without favouring any narrow frequency region.

The result is a spatial map of coherence that directly reveals how spanwise organisation and streamwise persistence of the inflow structures change across the measurement plane, separately for tonal and broadband content. These maps are generated for the three blowing settings (baseline, $U_j/U_\infty = 0.35$, $U_j/U_\infty = 3.86$) at the anisotropic reference condition $D = 20\ \mathrm{mm}$, $x/D = 15$.

Figure 5.19 compares spanwise–streamwise maps of the magnitude–squared coherence γ^2 between the traversing probe and the near leading-edge reference probe for two band selections. Panels (a–c) show the broadband mask and panels (d–f) show the tonal mask. Within each row

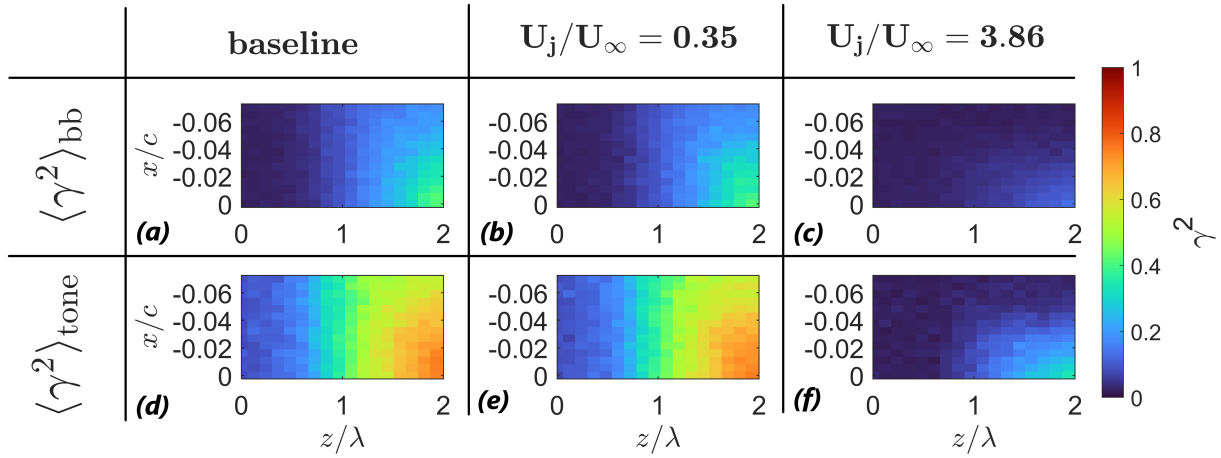

Figure 5.19: Spatial coherence maps γ^2 in the upstream measurement plane, shown for both the band-weighted tonal masks and the broadband component. Results are presented for the baseline case and the two blowing configurations ($U_j/U_\infty = 0.35$ and $U_j/U_\infty = 3.86$).

the operating point progresses from baseline [(a),(d)] to $U_j/U_\infty = 0.35$ [(b),(e)] and then to $U_j/U_\infty = 3.86$ [(c),(f)].

For the broadband selection, the baseline map exhibits a physically expected structure: coherence is largest when the probes are closest and decays as their separation increases in either direction. The peak occurs at the measurement origin near the leading-edge apex ($z/\lambda = 2,\ x/c = 0$) with $\gamma^2 \approx 0.42$, and it decreases monotonically with spanwise offset (z) and with upstream separation ($x < 0$).

Introducing weak blowing at $U_j/U_\infty = 0.35$ leaves this broadband pattern essentially unchanged: the maximum remains $\gamma^2 \approx 0.41$ at the origin and the spatial decay is almost identical to baseline. This is consistent with the acoustic result that the same low level has negligible impact on far-field noise. In contrast, high blowing at $U_j/U_\infty = 3.86$ preserves the same geometric footprint of the map but compresses its amplitude scale: the maximum drops to $\gamma^2 \approx 0.13$ at ($z/\lambda = 2,\ x/c = 0$), and the entire field is lowered. A plausible mechanism is that the jets impose strong local shear and crossflow near the slot exits that disturb the phase alignment of the incoming wake structures before they reach the leading-edge apex. The resulting spanwise phase jitter and small deflections in convective direction reduce the two-point cross-spectrum magnitude relative to the autospectra in the selected band, thus lowering γ^2 without necessarily altering the gross footprint set by probe geometry.

The tonal selection [panels (d–f)] displays the same qualitative ordering. Baseline and $U_j/U_\infty = 0.35$ are nearly indistinguishable, with a strong peak of $\gamma^2 \approx 0.76$ at ($z/\lambda = 2,\ x/c = 0$) and a gradual decay with separation, whereas $U_j/U_\infty = 3.86$ reduces the peak to $\gamma^2 \approx 0.33$ and depresses the field elsewhere. The larger baseline coherence in the tonal band compared with the broadband band reflects the coherent nature of cylinder shedding: narrowband vortical structures convect with relatively uniform phase speed and orientation, which sustains cross-probe phase locking

over longer separations. By contrast, the broadband band aggregates contributions from a wider range of scales and angles, so phase dispersion and directional spread accelerate decorrelation and yield lower γ^2 for the same separations.

In summary, the coherence maps show that $U_j/U_\infty = 3.86$ reduces the correlation of the incoming anisotropic structures at the leading-edge plane in both the broadband and tonal bands, while $U_j/U_\infty = 0.35$ does not. This reduction in γ^2 is consistent with the spanwise-decoherence pathway inferred throughout this chapter and aligns with the far-field spectra trends reported in Figure 5.13, where the highest blowing level produced the largest reductions within the broadband and tone-masked regions.

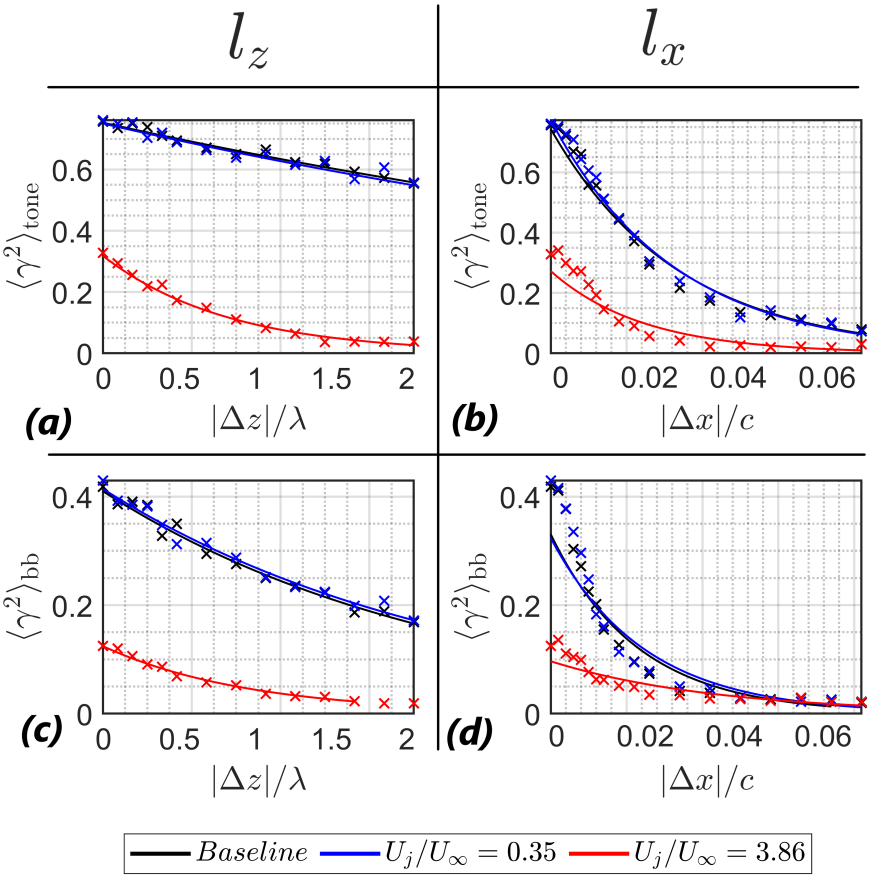

Figure 5.20: Coherence decay lengths. Panels (a) and (c) show the spanwise e-folding length l_z for the tone and broadband masks, respectively; panels (b) and (d) show the corresponding streamwise length l_x. Results are given for Baseline, $U_j/U_\infty = 0.35$, and $U_j/U_\infty = 3.86$ at the leading-edge plane.

Building on these maps, we now condense the coherence changes into a single length–scale metric by extracting spatial decay lengths of the magnitude–squared coherence. At the leading-edge plane, the reference sensor is fixed at the location of peak tonal coherence and the companion sensor is stepped along cardinal baselines in the spanwise (z) and streamwise (x) directions.

For each offset Δd the band-limited coherence $\langle \gamma^2 \rangle$ is evaluated in two ways: (i) within the tone mask that isolates the shedding peak and its near harmonics, and (ii) within the broadband mask that excludes those tones. The resulting decay curves are fitted with an exponential form,

$$\langle \gamma^2 \rangle(\Delta d) \;\approx\; \exp(-\,\beta\,\Delta d)\,,$$

from which an e-folding length $\ell = 1/\beta$ is obtained. Reporting ℓ_z and ℓ_x for the spanwise and streamwise baselines provides a compact, directionally resolved measure of the spatial footprint of the incoming coherent structures that drive leading-edge scattering. Because ℓ increases with the size and organization of these structures, comparing ℓ across the baseline, $U_j/U_\infty = 0.35$, and $U_j/U_\infty = 3.86$ cases directly quantifies how blowing modifies the effective source extent in both the tonal and broadband bands. Figure 5.20 presents these decay fits and the corresponding e-folding lengths for the four combinations (tone/BB $\times$ spanwise/streamwise), providing a quantitative bridge between the coherence maps and the far-field noise trends.

The coherence–decay fits distill the maps into a single, scale-interpretable metric: the e-folding length $\ell = 1/\beta$ from $\langle \gamma^2 \rangle(\Delta d) \approx e^{-\beta\,\Delta d}$. The values compiled in Figure 5.21 show that the highest blowing level reduces decay lengths in every category except the streamwise broadband measure $l_x^{(\mathrm{bb})}$. The spanwise result is the most consequential for leading-edge scattering: smaller l_z signifies shorter spanwise coherence and therefore a reduced effective integration length of the incoming field along the leading edge, which directly weakens the radiated power in both the tone-masked and broadband bands. In contrast, a moderate increase of l_x under high blowing is consistent with jets opposing the mean inflow near the stagnation region, stretching residual eddies in the streamwise direction without restoring their spanwise phase alignment. Because leading-edge turbulence-interaction noise is far more sensitive to spanwise coherence than to streamwise extent, the net effect remains beneficial: l_z contracts while l_x elongates, and the radiated levels drop. This pattern is fully aligned with the far-field spectra, where the highest blowing rate produced the largest reductions within the tone and broadband masks, and with the coherence maps, which showed a uniform suppression of $\langle \gamma^2 \rangle$ at the leading-edge plane under high blowing.

	$l_{z,tone}/\lambda$	$l_{x,tone}/c$	$l_{z,bb}/\lambda$	$l_{x,bb}/c$
baseline	0.233	0.844	0.077	0.573
$\mathbf{U_j/U_\infty = 0.35}$	0.224	0.816	0.080	0.615
$\mathbf{U_j/U_\infty = 3.86}$	0.028	0.612	0.033	1.098

Figure 5.21: E-folding coherence lengths from exponential fits, reported for tonal and broadband masks in the spanwise (l_z) and streamwise (l_x) directions. Cells are colour-coded relative to the baseline: green denotes a decrease (shorter coherence length), red denotes an increase.

5.5 Summary

This chapter has examined how steady leading-edge blowing modifies leading-edge broadband noise under both isotropic and anisotropic inflow, and has identified the conditions under which the technique delivers reliable acoustic benefit. Under grid-generated turbulence, the inflow characterisation showed that varying mesh size at fixed solidity alters both the turbulence intensity and integral scales at the leading-edge plane without introducing strong anisotropy: Grids 1–2 supplied higher incident energy and slightly larger integral scales than Grids 3–4, while all cases were well described by von Kármán spectra parameterised by the locally measured σ, L_x, and U_c. Within this controlled environment, performance maps demonstrated a pronounced incidence bias. For Grid 4 at $U_\infty = 30\ \mathrm{m\,s^{-1}}$, moving from $\alpha = -11.7°$ to $\alpha = -13.5°$ broadened the band of favourable response, shifted the onset of benefit to lower frequency (down to $\sim 100\ \mathrm{Hz}$), and increased peak reductions to approximately $7\ \mathrm{dB}$ over 200–$350\ \mathrm{Hz}$, with the reduction ridge sustained over a wider range of U_j/U_∞. Fixing this most effective incidence, the subsequent speed study showed that at moderate speed ($U_\infty = 20\ \mathrm{m\,s^{-1}}$) high-frequency reductions reached about $9\ \mathrm{dB}$ and grew systematically with jet ratio, while at lower speed ($10\ \mathrm{m\,s^{-1}}$) the corresponding maximum was $\sim 5.5\ \mathrm{dB}$. As U_∞ increased, the high-frequency peak gradually weakened, but a low-frequency band became increasingly amenable to control, culminating at $U_\infty = 60\ \mathrm{m\,s^{-1}}$ in reductions of up to $\sim 4.5\ \mathrm{dB}$ at a relatively modest $U_j/U_\infty \approx 0.26$. Together, these trends established that under isotropic inflow, leading-edge blowing can be tuned to deliver several decibels of broadband reduction, with the most robust envelope obtained for Grid 4 at $\alpha \approx -13.5°$, and that the controllable frequency range and required jet ratio depend systematically on flow speed.

The anisotropic rod–airfoil campaign extended these findings to a more application-relevant inflow in which a cylinder wake supplies organised shear, enhanced turbulence, and embedded shedding tones. Baseline spectra and inflow profiles showed that increasing rod diameter and adjusting the streamwise spacing $(D, x/D)$ systematically changed the energetic scales and coherence of the disturbances arriving at the leading edge. When steady blowing was introduced, band-averaged metrics revealed that broadband and tonal components respond differently. For the broadband band, the largest reduction ΔL_{bb} occurred for the thickest wake at the larger spacing, $D = 20\ \mathrm{mm}$, $x/D = 15$, with a decrease of $2.25\ \mathrm{dB}$, followed by $1.35\ \mathrm{dB}$ for $D = 15\ \mathrm{mm}$, $x/D = 15$; all remaining cases yielded $\lesssim 1\ \mathrm{dB}$, with $D = 10\ \mathrm{mm}$ essentially unchanged ($0.04\ \mathrm{dB}$). In contrast, tonal suppression ΔL_{tone} peaked at an intermediate wake strength and shorter spacing: $5.86\ \mathrm{dB}$ at $D = 15\ \mathrm{mm}$, $x/D = 10$, compared with $4.39\ \mathrm{dB}$ and $4.03\ \mathrm{dB}$ for $D = 10$ and $20\ \mathrm{mm}$ at the same spacing, and $\leq 2.62\ \mathrm{dB}$ for all cases at $x/D = 15$. Beamforming for the broadband band confirmed that the dominant source is anchored at the geometric leading edge, with the median beamformed level dropping from $46.5\ \mathrm{dB}$ in the baseline to $41.5\ \mathrm{dB}$ under the most effective blowing rate, while tonal-band maps placed the primary narrowband contribution just downstream of the rod, with a median of $50.5\ \mathrm{dB}$. These observations support a picture in which the rod provides the tonal shedding source, the leading edge radiates the broadband component, and steady blowing attenuates

the latter without displacing its spatial footprint.

The flow measurements for the anisotropic reference case ($D = 20$ mm, $x/D = 15$) provided a mechanistic link between these acoustic trends and the underlying turbulence organisation. Space–time cross-correlation maps showed that strong blowing ($U_j/U_\infty = 3.86$) compresses the spatial footprint and amplitude of correlated motion near the leading-edge apex: peak zero-lag correlations dropped from values approaching ~ 0.8 in the baseline to ~ 0.42, and the high-correlation region became more localised and less persistent in time. Coherence maps quantified the same effect in the frequency domain. For the broadband selection, the maximum magnitude-squared coherence at the leading-edge plane decreased from $\gamma^2 \approx 0.42$ in the baseline (and ≈ 0.41 at $U_j/U_\infty = 0.35$) to ≈ 0.13 at $U_j/U_\infty = 3.86$; for the tonal band, the peak dropped from $\gamma^2 \approx 0.76$ to ≈ 0.33. The associated e-folding analysis showed that the highest blowing level consistently shortened spanwise coherence lengths in both tonal and broadband masks, while changes in streamwise length were modest and in some cases slightly increased. Since leading-edge turbulence–interaction noise is far more sensitive to spanwise than to streamwise coherence, this reduction in effective spanwise integration length provides a direct and quantitative explanation for the several-decibel decreases in both broadband and tonal measures.

In combination, the chapter has shown that steady leading-edge blowing is a viable and physically interpretable strategy for mitigating leading-edge broadband noise, provided that the actuation is matched to the inflow scales and incidence. Under isotropic conditions, the most robust performance was obtained for Grid 4 at $\alpha \approx -13.5°$, with peak spectral reductions of order 7–9 dB in the most responsive bands and a clear dependence on flow speed. Under anisotropic rod–airfoil inflow, the best broadband improvement ($\Delta L_{\mathrm{bb}} = 2.25$ dB) occurred for the thickest, partially diffused wake, while tonal reductions up to 5.86 dB were achieved for an intermediate diameter and shorter spacing. Across both regimes, the results are most consistent with steady blowing reducing the spanwise coherence of the disturbances incident on the leading edge, as reflected in the coherence fields and coherence lengths, rather than being explained by turbulence-intensity changes alone.

Chapter 6

Leading Edge Blowing to Mitigate Separation-Stall Noise from Aerofoil at High Angles of Attack

6.1 Introduction

Aerofoil separation–stall noise, which typically arises under low-turbulence conditions, is an aeroacoustic phenomenon that remains comparatively under-studied. The underlying noise-generation mechanism differs from the separation-bubble noise that typically occurs at low-to-moderate angles of attack [78]. At sufficiently high angles of attack, corresponding to near-stall or fully stalled conditions, the far-field acoustic characteristics can be attributed to three mechanisms, as reported by Lacagnina *et al* [38]. These mechanisms were discussed in Chapter 2.

To mitigate separation–stall noise, permanent geometric modifications such as serrated edges are among the most effective approaches. However, serrations remain under-utilised in industry due to their detrimental impact on aerodynamic performance and potential structural vulnerabilities. Results from the previous chapters have demonstrated that low flow-rate jets delivered through small nozzles at the leading edge can reproduce similar spanwise unsteady loading variations as serrated edges. Leading edge blowing thus offers an alternative route to reproduce the serration effect while offering a dynamical tuning advantage without the liabilities of drag increase and structural vulnerability.

This chapter presents aeroacoustic validation and flow diagnostics to clarify the control mechanisms associated with leading-edge blowing for the mitigation of separation-stall noise. Section 6.2 compares the aerodynamic and acoustical behaviours of the baseline (non-blowing) aerofoil across a wide range of effective angles of attack, α_{eff}. Section 6.3 examines the influence of leading-edge blowing on the far-field noise and aerodynamic performance. The corresponding flow fields are presented in Section 6.5, where key parameters such as mean velocity, Reynolds shear stress, and the coherence between wall pressure fluctuations and vertical velocity fluctua-

tions are analysed to explore the relevant noise reduction mechanisms. Section 6.6 summarises the findings.

6.2 Baseline characterisation and regime definition

6.2.1 Baseline acoustic signature across α_{eff}

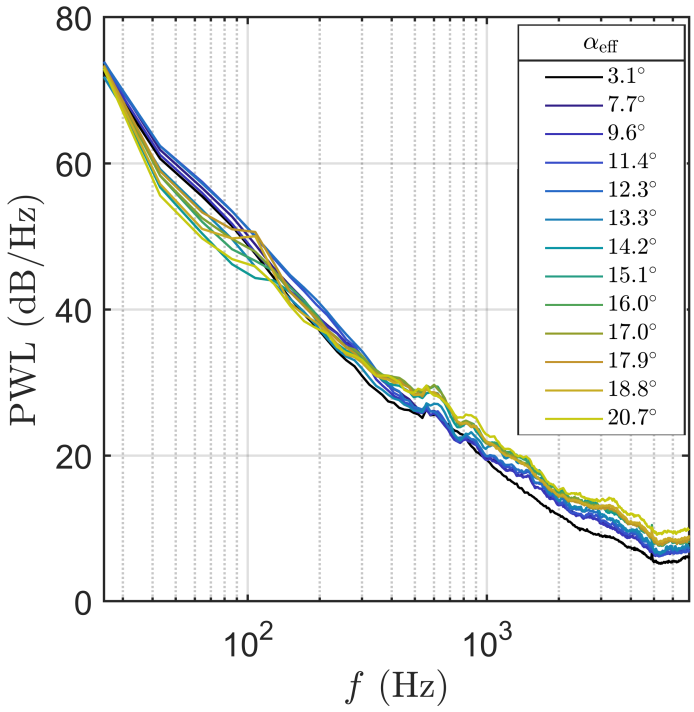

Figure 6.1: Sound power spectra PWL (dB) of the baseline NACA65(12)-10 at $3.1° \leq \alpha_{\mathrm{eff}} \leq 20.7°$.

For consistency, all the results presented herein were obtained under a freestream velocity of $U_\infty = 24\ \mathrm{m\,s^{-1}}$. Figure 6.1 presents the sound power spectra PWL (dB) of the baseline NACA65(12)-10 at $3.1° \leq \alpha_{\mathrm{eff}} \leq 20.7°$, where the PWL spectrum produced at $\alpha_{\mathrm{eff}} = 3.1°$ is chosen as the reference when comparing with other PWL spectra produced at higher angles of attack. As shown in the figure, the PWL spectra exhibit a relatively broadband characteristic across the wide range of angle of attack. The PWL spectra produced at $\alpha_{\mathrm{eff}} \leq 12.3°$ are herein denoted as Group 1, while Group 2 refers to the PWL spectra beyond that. From the figure, Group 1 produces higher PWL levels than the reference case at $\alpha_{\mathrm{eff}} = 3.1°$ across most of the frequency range, as reflected by the relative level differences between spectra. However, in Group 2 (higher loading / near- and post-stall), the baseline spectra exhibit two notable frequency regimes, which later provide a useful basis for interpreting the effects of leading-edge blowing:

1 At low frequency (typically $f < 100$ Hz), while the PWL levels in Group 1 are generally higher,

further increases in angle of attack into Group 2 cause a sudden drop in PWL by up to 8 dB.

2 Following the low-frequency dip, the spectra recover for $f > 200$ Hz and exceed Group 1 levels for $f > 400$ Hz.

As will be shown later, Group 1 encompasses both the pre-stall and stall regime for the aerofoil. The results in Figure 6.1 demonstrates that, when the loading on the aerofoil increases, the noise level also increases across a large frequency range. This seemingly linear relationship breaks down at low frequency when a critical angle of attack is reached, i.e. $\alpha_{\text{eff}} = 12.3°$, which is identified as the stall-onset (incipient stall) condition.

6.2.2 Baseline aerodynamic indicators: C_p, C_L, and ΔOAPWL

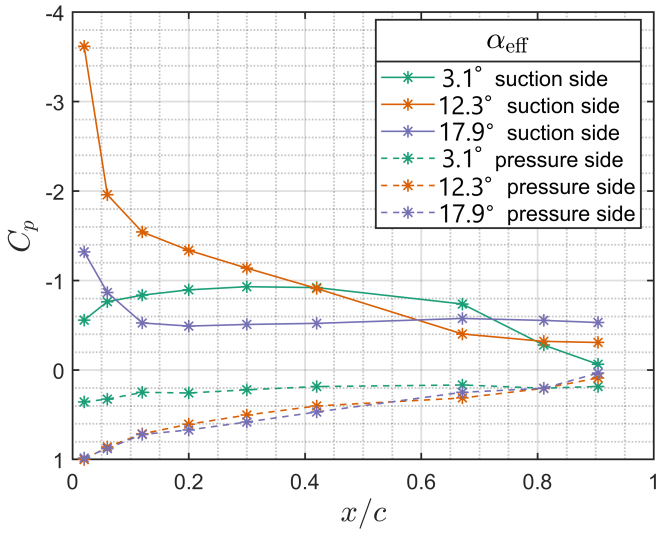

Figure 6.2: Distributions of pressure coefficients C_p on the suction side and pressure side of aerofoil at $\alpha_{\text{eff}} = 3.1°, 12.3°$ and $17.9°$

To provide an indication of the aerodynamic behaviours for the NACA65(12)-10 at both the pre-stall and post-stall regimes, Figure 6.2 shows the distributions of pressure coefficient C_p on the suction side and pressure side of aerofoil at $\alpha_{\text{eff}} = 3.1°, 12.3°$ and $17.9°$. In the context of separation stall noise, the analysis will focus on the pressure coefficients on the suction side. For the reference case at $\alpha_{\text{eff}} = 3.1°$, C_p increases steadily near the leading edge down to $x/c \approx 0.42$ due to the adverse pressure gradient effect where $\mathrm{d}p/\mathrm{d}x > 0$. Beyond that, the C_p begins to decay and experiences a large drop towards the trailing edge.

At $\alpha_{\text{eff}} = 12.3°$, the C_p predominantly decays from the leading edge down to $x/c = 0.65$. From there onward, the C_p remains constant. The near-constant C_p is a common signature of local boundary-layer separation. Therefore, $\alpha_{\text{eff}} = 12.3°$ represents a stall-onset (incipient separation) condition.

At $\alpha_{\text{eff}} = 17.9°$, the C_p mostly exhibits a flat-lining characteristic across much of the suction surface. This is a strong indication that, at this particular angle of attack, the boundary layer at the suction surface has entered a post-stall regime.

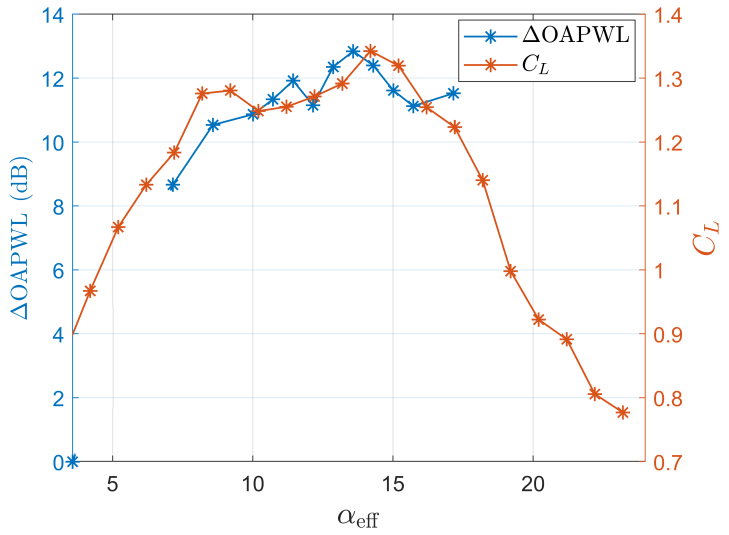

Figure 6.3: Comparison between ΔOAPWL and C_L across the angle of attack

After establishing the individual trends of acoustic and aerodynamic responses against the angles of attack, it is of interest to investigate whether there is any correlation between the two. Figure 6.3 compares the ΔOAPWL and C_L across a large range of α_{eff}. Note that ΔOAPWL is the difference in overall sound power levels between the reference value at $\alpha_{\text{eff}} = 3.1°$ and that produced at a particular α_{eff}. The lift coefficients C_L were measured directly from force balance. While the limits of y-axis for both the ΔOAPWL (LHS) and C_L (RHS) in Figure 6.3 are adjusted to facilitate a better visual comparison, the strong correlation between them is well demonstrated. This indicates that the overall noise level produced by an aerofoil is considerably influenced by its aerodynamic loading.

6.3 Aerodynamic response to leading-edge blowing

Several characteristics of aerofoil noise under the pre-stall, stall and post-stall regimes have been demonstrated in the previous section. This section investigates the effect of leading edge blowing on the far field and aerodynamic behaviours of stalled and post-stalled aerofoil. The stall-onset condition is established at around $\alpha_{\text{eff}} = 12.3°$. On the other hand, $\alpha_{\text{eff}} = 17.9°$ is chosen as a representative for the post-stall angle.

In reference to the inlet freestream velocity U_∞, the effect of leading edge blowing is investigated at three non-dimensionalised blowing speeds, U_j/U_∞ = 0.35, 2.10 and 3.89, which can be loosely interpreted as low, medium and high jet ratios, respectively.

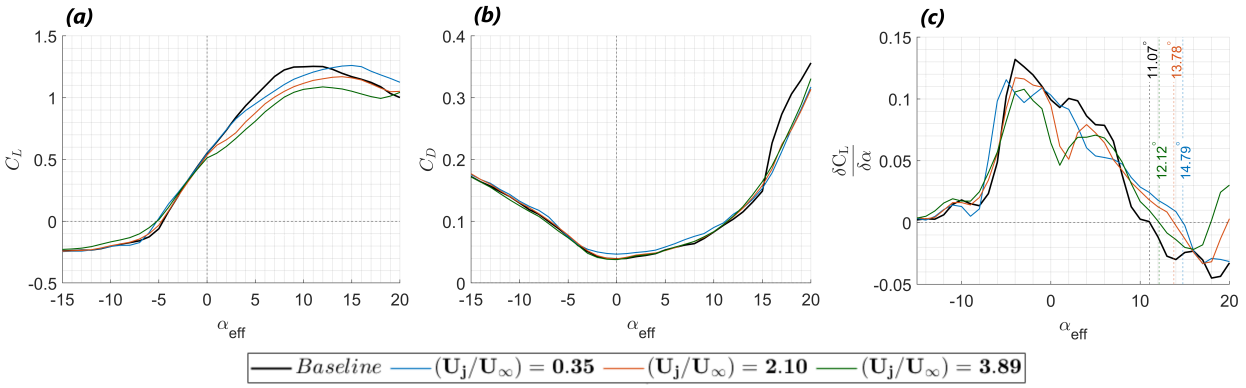

Figure 6.4: Effects of leading edge blowing ratios (U_j/U_∞ = 0.35, 2.10 and 3.89) for (a) C_L, (b) C_D and (c) $dC_L/d\alpha_{eff}$ against effective angles of attack α_{eff}

Figure 6.4 shows the lift coefficients C_L, drag coefficients C_D and $dC_L/d\alpha_{eff}$ against effective angles of attack α_{eff}. In Figure 6.4(a), thin aerofoil theory (i.e. C_L gains 0.1 for every increase of 1 degree α_{eff}) establishes at $-5° \leq \alpha_{eff} \leq 5°$. At the very large negative angles of attack range, the increase of C_L with respect to α_{eff} is very slow. On the other hand, at $\alpha_{eff} > 5°$, deviation against the thin aerofoil theory begins to emerge, which also indicates the emergence of unstable boundary layer at the suction side. By examining Figure 6.4(c), $dC_L/d\alpha_{eff} < 0$ can be interpreted as the instance when a complete stall occurs. This is found to occur at $\alpha_{eff} = 11.07°$, which is consistent with that obtained from the acoustic analysis performed earlier in Section 6.2. The small difference reflects the use of different stall indicators (force-balance slope change versus spectral transition), both pointing to stall onset near $\alpha_{eff} \approx 11°$.

Analysis of the effect of leading edge blowing in Figure 6.4(a) starts with the highest blowing ratio at U_j/U_∞ = 3.89. It is clear that adopting such a high blowing jet at the leading edge is counter-productive as far as the lift coefficient is concerned. While the C_L produced at $\alpha_{eff} < 0°$ remains largely unchanged, deviation against the baseline case is obvious and consistent throughout the positive α_{eff} where significant lower level of lift coefficient is produced. Nevertheless, high blowing ratio of U_j/U_∞ = 3.89 can still improve slightly the stall angle. As shown in Figure 6.4(c), $dC_L/d\alpha_{eff} < 0$ occurs at $\alpha_{eff} = 12.12°$, which is slightly higher than the baseline one.

Changing to the medium blowing ratio of U_j/U_∞ = 2.10 could improve the absolute level of lift coefficients compared to the one with the highest blowing ratio, but still inferior to the baseline aerofoil. On the other hand, the stall angle under the medium blowing ratio follows the same trend and further increases to $\alpha_{eff} = 13.78°$ (see Figure 6.4(c)).

The lowest blowing ratio of U_j/U_∞ = 0.35, unlike the highest and medium blowing ratios discussed earlier, represents the case where the blowing jet from the leading edge has a lower speed than the incoming freestream velocity. Interestingly, the lowest blowing jet can maintain the same C_L level as the baseline aerofoil up to $\alpha_{eff} = 3°-$ an improvement compared to the highest and medium blowing jets. More importantly, the stall angle for the lowest blowing jet is further improved

to $\alpha_{\text{eff}} = 14.79°$. At this stall angle, the level of C_L produced by the lowest blowing jet is even slightly higher than that produced by the baseline aerofoil.

In summary, while stall was delayed, the maximum C_L values achieved were progressively reduced with increasing blowing ratios, with the case of $U_j/U_\infty = 3.89$ exhibiting the largest reduction (up to 0.2). This suggests that although the leading edge blowing can mitigate the stall, it may introduce trade-offs in lift generation at higher blowing rates.

The drag coefficient C_D trends indicate that for all the leading edge blowing ratios, the values remain relatively similar to the baseline condition, except at very high angles of attack ($\alpha_{\text{eff}} > 15°$) where the leading edge blowing reduces the drag coefficient from the baseline level. This suggests that the blowing system does not significantly affect drag under most conditions, but its positive influence becomes more pronounced at the post-stall regime. Note that, with the lowest blowing ratio of $U_j/U_\infty = 0.35$, higher drag coefficient is produced at the pre-stall and stall regimes.

6.4 Far-field acoustic response under leading-edge blowing

6.4.1 Stall-onset: $\alpha_{\text{eff}} = 12.3°$

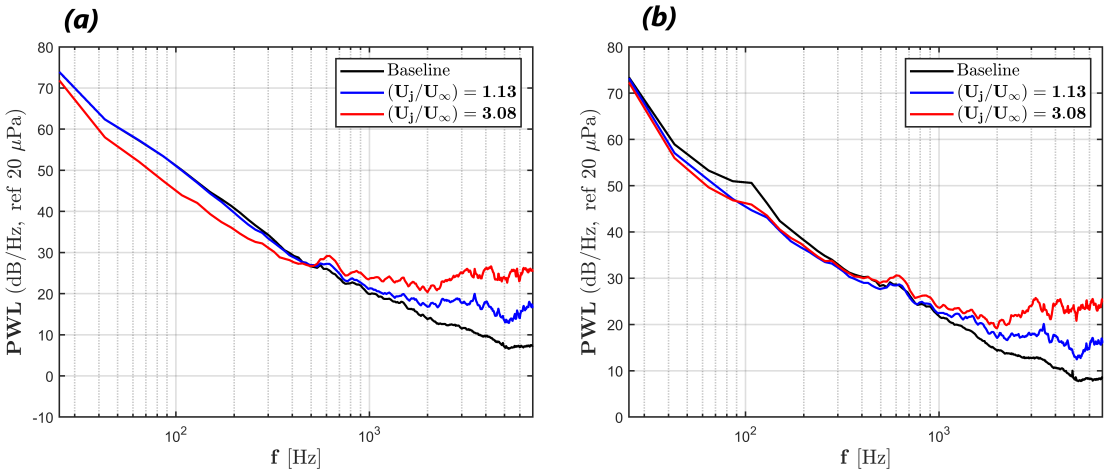

Figure 6.5: Far field sound power level (PWL) produced by the baseline ($U_j/U_\infty = 0$), $U_j/U_\infty = 1.13$ and $U_j/U_\infty = 3.08$ at α_{eff} = (a) $12.3°$ and (b) $17.9°$

The aerodynamic polars in Figure 6.4 were obtained in a force-balance campaign at three representative jet ratios ($U_j/U_\infty = 0.35,\ 2.10$ and 3.89). The far-field acoustic measurements and the accompanying hot-wire and wall-pressure diagnostics were acquired in a separate campaign, for which the closest repeatable operating points were $U_j/U_\infty = 1.13$ and 3.08. These cases are therefore used below to interrogate the flow–acoustic mechanisms at moderate and high forcing; the discussion focuses on qualitative changes rather than a one-to-one parametric comparison at identical U_j/U_∞. To further elucidate the trends observed in Figure 6.4 regarding the influence of leading edge blowing on the aerodynamic performances, far field acoustic measurements were

conducted. Figure 6.5 presents the sound power spectra for blowing ratios $U_j/U_\infty = 1.13$ and 3.08 at $\alpha_{\text{eff}} = 12.3°$ and $17.9°$, where previous aerodynamic measurements confirmed stall and post-stall characteristics, respectively, in the baseline case.

For the stall regime at Figure 6.5(a), using a blowing ratio of $U_j/U_\infty = 1.13$ does not seem to affect the noise radiation much, except at $f > 500$ Hz where noise increase can be observed. Such increase is attributed to the contribution of jet self-noise, which begins to dominate the spectrum at higher frequencies. On the other hand, using a higher blowing ratio of $U_j/U_\infty = 3.08$ can significantly reduce the far field noise at $f < 500$ Hz by up to 5 dB. The contribution of jet self-noise at higher frequency is expectedly more pronounced for the higher blowing ratio.

6.4.2 Post-stall: $\alpha_{\text{eff}} = 17.9°$

For the post-stall regime at Figure 6.5(b), noise reduction at $f < 500$ Hz can be achieved by both blowing ratios $U_j/U_\infty = 1.13$ and 3.08. Similarly, jet self-noise becomes evident at $f > 500$ Hz.

It is noteworthy that, within the stall regime, a higher blowing ratio is more effective than a lower one for reducing broadband noise at $f < 500$ Hz. This differs from the trend suggested by Figure 6.4, where a lower blowing ratio is more favourable for increasing the lift coefficient C_L. Since the aerodynamic polars and the acoustic/flow diagnostics were obtained in different campaigns with different available jet-ratio operating points, a direct one-to-one comparison at identical U_j/U_∞ is not implied here. Although Figure 6.3 shows that stall noise generation correlates with aerodynamic lift for the baseline aerofoil, the mechanisms responsible for lift enhancement and stall-noise mitigation under leading edge blowing may differ.

It is emphasised that the noise-mitigation benefit discussed here concerns the low-frequency band associated with separated-flow dynamics (typically $f < 500$ Hz), whereas the high-frequency portion increasingly reflects the contribution of jet self-noise.

6.5 Flow diagnostics at stall-onset and proposed mechanism

6.5.1 Mean flow topology

While leading edge blowing has been positively identified as an effective active control method to enhance the aerodynamic performance and mitigate the acoustical radiation of aerofoil at both the stall and post-stall regimes, the underlying flow physics and mechanisms remain of interest for further investigations. Detailed hot-wire and wall-pressure coherence diagnostics are presented for the stall-onset condition ($\alpha_{\text{eff}} = 12.3°$), where repeatable flow structure and clear acoustic changes were obtained; the post-stall case is discussed primarily in terms of integrated aerodynamic and far-field acoustic response.

Figure 6.6 presents the contours of mean longitudinal velocity ($\overline{u}$) in the $y-z$ spanwise planes at $\alpha_{\text{eff}} = 12.3°$ for blowing ratios of $U_j/U_\infty = 0\ (\text{baseline}), 1.13$ and 3.08. Reference can be made against the associated far field radiated spectra shown in Figure 6.5(a). For the baseline case

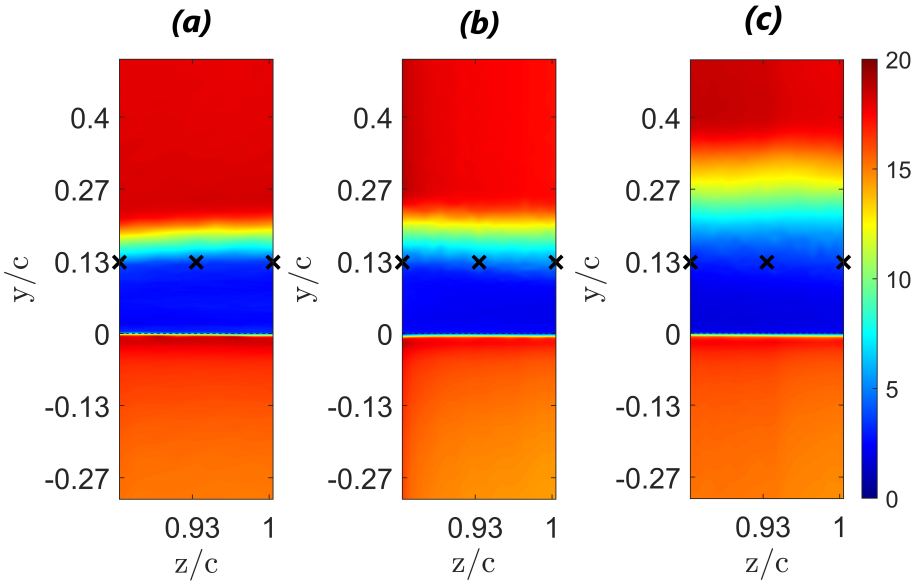

Figure 6.6: Contours of mean longitudinal velocity ($\overline{u}$) in the $y-z$ spanwise planes at $\alpha_{\text{eff}} = 12.3°$ for blowing ratios of (a) $U_j/U_\infty = 0$ (baseline), (b) $U_j/U_\infty = 1.13$ and (c) $U_j/U_\infty = 3.08$. The asterisks indicated in the contours represent the location of the blowing orifices, where $y = 0$ represents the location of the trailing edge, and the contours are measured at $x/c = 1.01$

in Figure 6.6(a), a significant and spanwise-uniform "dead air" zone can be found on the suction surface at approximately $0 < y < 20$ mm. Such a relatively thick zone demonstrates that boundary layer separation has already commenced at some distances upstream of the trailing edge. This is demonstrated vividly in Figure 6.7(a) for the corresponding mean longitudinal velocity ($\overline{u}$) in the $y - x/c$ streamwise plane. Based on the C_p distribution in Figure 6.2, the separation point could occur at $x/c = 0.65$. The absence of negative $\overline{u}$ in the nominal reverse-flow region reflects the lack of directional sensitivity of the single hot-wire probes; consequently, the analysis below focuses on the shear-layer location and turbulence metrics rather than the magnitude of reverse flow. The separating shear layer is located at $20 \text{ mm} < y < 30$ mm, as reflected by the presence of velocity gradient. Beyond that, at $y > 30$ mm, the flow field is dominated by potential flow.

The contour of mean longitudinal velocity ($\overline{u}$) under a leading edge blowing ratio of $U_j/U_\infty = 1.13$ is shown in Figure 6.6(b). Overall, the mean flow characteristics are not significantly different from the baseline aerofoil case described in the previous paragraph. Interestingly, the $\overline{u}$ contour in the $y - z$ plane does not exhibit any undulated pattern that is otherwise expected for a leading edge with active blowing holes distributed discretely along the spanwise direction. Examination of the streamwise $y - x/c$ plane in Figure 6.7(b) only reveals a very slight vertical displacement of the separating shear layer while other characteristics remain largely the same as the baseline case. The similarity in the mean longitudinal velocity between the two is reflected in the acoustic field (see Figure 6.5a). Overall, leading edge with a medium blowing rate at the stall regime does not seem to alter both the flow and acoustic fields significantly.

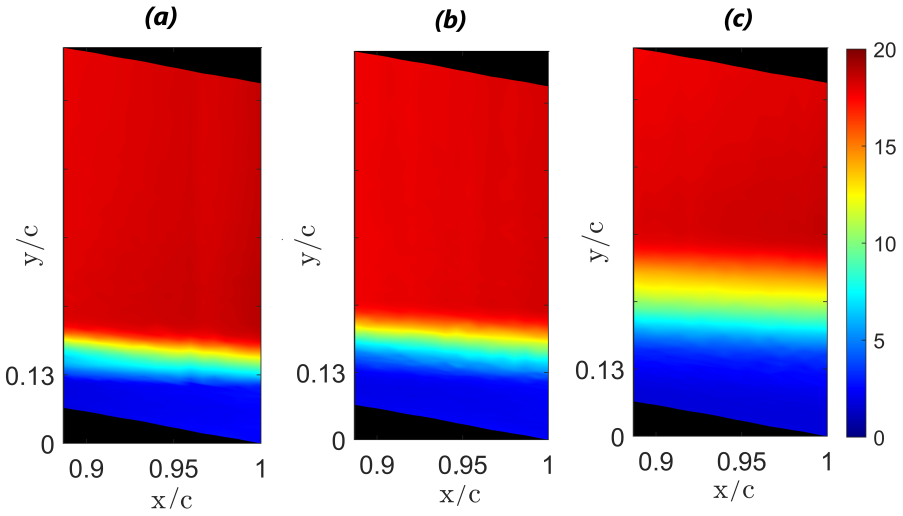

Figure 6.7: Contours of mean longitudinal velocity ($\overline{u}$) in the $y - x/c$ streamwise planes at $\alpha_{\text{eff}} = 12.3°$ for blowing ratios of (a) $U_j/U_\infty = 0$ (baseline), (b) $U_j/U_\infty = 1.13$ and (c) $U_j/U_\infty = 3.08$. The streamwise planes align with one of the leading edge orifices (marked by the asterisks in Figure 6.6)

For higher blowing ratio of $U_j/U_\infty = 3.08$ at the leading edge, the mean longitudinal velocity ($\overline{u}$) in both the $y - z$ spanwise plane (Figure 6.6c) and $y - x/c$ streamwise plane (Figure 6.7c) are quite different from the baseline aerofoil. First, the "dead air" separated zone has been enlarged. Second, the separating shear layer not only has been displaced further upwards, but it is also more stretched and spread out. These features reflected in the mean longitudinal velocity ($\overline{u}$) are inconsistent as the leading edge with high blowing ratio seem to actually enhance the boundary layer separation rather than suppressing it. However, the acoustic response differs because reduction of separation noise at $f < 500$ Hz is observed in Figure 6.5(a). This indicates that the low-frequency acoustic benefit is more consistent with changes in separating-shear-layer turbulence and its near-wall coupling than with a reduction in the mean separated-region extent.

6.5.2 Turbulence statistics and quadrant analysis

While the above analysis focuses on the mean properties of the flow field, the turbulence characteristics should also be investigated. Figure 6.8 shows the streamwise plane $y-x/c$ in the contexts of Reynolds shear stress $-\rho u'v'$ and vertical velocity fluctuation v_{rms}. For the baseline aerofoil in Figure 6.8(a), the Reynolds shear stress $-\rho u'v'$ at the previously identified flow separation zone is close to zero. However, the separating shear layer exhibits dominant negative Reynolds shear stress $\rho u'v'$, which becomes positive contour level under the representation of $-\rho u'v'$ in the figure. The figure is also embedded with a vertical broken line representing the $-\rho u'v'$ value at $x/c = 0.95$. From the figure, positive Reynolds shear stress $-\rho u'v'$ at the separating shear layer is mainly contributed by the Q2 ($u' < 0, v' > 0$) and Q4 ($u' > 0, v' < 0$) events in the quadrant

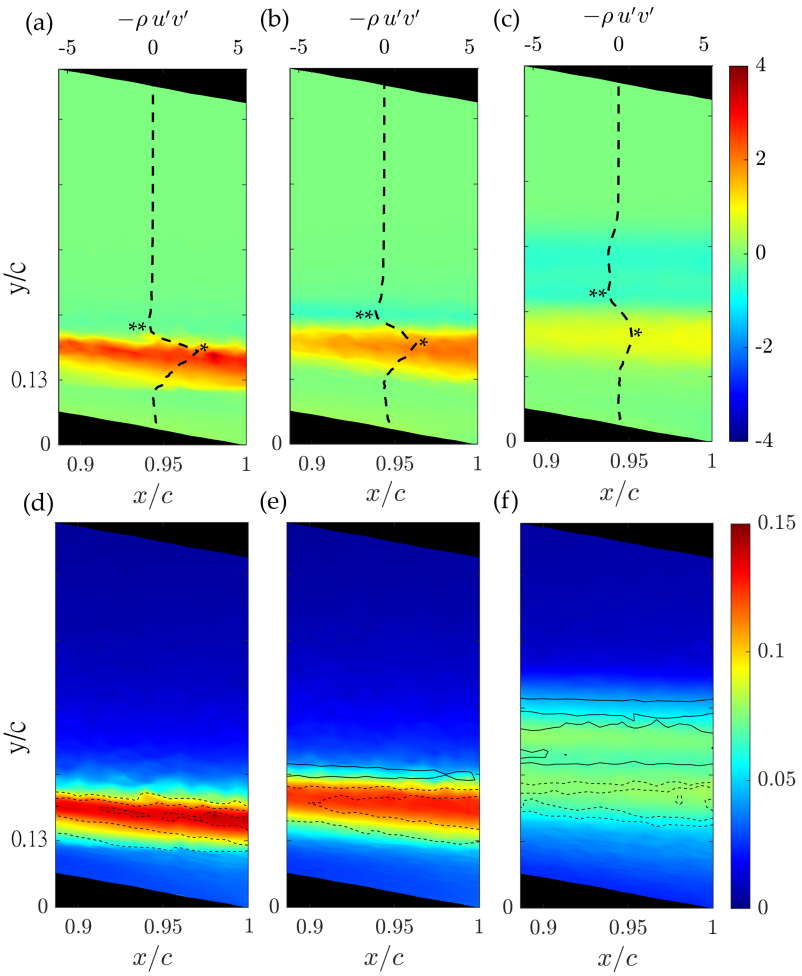

Figure 6.8: Contours of (a−c) Reynolds shear stress $-\rho u'v'$ and (d−f) vertical velocity fluctuation v_{rms} in the $y - x/c$ streamwise planes at $\alpha_{\text{eff}} = 12.3°$ for blowing ratios of (a, d) $U_j/U_\infty = 0$ (baseline), (b, e) $U_j/U_\infty = 1.13$ and (c, f) $U_j/U_\infty = 3.08$. The streamwise planes align with one of the leading edge orifices (marked by the asterisks in Figure 6.6)

analysis. Essentially, Q2 is associated with lifting up of low momentum fluids away from the wall (ejection), while Q4 is the opposite where high momentum fluids is accelerating towards the wall (sweep). These two quadrants are dominant in the turbulence generation compared to the other two quadrants Q1 (outward) and Q3 (inward). Figure 6.8(d) shows the v_{rms} for the baseline aerofoil. The superimposed Reynolds shear stress contour lines overlap with the dominant region of v_{rms}. As expected, both the Reynolds shear stress and vertical velocity fluctuation are negligible in the freestream flow.

When a medium blowing ratio $U_j/U_\infty = 1.13$ is applied at the leading edge, there are no significant changes for both the Reynolds shear stress (Figure 6.8b) and vertical velocity fluctuation (Figure 6.8e) compared to the baseline case. This is in agreement with the far field noise in Figure 6.5(a) whose spectra characteristics remain the same for both, except at $f > 500$ Hz where the jet self-noise eventually takes over. However, a noticeable negative streak of $-\rho u'v'$ can be found

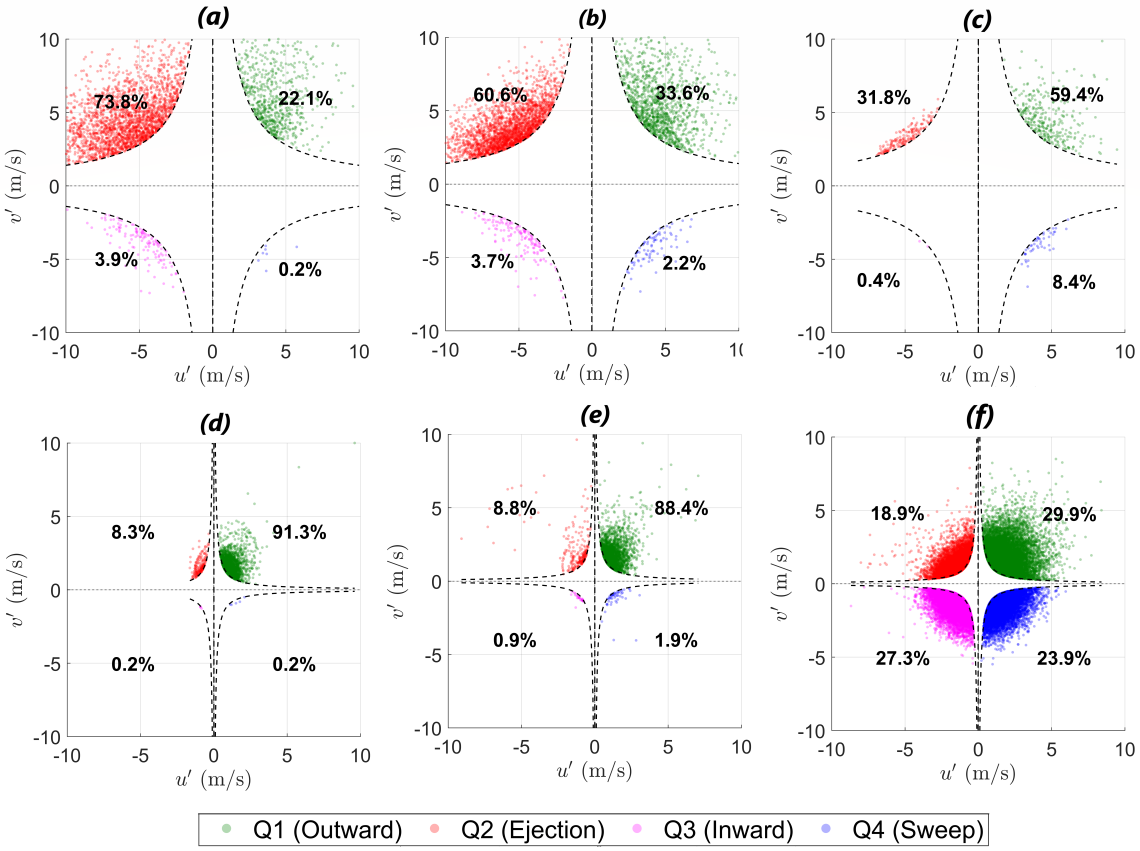

Figure 6.9: Quadrant analysis pertaining to the (a−c) positive $-\rho u'v'$ peaks (*) and (d−f) negative $-\rho u'v'$ peaks (**) in reference to Figure 6.8 at $\alpha_{\text{eff}} = 12.3°$ for blowing ratios of (a, d) $U_j/U_\infty = 0$ (baseline), (b, e) $U_j/U_\infty = 1.13$ and (c, f) $U_j/U_\infty = 3.08$. Note that the hyperbola curves in each figure represent the $|u'v'| > H \cdot u_{\text{rms}} \cdot v_{\text{rms}}$ pertaining to the baseline aerofoil level, where $H = 4$

atop the separating shear layer.

When a high blowing ratio $U_j/U_\infty = 3.08$ is applied at the leading edge, both the Reynolds shear stress (Figure 6.8c) and vertical velocity fluctuation (Figure 6.8f) undergo significant changes. For the $-\rho u'v'$, the Reynolds shear stress level pertaining to the separating shear layer is reduced. On the other hand, the negative streak that was previously identified in the medium blowing case has now become more significant both for the shear stress level and overall size. Examination of the corresponding v_{rms} also reveals a significant reduction of the turbulence level. These phenomena indeed corroborate with the far field spectra in Figure 6.5(a) where reduction of noise at $f < 500$ Hz can be achieved by the leading edge blowing.

The negative streaks identified in both the medium and high leading edge blowing cases warrant further investigation. The opposite sign in Reynolds shear stress of the negative streaks compared to the separating shear layer suggests that it is associated to, and possibly produced by the leading edge blowing. Figure 6.9 presents the quadrant diagram pertaining to the positive $-\rho u'v'$ peaks (marked by single asterisk in Figure 6.8) and negative $-\rho u'v'$ peaks (marked by

double asterisk in Figure 6.8) for the baseline case and two blowing ratios of $U_j/U_\infty = 1.13$ and 3.08. The hyperbola curves in each figure represent the $|u'v'| > H \cdot u_{\rm rms} \cdot v_{\rm rms}$ pertaining to the baseline aerofoil level, where $H = 4$. The use of such a threshold for $|u'v'|$ is adopted to filter out low-intensity events when estimating the relative quadrant contributions to the Reynolds shear stress. The conclusions drawn from Figure 6.9 are based on the relative changes between cases, rather than the absolute percentage values.

For the baseline and medium blowing ratio cases in Figure 6.9(a) and (b) pertaining to the positive $-\rho u'v'$ peaks, Q2 quadrant event (ejection) dominates the dynamics with a low level of contribution from the Q1 event (outward). However, at high blowing ratio in Figure 6.9(c), the turbulence generating quadrant Q2 experiences a significant drop in percentage. On the other hand, the Q1 event that does not contribute much to the turbulence generation now possesses the largest percentage, albeit the u' and v' distributions in this quadrant remain low in comparison with the baseline and $U_j/U_\infty = 1.13$ cases.

For the baseline and medium blowing ratio cases in Figure 6.9(d) and (e) pertaining to the negative $-\rho u'v'$ peaks, the local Reynolds shear stress is very low. The distribution of the u' and v' seems to focus mainly in Q1. Interestingly, for the high blowing case in figure 6.9(f), all four quadrants take almost an equal share of the u' and v'.

When the aerofoil is set at a positive angle of attack, the high momentum blown jet (i.e. $u' > 0$) from the leading edge will naturally be pointing upwards (i.e. $v' > 0$) with an inclined angle, promoting Q1 event as a result. The blown jet direction will also be opposing the incoming main flow, and may promote vortical structures consistent with Kelvin–Helmholtz-type instability. These secondary flow structures will then propagate along the main flow towards the trailing edge, potentially acting as a partial neutraliser when interacting with the separating shear layer due to the opposite sign of the Reynolds shear stress. Although the leading edge blowing does not seem to be able to completely suppress the boundary layer separation in the stall regime, the secondary flow structure generated by leading edge blowing with high blowing ratio is still capable of reducing turbulence level in the separating shear layer, thereby reducing the near-wall coupling and the transmission of boundary layer velocity fluctuation to the wall pressure and noise radiation.

6.5.3 Near-wall coupling: p'–v' coherence

To elucidate the relationship between the boundary-layer vertical velocity fluctuation $v'(t)$ and unsteady wall pressure $p'(t)$, a coherence study between these time-resolved signals was performed for the baseline aerofoil, as well as those subjected to leading edge blowing ratios of $U_j/U_\infty = 1.13$ and $U_j/U_\infty = 3.08$. For the baseline aerofoil results shown in Figure 6.10(a), a high-coherence region can be found at $100 < f < 500$ Hz at wall-normal locations in the vicinity of the peak vertical velocity fluctuations (i.e. near the $v_{\rm rms}$ maximum identified from Figure 6.8d). The coherence result strongly suggests that the dominant unsteady wall-pressure fluctuations are coupled to velocity fluctuations within the separating shear layer. The outlook is similar for the leading edge blowing with medium blowing rate (Figure 6.10b). However, the coherence level is noticeably

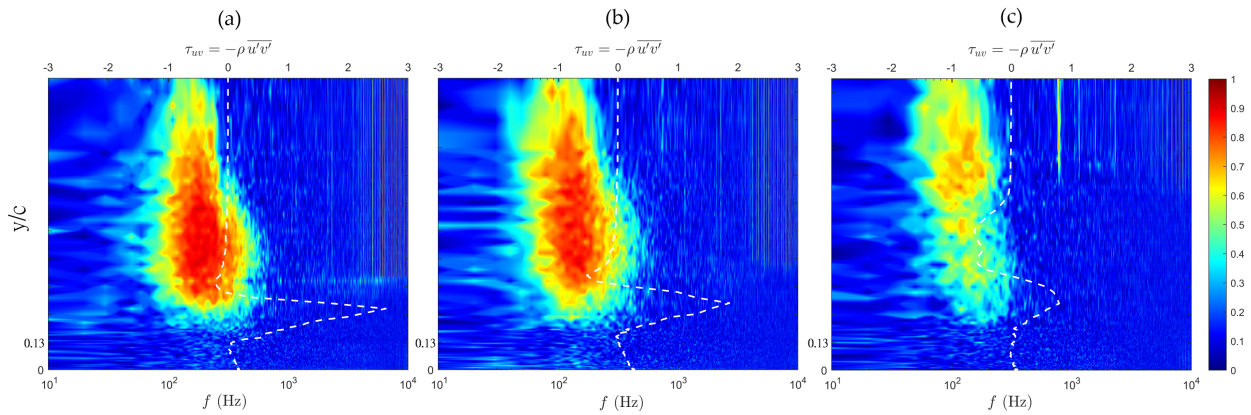

Figure 6.10: Magnitude-squared coherence between the wall-pressure fluctuation $p'(t)$ and the vertical velocity fluctuation $v'(t)$ measured across the boundary layer at $x/c = 0.95$ with $\alpha_{\text{eff}} = 12.3°$ for blowing ratios of (a) $U_j/U_\infty = 0$ (baseline), (b) $U_j/U_\infty = 1.13$ and (c) $U_j/U_\infty = 3.08$.

lower for the high blowing case in Figure 6.10(c), over the same frequency band in which far-field noise reduction is observed in Figure 6.5(a). This provides a direct link between reduced near-wall coupling and the measured reduction in radiated noise. The concurrent reduction in far-field levels and in p'–v' coherence over the same frequency band supports a genuine source modification rather than spectral contamination by jet self-noise.

6.6 Summary

The results presented thus far demonstrate the potential of leading edge blowing as a means to influence separated-flow behaviour on an aerofoil. Although leading edge blowing does not completely suppress separation in the stall regime, the secondary flow structures generated at higher blowing ratios are still effective in weakening the turbulence within the separating shear layer. This reduces the transmission of boundary layer velocity fluctuations into wall pressure fluctuations, thereby lowering the resulting noise radiation.

It is important to recognise that the present study, in which the discharge jet angle is fixed and varies implicitly with the angle of attack, does not constitute an optimisation study. The ability to generate a vectored discharge jet at the leading edge represents a key optimisation parameter that warrants investigation in future work.

Chapter 7

Conclusion and Further Work

7.1 Chapter 4: Influence of Leading-edge Blowing on Trailing Edge Tonal Noise

The main outcomes of the tonal-noise study with leading-edge (LE) blowing on the NACA 65-series airfoil can be summarised as follows:

- **Baseline tonal mechanism**
  - At $U_\infty = 20\ \mathrm{m/s}$ a strong trailing-edge tonal peak ($4 \leq St \leq 10$, $\approx 46\ \mathrm{dB}$) is governed primarily by a suction-side laminar separation bubble; the pressure side is largely acoustically passive except at high incidence.
- **Effect of LE blowing on tonal levels**
  - LE blowing is weakly effective at negative/near-zero incidence, but at high positive incidence it can reduce the tonal peak by up to $\sim 25\ \mathrm{dB}$.
  - The benefit is non-monotonic in U_j/U_∞: an optimum occurs near $U_j/U_\infty \approx 0.35$–$0.5$, while higher jet ratios reintroduce low-frequency broadband noise.
- **Amplitude suppression versus mode replacement**
  - At optimal blowing, the tonal frequency is preserved but loop gain collapses (amplitude suppression without detuning).
  - At high blowing, the original tone is replaced by lower-frequency, broadband-dominated unsteadiness ($St \approx 1$).
- **Wake structure and three-dimensional entrainment**
  - Maximum tonal suppression coincides with a thin, nearly symmetric wake and modestly reduced vorticity, whereas high blowing produces an over-thickened, fragmented wake that favours low-frequency noise.

  - Jet-induced vortical structures form near the LE, extend over much of the chord on both sides, and destabilise the suction-side bubble despite the jets being nominally on the pressure side.

- **Hydrodynamic–acoustic coherence and control mechanism**
  - The baseline exhibits near-unity coherence between near-wall velocity, wall pressure and far-field sound at the tonal frequency, confirming a tightly phase-locked feedback loop.
  - Optimal LE blowing ($U_j/U_\infty \approx 0.35$) collapses this coherence to $\gamma^2 \lesssim 0.1$ while keeping broadband levels moderate, whereas high blowing suppresses tonal coherence but introduces a new low-frequency coherent band.

7.2 Chapter 5: Influence of Leading-edge Blowing on Leading Edge Broadband Noise

The leading-edge broadband noise (LEBN) study demonstrates that steady leading-edge blowing can provide repeatable broadband noise reductions when the actuation is matched to the inflow scales, angle of attack, and wake topology. The principal findings are:

- **Isotropic inflow: baseline and incidence effects**
  - Four grids with identical solidity but different mesh scales produced two inflow families at the leading-edge plane: a higher-intensity, larger-scale pair and a lower-intensity, smaller-scale pair, all well described by von Kármán-type models.
  - Leading-edge blowing was strongly incidence dependent. For Grid 4, moving from weakly negative to more negative incidence shifted the benefit into a broad band from about 100 to 800 Hz and, at $\alpha \approx -13.5°$, yielded peak reductions of about 7 dB over 200 to 350 Hz with a wide usable range of U_j/U_∞.

- **Isotropic inflow: speed-dependent control regimes**
  - At fixed Grid 4 and $\alpha \approx -13.5°$, varying U_∞ from 10 to $60\ \mathrm{m\,s^{-1}}$ revealed two controllable bands: a high-frequency band that was most responsive at low to moderate speeds, and a low-frequency band that became progressively more controllable as speed increased.
  - These trends support a speed-aware strategy: at low to moderate U_∞ use higher U_j/U_∞ to target high-frequency content, while at higher U_∞ smaller jet ratios are sufficient to reduce low-frequency energy carried by larger outer-layer structures.

- **Anisotropic inflow: rod–airfoil baseline and tonal–broadband separation**

  - An upstream cylinder generated an anisotropic wake with clear shedding tones and elevated turbulence at the leading edge, controlled by diameter D and spacing x/D.
  - Rod-only, airfoil-only and combined spectra were used to build tonal masks and a clean broadband band, confirming that tones originate from the cylinder while the broadband rise in the combined case is due to gust–leading-edge interaction.

- **Anisotropic inflow: spectral response and compressed metrics**
  - Increasing U_j/U_∞ systematically reduced both tonal and broadband levels for all $(D, x/D)$, although very strong blowing sometimes added a small low-frequency rise.
  - Broadband reductions were largest for the thickest, partially diffused wake ($D = 20$ mm, $x/D = 15$, about 2.25 dB), whereas tonal reductions were largest for an intermediate wake strength at shorter spacing ($D = 15$ mm, $x/D = 10$, about 5.9 dB), reflecting different sensitivities of broadband and tonal mechanisms.
  - Beamforming confirmed that tones are dominated by the rod region, while broadband LEBN is anchored at the geometric leading edge; effective blowing reduces the leading-edge source level without shifting its location.

- **Anisotropic inflow: correlation, coherence and coherence length**
  - Space–time cross-correlation maps showed that high blowing reduces the peak correlation near the apex and shrinks the spatial footprint of coherent structures relative to baseline and low blowing.
  - Band-averaged coherence maps and e-folding lengths demonstrated that effective blowing significantly lowers magnitude-squared coherence and shortens spanwise coherence lengths in both tonal and broadband bands, while streamwise coherence changes are weaker and sometimes slightly increased.
  - The combined reduction of coherence and spanwise coherence length provides a quantitative explanation for the observed order 1 to 2.5 dB broadband reductions and order 4 to 6 dB tonal reductions in the most responsive anisotropic configurations.

- **Overall implications for LEBN control**
  - Across isotropic and anisotropic inflows, steady leading-edge blowing is most effective when the incidence is sufficiently negative, the jet ratio is high enough to impose spanwise dephasing without over-driving the flow, and the inflow scales are at least comparable to the orifice spacing.
  - Under these conditions, the dominant mechanism is a reduction of spanwise coherence and effective integration length at the leading edge rather than a simple reduction of turbulence intensity, which weakens gust-to-sound conversion while leaving the broadband source location essentially unchanged.

7.3 Chapter 6: Leading Edge Blowing to Mitigate Separation-Stall Noise from Aerofoil at High Angles of Attack

This chapter has assessed the potential of steady leading-edge blowing as an active control strategy for aerofoil separation stall noise at high effective angles of attack, α_{eff}. The main findings are:

- **Baseline separation stall noise and stall onset**
  - The baseline NACA 65(12)-10 at $U_\infty = 24\ \text{m}\,\text{s}^{-1}$ shows broadband noise over $3.1° \leq \alpha_{\text{eff}} \leq 20.7°$ with two regimes: Group 1 ($\alpha_{\text{eff}} \leq 12.3°$) where noise rises almost monotonically with lift, and Group 2 ($\alpha_{\text{eff}} > 12.3°$) where low frequency noise drops by up to about 8 dB while higher frequencies recover or increase.
  - Suction-side C_p distributions indicate attached or mildly separated flow at $\alpha_{\text{eff}} = 3.1°$, incipient separation stall at $\alpha_{\text{eff}} = 12.3°$, and a fully post-stall separated state at $\alpha_{\text{eff}} = 17.9°$.
  - Changes in overall PWL track the lift coefficient C_L closely across α_{eff}, so for the baseline aerofoil overall noise is strongly tied to aerodynamic loading.
- **Effect of leading-edge blowing on lift, drag and stall angle**
  - Blowing ratios $U_j/U_\infty = 0.35$, 2.10 and 3.89 delay stall but also modify C_L.
  - Stall moves from about $\alpha_{\text{eff}} = 11.1°$ (baseline) to about $12.1°$, $13.8°$ and $14.8°$ for high, medium and low blowing respectively, while the maximum C_L decreases progressively with jet ratio.
  - Drag is only weakly affected in pre-stall conditions, but all blowing ratios reduce C_D in the post-stall range; the low-ratio case can incur slightly higher drag in the stall region.
- **Far-field noise at stall and post-stall**
  - At stall ($\alpha_{\text{eff}} = 12.3°$), $U_j/U_\infty = 1.13$ leaves low frequency noise almost unchanged and increases high frequency levels due to jet noise, whereas $U_j/U_\infty = 3.08$ reduces noise by up to about 5 dB for $f < 500$ Hz but again raises high frequency content.
  - At post-stall ($\alpha_{\text{eff}} = 17.9°$), both jet ratios reduce low frequency noise, with the higher ratio generally more effective while high frequencies are dominated by jet self-noise.
  - A higher jet ratio is thus better for low frequency noise reduction, whereas a lower ratio is better for lift; once blowing is applied, noise no longer follows C_L trends in a simple way.
- **Mean flow and separation topology at stall**

  - At $\alpha_{\text{eff}} = 12.3^\circ$ the baseline flow shows a thick dead-air region near the suction surface and an overlying separating shear layer, indicating separation starting upstream of the trailing edge.
  - Medium blowing ($U_j/U_\infty = 1.13$) produces mean velocity fields very similar to the baseline, with only a slight lifting of the shear layer and negligible impact on low frequency noise.
  - High blowing ($U_j/U_\infty = 3.08$) thickens the dead-air zone and lifts and diffuses the shear layer, which appears as enhanced separation in the mean, yet still coincides with reduced low frequency noise, indicating that noise control is linked to turbulence structure rather than simple reattachment.

- **Turbulence structure, Reynolds shear stress and quadrant dynamics**
  - At stall, the baseline separating shear layer is the main turbulence production region, with strong positive $-\rho u'v'$ co-located with peak v_{rms}.
  - Medium blowing leaves these fields almost unchanged apart from a weak negative $-\rho u'v'$ streak above the shear layer, consistent with the small acoustic effect.
  - High blowing reduces $-\rho u'v'$ and v_{rms} in the shear layer and strengthens the negative streak above it, in line with the observed low frequency noise reduction.
  - Quadrant analysis shows that high blowing suppresses turbulence-generating Q2 events and promotes Q1 activity associated with upward high-momentum jets and secondary structures that partially neutralise the original shear layer.

- **Coherence between boundary-layer fluctuations and wall pressure**
  - For the baseline, high coherence between wall pressure and vertical velocity occurs in the separating shear layer over about 100 to 500 Hz, confirming this region as the dominant separation noise source.
  - For $U_j/U_\infty = 1.13$, coherence remains similar in level and frequency range, matching the small change in far-field noise.
  - For $U_j/U_\infty = 3.08$, coherence is significantly reduced in the same band and at the same wall-normal location, in direct correspondence with the reduced far-field PWL, which shows that noise mitigation arises from weakened velocity pressure coupling in the shear layer.

- **Overall implications for separation stall noise control**
  - Steady leading-edge blowing can delay stall, lower low frequency separation stall noise by several decibels in stall and post-stall regimes, and do so by reducing turbulence intensity, Reynolds shear stress and velocity pressure coherence in the separating shear layer through jet-induced secondary motions rather than by fully suppressing separation.

- There is a clear trade-off: higher jet ratios favour noise reduction but reduce maximum lift and raise high frequency jet noise, while lower jet ratios favour lift but are less effective for stall noise control.
- Since the jet angle was fixed in this study, the results identify discharge direction as a key optimisation parameter that could be exploited in future work to better balance stall delay, lift retention and separation stall noise reduction.

7.4 Future Work

Beyond the present study, several research directions appear to be largely unexplored in the open literature and therefore offer promising avenues for genuinely novel work:

- **Closed-loop, coherence-targeted leading-edge blowing.** Develop a feedback control strategy in which wall-pressure or near-field microphone signals are used in real time to modulate the leading-edge jets so as to minimise an objective based explicitly on spanwise coherence (rather than on mean lift or broadband SPL alone). To the author's knowledge, no study has yet demonstrated closed-loop leading-edge jet control aimed directly at reducing coherence-based source descriptors of airfoil self-noise or separation-stall noise.
- **Jet-vectoring as a primary design variable for stall-noise control.** Systematically vary and actively vector the discharge angle of the leading-edge jets (relative to the local surface and oncoming flow) across pre-stall, stall and post-stall conditions, with noise and coherence metrics as the optimisation target. Existing leading-edge blowing studies generally fix jet orientation for lift/drag benefits; a parametric and possibly time-varying jet-vectoring map explicitly tuned for separation-stall *noise* appears to be unexplored.
- **Extension to rotating blades in deep-stall operating windows.** Extend the leading-edge blowing concept from a canonical 2D aerofoil to a rotating blade (e.g. small-scale wind turbine or fan) operating near or beyond stall, with combined measurements of unsteady loading, stall noise and blade-to-blade coherence. A systematic study of leading-edge jets for *stall-noise mitigation* on rotating machinery, rather than for pure performance augmentation, appears to be largely absent from current literature.

References

[1] M. Basner et al. “Auditory and non-auditory effects of noise on health”. In: *The Lancet* 383.9925 (2014), pp. 1325–1332. DOI: 10.1016/S0140-6736(13)61613-X.

[2] International Civil Aviation Organization. *ICAO environmental report 2019*. Montréal: International Civil Aviation Organization, 2019.

[3] International Civil Aviation Organization. *Annex 16 to the Convention on International Civil Aviation: environmental protection, Volume I: aircraft noise*. As amended through Amendment 13 (20 July 2020). Montréal, 2017.

[4] M. E. Goldstein. *Aeroacoustics*. New York: McGraw-Hill, 1976.

[5] J. R. Stone, E. A. Krejsa, and B. J. Clark. *Jet noise modeling for supersonic business jet application*. Tech. rep. NASA/CR–2004-212984. Washington, DC: NASA, 2004.

[6] T. F. Brooks, D. S. Pope, and M. A. Marcolini. *Airfoil self-noise and prediction*. Tech. rep. NASA Reference Publication 1218. Hampton, VA: NASA Langley Research Center, 1989.

[7] M. Roger and S. Moreau. “Back-scattering correction and further extensions of Amiet’s trailing-edge noise model. Part 1: theory”. In: *Journal of Sound and Vibration* 286.3 (2005), pp. 477–506. DOI: 10.1016/j.jsv.2004.10.054.

[8] R. K. Amiet. “Noise due to turbulent flow past a trailing edge”. In: *Journal of Sound and Vibration* 47.3 (1976), pp. 387–393. DOI: 10.1016/0022-460X(76)90948-2.

[9] H. Arbey and J. Bataille. “Noise generated by airfoil profiles placed in a uniform laminar flow”. In: *Journal of Fluid Mechanics* 134 (1983), pp. 33–47. DOI: 10.1017/S0022112083003148.

[10] M. V. Lowson and S. P. Fiddes. “Aeroacoustic investigations of a laminar airfoil at moderate Reynolds number”. In: *Journal of Sound and Vibration* 154.3 (1992), pp. 465–484. DOI: 10.1016/0022-460X(92)90460-V.

[11] R. K. Amiet. “Acoustic radiation from an airfoil in a turbulent stream”. In: *Journal of Sound and Vibration* 41.4 (1975), pp. 407–420. DOI: 10.1016/S0022-460X(75)80105-2.

[12] A. McAlpine, E. C. Nash, and M. V. Lowson. “On the generation of discrete frequency tones by the flow around an aerofoil”. In: *Journal of Sound and Vibration* 222.5 (1999), pp. 753–779. DOI: 10.1006/jsvi.1998.2085.

[13] M. S. Howe. “Noise produced by a sawtooth trailing edge”. In: *Journal of the Acoustical Society of America* 90.1 (1991), pp. 482–487. DOI: 10.1121/1.401285.

[14] M. Gruber, P. F. Joseph, and T. P. Chong. “On the mechanisms of serrated airfoil trailing edge noise reduction”. In: *17th AIAA/CEAS Aeroacoustics Conference*. AIAA 2011-2781. Portland, Oregon, 2011. DOI: 10.2514/6.2011-2781.

[15] F. E. Fish and J. M. Battle. “Hydrodynamic design of the humpback whale flipper”. In: *Journal of Morphology* 225.1 (1995), pp. 51–60. DOI: 10.1002/jmor.1052250105.

[16] J. W. Kim, S. Haeri, and P. F. Joseph. “On the reduction of aerofoil–turbulence interaction noise associated with wavy leading edges”. In: *Journal of Fluid Mechanics* 792 (2016), pp. 526–552. DOI: 10.1017/jfm.2016.95.

[17] T. Geyer, E. Sarradj, and C. Fritzsche. “Measurement of the noise generation at the trailing edge of porous airfoils”. In: *Experiments in Fluids* 48 (2010), pp. 291–308. DOI: 10.1007/s00348-009-0739-x.

[18] A. R. Carpio et al. “Experimental characterization of the turbulent boundary layer over a porous trailing edge for noise abatement”. In: *Journal of Sound and Vibration* 443 (2019), pp. 537–558. DOI: 10.1016/j.jsv.2018.12.010.

[19] I. A. Clark et al. “Bioinspired trailing-edge noise control”. In: *AIAA Journal* 55 (2017), pp. 740–754. DOI: 10.2514/1.J055243.

[20] M. Wang and P. Moin. “Computation of trailing-edge flow and noise using large-eddy simulation”. In: *AIAA Journal* 38.12 (2000), pp. 2201–2209. DOI: 10.2514/2.904.

[21] D. P. Lockard. “An efficient, two-dimensional implementation of the Ffowcs Williams and Hawkings equation”. In: *Journal of the Acoustical Society of America* 107.2 (2000), pp. 874–884. DOI: 10.1121/1.428270.

[22] L. J. Ayton and J. Gill. “Airfoil noise prediction methods: current status and future challenges”. In: *Annual Review of Fluid Mechanics* 53 (2021), pp. 479–507. DOI: 10.1146/annurev-fluid-010719-060107.

[23] M. Gad-el-Hak. “Modern developments in flow control”. In: *Applied Mechanics Reviews* 49.7 (1996), pp. 365–379. DOI: 10.1115/1.3101931.

[24] M. Amitay and A. Glezer. “Controlled transients of flow reattachment over stalled airfoils”. In: *International Journal of Heat and Fluid Flow* 23.5 (2002), pp. 690–699. DOI: 10.1016/S0142-727X(02)00157-4.

[25] B. L. Smith and A. Glezer. “The formation and evolution of synthetic jets”. In: *Physics of Fluids* 10.9 (1998), pp. 2281–2297. DOI: 10.1063/1.869828.

[26] T. C. Corke, C. L. Enloe, and S. P. Wilkinson. “Dielectric barrier discharge plasma actuators for flow control”. In: *Annual Review of Fluid Mechanics* 42 (2010), pp. 505–529. DOI: 10.1146/annurev-fluid-121108-145550.

[27] M. M. Choudhari and M. R. Khorrami. “Active control of airfoil noise using surface blowing”. In: *9th AIAA/CEAS Aeroacoustics Conference*. AIAA 2003-3110. Hilton Head, South Carolina, 2003. DOI: 10.2514/6.2003-3110.

[28] L. N. Cattafesta and M. Sheplak. “Actuators for active flow control”. In: *Annual Review of Fluid Mechanics* 43 (2011), pp. 247–272. DOI: 10.1146/annurev-fluid-122109-160634.

[29] M. J. Lighthill. “On sound generated aerodynamically. I. General theory”. In: *Proceedings of the Royal Society of London. Series A, Mathematical and Physical Sciences* 211.1107 (1952), pp. 564–587. DOI: 10.1098/rspa.1952.0060.

[30] S. Moreau and M. Roger. “Compendium of airfoil self-noise”. In: *AIAA Journal* 47.1 (2009), pp. 68–84. DOI: 10.2514/1.41552.

[31] N. Curle. “The influence of solid boundaries upon aerodynamic sound”. In: *Proceedings of the Royal Society of London. Series A, Mathematical and Physical Sciences* 231.1187 (1955), pp. 505–514. DOI: 10.1098/rspa.1955.0191.

[32] J. E. Ffowcs Williams and D. L. Hawkings. “Sound generation by turbulence and surfaces in arbitrary motion”. In: *Philosophical Transactions of the Royal Society of London. Series A, Mathematical and Physical Sciences* 264.1151 (1969), pp. 321–342. DOI: 10.1098/rsta.1969.0031.

[33] M. S. Howe. *Acoustics of fluid-structure interactions*. Cambridge: Cambridge University Press, 1998. DOI: 10.1017/CBO9780511662898.

[34] P. R. Spalart. “On the precise implications of acoustic analogies for aerodynamic noise at low Mach numbers”. In: *Journal of Sound and Vibration* 332.11 (2013), pp. 2808–2815. DOI: 10.1016/j.jsv.2012.12.029.

[35] S. Lee et al. “Turbulent boundary layer trailing-edge noise: theory, computation, experiment, and application”. In: *Progress in Aerospace Sciences* 126 (2021), p. 100737. DOI: 10.1016/j.paerosci.2021.100737.

[36] A. Piccolo et al. “Turbulence distortion and leading-edge noise”. In: *Physics of Fluids* 36.12 (2024), p. 125183. DOI: 10.1063/5.0244627.

[37] S. Zhong et al. “An analytical correction to Amiet’s solution of airfoil leading-edge noise in non-uniform mean flows”. In: *Journal of Fluid Mechanics* 882 (2020), A29. DOI: 10.1017/jfm.2019.839.

[38] G. Lacagnina et al. “Mechanisms of airfoil noise near stall conditions”. In: *Physical Review Fluids* 4 (2019), p. 123902. DOI: 10.1103/PhysRevFluids.4.123902.

[39] J. M. Turner and J. W. Kim. “Aerofoil dipole noise due to flow separation and stall at a low Reynolds number”. In: *International Journal of Heat and Fluid Flow* 86 (2020), p. 108715. DOI: 10.1016/j.ijheatfluidflow.2020.108715.

[40] D. W. Carter and B. Ganapathisubramani. “Data-driven determination of low-frequency dipole noise mechanisms in stalled airfoils”. In: *Experiments in Fluids* 64.2 (2023). DOI: 10.1007/s00348-023-03577-z.

[41] S. Pröbsting and S. Yarusevych. “Laminar separation bubble development on an airfoil emitting tonal noise”. In: *Journal of Fluid Mechanics* 780 (2015), pp. 167–191. DOI: 10.1017/jfm.2015.427.

[42] R. W. Paterson et al. “Vortex noise of isolated airfoils”. In: *Journal of Aircraft* 10.5 (1973), pp. 296–302. DOI: 10.2514/3.60229.

[43] M. R. Fink. “Prediction of airfoil tone frequencies”. In: *Journal of Aircraft* 12.2 (1975), pp. 118–120. DOI: 10.2514/3.44421.

[44] E. C. Nash, M. V. Lowson, and A. McAlpine. “Boundary-layer instability noise on aerofoils”. In: *Journal of Fluid Mechanics* 382 (1999), pp. 27–61. DOI: 10.1017/S002211209800367X.

[45] S. Pröbsting, J. Serpieri, and F. Scarano. “Experimental investigation of aerofoil tonal noise generation”. In: *Journal of Fluid Mechanics* 747 (2014), pp. 656–687. DOI: 10.1017/jfm.2014.156.

[46] T. P. Chong and P. Joseph. ““Ladder” structure in tonal noise generated by laminar flow around an airfoil”. In: *The Journal of the Acoustical Society of America* 131.6 (2012), EL461–EL467. DOI: 10.1121/1.4710952.

[47] C. K. W. Tam and H. Ju. “Aerofoil tones at moderate Reynolds number”. In: *Journal of Fluid Mechanics* 690 (2012), pp. 536–570. DOI: 10.1017/jfm.2011.465.

[48] S. Pröbsting, F. Scarano, and S. C. Morris. “Regimes of tonal noise on an airfoil at moderate Reynolds number”. In: *Journal of Fluid Mechanics* 780 (2015), pp. 407–438. DOI: 10.1017/jfm.2015.475.

[49] T. P. Chong and P. F. Joseph. “An experimental study of airfoil instability tonal noise with trailing edge serrations”. In: *Journal of Sound and Vibration* 332.24 (2013), pp. 6335–6358. DOI: 10.1016/j.jsv.2013.06.033.

[50] S. Kumar and Y. G. Bhumkar. “Modification in airfoil’s tonal noise using periodic suction-blowing excitation”. In: *Journal of Sound and Vibration* 587 (2024), p. 118495. DOI: 10.1016/j.jsv.2024.118495.

[51] R. F. Miotto, W. R. Wolf, and L. D. de Santana. “Leading-edge noise prediction of general airfoil profiles with spanwise-varying inflow conditions”. In: *AIAA Journal* 56.5 (2018), pp. 1711–1716. DOI: 10.2514/1.J056716.

[52] L. J. Ayton and P. Chaitanya. “Analytical and experimental investigation into the effects of leading-edge radius on gust-aerofoil interaction noise”. In: *Journal of Fluid Mechanics* 829 (2017), pp. 780–808. DOI: 10.1017/jfm.2017.594.

[53] J. Gill, X. Zhang, and P. Joseph. “Symmetric airfoil geometry effects on leading-edge noise”. In: *The Journal of the Acoustical Society of America* 134.4 (2013), pp. 2669–2680. DOI: 10.1121/1.4818769.

[54] W. J. Devenport, J. K. Staubs, and S. A. L. Glegg. “Sound radiation from real airfoils in turbulence”. In: *Journal of Sound and Vibration* 329.17 (2010), pp. 3470–3483. DOI: 10.1016/j.jsv.2010.02.022.

[55] I. Evers and N. Peake. “On sound generation by the interaction between turbulence and a cascade of airfoils with non-uniform mean flow”. In: *Journal of Fluid Mechanics* 463 (2002), pp. 25–52. DOI: 10.1017/S0022112002008698.

[56] F. L. dos Santos et al. “Inflow turbulence distortion for airfoil leading-edge noise prediction for large turbulence length scales for zero-mean loading”. In: *The Journal of the Acoustical Society of America* 153.3 (2023), pp. 1811–1822. DOI: 10.1121/10.0017458.

[57] R. Zamponi et al. “On the role of turbulence distortion on leading-edge noise reduction by means of porosity”. In: *Journal of Sound and Vibration* 485 (2020), p. 115561. DOI: 10.1016/j.jsv.2020.115561.

[58] J. Gershfeld. “Leading-edge noise from thick foils in turbulent flows”. In: *The Journal of the Acoustical Society of America* 116.3 (2004), pp. 1416–1426. DOI: 10.1121/1.1780575.

[59] W. Dobrzynski. “Almost 40 years of airframe noise research: what did we achieve?” In: *Journal of Aircraft* 47.2 (2010), pp. 353–367. DOI: 10.2514/1.44457.

[60] S. Moreau, M. Roger, and J. Christophe. “Flow features and self-noise of airfoils near stall or in stall”. In: *15th AIAA/CEAS Aeroacoustics Conference*. AIAA 2009-3198. 2009. DOI: 10.2514/6.2009-3198.

[61] A. Laratro et al. “Self-noise and directivity of simple airfoils during stall: an experimental comparison”. In: *Applied Acoustics* 127 (2017), pp. 133–146. DOI: 10.1016/j.apacoust.2017.05.027.

[62] D. Raus et al. “Experimental study of the dynamic stall noise on an oscillating airfoil”. In: *Journal of Sound and Vibration* 537 (2022), p. 117144. DOI: 10.1016/j.jsv.2022.117144.

[63] P. Jaiswal, J. Rendón, and S. Moreau. “Aeroacoustic investigation of airfoil at near-stall conditions”. In: *Physics of Fluids* 35.9 (2023), p. 095132. DOI: 10.1063/5.0166646.

[64] J. A. Branch et al. “Aeroacoustic investigation of thin-airfoil stall with a view to improving the BPM model”. In: *Journal of Aerospace Engineering* 38.1 (2025), p. 04024099. DOI: 10.1061/JAEEEZ.ASENG-5705.

[65] F. Bertagnolio et al. “A semi-empirical airfoil stall noise model based on surface pressure measurements”. In: *Journal of Sound and Vibration* 387 (2017), pp. 127–162. DOI: 10.1016/j.jsv.2016.09.033.

[66] J. M. Turner and J. W. Kim. “Quadrupole noise generated from a low-speed aerofoil in near- and full-stall conditions”. In: *Journal of Fluid Mechanics* 936 (2022), A24. DOI: 10.1017/jfm.2022.75.

[67] D. Raus et al. “Experimental characterization of the noise generated by an airfoil oscillating above stall”. In: *27th AIAA/CEAS Aeroacoustics Conference*. AIAA 2021-2291. 2021. DOI: 10.2514/6.2021-2291.

[68] S. Moreau. “Airfoil self-noise and control: review and perspectives”. In: *International Journal of Aeroacoustics* 10.5-6 (2011), pp. 685–709. DOI: 10.1260/1475-472X.10.5-6.685.

[69] U. Michel, B. Barsikow, and A. Hellmig. “Airframe noise reduction: passive and active concepts”. In: *Progress in Aerospace Sciences* 93 (2017), pp. 1–32. DOI: 10.1016/j.paerosci.2017.05.001.

[70] J. W. Jaworski and N. Peake. “Aerodynamic noise from a poroelastic edge with implications for the silent flight of owls”. In: *Journal of Fluid Mechanics* 708 (2013), pp. 329–348. DOI: 10.1017/jfm.2012.366.

[71] J. M. Seiner, R. Reba, and J. C. Simonich. “Active flow and noise control: progress and future directions”. In: *Progress in Aerospace Sciences* 44.5 (2008), pp. 479–502. DOI: 10.1016/j.paerosci.2008.06.001.

[72] Y. Wang et al. “Experimental investigation of airfoil instability tonal noise reduction using structured porous trailing edges”. In: *Applied Sciences* 14.7 (2024), p. 2992. DOI: 10.3390/app14072992.

[73] Y. Al-Okbi, T. P. Chong, and O. Stalnov. “Leading edge blowing to mimic and enhance the serration effects for aerofoil”. In: *Applied Sciences* 11.6 (2021), p. 2593. DOI: 10.3390/app11062593.

[74] T. F. Brooks and W. M. Humphreys. “Effect of serrated trailing-edge modifications on broadband noise reduction”. In: *The Journal of the Acoustical Society of America* 131.6 (2012), EL393–EL399. DOI: 10.1121/1.4718574.

[75] P. C. Woodhead et al. “Aerofoil self-noise radiations subjected to serration flap angles”. In: *Experiments in Fluids* 62.152 (2021). DOI: 10.1007/s00348-021-03239-y.

[76] P. Chaitanya et al. “Performance and mechanism of sinusoidal leading edge serrations for the reduction of turbulence–aerofoil interaction noise”. In: *Journal of Fluid Mechanics* 818 (2017), pp. 435–464. DOI: 10.1017/jfm.2017.141.

[77] S. Narayanan et al. “Airfoil noise reductions through leading edge serrations”. In: *Physics of Fluids* 27.2 (2015), p. 025109. DOI: 10.1063/1.4907798.

[78] T. P. Chong et al. “On the effect of leading edge serrations on aerofoil noise production”. In: *24th AIAA/CEAS Aeroacoustics Conference*. AIAA 2018-3289. 2018. DOI: 10.2514/6.2018-3289.

[79] T. M. Biedermann et al. “Statistical–empirical modeling of airfoil noise subjected to leading-edge serrations”. In: *AIAA Journal* 55.9 (2017), pp. 3128–3142. DOI: 10.2514/1.J055633.

[80] L. L. Bowen et al. “The effect of leading edge porosity on airfoil turbulence interaction noise”. In: *The Journal of the Acoustical Society of America* 152.3 (2022), pp. 1437–1448. DOI: 10.1121/10.0013703.

[81] C. Teruna et al. “Numerical investigation of leading edge noise reduction on a rod–airfoil configuration using porous materials and serrations”. In: *Journal of Sound and Vibration* 494 (2021), p. 115880. DOI: 10.1016/j.jsv.2020.115880.

[82] C. Yang et al. “Active control of airfoil turbulent boundary layer noise with trailing-edge blowing”. In: *The Journal of the Acoustical Society of America* 153.4 (2023), p. 2115. DOI: 10.1121/10.0017787.

[83] T. P. Chong and C. Muhammad. “On the enhancement and suppression of turbulent wall pressure by the large eddy break-up devices”. In: *Physics of Fluids* 36.4 (2024), p. 045157. DOI: 10.1063/5.0195041.

[84] S. Santra and D. Greenblatt. “Dynamic stall control model for pitching airfoils with slot blowing”. In: *AIAA Journal* 59.1 (2021), pp. 400–404. DOI: 10.2514/1.J059818.

[85] X. Huang and X. Zhang. “Plasma actuators for noise control”. In: *International Journal of Aeroacoustics* 9.4-5 (2010), pp. 679–703. DOI: 10.1260/1475-472X.9.4-5.679.

[86] T. De Troyer et al. “Plasma-based dynamic stall control and modeling on an aspect-ratio-one wing”. In: *AIAA Journal* 60.5 (2022), pp. 2905–2915. DOI: 10.2514/1.J060933.

[87] European Commission. *FLOCON: adaptive and passive flow control for fan broadband noise reduction*. Tech. rep. FP7 Project 213411. Seventh Framework Programme (FP7), Transport (including Aeronautics), project duration 1 September 2008–31 August 2012. Brussels: European Commission, 2008.

[88] A. Naberezhnykh et al. “How applicable are turbulence assumptions used in the tidal energy industry?” In: *Energies* 16.4 (2023), p. 1881. DOI: 10.3390/en16041881.

[89] International Electrotechnical Commission. *IEC 61400-1: wind energy generation systems — Part 1: design requirements*. Includes Kaimal and von Kármán spectra in frequency domain with the 70.8 constant. Geneva, 2019.